UNIVERSITAT DE BARCELONA

High-pressure optical and vibrational properties of InN and InGaN

Robert Oliva Vidal

High-pressure optical and vibrational properties of InN and InGaN

Robert Oliva Vidal

Tesi presentada per a optar al títol de Doctor per la Universitat de Barcelona

Programa de doctorat: Nanociències

Director:

Jordi Ibáñez Insa

Institut de Ciències de la Terra Jaume Almera

Consell Superior d'Investigacions Científiques

Tutor: Blas Garrido Fernández

Departament d'Enginyeries: Secció d'Electrònica. Universitat de Barcelona

Universitat de Barcelona

Programa de Doctorat en Nanociències

Barcelona, 2016

High-pressure optical and vibrational properties of InN and InGaN

Tesi presentada per:

Robert Oliva Vidal

per a optar al títol de Doctor per la Universitat de Barcelona en el programa de doctorat de Nanociències

Director:
Dr. Jordi Ibáñez Insa
Institut de Ciències de la Terra Jaume Almera
Consell Superior d'Investigacions Científiques

Tutor:
Prof. Blas Garrido Fernández
Departament d'Enginyeries: Secció d'Electrònica. Universitat de Barcelona

Programa de Doctorat en Nanociències
Línia d'investigació: Nanomagnetisme, nanoelectrònica i nanofotònica

This PhD thesis has been developed at the Crystallography and Optical Properties Group from the Institute of Earth Sciences Jaume Almera (ICTJA-CSIC) under the FPI Program of the Spanish Ministry of Economy and Competitiveness. The research work has been funded by the project MAT2010-16116.

Acknowledgements

En primer lloc agraeixo al director d'aquesta tesi, el Dr. Jordi Ibáñez, tots els esforços que ha fet per a ajudar-me a progressar científicament. Li agraeixo especialment que m'hagi fet partícip i protagonista de tots els treballs realitzats durant aquests anys. També voldria destacar que sempre ha intentat ensenyar-me tots els seus coneixements en el camp de forma plenament didàctica. D'ell n'he après una forma de fer i viure la recerca, i la importància de treballar amb rigor. M'ha transmès passió per empènyer els límits del coneixement científic, i per a renovar-se i obrir-se als nous canvis que s'hi produeixen. També m'agradaria destacar la seva dimensió humana, la qual ha permès crear un clima de treball positiu i col·laboratiu. En particular, la seva capacitat d'empatitzar i anticipar-se a totes aquelles qüestions que deriven del treball en equip m'han aportat molta serenor a nivell emocional al llarg dels anys de doctorat.

Voldria agrair al Dr. Lluís Artús, Investigador Principal del Grup de Propietats Òptiques de l'ICTJA-CSIC, la confiança que va dipositar en mi des del primer moment per a desenvolupar una tesi doctoral en el seu grup. Agraeixo especialment la seva predisposició per a facilitar-me la tasca de recerca científica, així com donar-me accés i facilitats per a la realització de mesures experimentals en un laboratori d'espectroscòpia Raman perfectament equipat. El seu anhel pel treball ben fet sens dubte impregna aquesta tesi. També voldria destacar el seu suport per aconseguir una beca FPI del *Ministerio de Economía y Competitividad*, sense la qual aquesta tesi no hauria estat possible.

Al Dr. Ramon Cuscó vull agrair-li la seva amabilitat i paciència per a ajudar-me a resoldre problemes de recerca i de treball experimental al laboratori. Sempre m'he sentit molt còmode mantenint xerrades científiques amb ell, ja que aquestes sempre resulten ser molt profitoses i aclaridores.

Quisiera agradecer al Dr. Alfredo Segura la oportunidad que me ha brindado para realizar medidas experimentales bajo condiciones de alta presión mediante FTIR y absorción óptica en el Departamento de Física Aplicada de la Universidad de Valencia. Sin duda agradezco su dedicación y contribución para que los experimentos resultaran exitosos. También quisiera agradecer al Dr. Francisco Javier

Manjón que me haya permitido realizar medidas Raman de alta presión en la Universidad Politécnica de Valencia durante mis estancias en los años 2010-2013, así como sus contribuciones a los artículos publicados fruto de estas medidas.

Je remercie le Dr. Alain Polian pour l'accueil qu'il m'a réservé à l'Institut de Minéralogie, de Physique des Matériaux et de Cosmochimie de l'Université Pierre-et-Marie-Curie. Je lui sais plus particulièrement gré de la qualité de son enseignement des fondements de la spectroscopie de Brillouin à haute pression ainsi que du temps qu'il a bien voulu consacrer pour mes recherches.

Vull agrair a la Núria Domènech la seva agradable companyia de despatx al llarg d'aquests anys. Amb ella he mantingut interessants converses científiques i n'he après la importància de la metodologia i la constància en el treball. Ha sigut especialment interessant que m'introduís al "moment del cafè" com a excusa per a relacionar-se. Amb ella he pogut compartir les penes i les glòries que comporta la tasca de l'estudiant de doctorat (maleïdes unitats cgs!). No oblidaré els moments compartits en les excursions de grup als Pirineus, Montserrat o Collserola.

Quiero agradecer a todos los miembros del proyecto MALTA por su labor integradora, divulgativa y por supuesto de excelencia científica en el campo de la ciencia de las altas presiones. Los cursos que han diseñado para estudiantes de doctorado o de máster me han resultado muy enriquecedores desde un punto de vista competencial. Quiero hacer especial mención a todos los estudiantes o aspirantes a estudiantes de doctorado en el mundo de la alta presión, con quienes he podido compartir inquietudes e intereses, ya sea en congresos o tomando unas cervezas en nuevas ciudades. En especial quiero agradecer la buena compañía de Braulio García, Gloria Almonacid y Carlos Renero.

També vull donar les gràcies a totes aquelles persones que m'han ajudat a ampliar les meves capacitats en la realització de diferents tipus d'experiments i anàlisi de dades com el Lluís López, el Julio Pellicer, el Juan Angel, o el Catalin Popescu.

Fora de l'àmbit estrictament científic, vull agrair en primer lloc tot el suport que he rebut per part dels meus pares, el Rafael i la Maribel, al llarg de tota la meva vida. S'han bolcat en oferir-me uns estudis de qualitat, i en assegurar-me que els aprofités correctament. M'han educat en valors com la humilitat, la generositat o

l'esforç que sempre requereix la feina ben feta. Ells han sigut la guspira del meu interès per la ciència i la recerca; i m'han donat total suport en la persecució dels meus somnis, ajudant-me en tot allò que he necessitat mentre estudiava la carrera de Física, el màster i el doctorat. Els meus germans, el Víctor i la Laura, també han format part de la meva família i m'han acompanyat al llarg de tots aquests anys de doctorat, sempre mostrant interès per la temàtica de la meva recerca i proporcionant-me l'afecte que necessito. Alhora, em sento molt afortunat de tenir al meu costat quatre avis tan afables i intel·ligents. Tots ells, la Teresa, el Francesc, la Vicenta i el Júlio, m'han animat a seguir treballant en allò que saben que m'agrada. Sempre estaré en deute amb tots ells per tot el suport emocional que m'han regalat.

Aquest apartat d'agraïments no tindria sentit si no mencionés als meus amics de tota la vida, el Marc (*Mesa*), Sergi (*Txetxu*), Xavier (*Monto*), Guillem (*Clari*), Gerard (*Suko*), Miquel (*Yago*) i Albert (*Labat*). Ells m'han demostrat que un amic és un tresor, i que els amics de veritat mai es perden. M'he deixat d'incloure moltes amistats (també del Jaume Almera), ells/es ja saben qui són, totes elles m'han donat suport emocional al llarg de la tesi doctoral.

En darrer lloc, i de forma més especial, vull agrair a la meva parella, l'Estel·la, haver estat al meu costat i haver-me recolzat en tot moment. Ella ha sigut un pilar fonamental amb el que sempre he pogut comptar. També li agraeixo la paciència que ha tingut en aquells moments en que havia de dedicar hores addicionals a la realització dels treballs de la tesi. L'Estel·la m'ha aportat tot l'amor que podria desitjar.

Dedico aquesta tesi

a la Maribel i el Rafael,

els meus pares

Table of contents

CHAPTER 1

Introduction

1.1. Motivation and scope of this thesis

Semiconductors play a key role in our daily life, as they are at the heart of virtually all technological products such as computers and smartphones, light-emitting diode (LED) lamps, flat-screen monitors, photovoltaic cells, fiber-optic communication systems, medical devices, military and civil aerospace systems, sensing devices, etc. The semiconductor industry, with the support of numerous public research centers worldwide, faces the challenge of designing new applications and improving the performance of existing devices. Also, there is a continuous need to develop new materials and devices with improved optical and electronic properties. This is the case of group III-nitride semiconductors, which have become the focus of extremely intensive research over that last decades due to their remarkable physical properties and which are already being used in numerous electronic and optoelectronic devices. Research on III-nitrides was boosted in the 90s with the attainment of *p*-type gallium nitride (GaN), which permitted the commercial production of efficient blue light-emitting diodes (LEDs) based on the indium gallium nitride ($In_xGa_{1-x}N$) ternary alloy and GaN. For this achievement, I. Akasaki, H. Amano and S. Nakamura were awarded with the 2014 Nobel Prize in Physics.[1,2]

Additional research efforts were put into the growth and characterization of the InGaN alloy after the discovery of the low energy bandgap of InN in 2002,[3–5] which was established at ~0.65 eV. Such low value implies that the direct bandgap of InGaN covers a wide spectral range (see Fig. 1.1), from the infrared for InN to the ultraviolet for GaN (3.4 eV). Thus, InGaN emerges as a promising candidate to design and fabricate novel light-emitting and light-detecting devices, such as LEDs or solar cells, operating over a large range of wavelengths.

Despite the high technological interest of the InGaN alloy and its compositional end-members, the optical, electronic and vibrational properties of

these compounds are not yet fully understood. In particular, there are still open questions with regard to the optical and vibrational properties of InN and InGaN at high hydrostatic pressures. With regard to this, we would like to recall that the application of high pressures is a highly valuable tool in semiconductor physics, since pressure provides a controlled means to tune the fundamental properties of the investigated material.[6] In particular, high-pressure optical techniques provide a highly useful benchmark to test computational models (such as density functional theory) to calculate the structural, vibrational or electronic properties of semiconductors. The organization of the series of the HPSP (High-Pressure in Semiconductor Physics) conferences as a satellite of the International Conference on the Physics of Semiconductors (ICPS), sponsored by the International Union of Pure and Applied Physics (IUPAP), provides a hint about the importance of high-pressure studies in semiconductor science.

In order to investigate the optical and electronic properties of semiconductors at room and high-pressure conditions, optical techniques such as absorption or photoluminescence are routinely employed. For instance, absorption experiments allow one to measure the optical gaps and observe the direct-to-indirect bandgap transition of InN at high pressure,[7] which takes place after a wurtzite-to-rocksalt phase transition at around 13 GPa. However, there are still open questions with regard to the pressure dependence of the bandgaps of InN, like for instance the effect of free electrons on the experimental pressure coefficients of the wurtzite polymorph. This is also the case of other relevant properties of this compound such as the refractive index or the dielectric constants. With regard to rocksalt InN, very few works dealing with the high-pressure optical properties of this phase can be found in the literature. And, in the case of InGaN, it is not even clear whether the room-pressure optical emission of the as-grown samples is dominated by band-to-band transitions or by localized states, and therefore the interpretation of the high-pressure optical experiments is not straightforward. In this case, very scarce information about the compositional dependence of the phase-transition pressure and the indirect bandgap of the rocksalt phase has been published so far.

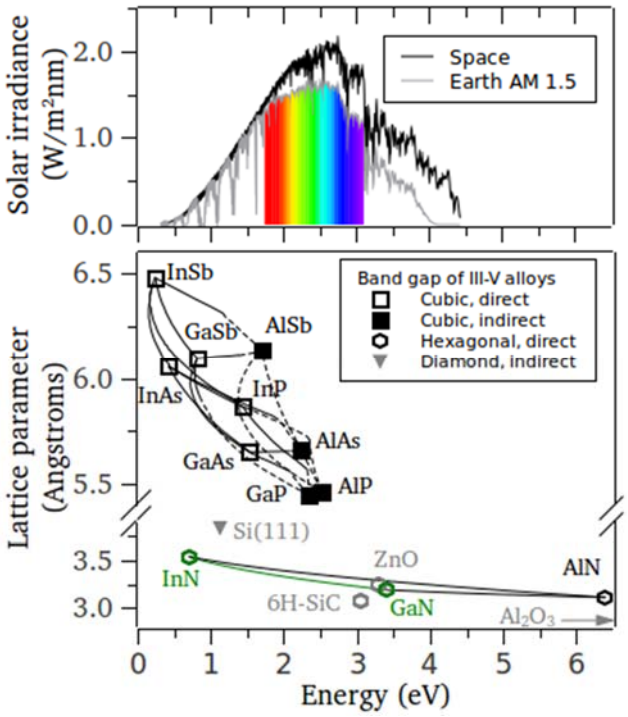

Fig. 1.1.

Upper panel: The solar radiation spectra as provided by the American Society for Testing and Materials (ASTM) as a function of energy. The spectra were taken on earth at AM 1.5 and Earth orbit.

Bottom panel: The direct (solid lines) and indirect (dashed lines) band gap energy of III-V semiconductors and other important crystals is plotted as a function of the in-plane lattice parameter. It can be seen that only InGaN (highlighted in green colour) and InAlN covers most of the solar spectral range. Note that the InGaN alloy can be grown on a variety of substrates (show in grey colour).

Raman spectroscopy is now a standard tool for the study of semiconductor materials and structures.[8] At room pressure, Raman scattering provides a wealth of information on crystal quality, strain, composition, sample orientation and even on electronic properties and free-carrier effects. At high pressures, information about phase stability can be gained, and thermodynamic properties such as the mode Grüneisen parameters can be experimentally determined. In the case of InN, several high-pressure Raman-scattering studies on InN have been published so far.[9,10] Despite these previous investigations, there are still open questions with regard to the high-pressure lattice dynamics of InN, like for instance the pressure-behaviour of the large wavevector longitudinal optical (LO) modes, which have been shown to be excited through a double-resonance excitation process.[11] On the other hand, a relatively large dispersion of pressure coefficients and mode Grüneisen parameters for both the polar and nonpolar modes of wurtzite and rocksalt InN can be found in the literature. The observed discrepancies could be in part related to residual strains in the studied epilayers, and therefore it would be interesting to perform high-pressure Raman experiments on layers grown on different substrates and/or with different levels of residual strain. In the case of heavily doped n-type samples, the coupling of LO phonons with free carriers gives rise to the LO-plasmon coupled modes

(LOPCMs). The pressure dependence of the LOPCMs could provide interesting information about the electronic structure of InN. With regard to the compositional behaviour of the optical phonons of InGaN at room conditions, there are also some open questions like, for instance, the effect of strain and lateral compositional inhomogeneities on the experimental frequencies of the optical modes. At high pressure, no data are available so far with regard to the phonon pressure coefficients and mode Grüneisen parameters of InGaN.

Thus, the aim of this thesis is to gain further knowledge on the high-pressure optical and vibrational properties of InN and InGaN. The fundamental properties of these materials at room pressure are also revisited when necessary, which is particularly relevant in the case of the InGaN alloy, for which special attention is paid to the compositional dependence of the optical bandgaps and phonon frequencies.

Objectives of this work

The aim of this thesis is to deepen the understanding of the optical and vibrational properties of both InN and the InGaN ternary alloy at room and high-pressure conditions. For this purpose, different spectroscopic techniques such as Raman spectroscopy, Brillouin spectroscopy, optical absorption, Fourier transform infrared (FTIR) spectroscopy or photoluminescence have been employed to investigate these compounds. In the case of high-pressure experiments, the diamond anvil cell technique has been used. Structural and lattice-dynamical *ab initio* calculations based on the density function theory (DFT) have also been performed in order to analyse and complement the experimental results.

Next, we list the main objectives of this thesis:

- To measure the optical band gap of wurtzite and rocksalt InN as a function of pressure and to study the effect of free-electron density on the pressure behaviour of the bandgap in the case of the wurtzite phase

- To re-evaluate the composition dependence of the band gap of InGaN and its pressure dependence
- To study the pressure dependence of the refractive index and high-frequency dielectric constant of wurtzite and rocksalt InN
- To revisit the composition behaviour of the optical phonons of the InGaN alloy, evaluating the effect of selective resonance on the frequency of the A_1(LO) mode and the effect of strain on the frequency of the E_{2h} and A_1(LO) modes
- To study the acoustic phonon modes of InGaN epilayers and also in InGaN/GaN superlattices at room conditions, with the aim of obtaining information about the compositional dependence of the sound velocity and elastic constants
- To experimentally determine the pressure coefficients of the Raman-active phonon modes of InN and InGaN and to obtain their corresponding mode Grüneisen parameters
- To investigate the pressure dependence of the LOPCMs in highly-doped, n-type InN

1.2. Outline of this thesis

The present thesis is grounded in the results of different studies dealing with the optical and vibrational properties, at room and high-pressure conditions, of InGaN and InN epilayers and InGaN/GaN superlattices. This thesis is presented as a compendium of nine articles that have been published in international journals of the first and second quartile. All the work included in these papers has been carried out during the thesis period.

In the next chapter (Chapter 2) the experimental setup of the high-pressure experiments performed in this work is described. The results of this thesis are then presented in the following chapters (Chapters 3 to 5), entitled "Optical properties of InN", "Vibrational properties of InN" and "Optical and vibrational properties of InGaN". These chapters include a general introduction, where an overview of the known physical properties and perspectives of the studied materials is given, as well as the theoretical framework behind the work that has been performed. In some cases, additional results and analyses are provided in order to support and extend the results published in the articles. The articles published after this thesis can be found attached to each of the corresponding chapters. The main conclusions reached throughout this thesis are listed in the last chapter, entitled "Summary and conclusions" (Chapter 6).

1.3. References

[1] S. Nakamura, J. Vac. Sci. Technol. A **13**, 705 (1995).
[2] S. Nakamura, Science **281**, 956 (1998).
[3] V.Y. Davydov, A. a. Klochikhin, R. p. Seisyan, V. v. Emtsev, S. v. Ivanov, F. Bechstedt, J. Furthmüller, H. Harima, A. v. Mudryi, J. Aderhold, O. Semchinova, and J. Graul, Phys. Status Solidi B **229**, r1 (2002).
[4] J. Wu, W. Walukiewicz, W. Shan, K.M. Yu, J.W. Ager, E.E. Haller, H. Lu, and W.J. Schaff, Phys. Rev. B **66**, 201403 (2002).
[5] M. Hori, K. Kano, T. Yamaguchi, Y. Saito, T. Araki, Y. Nanishi, N. Teraguchi, and A. Suzuki, Phys. Status Solidi B **234**, 750 (2002).
[6] T. Suski and W. Paul, *High Pressure in Semiconductor Physics I and II, Semiconductors and Semimetals Vols. 54 and 55* (Academic Press, 1998).
[7] J. Ibáñez, A. Segura, F.J. Manjón, L. Artús, T. Yamaguchi, and Y. Nanishi, Appl. Phys. Lett. **96**, 201903 (2010).
[8] A.F. Goncharov and A.F. Goncharov, Int. J. Spectrosc. Int. J. Spectrosc. **2012, 2012**, e617528 (2012).
[9] C. Pinquier, F. Demangeot, J. Frandon, J.-C. Chervin, A. Polian, B. Couzinet, P. Munsch, O. Briot, S. Ruffenach, B. Gil, and B. Maleyre, Phys. Rev. B **73**, 115211 (2006).
[10] C. Pinquier, F. Demangeot, J. Frandon, J.W. Pomeroy, M. Kuball, H. Hubel, N.W.A. van Uden, D.J. Dunstan, O. Briot, B. Maleyre, S. Ruffenach, and B. Gil, Phys. Rev. B **70**, 113202 (2004).
[11] V.Y. Davydov, A.A. Klochikhin, A.N. Smirnov, I.Y. Strashkova, A.S. Krylov, H. Lu, W.J. Schaff, H.-M. Lee, Y.-L. Hong, and S. Gwo, Phys. Rev. B **80**, 081204 (2009).

CHAPTER 2

Experimental methods

In the present thesis the optical and vibrational properties of several III-nitride semiconductor materials are studied under high-pressure conditions. Throughout this work, pressure is applied by using a diamond anvil cell (DAC). This type of cells is widely employed in experimental high-pressure physics because they allow performing experiments well above 5 GPa and because the diamonds provide optical access to the samples, from the far infrared to the ultraviolet spectral range. In this thesis, different optical measurements are performed at ambient and high-pressure conditions. These techniques are widely employed in materials science, and therefore their working principles can be found in any standard textbook. Much less information can be found in the literature in relation to high-pressure measurements. Thus, in the present chapter we focus on the description of the experimental setups for the high pressure optical and vibrational measurements performed in this thesis.

2.1. The diamond anvil cell

High-pressure techniques were initially developed during the first decades of the 20th century, when Percy W. Bridgman achieved pressures above 10^5 Kg_F/cm^2 (~10 GPa). This achievement supposed a large breakthrough taking into account that machinery at that time could not overcome $3 \cdot 10^3$ Kg_F/cm^2. He was awarded (1946) with the Nobel Prize in Physics "*for the invention of an apparatus to produce extremely high pressures, and for the discoveries he made therewith in the field of high pressure physics*". A second revolution took place in 1959 when the DAC was designed simultaneously by the National Bureau of Standards (NBS) and the University of Chicago. Ever since, high-pressure techniques have been largely developed and incorporated in a large variety of experimental methods covering many scientific disciplines.

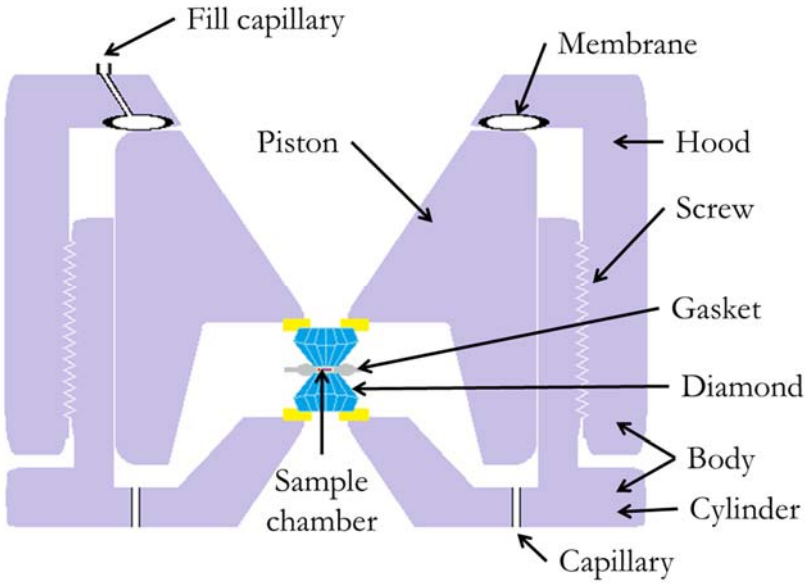

Fig. 2.1. Schematic representation of the membrane-type DAC. This is composed of three independent parts, the piston, and those comprising the body: the cylinder and the hood.

All the high-pressure experiments presented on this thesis have been performed using DACs. The operation of the DAC relies on the very definition of pressure, P,

$$P = \frac{F}{A}, \qquad [2.1]$$

where F is the force applied to a surface with total area A. In order to achieve great pressures, a moderate force is applied in a large area which is transmitted to a smaller area (the anvils), where the sample is located. Diamond, which exhibits an exceptionally high hardness, is the best choice material for the anvils. By using DACs, pressures up to the megabar (~100 GPa) can be generated. Moreover, the fact that diamond is transparent along a wide spectral range, from far infrared to visible and UV radiation, allows one to perform *in situ* spectroscopic measurements at high hydrostatic pressures.

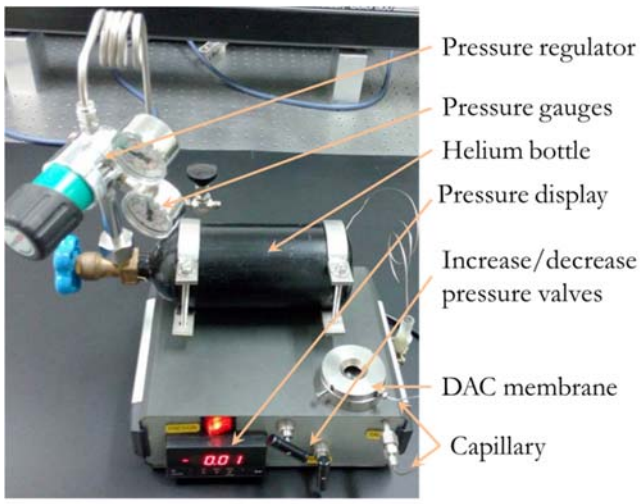

Fig. 2.2. Picture of pressure controller device. The helium from the bottle (~200 bar) travels to a second stage of reduced pressure (controlled by the regulator, ~60 bar). The pressure in the membrane of the DAC (shown in the pressure display) is increased or released using needle-type valves.

Experimental setup

A scheme of the membrane-type DAC as used in this thesis is shown in Fig. 2.1. It can be seen that the DAC is composed of three independent parts; the piston, the cylinder and the hood as it can be seen in the figure. A metallic membrane in the hood is responsible of applying pressure to the piston and cylinder. A gasket is set between the diamonds; it contains a small hole (~200 μm) in which the sample, the ruby and the pressure transmitting medium are located. A cross-section representation of the gasket is shown in Fig. 2.1.

Force generation, anvils and gasket preparation

Uniaxial pressure is applied to the anvils using pneumatic pressure applied to the membrane, as depicted in Fig. 2.1. The gas used in this thesis is helium, which prevents metal corrosion. Pressures up to 60 bar are applied to the membrane of the DAC. At this membrane pressure values, the pressure inside the DAC is around ~20 GPa.

A figure of the pressure-control system is shown in Fig. 2.2. It consists of two valves that connect the helium bottle with the DAC membrane via a metallic capillary. The first valve is a manorreductor and is used to reduce the ~200 bar down to a

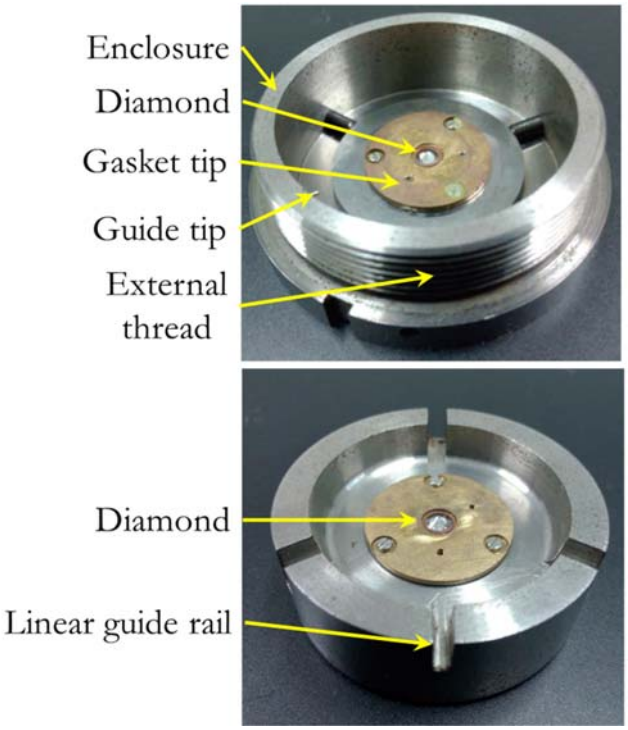

Fig. 2.3.
Pictures of the two anvils used in this thesis.

Upper picture: Cylinder part in which the gasket is fit. A guide tip inside the enclosure is used to guide the piston (bottom picture) for the closure.

Bottom picture: Piston that slides inside the cylinder part. A linear guide rail is used to ensure that the gasket-diamonds relative position is maintained after the indentation.

pressure ~10 bar above that desired inside the DAC. The second valve is a needle valve that allows for a precise regulation of gas flow. In order to prevent damaging the DAC, the pressure is never increased or released at a rate higher than 2 bar/minutes.

The anvils of the DAC here used are two CVD-grown IIa type diamonds with a diameter of 4 mm and a culet size of 480 μm. The diamonds exhibit low birefringence and ultra-low fluorescence, which allows performing Raman-scattering measurements with low background signal. The Raman active mode of diamond is at 1332 cm^{-1}; second-order Raman signal below this frequency is very low.

A picture of the unmounted piston and cylinder is shown in Fig. 2.3. The sample and rubies are typically prepared on the diamond of the cylinder, where the gasket is fixed with the help of two small tips. Once the pressure transmitting medium is poured into the gasket cavity, the piston (bottom picture) slides inside the enclosure following a linear guide rail and rests on the top of the gasket, closing the high-pressure cavity. This process must be carried out carefully and smoothly in order to avoid breaking the diamonds by sudden impact.

The gaskets here used were made of Inconel or steel. Pre-indentations are performed by using the DAC in order to decrease the thickness of the central part of

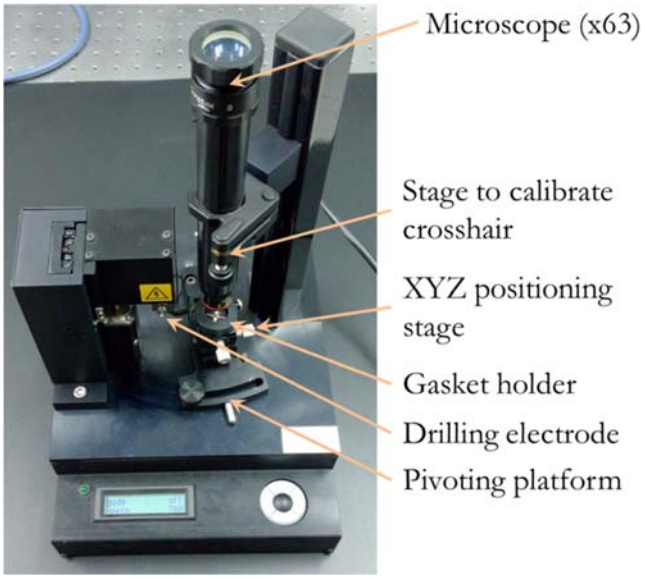

Fig. 2.4.
Micro-driller used to perform the holes in the gasket. A pivoting platform is used to sweep the sample between the drilling stage and the optical stage. Calibration screws attached to the microscope allow to manually align the system so that a test hole coincides with the microscope crosshair. Once the position of the hole is well determined, the drilling at the center of the indentation can be performed.

the gasket down to ~50 μm. Then, a ~200 μm diameter hole is drilled by electrical discharge machining (EDM). In general, the lower the thickness the larger the pressure it can be reached, but the diameter of the hole can increase or decrease as the pressure is increased. Hence, the gasket thickness and hole size values will depend on the experimental conditions (such as maximum target pressure or sample size) and diamond culet size.

The device here used for the hole drilling is a Boehler μDriller (easyLab), a picture of which is shown in Fig. 2.4. An ocular is used to gain optical access to the gasket. For the drilling procedure, the first step is to perform a test hole in the gasket away from the indentation; this is done by sweeping the gasket stage with a pivoting platform from the optical stage to the drilling stage where an electrode automatically drills the gasket by spark eroding. Then, the gasket holder is brought to the optical stage, and the position of the crosshair is set to the hole with the help of a positioning calibration stage. The XYZ positioning stage is manipulated to bring the crosshair on the center of the indentation. Finally, a hole is drilled in the drilling stage and it is checked that the hole is well centered on the indentation.

The pressure-transmitting medium and pressure calibration

In this thesis, a mixture of methanol-ethanol-water (16:3:1), also referred as MEW, has been used as a pressure transmitting medium. This liquid allows performing measurements up to 15 GPa with fairly good hydrostaticity. The Raman

signal from MEW is low but non-negligible for experiments with large acquisition times (~30 minutes using a laser power of 100 mW). Raman bands appear in the frequencies 884 cm^{-1}, 1034 cm^{-1} and 1097 cm^{-1}.[1] Other liquids can be used as pressure transmitting medium, such as noble gases. While these provide a fairly good hydrostaticity for pressures beyond 15 GPa, it is more expensive and time consuming to load a DAC with these gases. In this case powerful compressors are required to liquefy the gas and fill the whole DAC. When the liquid has entered the cell from the bottom capillaries depicted in Fig. 2.1, the body is strongly closed so that liquid is retained inside the high-pressure cavity. Then, the excessive liquefied noble gas is released by decreasing the pressure and the DAC is ready to use.

It is not possible to stablish a reliable correspondence between the applied pressure to the membrane with the pressure inside the DAC. In fact, as expected for a quasi-elastic system, an hysteresis curve is found when plotting the membrane pressure versus the pressure in the DAC for the upstroke and downstroke cycles. Hence, it is necessary to independently measure the pressure inside the DAC. In this thesis, the pressure has been determined by the ruby fluorescence method which allows one to accurately measure pressures up to 50 GPa.[2] This is done by leaving small Cr-doped corundum (α-Al_2O_3) chips (~5 μm diameter) close to the sample inside the gasket hole. Under excitation, two emission lines arise from energy levels of $3d^3$ electrons, which are the R_1 (694.25 nm) and R_2 (692.86 nm) lines. The pressure coefficient of these lines is approximately 0.3646 nm/GPa, but it can be calculated more precisely by using the following expression for the R1 line,[3]

$$P = \frac{A}{B}[(\lambda/\lambda_0)^B - 1], \qquad [2.2]$$

with the values A = 1876, B = 10.71 and λ_0 = 694.25 nm.

2.2. Optical reflectivity and absorption

As is well known, electromagnetic radiation impinging on a material can be reflected (from its surface), transmitted or absorbed. The fraction of energy involved in each of these processes receives the name of reflectance, R, transmittance, T, and absorptance, A. Due to conservation of energy

$$R + T + A = 1\,. \qquad [2.3]$$

These three physical magnitudes clearly depend on photon energy, since the optical spectrum of a given material is determined by its fundamental properties. For instance, it is well known that absorption processes in semiconductors are determined by the gaps within the electronic structure of the material, and therefore the optical experiments allow one to measure the energy the optical bandgaps and, in high-pressure experiments, their pressure dependence.

Experimental setup

A schematic representation of the experimental setup for optical absorption is shown in the panel A of Fig. 2.5. Deuterium, tungsten or halogen lamps have been used in this thesis in order to perform absorption, reflectance or FTIR measurements in the IR-UV range. A chopper connected to a lock-in amplifier is used to improve the signal to noise ration. The aperture diaphragms act as a small focus and spatial filter, decreasing parasitic light and fixing the optical axis of the system. A folding mirror (FM), allows exciting the ruby in the DAC with a visible laser. A beam splitter gives optical access to the sample, so that the 3D stage can be adjusted to focus the beam onto the sample or ruby. The pressure is measured from the R1 fluorescence line of the ruby. The ruby spectra is measured using a laser beam and an Ocean multichannel spectrophotometer connected to the eyepiece with an optical fiber.

The experimental setup for the reflectivity or transmittance measurements in the FIR excitation range is shown in the panel B of Fig. 2.5. Here, gold-coated 90º reflective mirrors and Cassegrain-type objectives (15× magnification) have been used. A thermal light source (Globar™) has been used, coupled with a Michelson FTIR

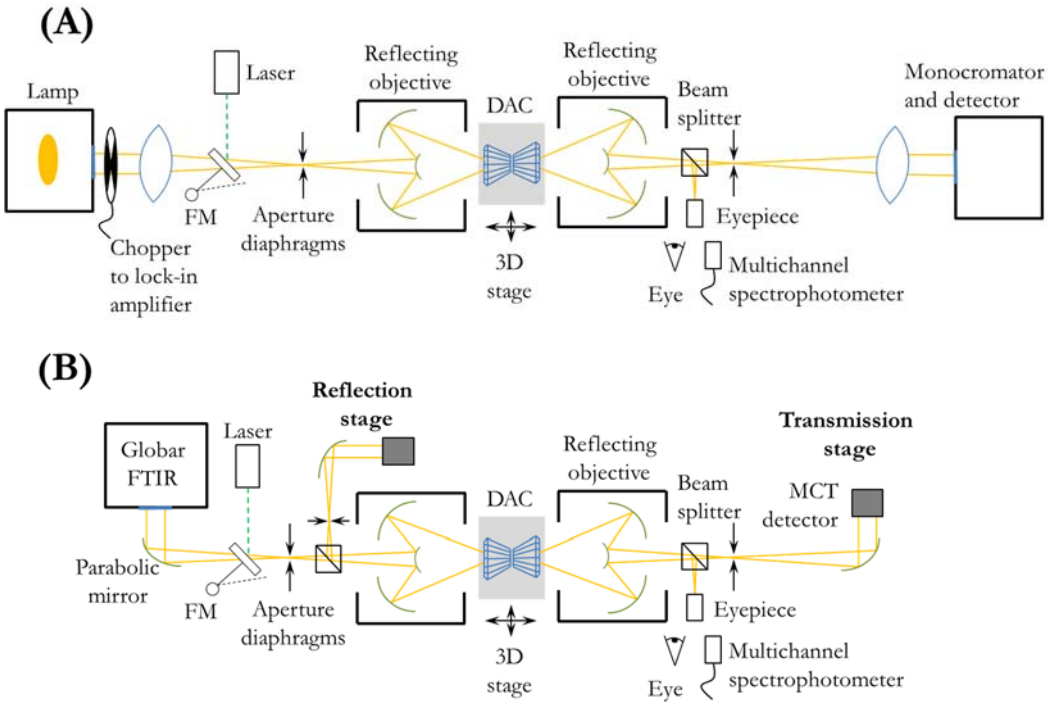

Fig. 2.5. Panel A; (top) experimental setup for high-pressure optical absorption measurements. **Panel B;** (bottom) experimental setup for high-pressure reflectance and transmittance FTIR measurements.

spectrometer (TEO 400 FTIR Module by Science Tech). The exit window is made of KBr. The second aperture diaphragm is used to control the size of the IR beam onto the sample. The signal is recorded by using nitrogen-cooled mercury-cadmium-telluride (MCT) detectors. The Diamond is transparent in the 10-100 μm wavelength range. Typical low-frequency FTIR measurements are performed using CsI, He, Ne or Ar as a pressure transmitting medium, which allow measurements in the 50-1000 cm^{-1} window. For the measurements performed in this thesis, KBr has been used, which allows measurements in the 400-5000 cm^{-1} range.

2.3. Photoluminescence and Raman scattering

The study of optical emission (luminescence) provides a wealth of information about the bandgaps and impurity levels in semiconductor materials and structures. In turn, Raman scattering, i.e., the inelastic light scattering by phonons or other dynamical excitations in materials, is a powerful, nondestructive technique that allows one to obtain information about the crystal quality, composition or the strain state of semiconductor compounds. In this thesis we have performed photoluminescence

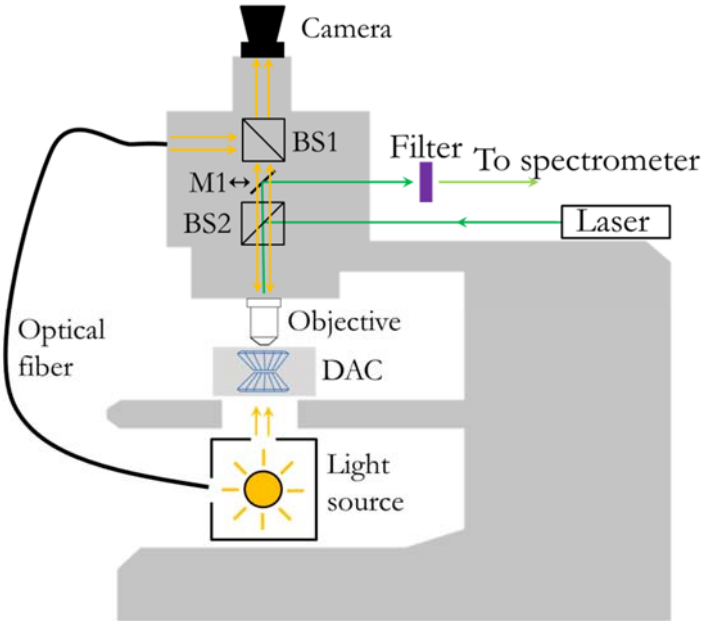

Fig. 2.6.

Schematic representation of the experimental setup for PL and Raman measurements mounted on a microscope. The DAC is fixed on a 3D stage. The optical access to the sample and focus of the laser beam is achieved by a series of beam splitter (BS1 and BS2) and a folding mirror (M1).

(PL) and Raman scattering measurements at ambient conditions and as a function of hydrostatic pressure. Next, we briefly describe the typical setup for high-pressure PL and Raman experiments.

Experimental setup

A schematic representation of the experimental setup for PL and Raman measurements as used in this thesis (both setups are basically analogue) is shown in Fig. 2.6. A microscope is required in order to focus the laser beam into a microscopic sample inside the DAC and to collect the optical emission or the inelastically scattered radiation. The diameter of the focused laser spot into the DAC is typically around 5 μm.

For the PL measurements, single-grating spectrometers have been employed in this thesis: i) Jobin Yvon T64000 in single-mode of operation (see below), equipped with a liquid nitrogen-cooled CCD; ii) Horiba Jobin Yvon FHR 1000, equipped with a Peltier-cooled CCD; iii) USB2000+ spectrometer from Ocean Optics. The microscope objective employed in this thesis (Olympus) has a large working distance, 18 mm, and 50× magnification. A notch filter is positioned before the spectrometer in order to subtract the laser wavelength. In turn, most of the Raman experiments presented in this thesis have been performed using a T64000 Jobin Yvon

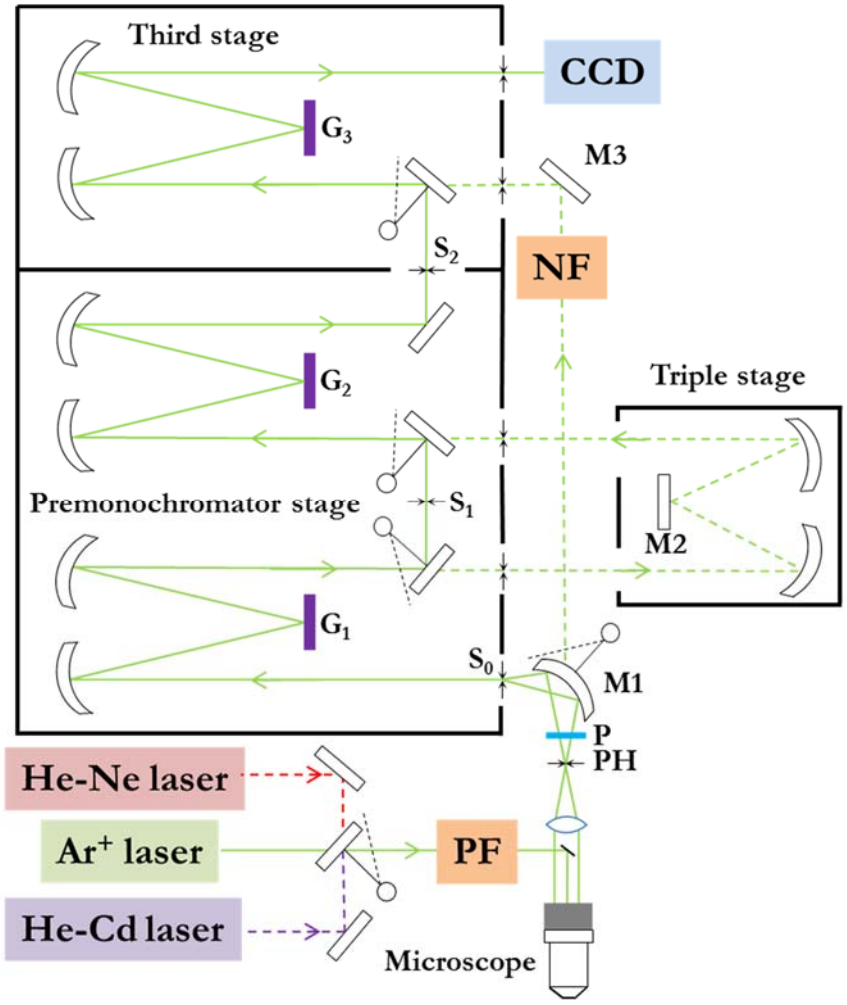

Fig. 2.7. Schematic representation of the T-64000 Jobin Yvon spectrometer used for high-pressure Raman measurements. All the equipment is placed on an optical table with pneumatic legs to isolate the system from vibrations.

spectrometer. A sketch of this spectrometer is shown in Fig. 2.7. The Jobin-Yvon T64000 Raman spectrometer contains three diffraction gratings that can work in the three different modes of operation: the double subtractive configuration, the triple additive configuration, and the single-stage configuration.

In the double subtractive configuration, the first grating (G_1) in the so-called premonochromator stage is used to scatter the light so that an intermediate slit (S_1) can block the laser light (Rayleigh radiation), which is necessary to protect the detector (the CCDs are highly sensitive and could be damaged by intense light beams) and, more important, to gain access to scattered wavelengths very close to that of the excitation laser. Indeed, the double subtractive configuration allows performing measurements in the low-frequency region of the Raman shift (down to 5 cm^{-1} for

visible light). A second grating is used to recompose the rest of (unfiltered) wavelengths into the S2 slit. The collected light then enters the third stage (monochromator) where the third grating (G_3) acts as a simple monochromator.

In the triple additive configuration, the three gratings (G_1−G_3) are employed to successively disperse and analyse the collected radiation, which is achieved by by-passing the intermediate slit (S1) through the triple stage (the optical path is shown in figure 2.6 as a dashed line). This configuration allows one to perform high-resolution measurements (around 0.7 cm^{-1} for visible wavelengths), in contrast with the resolution achieved with the double subtractive configuration (around 2 cm^{-1}).

Finally, in the single-stage mode of operation, the spectrometer acts as a simple monochromator, i.e., the collected light enters into the spectrometer directly through the last stage of the spectrometer, where it is dispersed analysed with grating G_3.

In this thesis three lasers have been used to excite the PL and Raman measurements:

- **Helium-Cadmium laser (Research Electro-Optics):** The emission lines are 441.6 nm and 325 nm. A filter is used to select only the 325 nm line. The output power is <50 mW.
- **Frequency-doubled Nd:YAG diode laser (Spectra Physics):** The emission line is 532 nm and the output power is < 300 mW.
- **Argon-ion laser (Spectra Physics)**: The emission lines are 351.1 nm, 363.8 nm, 454.6 nm, 457.9 nm, 465.8 nm, 476.5 nm, 488.0 nm, 496.5 nm, 501.7 nm, 514.5 nm, 528.7 nm and 1092.3 nm. One of these lines is selected by a prism inside the optical (resonant) cavity. Then, an external plasma filter is used to remove plasma lines around the selected excitation line. This is particularly important for Raman measurements, which involves very small signals. A popular line in Raman scattering is the 514.5-nm line. Typical working powers are around 10 mW − 100 mW. In order to avoid laser heating effects, it is usually necessary to reduce the output power, which can be accomplished by using optical filters.

- **Helium-Neon laser (Research Electro-Optics):** The emission lines are 543.5 nm, 593.9 nm, 611.8 nm and 632.8 nm. A filter is used to select only the 632.8-nm line. The output power is 35 mW.

2.4. Brillouin spectroscopy

Brillouin scattering is a non-destructive technique that allows measuring the inelastic scattering of light by acoustic phonons. From this technique valuable information on the opto-elastic properties of crystals can be obtained, and the elastic stiffness of both liquids and solids can be measured. This technique offers many practical advantages over other techniques; it doesn't require a special sample preparation and allows performing measurements on microscopic sample volumes. High-pressure[4] and high-temperature[5] Brillouin experiments can also be performed. Since the experimental setup required for Brillouin scattering is comparatively much less known than that for Raman or PL, next we will describe with some detail the equipment used in this thesis.

Experimental setup

The high-resolution Brillouin scattering (HRBS) measurements presented in this thesis have been performed with a triple-pass tandem Fabry-Perot interferometer and using the 514.5-nm line of an Ar^+ laser.[6] The fundamentals of the working principle of a Fabry-Perot interferometer and tandem interferometry are provided in this section.

Detection

Owing to the fact that the Brillouin setup here used consists of two Fabry-Perot interferometers that scans the spectrum wavelengths by means of a piezoelectric stage, there is no need to use a multichannel detector and the signal is recorded by using a single channel detector. For the detection we used a photon counting detector (module Perkin Elmer MP series 900+). The signal is displayed in

an oscilloscope and stored in a multichannel analyzer (MCA multichannel analyzer). The data is then send to a computer that records and process the Brillouin spectra.

The Fabry-Pérot interferometer

Brillouin measurements require high spectral resolution (in the order of MHz−GHz) and for this reason a Fabry-Pérot interferometer (FP, or etalon) is used. It consists of two mirrors facing each other with a spacing d. The transmission condition will be given by,

$$d = \frac{m\lambda_m}{2} \ , \qquad [2.4]$$

where m is an integer and λ_m are the wavelengths that will be transmitted. The spacing between two successive transmitted wavelengths, $\Delta\lambda$, is known as the free spectral range (FSR), and its ratio to the width of a given transmitted peak is known as finesse, F, which is a quality factor that primarily depends on the mirrors flatness (typically better than $\lambda/200$) and reflectivity (typically R~92-96%).

From Eq. [2.4], it can be seen that the FP can be used as an spectrometer because each wavelength can be scanned by varying the spacing, d. However, the transmission condition is valid for many orders, m, which makes it difficult to unambiguously interpret the resulting spectra. In general, this method only works if the whole spectrum is inside the FSR range. Since, $\Delta\lambda \approx \lambda^2/2d$, a large spectral range can be achieved by decreasing d, but the width of the transmitted peaks increases as d is reduced, hence decreasing the resolution. Therefore, a compromise between resolution and spectral range is pursued. The mirror spacing, d, is minimized so that the target Brillouin peak is inside the FSR. The relation between the FSR and mirror spacing is given by,

$$\nu(Hz) = \frac{c(\frac{m}{s})}{2d(m)} \ , \qquad \nu(GHz) \approx \frac{150}{d(mm)} \ , \qquad [2.5]$$

where c is the speed of light.

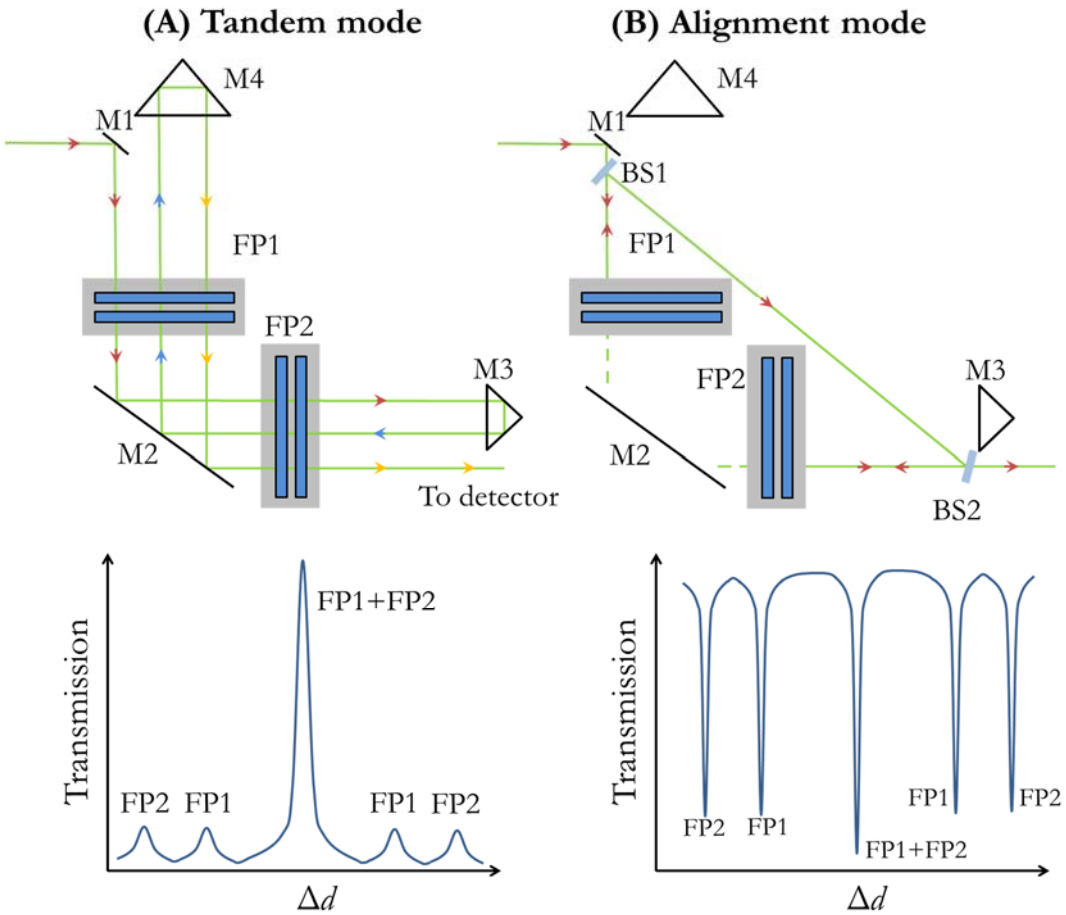

Fig. 2.8. Schematic representation of the arrangement of a tandem triple-pass Fabry-Perot interferometer in the **(A)**; tandem mode and **(B)**; alignment mode. The transmitted beam for each configuration is shown below (the transmission scale is logarithmic).

Tandem interferometry

There exists one practical solution to increase the FSR without losing resolution. It consists in arranging two FPs in series along the optical path, each FP has a different thickness, d_1 and d_2. The beam is sequentially passed through each FP three times (with an overall of six pass), as shown in the panel A of Fig. 2.8. A spacing $d_1 - d_2$ can be found so that one wavelength satisfies the transmission condition (see Eq. [2.4]) for both FP simultaneously, which is known as synchronization. A typical transmitted spectrum when synchronization is achieved can be seen in the panel A of Fig. 2.8. Note that the other four beams are attenuated as a consequence of the different FSR of each FP. The peaks will not coincide until several times the FSR of FP1, hence by using the tandem system it has been possible to largely extend the FSR

without losing resolution. In order to prevent that the transmitted ghosts of the FP1 are too obtrusive, similar thickness values $d_1/d_2 \approx 0.95$, are used.

In the tandem mode, the scanning, δd, must be performed synchronously and satisfying the amplitude scanning condition $\delta d_1/\delta d_2 = d_1/d_2$ (typical scanning values are in the order of $\delta d \approx 2$ μm) for a given FSR. This can be done by fixing one mirror of each FP and moving simultaneously the other two in a direction that satisfies the amplitude scanning condition. This method allows maintaining a good synchronization within an error of 20 Å.

Before the tandem mode is operational it is necessary to align the mirrors and adjust the relative spacing. This is achieved with a series of piezoelectric transducers mounted on the mirrors. As shown in the panel B of Fig. 2.8, the beam is reflected on the etalons and directed to the detector. The alignment mode relies on a simple principle; when the FP is transmitting the reflected intensity tends to zero. The mirrors are completely parallel when the transmitted spectrum exhibit deep bands, as shown below the experimental setup, in the panel B of Fig. 2.8. Once the alignment is done, the beam splitters, BS1 and BS2, are removed and the system is ready to perform Brillouin measurements in the tandem mode.

Early Brillouin scattering (BS) measurements were limited to transparent materials, but after the development of the tandem multi-pass interferometer, opaque materials could be studied with the so-called surface Brillouin spectroscopy (SBS).[7,8] A theoretical description of both techniques is given in Chapter 5 for the study of InGaN epilayers.

Scattering configurations

Brillouin or Raman scattering experiments allow one to measure the phonons of the center of the Brillouin zone (i.e. the Γ point) because the wavenumber of visible light (for a backscattering experiment, $k \approx 3 \cdot 10^7$ m^{-1}) is typically three orders of magnitude lower than that of the edge of the Brillouin zone (e.g. the A-point of the Brillouin zone of InN, $k \approx 10^{10}$ m^{-1}). Unlike the frequency of optical phonons, which exhibit an almost flat dispersion, the acoustic modes exhibit an almost linear

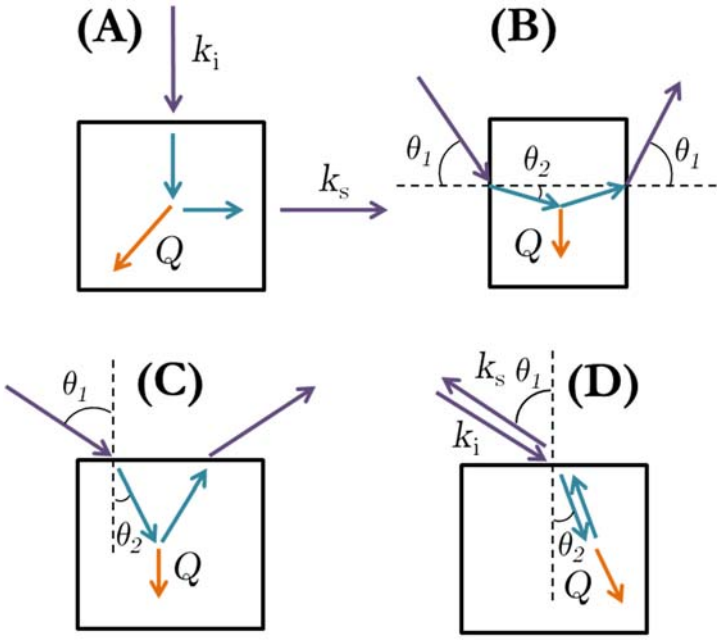

Fig. 2.9.

Four typical Brillouin scattering geometries. **(A)** 90º scattering, **(B)** platelet, **(C)** reflection, **(D)** backscattering. The wave vectors of the incident and scattered light beam are represented with purple (blue) arrows outside (inside) the sample. The resulting acoustic phonon, with wavevector $\boldsymbol{Q}$, is represented with an orange arrow.

dispersion with the wavevector. Around Γ, the slope of the acoustic branch corresponds to the velocity of the wave in the medium. Hence, the Brillouin shift, typically expressed in GHz is given by

$$\nu = v \cdot Q \ , \qquad [2.6]$$

where v is the phase velocity of the sound wave with wavevector, Q. Thus, in order to determine v, it is important to precisely know the value of Q.

Typical Brillouin scattering geometries for bulk acoustic waves are shown in Fig. 2.9. The values of Q for the 90º geometry is

$$Q = \sqrt{2}nk \ , \qquad [2.7]$$

for the platelet geometry, using the Snell's law,

$$Q = 2nksin(\theta_2) = 2ksin(\theta_1) \ , \qquad [2.8]$$

for the reflection scattering geometry,

$$Q = 2k\sqrt{n^2 - sin^2\theta_1} \ , \qquad [2.9]$$

and for the backscattering geometry,

$$Q = 2nk \ , \qquad [2.10]$$

where $k = 1/\lambda$, is the wavevector of the incident (scattered) radiation.

Note that, only the platelet geometry allows measuring the velocity without the need to know the refractive index of the medium. In fact, Eq. [2.8] is still valid even if the sample is inside a DAC as long as θ_1 corresponds to the angle of incidence in air. It is also important to note that, for some of these configurations, the flatness of the samples is critical, and mechanical polishing might not be sufficient to obtain satisfactory results.[9]

For an opaque material, surface acoustic waves (SAW) dominate the Brillouin spectrum, and the scattering geometry used to measure these modes is backscattering. Under this configuration, only the wavevector components parallel to the surface are real and the phonon wavevector is given by $Q = 2nsin(\theta_1)k$, where θ_1 is the angle of incidence with respect to the normal vector of the surface.

2.5. References

[1] D. Singh, Y. Li, and S.C. Sharma, J. Raman Spectrosc. **36**, 24 (2005).
[2] K. Syassen, High Press. Res. **28**, 75 (2008).
[3] A.D. Chijioke, W.J. Nellis, A. Soldatov, and I.F. Silvera, J. Appl. Phys. **98**, 114905 (2005).
[4] C. Zha, R.J. Hemley, H. Mao, T.S. Duffy, and C. Meade, Phys. Rev. B **50**, 13105 (1994).
[5] E.S. Zouboulis and M. Grimsditch, J. Appl. Phys. **70**, 772 (1991).
[6] R. Mock, B. Hillebrands, and R. Sandercock, J. Phys. [E] **20**, 656 (1987).
[7] J.R. Sandercock, in *Proc. Seveth Int. Conf. Raman Spectrosc.* (W. F. Murphy (Ed.), Paris, 1980).
[8] J.R. Sandercock, in *Proc. Second Int. Conf. Light Scatt. Solids Paris* (M. Balkanski (Ed.), Paris, 1971), pp. 9–12.
[9] S. Speziale, H. Marquardt, and T.S. Duffy, Rev. Mineral. Geochem. **78**, 543 (2014).

CHAPTER 3

Optical properties of InN

3.1. Introduction

Since the growth of the first wurtzite InN (w-InN) samples,[1] the determination of the fundamental properties of this compound has been hindered by the low crystalline quality of the grown material. Early investigations established the fundamental bandgap (E_G) of w-InN grown by sputtering techniques[2] and metalorganic vapor phase epitaxy[3] around $E_G \approx 1.9$ eV. Some of the difficulties for determining E_G were low PL signal at room temperature, large concentrations of oxygen, which might lead to oxynitrides with wide bandgaps,[4–6] or the Burstein-Moss effect which takes place in low-quality, unintentionally n-type doped InN.[7] On the other hand, important discrepancies arose in theoretical band-structure calculations. Typical calculated values of the fundamental bandgap were about $E_G \approx 1.1$ eV, as reported by Davydov et al. in 2002 by means of *ab initio* calculations.[8] With the improvement of the crystal quality of wurtzite InN (w-InN) by means of epitaxial techniques, several authors found that the fundamental bandgap was around $E_G = 0.7$ eV in 2002.[9–14] Later, the fundamental bandgap was finally established at $E_G = 0.65$ eV at room temperature.[6,15,16]

It was then clear that a revision of the electronic band-structure calculations and a re-evaluation of the fundamental parameters of InN was needed.[17] For this reason, large efforts were put into the improvement of growth methods as well as the characterization of the electronic, structural, optical and vibrational properties of InN.[18–25] It was concluded that InN exhibits excellent electronic properties. For instance, the effective mass of InN is the lowest amongst all III-V group semiconductors. This implies large mobilities (at ambient temperature mobilities of of 2200 $cm^2V^{-1}s^{-1}$ have been measured[26]) and large drift velocities (peak velocities around $3 \cdot 10^7$ cm/s have been reported[17]). Moreover, InN can be alloyed with GaN or AlN, thus making it possible to extend the direct bandgap from IR to the visible

and UV energies. Hence, the range of applications of InN and InGaN for optoelectronic devices is very wide.

Since the technological interest of InN is high, it is crucial to accurately determine its fundamental properties in order to understand the performance of new devices based on this compound. From this perspective, the use of high-pressure techniques is highly valuable because it enables to gain further insight into the optical, structural, and vibrational properties of semiconductors.[27] Despite the huge amount of research carried out for indium nitride to date, many questions remain to be solved regarding the pressure behavior of InN.

In fact, there are still open issues concerning the high-pressure optical properties of wurtzite InN (the stable phase at room conditions). In particular, the pressure coefficient of the fundamental direct bandgap has not been precisely determined. This is due to difficulties in the measurement by optical techniques. For the case of PL measurements, some of these handicaps are radiative impurity bands or the presence of high electron concentration effects, which will be explained in detail throughout this chapter. Concerning the high-pressure phase (rocksalt), *rs*-InN, an indirect bandgap of ≈1 eV was reported.[28] Nevertheless, the epilayer measured in that work was too thin (500 nm) to obtain an absorbance spectra with enough resolution. This fact made it difficult to precisely determine the value of the rocksalt indirect bandgap and its pressure dependence.

The growth of zinc-blende InN has also been demonstrated using molecular beam epitaxy on specific substrates.[29] Note that while most research is devoted to w-InN, some theoretical studies have focused on the electronic properties of the zinc-blende structure.[30–32] On the other hand, the rocksalt phase of InN is only stable at high-pressure. Early theoretical calculations[33–37] found a large range of values for the transition pressure (5 GPa[33] < P_t < 25.4 GPa[34]), which has been later experimentally established around $P_t = 13$ GPa[38–40,28,41,42] by means of X-ray diffraction, Raman scattering and optical techniques. The differences in the reported experimental values could be explained by biaxial strain arising from the substrate or by the low crystalline quality of the investigated samples. In this context, the study of high-quality material is necessary to determine P_t more accurately.

Another fundamental property of InN that needs further investigation is the pressure coefficient of the high-frequency dielectric constant, which has not been experimentally measured so far under high pressure. While many efforts have been devoted to investigate experimentally and theoretically the DF (DF) of InN at ambient conditions,[21,43,44] important discrepancies arise regarding its pressure dependence. Christensen et al.[35] performed band-structure calculations to investigate the effect of hydrostatic pressure on the optical and structural properties of InN and other III-V group semiconductors. They obtained a relative pressure coefficient for the high-frequency dielectric constant of $d ln\varepsilon_\infty/dP = -8.6 \cdot 10^{-3}$ GPa^{-1}, reporting a low bandgap value for InN, $E_G \approx 0.43$ eV, slightly below the currently accepted value $E_G = 0.65$ eV. Abbar et al.[45] performed first-principle calculations and obtained a much higher relative pressure coefficient, of $-68.0 \cdot 10^{-3}$ GPa^{-1}. On the other hand, other first-principle calculations focused on the zinc-blende structure. These works are also relevant for the evaluation of the optoelectronic properties of the wurtzite polytype because both structures are closely related (the atomic coordination is four, with similar cohesion energies), with similar densities (6.81 for w-InN[46] and 6.97 g/cm^3 for *zb*-InN[47]) and comparable bandgaps (0.65 eV for w-InN and ~0.64 eV for *zb*-InN[29]). But the relative pressure coefficient values reported for *zb*-InN also show important discrepancies. Wang et al.[31] found a value similar to that reported by Christensen et al., $-7.4 \cdot 10^{-3}$ GPa^{-1}. However, other authors[30] reported more recently a much larger pressure coefficient, $-52.0 \cdot 10^{-3}$ GPa^{-1}, closer to the value reported by Abbar et al.[45] Note that the discrepancies on this parameter are as large as one order of magnitude. Therefore, an experimental determination of the pressure coefficient of the high-frequency dielectric constant is highly desirable. Moreover, the study of the high-frequency dielectric constant allows one gaining a deeper insight into the nature of the chemical bonding owing to the fact that the volume dependence of the high-frequency dielectric constant is related with the ionicity of the material.

The aim of this chapter is to investigate the high-pressure optical properties of w-InN and rs-InN. In particular, we study in some detail the effect of free electron density on the high-pressure optical absorption of w-InN. A reevaluation

of the indirect bandgap of rs-InN is presented, and a comprehensive study of the pressure dependence of the refractive index of both w-InN and rs-InN is carried out. In this chapter, we will introduce different conceptual aspects required in the discussion of the main results here obtained (Section 3.2), which are then presented in Section 3.3 (list of published works).

Goals of this chapter

- To determine the pressure coefficient of the fundamental bandgap of wurtzite InN.
- To evaluate the effect of electron density on the optical bandgap of w-InN and its pressure dependence.
- To measure the wurtzite to rocksalt transition pressure (P_t) by means of high-pressure absorption measurements and compare this value with reported Raman and XRD measurements.
- To determine the fundamental indirect bandgap of rs-InN and its pressure dependence.
- To determine the pressure coefficient of the refractive index and high-frequency dielectric constant of w-InN and compare the results with theoretical determinations published in the literature.
- To measure the refractive index and high-frequency dielectric constant of rs-InN and its pressure coefficient.

List of samples used in this chapter

In this chapter, high-pressure optical measurements are performed on a set of high-quality InN epilayers grown on sapphire (Al_2O_3) substrates or GaN/Al_2O_3 templates, which are listed in Table 3.1. The electron densities, obtained by Hall-effect measurements, the nominal thickness, and the corresponding substrates are displayed in the table.

In this chapter, high-pressure optical absorption and Fourier transform infrared spectroscopy (FTIR) measurements are performed. Note that these samples

Sample	Structure	N_e ($\cdot 10^{18}$ cm^{-3})	Nominal thickness (μm)
A	InN/GaN/Al_2O_3	2	0.5
B1	InN/Al_2O_3	6.5	0.4
B2	InN/Al_2O_3	16	0.4
C	InN/Al_2O_3	0.5	5.7 (3.4)
D	InN/Al_2O_3 (a-face)	4	0.5

Table 3.1. List of InN samples used in this chapter.[41,42,49,50] Sample A is grown on a buffer layer of GaN, and sample D is grown along the a-face crystallographic direction. Residual electron concentrations as measured from Hall-effect and nominal thickness are shown. Note that the thickness value of the sample C reported in Article 3.2. is 3.4 μm, as was optically determined on a small flake used for the experiments. This value is lower than the nominal thickness of the epilayer (5.7 μm).

are ideal for performing optical absorption experiments because the bandgap energy of InN with low electron concentration, around 0.7 eV, is much lower than those of the substrate materials. On the other hand, the thickest InN layer (sample C) is particularly well suited to perform an accurate measurement of the indirect bandgap of rocksalt InN because the absorbance spectra are better resolved in thicker layers.[41] Moreover, the larger thickness of this sample allows detection of multiple internal reflections in the IR, which we have used to determine the refractive index of w-InN and rs-InN as a function of pressure.

3.2. Theoretical framework

Transmission of light in a dielectric medium

From a macroscopic point of view, the interaction of radiation with matter is described by the Maxwell's equations. The DF, $\varepsilon(\omega)$, provides a measure of how a dielectric medium responds to a frequency-dependent electric field. For a homogeneous, isotropic, linear (HIL) medium the DF is,

$$\boldsymbol{D} = \varepsilon(\omega)\mathbf{E} \ , \qquad [3.1]$$

where $\boldsymbol{D}$ is the displacement electric field originated by the external electric field $\boldsymbol{E}$. In general, $\varepsilon(\omega)$ is a complex second rank tensor. Under the HIL assumption the DF is a scalar,

$$\varepsilon = \varepsilon_1 + \mathrm{i}\varepsilon_2 \ , \qquad [3.2]$$

which is related to the complex refractive index, $\tilde{n}$ by

$$\varepsilon = (n + \mathrm{i}\kappa)^2 = \tilde{n}^2, \qquad [3.3]$$

where n and κ are the real and imaginary parts of the complex refractive index, respectively. The imaginary part, κ, is also known as the extinction coefficient.

Considering that the electromagnetic radiation can be described by plane waves propagating along the $\boldsymbol{k}$ direction with frequency w, the electric and magnetic fields of the light are,

$$\boldsymbol{E} = \boldsymbol{E}_0 \mathrm{e}^{i(\boldsymbol{kr}-\omega t)} \ , \qquad [3.4]$$

and,

$$\boldsymbol{H} = \boldsymbol{H}_0 \mathrm{e}^{i(\boldsymbol{kr}-\omega t)} \ , \qquad [3.5]$$

respectively. The relation of the wavevector in the vacuum, $\boldsymbol{k}_0$, and the medium, $\boldsymbol{k}$, is given by,

$$\boldsymbol{k} = \tilde{n}\boldsymbol{k}_0 \ . \qquad [3.6]$$

Using Eqs. [3.3] −[3.6],

$$\boldsymbol{E} = \boldsymbol{E}_0 \mathrm{e}^{-\boldsymbol{k}\boldsymbol{r}} \mathrm{e}^{i(n\boldsymbol{k}_0\boldsymbol{r}-\omega t)} \ , \qquad [3.7]$$

The transmitted electromagnetic flux intensity inside a medium can be calculated with Poynting's theorem,

$$\Phi_{\mathrm{T}} = |\boldsymbol{E} \times \boldsymbol{H}^*| = \boldsymbol{E}_0 \boldsymbol{H}_0 \mathrm{e}^{-2\kappa \boldsymbol{k}_0 \boldsymbol{r}} = \Phi_0 \mathrm{e}^{-2\kappa \boldsymbol{k}_0 \boldsymbol{r}} \ , \qquad [3.8]$$

where Φ_0 is the incoming flux; the absorption coefficient can then be defined as,

$$\alpha = \frac{4\pi\kappa}{\lambda_0} \ . \qquad [3.9]$$

For an arbitrary direction, $\hat{\boldsymbol{r}}$, the transmittance of the medium is just,

$$\mathrm{T} = (1 - \mathrm{R}) \frac{\Phi_{\mathrm{T}}}{\Phi_0} = (1 - R) e^{-\alpha d} \ . \qquad [3.10]$$

At energies below the bandgap semiconductor materials are transparent, $\alpha = 0$ and therefore $\mathrm{T} = (1 - \mathrm{R})$. The transmittance and reflectance spectra can then be readily obtained by using the Fresnel equation

$$\mathrm{R} = \left| \frac{n_1 - n_2}{n_1 + n_2} \right|^2 , \qquad [3.11]$$

where n_1 and n_2 are the refractive index outside and inside the medium respectively, which is real in transparent materials.

However, when the energy of the photons is higher than the electronic bandgap, the material becomes opaque and $\alpha \neq 0$. In this case, if the reflectivity is not strongly dependent on the frequency, from Eq. [3.10] it can be seen that the transmission spectra will basically depend on $\alpha(\omega)$.

Optical absorption in semiconductors

The fundamental absorption in a semiconductor refers to the transition of an electron in the maximum of the valence band to the minimum of the conduction band by an incident photon. The lineshape of the fundamental absorption edge will

thus depend on the shape of the electronic structure of the conduction and valence bands around the fundamental bandgap, of energy E_g. The absorption coefficient is defined as the power lost from the incident beam per unit volume and per unit of incident flux of electromagnetic energy,

$$\alpha(h\nu) = \frac{(h\nu) \times P}{|\boldsymbol{S}|}\ , \qquad [3.12]$$

where $\boldsymbol{S}$ is the Poynting vector, which is related to the incident electromagnetic flux, and P represents the number of transitions per unit of volume and time.

Typically, the optical bandgap of semiconductor crystals may be obtained from the experimental $\alpha(h\nu)$ curves by representing a so-called Tauc plot,[48] which is based in the fact that the absorption coefficient of semiconductors depends on photon energy as

$$\alpha(h\nu) = \frac{B}{h\nu}(h\nu - E_g)^n\ , \qquad [3.13]$$

where B is the Tauc coefficient, $h\nu$ the energy of the photon and n is a parameter that depends on the nature of the electronic transitions. For direct bandgap semiconductors $n = 1/2$, while for the case of indirect bandgap $n = 2$ (see the next subsections).

Direct bandgap absorption

Electric dipole transitions, which are responsible for absorption in semiconductors, can be described within time-dependent perturbation theory.[49] Assuming that the electronic transition is allowed, the transition probability, P, per unit of time of a photon with energy $h\nu$ is given by Fermi's Golden Rule:

$$P = \frac{2\pi}{\hbar}|\langle v|H_{em}|c\rangle|^2 g(\omega) = \frac{2\pi}{\hbar}\left(\frac{e}{mc}\right)^2 |A||\langle v|p|c\rangle|^2 g(\omega), \qquad [3.14]$$

where $\langle v|$ and $|c\rangle$ are the initial (valence band) and final (conduction band) states involved in the absorption process, $g(\omega)$ is the joint density of states, and H_{em} is the electromagnetic interaction Hamiltonian, which depends on the vector potential

$\boldsymbol{A}(\boldsymbol{r},t)$. Note that the matrix element of Eq. [3.14] has been derived under the electric dipole approximation. The joint density of states for an M_0 critical point (direct bandgap) is[49]

$$g(\omega) = \frac{1}{2\pi^2}\left(\frac{2\mu}{\hbar^2}\right)^{\frac{3}{2}}\sqrt{h\nu - E_g}\ , \qquad [3.15]$$

where μ is the reduced mass. From Eq. [3.12] it follows that

$$\alpha(h\nu) \propto \frac{1}{h\nu}\sqrt{h\nu - E_g}\ , \qquad [3.16]$$

thus obtaining Eq. [3.13] with $n = 1/2$.

Indirect bandgap absorption

For an indirect bandgap transition process the energy and momentum must be conserved. Hence, the participation of a phonon is necessary. The conservation of momentum is achieved by the emission or absorption of one phonon with the momentum, $\boldsymbol{q}$,

$$\pm\boldsymbol{q} = \boldsymbol{k}_v - \boldsymbol{k}_c\ , \qquad [3.17]$$

where $\boldsymbol{k}_v$ and $\boldsymbol{k}_c$ are the momentum of the electron in the valence and conduction bands respectively. The photon momentum has been neglected in Eq. [3.17] (dipole approximation). The condition for conservation of energy is given by,

$$h\nu = E_{cv} \pm E_p\ , \qquad [3.18]$$

where E_p is the phonon energy and E_{cv} the difference in energy between the conduction and valence band edges.

The indirect absorption is a second order process and therefore the transition probability is given by

$$P = \frac{2\pi}{\hbar}\left|\sum_i \frac{\langle c|H_{ep}|i\rangle\langle i|H_{em}|v\rangle}{E_{i0} - h\nu}\right|^2 g(\omega)\ , \qquad [3.19]$$

where H_{ep} is the electron- phonon interaction Hamiltonian. It can be proven that the joint density of states satisfying Eq. [3.17] is,[49]

$$g(\omega) \propto \left(h\nu - E_{cv} \pm E_p\right)^2 . \qquad [3.20]$$

Taking into account that the probability of absorption must be proportional to the Bose-Einstein occupation factor for the phonons involved in the process,

$$n(h\nu) = \frac{1}{\exp(h\nu/k_B T) - 1} , \qquad [3.21]$$

the absorption coefficient is

$$\alpha(h\nu) \propto \left[n \times (h\nu - E_{cv} + E_p)^2 + (n+1) \times (h\nu - E_{cv} - E_p)^2\right] , \qquad [3.22]$$

which is just Eq. [3.13] with n = 2.

Reflectivity in a thin film

Semiconductor materials and structures are often produced with epitaxial techniques, which is the case of the samples studied in this thesis. As a consequence, the typical thickness of the grown layers is of the order of a few hundreds of nanometers. Hence, in optical experiments it is important to consider interference effects. Next, we discuss the effect of interference on the reflectance of thin films.

The interferences that occur when light passes through a thin film are schematically shown in Fig. 3.1. In general, the reflectance spectra will exhibit an interference pattern with maxima and minima that result from constructive or destructive interference of light. The condition of constructive or destructive interferences for the reflected light depends on the refractive indexes of the layer and the surrounding mediums (typically air and the substrate). Following the scheme of Fig. 3.1, there are two cases:

In the first case, $n_3 > n_2 > n_1$. The constructive interference condition takes place when the difference in optical path is a multiple of the wavelength inside the thin film,

$$\mathrm{m}\lambda_{max}\cos\theta = 2n_2 d \ , \qquad [3.23]$$

and, conversely, the destructive interference condition is

$$\left(\mathrm{m}-\frac{1}{2}\right)\lambda_{min}\cos\theta = 2n_2 d \ , \qquad [3.24]$$

where m is an integer (the order of interference) and $\theta = \alpha_2/2$ (see Fig. 3.1).

When $n_2 > n_1$ and $n_2 > n_3$, the constructive interference condition is

$$\left(\mathrm{m}-\frac{1}{2}\right)\lambda_{max}\cos\theta = 2n_2 d \qquad [3.25]$$

and

$$\mathrm{m}\lambda_{min}\cos\theta = 2n_2 d \qquad [3.26]$$

for destructive interference, because a change of phase of 180º takes place when light is reflected on a surface with larger refractive index than that of the preceding medium. In general, the refractive index is affected at the relevant spectral regions by the vibrational and electronic excitations in the material. For instance, for the case of infrared reflectivity measurements, the real part of the DF due to the phononic contributions can be taken as

$$\varepsilon_1 = \varepsilon_\infty + (\varepsilon_0 - \varepsilon_\infty)\frac{\omega_{TO}^2(\omega_{TO}^2-\omega^2)}{(\omega_{TO}^2-\omega^2)^2+\gamma^2\omega^2} \ , \qquad [3.27]$$

and the imaginary part,

$$\varepsilon_2 = \frac{(\varepsilon_0 - \varepsilon_\infty)\omega_{TO}^2\omega\gamma}{(\omega_{TO}^2-\omega^2)^2+\gamma^2\omega^2} \ , \qquad [3.28]$$

where ε_∞ and ε_0 are the high and low frequency dielectric constants, respectively, and γ is a phenomenological damping constant that takes into account the finite lifetime of the phonons. As discussed above, the real and imaginary parts of the DF and the complex refractive index are related through Eqs. [3.2] and [3.3].

For quasi-normal incidence, the amplitude reflection and transmission coefficients are,

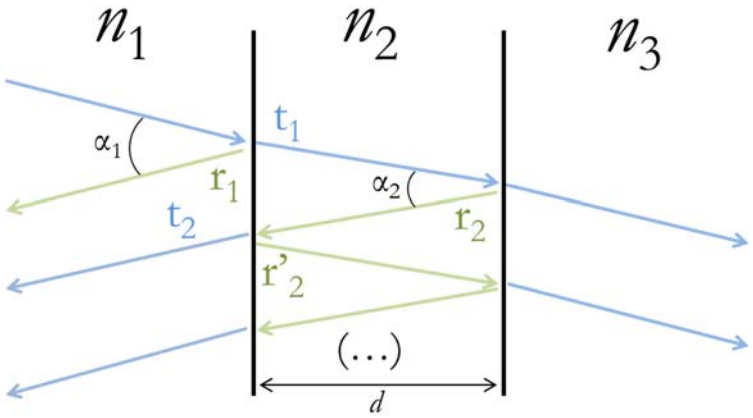

Fig. 3.1. Schematic representation of multiple interferences in a Fabry-Perot cavity. Three different mediums are considered. The transmitted beams are represented with blue arrows and the reflected beams with green arrows in an almost normal incidence.

$$\mathrm{r}_1 = \frac{n_1 - n_2}{n_1 + n_2}, \mathrm{r}_2 = \frac{n_2 - n_3}{n_2 + n_3}, r_2' = \frac{n_2 - n_1}{n_1 + n_2}, t_1 = \frac{2n_1}{n_1 + n_2}, t_2 = \frac{2n_2}{n_1 + n_2}, \qquad [3.29]$$

as derived from the Fresnel equations. Now, considering the multiple beam interference depicted in Fig. 3.1, the amplitude of reflected electromagnetic radiation is given by[50]

$$E_{0,r} = E_0[r_1 + t_1 t_2 r_2 e^{-2\alpha d - i\delta} + t_1 t_2 r_2 (r_2 r_2') e^{-4\alpha d - 2i\delta} + \cdots] e^{i\omega t}\ , \qquad [3.30]$$

where δ is the contribution to the phase arising from an optical path length difference between adjacent beams, $\delta = 4\pi nd/\lambda$; note that a π term should be added if the phase changes from r_2 and r_2' do not compensate each other. Eq. [3.30] can be rewritten as

$$E_{0,r} = E_0 \left[r_1 + t_1 t_2 r_2 e^{-2\alpha d - i\delta} \sum_{n=0}^{\infty} \left(r_2 r_2' e^{-2\alpha d - i\delta} \right)^n \right] e^{i\omega t}. \qquad [3.31]$$

The summation is just a geometric series that converges (as long as $|r_2 r_2' e^{-2\alpha d}| < 1$ which is satisfied in this case) and therefore

$$E_{0,r} = E_0 \left[r_1 + \frac{t_1 t_2 r_2 e^{-2\alpha d - i\delta}}{1 - r_2 r_2' e^{-2\alpha d - i\delta}} \right] e^{i\omega t}\ . \qquad [3.32]$$

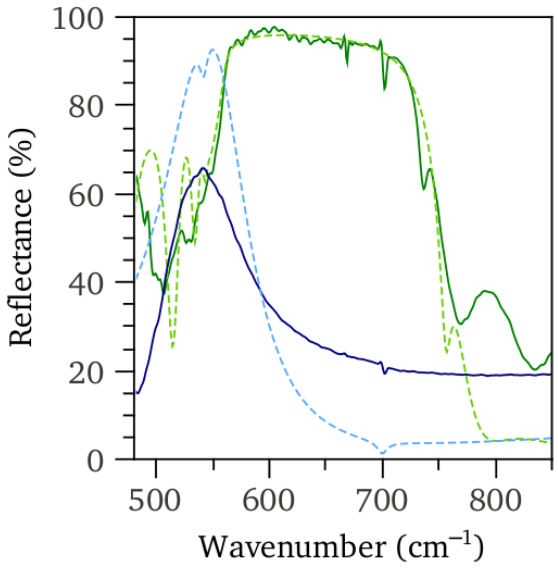

Fig. 3.2.
Reflectance spectra of a 5 μm thick GaN thin film grown sapphire (green lines) and a 300 nm thick $In_{0.19}Ga_{0.81}N$ epilayer grown on Si(111) (blue lines). Experimental data is shown with straight lines and calculations with dashed lines.

The reflectivity for a thin film is then

$$R_{tf} = \left| r_1 + \frac{t_1 t_2 r_2 e^{-2\alpha d - i\delta}}{1 - r_2 r_2' e^{-2\alpha d - i\delta}} \right|^2 . \qquad [3.33]$$

Similarly, the transmittance (taking $n_1 = n_3$) is

$$T_{tf} = \frac{(1-R)^2 e^{-\alpha d}}{1 - R^2 e^{-2\alpha d}} , \qquad [3.34]$$

where

$$R = \left| \frac{\tilde{n}_2 - \tilde{n}_1}{\tilde{n}_1 + \tilde{n}_2} \right|^2 . \qquad [3.35]$$

To illustrate all this, we have calculated by using Eq. [3.33] the reflectance spectra in the far IR of a 300 nm thick InGaN epilayer grown on a Si(111) substrate and that of a 5 μm thick GaN thin film grown on a Al_2O_3 substrate. The calculated curves are shown in Fig. 3.2. For the case of the calculation performed on the GaN thin film, it can be seen that the reflectivity approaches 100% between the TO and LO phonon energies, which is the well-known Reststrahlen effect. The experimental results are plotted in dashed lines, and good agreement is found in both cases.

Electronic density effects on the optical properties

The bandgap of an n-type doped semiconductor material is affected by two important mechanisms. These are the *Burstein-Moss effect* (BM) and the *bandgap renormalization effect* (BGR). For the case of InN, these effects might be very important because native defects in InN can lead to electron densities much higher than $N_e = 10^{19}$ cm^{-3}.[17] To some extent this is a consequence of the fact that in InN the Fermi-stabilization energy is above the Fermi level of intrinsic InN. This implies (as accounted for by the amphoteric defect model) that native defects are mostly donor-like, resulting in an overall increase of the residual electron concentration.[51,52,53]

The exceedingly high N_e results in an electron population of the lower states of the conduction band, thus pushing up the Fermi energy (E_F). For an optical absorption experiment this phenomenon increases the energy of the bandgap absorption edge through the so-called Burstein-Moss effect. On the other hand, the Coulomb interaction between electrons and impurity states result in an overall decrease of the bandgap as described by the bandgap renormalization effect. These effects are schematically shown in Fig. 3.3. The figure allows comparing the electronic band dispersion between an intrinsic (left panel of Fig. 3.3) and an n-type (right panel of Fig. 3.3) direct bandgap semiconductor. Following the scheme of Fig. 3.3 it can be seen that the bandgap energy (E_G) decreases for increasing electron concentration as a consequence of the BGR effect. The grey shadow in Fig. 3.3 represents the population of the electron carriers in the conduction band up to the Fermi energy (E_F). Thus, it is possible to define an optical gap for a degenerate semiconductor as $E_{opt} = E_G + E_{BM} + E_{BGR}$. The optical bandgap can be measured from absorption or luminescence experiments.[11]

For the case of an optical absorption experiment, the absorption edge corresponds to the optical bandgap and not the fundamental bandgap because, as implied by Pauli's exclusion principle, the photoexcited electrons cannot populate occupied energy levels in the conduction band and hence can only be excited above the Fermi level. Similarly, the PL peak energy also increases, but in this case other factors such as the participation of localized band tail states on the emission process

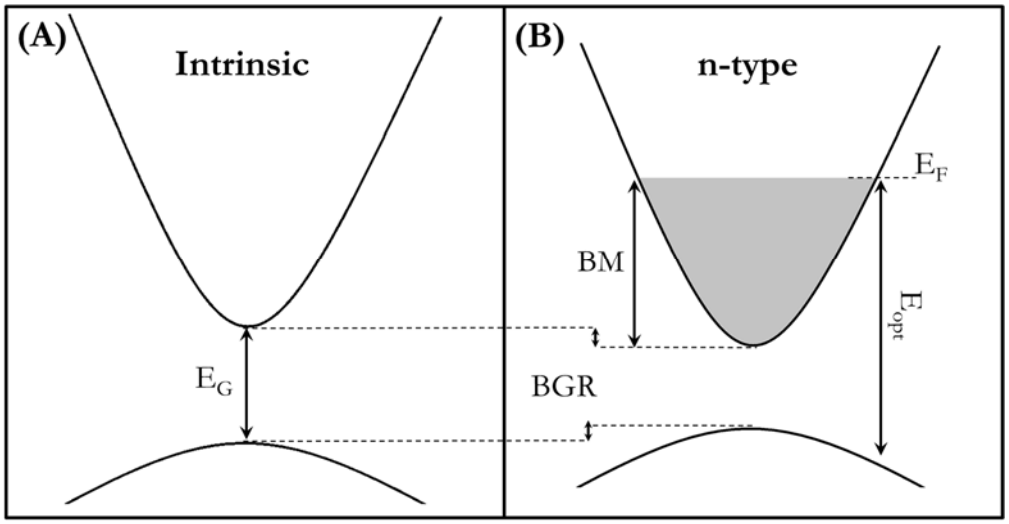

Fig. 3.3. Panel (A): Schematic representation of the valence and conduction band electronic dispersion for an intrinsic direct band gap semiconductor. **Panel (B):** The electronic bands are shifted for a degenerate semiconductor as a consequence of the BGR effect. Electrons occupy the lowest states of the conduction band up to the Fermi energy (E_F). The optical band gap (E_{opt}) is defined as the sum of the BGR, BM and fundamental bandgaps.

might importantly determine the lineshape of the emission spectra.[11,16,54–56]

In order to extract the fundamental bandgap from an absorption experiment on an n-type semiconductor it is necessary to know the position of the Fermi level. At low temperature, the Fermi level can be directly obtained from the Fermi wavevector, k_F, through the conduction band dispersion, $E(k)$, where $k_F = (3\pi^2 N_e)^{1/3}$. The Burstein-Moss shift is just $\Delta E_{BM} = E(k_F)$. For a general non-parabolic semiconductor, the conduction band dispersion can be expressed using a Kane's two-band $\boldsymbol{k}\cdot\boldsymbol{p}$ model,[57] which reads

$$E(k) = \frac{\hbar^2 k^2}{2m_e} + \frac{1}{2}\left(\sqrt{E_G^2 + 4E_P\frac{\hbar^2 k^2}{2m_e}} - E_G\right), \qquad [3.36]$$

where $E_P = 2P^2/m$ is the momentum matrix element for interband transitions. For InN at room temperature, Wu et al.[58] used $E_P \approx 10$ eV. Given that the effective mass $m^*/m_e \approx E_G/E_P$,[59] the Eq. [3.36] can be rewritten as,[19]

$$E(k) = \frac{E_G}{2}\left(\sqrt{1 + \frac{4}{E_G}\frac{\hbar^2 k^2}{2m^*}} - 1\right). \qquad [3.37]$$

Note that the first term of Eq. [3.36] is neglected, which is valid for semiconductors with small effective mass. This can be deduced from the Taylor expansion of Eq. [3.37] which results in the parabolic approximation $E(k) \approx \hbar^2 k^2 / 2m^*$, larger than the first term of Eq. [3.36], $\hbar^2 k^2 / 2m_e$ for semiconductors with small effective mass $m^* \ll m_e$. Hence, using $\Delta E_{BM} = E(k_F)$ the Eq. [3.37] can be used to evaluate the Burstein-Moss shift for small bandgap semiconductors at low temperatures. Along this thesis, an effective mass of $m^*/m_e = 0.7$ and a fundamental bandgap of $E_G = 0.65$ eV are used for InN.

The effect of the non-parabolicity of the electronic dispersion (Eq. [3.37]) of InN on the BM shift is significant for electronic densities higher than 10^{18} cm^{-3}.[58] This can be seen in Fig. 3.4 where the BM shift as calculated with the parabolic (dotted red line) and the non-parabolic (dashed red line) approaches is compared. From this figure it can be seen that for an electron concentration of 10^{19} cm^{-3}, the Burstein Moss shift is ~20% lower for the non-parabolic case (ΔE_{opt} = 216 meV) with respect the parabolic approach (ΔE_{opt} = 242 meV).

In addition to the non-parabolicity effect, the thermal effects on the optical gap energy are significant and cannot be neglected. The Fermi level for an n-type semiconductor with a free electron concentration (N_e), at a certain temperature (T) is given by the Fermi-Dirac statistics,[45]

$$N_e = \int_0^\infty g(E) \frac{dE}{e^{(E-E_F)/k_B T} + 1}, \qquad [3.38]$$

where k_B is the Boltzmann constant and $g(E)$ is the density of states of the conduction band which can be calculated from Eq. [3.37],

$$g(E) = \frac{\sqrt{E}}{2\pi^2} \left(\frac{2m^*}{\hbar^2}\right)^{\frac{3}{2}} \left(1 + \frac{2E}{E_G}\right) \left(1 + \frac{E}{E_G}\right)^{\frac{1}{2}}. \qquad [3.39]$$

From equation [3.39] it can be seen that the Burstein-Moss shift is particularly important for semiconductors with low effective mass. This is because the free electrons populate higher energy levels as a consequence of the reduced density of states of the conduction band, which results in an increase of the Fermi level. For

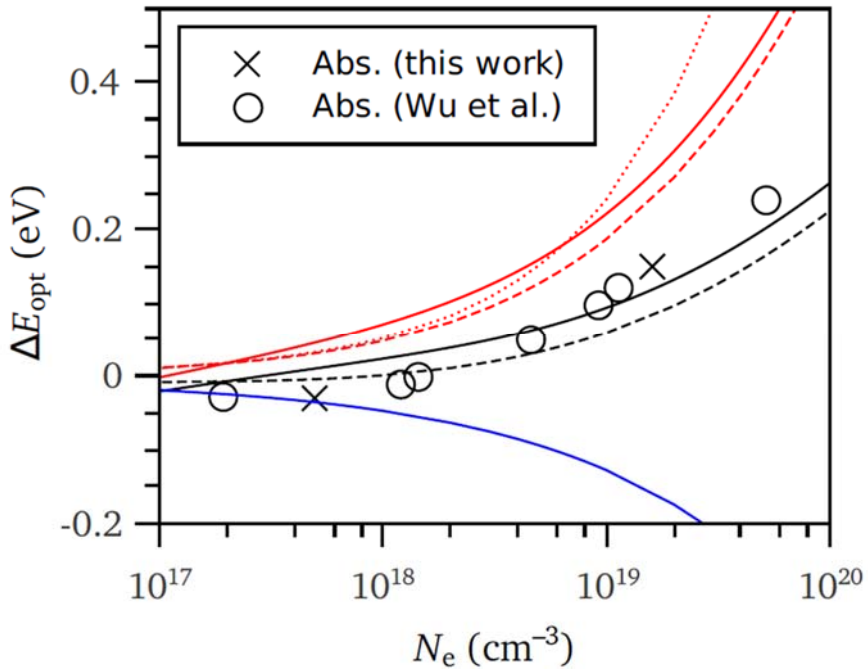

Fig. 3.4. Room-temperature absorption edge energy shift as a function of electron densities as measured by Wu et al.[57] (circles) and in this work (crosses, samples C and B2). The solid black line is the optical band gap obtained from the sum of the Fermi level at T = 300 K (solid red line) and the BGR effect (blue line). The dashed black line is the optical band obtained from the sum of the BM shift calculated assuming a non-parabolic dispersion of the conduction band (dashed red line) and the BGR effect. A calculation of the BM shift assuming a parabolic dispersion of the electronic band is shown as a dotted red line.

the case of InN, and assuming an effective mass of $m^* = 0.07m_e$,[58] an electron concentration of $1{\cdot}10^{19}$ cm^{-3} yields a Burstein-Moss shift as high as 187 meV.[58]

The dependence of the Fermi level with electron density at room temperature is plotted as a straight red line in Fig. 3.4. As it can be seen in the figure, the experimental results are not reproduced from the Burstein-Moss shift calculations alone (red curves in Fig. 3.4) because the BGR effect must also be considered.

As schematically shown in Fig. 3.3, the BM shift of the optical bandgap is partly compensated by the BGR effects. The later decreases the bandgap energy when the electron density is increased. This is caused by the Coulomb interaction between electrons in the conduction band ΔE_{e-e} and also between electrons and ionized donor impurity states ΔE_{e-i}.[58,60,61] Neglecting thermal effects, the electron-electron contribution to the bandgap renormalization is

$$\Delta E_{\text{e-e}} = -\frac{2e^2 k_{\text{F}}}{4\pi^2 \varepsilon_0 \varepsilon_r} - \frac{e^2}{8\pi\varepsilon_0\varepsilon_r}\sqrt{\frac{k_{\text{F}}}{a_{\text{B}}}}\left[1 - \frac{4}{\pi}\arctan\left(\sqrt{k_{\text{F}} a_{\text{B}}}\right)\right], \qquad [3.40]$$

where $a_{\text{B}} = \frac{4\pi\varepsilon\hbar^2}{m^* e^2} = 0.53\varepsilon_r m_e/m^*$ is the Bohr radius, in angstroms. The contribution to the electron-ion interaction band shift is given by the expression

$$\Delta E_{\text{e-i}} = -\frac{e^2 N_e \sqrt{a_{\text{B}}}}{\varepsilon_0 \varepsilon_r k_{\text{F}}^{3/2}}. \qquad [3.41]$$

The BGR variation of energy versus electron density has been plotted (blue line) in Fig. 3.4 using Eq. [3.40] and Eq. [3.41] taking m^*/m_e = 0.07 and ε_r = 11.75.[62] It can be seen that after adding the BM and BGR terms (black lines) the experimental optical bandgap energies are well adjusted. In particular, the calculations that also include thermal effects reproduce the experimental data remarkably well (see straight black line in Fig. 3.4).

Pressure dependence of the optical bandgap

To the date, a large amount of studies dealing with the pressure dependence of the optical bandgap of wurtzite InN and InGaN by means of absorption and luminescence measurements have been published.[16,63–66] Nevertheless, more research is needed in order to accurately determine the fundamental bandgap and its pressure dependence. For instance, it has been observed that the bandgap pressure coefficient as measured by PL is significantly lower than the pressure coefficient of the absorption band edge.[63,66] Some authors attribute this result to the fact that the PL emission arises from radiative recombination from localized impurity states,[66] which are almost pressure independent. On the contrary, other authors conclude that the PL emission for InN and InGaN has a band-to-band character as they measure significantly higher pressure coefficients, in agreement with absorption measurements.[67] Aside from impurity-states emission, Kaminska et al. showed that the optical pressure coefficient (dE_{opt}/dP) in InN depends on the free electron density.[16]

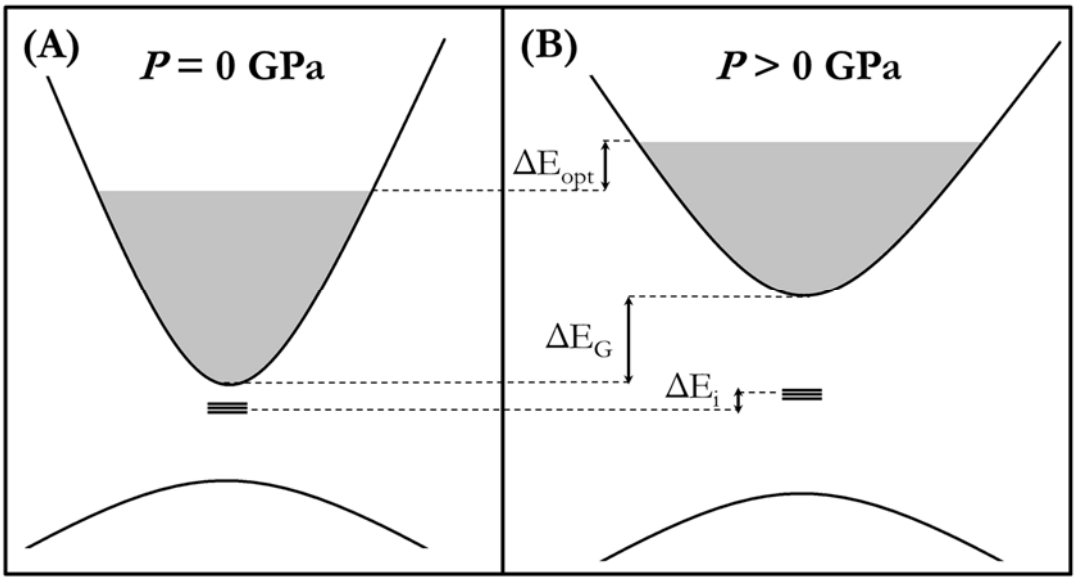

Fig. 3.5. Schematic representation of the electronic band dispersion for a n-type direct band gap semiconductor at zero pressure (left panel) and high pressure (right panel). It can be seen that the band gap (ΔE_G) increases with pressure more than the optical gap (ΔE_{opt}) as a consequence of the increase in effective mass. The increase of the energy of local states (ΔE_i) is small.

An accurate description of the dependency of the dE_{opt}/dP on the electron density would allow to better determine the pressure dependence of the fundamental bandgap of intrinsic InN. As introduced in the previous section, the optical bandgap can be expressed as a sum of three terms $E_{opt} = E_G + E_{BM} + E_{BGR}$. Under high pressure it is expected that the BM term plays an important role as a consequence of its strong dependency with the effective mass, as shown later in this section. Note that the density of states of the conduction-valence electronic dispersion is expected to increase with pressure as a consequence of the fact that the effective mass also increases with pressure. This can be seen in Fig. 3.5, where the electronic dispersion is schematically shown for an n-type direct bandgap semiconductor at room pressure (left panel) and high pressure (right panel). It can be seen that the fundamental bandgap (E_G) increases more than the optical bandgap (E_{opt}) because more states are available for the electron carriers at the bottom of the conduction band and the Fermi level decrease with respect the bottom of the CB. In Fig. 3.5 the low dependence with pressure of the impurity states is also shown.

Therefore the pressure dependence of the optical bandgap can be simply written as[16]

$$\frac{dE_{opt}}{dP} = \frac{dE_G}{dP} + \frac{dE_F}{dP} \,, \qquad [3.42]$$

where dE_F/dP at $T > 0$ K must be solved numerically from Eq. [3.38]. Note that the pressure-dependent terms of Eq. [3.38] are the fundamental bandgap and the effective mass.

The pressure dependence of the bandgap can be taken as

$$E_G(P) = E_G(0) + a_G P \,, \qquad [3.43]$$

where a_G is the band gap pressure coefficient. The pressure-dependence of the effective mass can be estimated from the **k·p** approximation,[59]

$$\frac{1}{m^*} = \frac{1}{m_e} + \frac{2}{m_e^2 k^2} \sum_{m \neq n} \frac{|\langle u_m | \boldsymbol{k} \cdot \boldsymbol{p} | u_n \rangle|^2}{E_m - E_n} \,, \qquad [3.44]$$

where $\boldsymbol{k}$ is the wavevector of the reciprocal space, $\boldsymbol{p}$ is the electron wavevector, E_m are the zone-centre energy bands, and u_n is the eigenfunction of the Schrödinger equation with the periodicity of the lattice. Note that, for small gap semiconductors such as InN, the first term of Eq. [3.44] is negligible with respect the last one. Assuming that the matrix elements of Eq. [3.44] are independent of the pressure it is found that the effective mass is proportional to the bandgap. Thus, the dependency of the effective mass with pressure can be simply evaluated as

$$m^*(P) \approx m^*(0) E_G(P)/E_G(0) \,, \qquad [3.45]$$

The validity of Eq. [3.45] can be contrasted by comparing the relative pressure coefficient of the effective mass, $\gamma = \frac{d \ln m^*}{dP}$, with experimental values. Taking the fundamental bandgap of InN, $E_G(0) = 0.65$ eV, and the pressure coefficient of the bandgap, $a_G = 32$ meV/GPa as obtained in this thesis (see Article 3.1 in the results section of this chapter) at room temperature, we get $\gamma \approx 0.05$ GPa^{-1}, in good agreement with the experimental value $\gamma = 0.056$ GPa^{-1} reported[68] for a sample of relatively low electron density ($4.2 \cdot 10^{17}$ cm^{-3}).

The pressure dependency of the effective mass is evaluated using Eq. [3.45] and $m^* = 0.07 m_e$ as determined by infrared reflection experiments reported

elsewhere.[58] This allows us to calculate the dE_{opt}/dP as a function of electron density. As it is reported in the results section (see Article 3.1) the calculated pressure coefficient of the optical gap for InN at 300 K decreases from 30.5 meV/GPa down to 22.7 meV/GPa for electron densities 10^{17} cm^{-3} and 10^{20} cm^{-3}, respectively. This result is in good agreement with the high-pressure optical experiments performed in this thesis (Article 3.1).

However, it has to be noted that the calculation here performed neglects the effects of the BGR described in the previous section. Next it is shown that the BGR effect is smaller than the experimental error and can be, therefore, neglected.

The evaluation of the BGR effect on the dE_{opt}/dP requires the knowledge of the pressure dependence of the low frequency dielectric constant. The pressure dependency of the static dielectric constant is evaluated from the Lydanne-Sachs-Teller relation. This relates the phonon frequencies of the polar modes with the dielectric constants, as shown later in this chapter (see Eq. [3.57]). The pressure coefficients of the A_1 phonon modes of InN have been taken from the results presented in Chapter 4, these are $d\omega_{A1(TO)}/dP = 5.3$ and $d\omega_{A1(LO)}/dP = 4.8$. The pressure dependency of the high-frequency dielectric constant needed to solve the Lydanne-Sachs-Teller relation is taken from the values measured by high-pressure FTIR measurements (more information on the experiment and analysis are detailed in the results section of this chapter, see Article 3.2.), $\varepsilon_\infty(P) = 6.7 + 6.2 \cdot 10^{-2} P$.

In general, the BGR effect on dE_{opt}/dP is lower than the BM effect for heavily doped semiconductors. For instance, solving Eqs. [3.36], [3.40] and [3.41] for a sample with an electron density of $1.6{\cdot}10^{19}$ cm^{-3} one finds that the BGR increases the optical pressure coefficient ≈3.1 meV/GPa, which is smaller in absolute terms than the BM effect, around ≈−5.7 meV/GPa for the same electronic density. Owing to the fact that the experimental error for a typical high-pressure absorption experiment is in the range of ≈2 meV/GPa, the pressure coefficient of the fundamental bandgap can be evaluated by considering only the BM contribution to the optical bandgap. Considering only the BM effects on the optical bandgap as described in this chapter, the pressure coefficient of the fundamental bandgap of intrinsic InN has been fitted for the experimental results obtained from a set of

samples with different doping values (shown in the Table 3.1). As is found in this thesis (see Article 3.1), a pressure coefficient of $a_G = 32$ meV/GPa has been obtained for intrinsic wurtzite InN. The value here reported is in good agreement with many-body perturbation-theory calculations that predict a pressure coefficient in the range 28−33 meV/GPa.[69]

Phase transition and electronic structure

The optoelectronic properties of a crystalline semiconductor are closely related with its chemical composition, crystal phase, interatomic distances and the nature of the chemical bonding. Performing high-pressure experiments allow gaining insight into the relation between the optoelectronic properties and the crystal structure. For instance, it has been shown that the ionicity importantly determines the high-pressure phase for semiconductors of the form $\boldsymbol{A}^N\boldsymbol{B}^{8-N}$, where $\boldsymbol{A}$ and $\boldsymbol{B}$ are metals or metalloids and N is the number of valence electrons of the cation.[70,71] For the case of InN ($N = 3$), XRD high-pressure measurements revealed that the wurtzite structure undergoes a phase transition to the rocksalt structure around ~12 GPa.[71] In turn, trends of the electronic structure in relation with the crystal phase have been observed for many binary semiconductor compounds; for the case of InN, the indirect bandgap of the rocksalt polymorph (*rs*-InN) of InN was theoretically predicted.[35,36,72] Owing to the fact that *rs*-InN can only be obtained after the phase transition (this phase remains metastable down to 4 GPa[42] and no other phase transition has been observed up to 50 GPa[40]), high-pressure optical absorption experiments were necessary to experimentally confirm the indirect nature of the bandgap of this phase.[28] In general, the study of the electronic structure of different crystalline compounds is highly desirable in order to better understand the phase diagram and electronic structure of novel high-pressure polymorphs.

Numerous high-pressure X-ray structural studies on tetrahedral semiconductors found that compounds of the form A^NB^{8-N} typically undergo a phase transition to a six-fold coordinated phase having either the rocksalt or the β–

Sn crystal structure.[70,73,74] The former takes place for semiconductors exhibiting large ionicity while the latter is adopted by more covalently bonded compounds. Moreover, theoretical calculations suggested that compounds with large ionicity entails decreased transition pressures.[71,75] These trends has been confirmed for one of the most ionic III-V semiconductors, InN. At ambient conditions, indium nitride can be stabilized in either the tetraedrically bonded wurtzite or zinc blende phases (w-InN and zb-InN, respectively), and at high pressure undergoes a phase transition to the six-fold coordinated rocksalt phase.

In this thesis we report that the rocksalt phase polymorph of InN exhibits an indirect electronic gap,[28] whose energy has been stablished by means of absorption measurements at 0.7 eV for a pressure of 15 GPa (see Article 3.1 for more details). This is in contrast with the fact that the wurtzite and zinc blende polymorphs of InN exhibit a direct electronic bandgap with similar energies at room (around 0.64 eV) and high pressure.[29] Such electronic transition can be attributed to a change of ion coordination from four for w-InN to six for rs-InN. In order to relate the fact that the gap is direct or indirect with the structural coordination, the case of InN can be compared with observed trends for many as-grown four-fold and six-fold semiconductor compounds. For instance, most crystals grown in the octahedral point symmetry of the rocksalt structure exhibit an indirect bandgap.

The electronic structure of the rocksalt phase is typically characterized by a maximum of the highest valence band in the L high-symmetry point of the Brillouin zone and a relatively sharp minimum of the conduction band in the X valley.[76] Interestingly, the indirect bandgap of the rocksalt phase has been observed in many rocksalt semiconductors which, on the other hand, exhibit a direct bandgap for other polytypes such as the tetrahedrally coordinated wurtzite or zinc blende structures. Such is the case for zinc and cadmium oxides and chalcogenides: ZnO,[77] ZnS,[78] ZnSe,[79] ZnTe,[80] CdO,[81,82] CdS,[83] CdSe[84,85] and CdTe[86,87]. III-V group semiconductors exhibit the same trend, like for instance, AlN,[88] GaN,[89] InN[28] or InAs[90]. Some of them, like GaAs,[91] AlP[92] or InP,[93] exhibit metallic character in the rocksalt phase, and others, like AlAs[94] or GaP,[92] are also indirect semiconductors in their stable phase (zinc blende). The indirect nature of the bandgap of the rocksalt

phase has been attributed to the symmetry-forbidden hybridization of the p-d electronic states in the center of the Brillouin zone.[77] Nevertheless, a rocksalt structure does not necessarily imply an indirect bandgap, as it is the case of highly ionic wide bandgap oxides like MgO.[95] Interestingly it has to be noted that despite indium nitride is one of the most ionic III-V compounds, such ionicity is not strong enough to retain a direct bandgap electronic structure after the phase transition.

Hence, we conclude that the optical properties of the high-pressure phase of InN (i.e. rocksalt) is determined by the large ionicity of this compound, in agreement with theoretical calculations. We confirm that indium nitride becomes an indirect bandgap semiconductor after its high-pressure phase transition, where a change of ion coordination takes place. This later result is in agreement with trends between the indirect nature of the bandgap and the structural coordination that is observed for many binary compounds.

Modelling the dielectric function

In this section a model for the frequency-dependent DF of a polar semiconductor is presented. The aim of this section is to provide the physical and mathematical background required to extract the high-frequency dielectric constant of InN, at different pressure values, from optical reflectivity measurements. As already discussed in this chapter, the DF (DF) is one of the most relevant parameters used to describe the optoelectronic properties of semiconductor materials and is closely related to the electronic structure or the ionic character of the chemical bonding. Here we would like to recall that the complex refractive index, $\tilde{n}$, is related to the real, ε_1, and imaginary, ε_2, parts of the DF by,

$$\tilde{n} = n + ik = \sqrt{\varepsilon_1 + i\varepsilon_2} \ . \qquad [3.46]$$

where n is the refractive index (this is, the ratio between the speed of light in vacuum and the phase velocity in the medium $n = c/v_{\mathrm{P}}$) and k is the extinction coefficient, which is related to the amount of electromagnetic radiation absorbed by the medium. As discussed above, for a given wavelength λ, k relates with the

absorption coefficient through $\alpha = 4\pi k/\lambda$. Both parameters, n and k can be expressed as a function of ε_1 and ε_2 from Eq. [3.46]. Hence, by modelling the DF it is possible to fit the experimentally measured refractive index through Eq. [3.46].

In general, the DF is a tensor. For the case of the wurtzite structure the ordinary part of the DF, $\varepsilon_{\parallel}$, is given by the field direction perpendicular to the c-axis, the directions along this plane are isotropic, while the extraordinary part, $\varepsilon_{\perp}$, corresponds to an electric field parallel to the c-axis of the crystal. For the case of III-group nitrides the difference between $\varepsilon_{\parallel}$ and $\varepsilon_{\perp}$ ($\Delta\varepsilon$) is rather low. For the case of InN, the difference of the DF between both directions in the frequency range above the phonon energy is $\Delta\varepsilon_{\infty}/\varepsilon_{\infty} \approx 3\%$,[96] while in the zero frequency limit, $\Delta\varepsilon_0/\varepsilon_0 \approx 7\%$.[97,98,99]

In this thesis only the ordinary part of the DF $\varepsilon_{\parallel}$ is considered. This is because the FTIR measurements performed in this thesis to determine the refractive index (see Article 3.2 in Section 3.3) were done in a backscattering configuration along the direction of the c-axis for a w-InN sample. Hence, the electric field and ionic oscillation takes place in the ordinary direction.

The DF is characterized by the response of different physical processes which can take place in the material. For the case of n-type doped InN, three processes must be taken into account. These are the electronic, the phononic and the plasmonic (free carriers) contributions to the DF. It is important to note that each of these interactions takes place for a characteristic frequency range, and the corresponding dielectric response only takes place when the frequency of the electric field is lower than the frequency of the interaction. The frequency ranges of each contribution are qualitatively shown in the top of Fig. 3.6, these are, from low to high energies; the plasmonic, phononic, and electronic (including the Penn gap that accounts for the electronic transitions with higher energy than the bandgap). The DF can be written as the sum of each of these interactions,

$$\varepsilon(\omega) = \varepsilon_e(\omega) + \varepsilon_l(\omega) + \varepsilon_p(\omega) \ , \qquad [3.47]$$

where the subscripts refer to the electronic, lattice (phononic) and plasmonic interactions. Next, each of these contributions to the DF is described. The lineshape

of the real, $\varepsilon_1(\omega)$, and imaginary, $\varepsilon_2(\omega)$, parts of the DF (as obtained from Eq. [3.47]) are shown in Fig. 3.6 with blue and red lines, respectively. The refractive index (calculated from Eq. [3.46]) is fitted to the experimental data points for w-InN at ambient pressure (open symbols).

Regarding the electronic contribution to the DF, the line-shape of the DF is determined by the electronic structure. For the sake of simplicity, in this work the DF is modelled using a simple single-oscillator model. This model assumes that the low frequency range of the DF can be described by averaging all the high-energy electronic transitions into a single electronic transition (i.e. the so-called Penn gap). In the present work, for the study of w-InN, the contribution of the direct bandgap transition to the DF has been included separately in order to better describe the lineshape of the DF around the direct bandgap energies, which is the spectral region where the experiments have been performed. The imaginary part of the DF arising from the direct bandgap contribution is proportional to the electronic states available for a certain energy (i.e. the joint density of states, D_j) between the valence and conduction bands, $\varepsilon_2(\omega) \sim D_j(\omega)\omega^{-2}$.[59,100] Assuming that the direct bandgap can be described by an M_0 critical point, $\varepsilon_2(\omega) \sim \theta(\omega-\omega_g)\sqrt{\omega-\omega_g}\,\omega^{-2}$, where θ is the Heaviside step function and ω_g is the bandgap frequency.[59] The real, $\varepsilon_1(\omega)$, and imaginary, $\varepsilon_2(\omega)$, parts of the DF are then obtained from the Kramers-Kronig relations,

$$\varepsilon_1(\omega) - 1 = \frac{2}{\pi}\mathcal{P}\int_0^\infty \frac{\omega'\varepsilon_2(\omega')d\omega'}{\omega'^2-\omega^2}\,, \qquad [3.48]$$

and,

$$\varepsilon_2(\omega) = -\frac{2\omega}{\pi}\mathcal{P}\int_0^\infty \frac{\varepsilon_1(\omega')d\omega'}{\omega'^2-\omega^2}\,. \qquad [3.49]$$

Thus, the real part of the DF corresponding to the electronic contribution can be written as

$$\varepsilon_{1e} = \frac{\omega_{PBV}^2}{\omega_0^2 - \omega^2} + \frac{C_0}{\chi_0^2}\left[2 - \sqrt{1+\chi_0} - \theta(\omega-\omega_g)\sqrt{|1-\chi_0|}\right] + 1 \ , \qquad [3.50]$$

where the first term corresponds to the Penn gap model, which has two free parameters, the plasma frequency of the valence band, ω_{PBV}, and the Penn gap, ω_0. Both are typically left as unknown parameters to be fitted.[101] The last term corresponds to the direct bandgap interaction, where C_0 is the strength of the oscillator and $\chi_0 = \omega/\omega_g$.

The imaginary part of the DF corresponding to the electronic contribution is

$$\varepsilon_{2e} = \varepsilon_{2e}^{Penn} + \frac{C_0}{\chi_0^2}\theta(\omega-\omega_g)\sqrt{\chi_0 - 1} \ , \qquad [3.51]$$

where the first term, ε_{2e}^{Penn}, can be derived from Eq. [3.50] by using the Kramers-Kronig relations (Eqs. [3.48] and [3.49]). The second term of Eq. [3.51] corresponds to the contribution of the direct bandgap. The lineshape of the real and imaginary parts of the DF arising from the electronic contributions can be seen in Fig. 3.6 with red and blue lines respectively for wavenumbers above the bandgap (i.e. $\omega_g \approx 5250$ cm^{-1}). It can be seen that the refractive index, n^2, exhibits a small peak around the bandgap wavenumber and a very intense band around the Penn gap (i.e. $\omega_0 \approx 39000$ cm^{-1}). It has to be noted that the lineshape of the DF around the Penn gap wavenumbers is fictitious, but allows to successfully accounts for the high-energy electronic contribution in the wavenumber range at which the experimental results are performed (shown as open symbols in Fig. 3.6, right below the direct bandgap).

Next, the phononic contribution to the DF must be considered (i.e. the second term of Eq. [3.47]). For the case of a polar semiconductor such as InN, the lattice interaction can be described with the Lorentz oscillation model. From the Lorentz oscillation equation,

$$\mu\frac{d^2u}{dt^2} - \mu\gamma_l\frac{du}{dt} + \mu\omega_T^2 u = QEe^{-i\omega t} \qquad [3.52]$$

where μ is the reduced mass of the anion and cation, γ_l is a phenomenological damping constant, ω_{T} is the transverse phonon frequency, and $QEe^{-i\omega t}$ is the

electric force generated by the charged oscillators of a polar crystal (this results in the longitudinal modes). The solution of Eq. [3.50] yields

$$u = \frac{-Q/\mu}{\omega_T^2 - \omega^2 - i\omega\gamma_l} E \ . \qquad [3.53]$$

For all (N) oscillators, $P(\omega,t) = -NQu$. Comparing Eq. [3.53] with the definition of the DF (which relates the polarizability, $\boldsymbol{P}$, with the electric field, $\boldsymbol{E}$, as $\boldsymbol{P} = \boldsymbol{E}(\varepsilon(\omega)-1)/4\pi k_e$), and bearing in mind that for the longitudinal modes the wavevector ($\boldsymbol{k}$) has the same direction than the macroscopic electric field $\boldsymbol{E}$, $Re(\varepsilon_l(\omega_L)) = 0$ (this is a consequence of the Maxwell equations, without external field, $\boldsymbol{\nabla D} = \varepsilon_l \boldsymbol{kE} = 0$[59,102]), one obtains the lattice contribution to the DF,

$$\varepsilon_l(\omega) = \frac{4\pi N k_e Q^2/\mu}{\omega_T^2 - \omega^2 - i\omega\gamma_l} = \frac{\varepsilon_\infty(\omega_L^2 - \omega_T^2)}{\omega_T^2 - \omega^2 - i\omega\gamma_l} \ . \qquad [3.54]$$

Finally, the dielectric contribution arising from the electron gas in a solid (i.e. plasmons) can be derived from the Drude theory,

$$m^* \frac{d^2u}{dt^2} + m^*\gamma_p \frac{du}{dt} = -QEe^{-i\omega t} \ , \qquad [3.55]$$

$$\varepsilon_p(\omega) = -\frac{4\pi k_e N_e Q^2/m^*}{\omega^2 + i\omega\gamma_p} = -\frac{\varepsilon_\infty \omega_P^2}{\omega^2 + i\omega\gamma_p} \ , \qquad [3.56]$$

where ω_P is the frequency at which the real part of the DF is zero and it is known as the plasma frequency. N_e is the electron density, Q is the free electron charge, m^* the electronic effective mass and γ_p a phenomenological plasmonic damping.

So, the different contributions to the DF included in Eq. [3.47] have been described. This model has been used in this thesis (Article 3.2) in order to fit the experimentally determined refractive index of w-InN. But, in this work the electronic contribution to the DF has been simplified assuming that the first term of [3.50] is constant, $\frac{\omega_{PBV}^2}{\omega_0^2-\omega^2} \cong K$, and the imaginary part of the electronic contributions (i.e. Eq. [3.51]) has been neglected because are zero in the experimental range. For the fitting there are only two free adjustable parameters, C_0 and K. Despite the

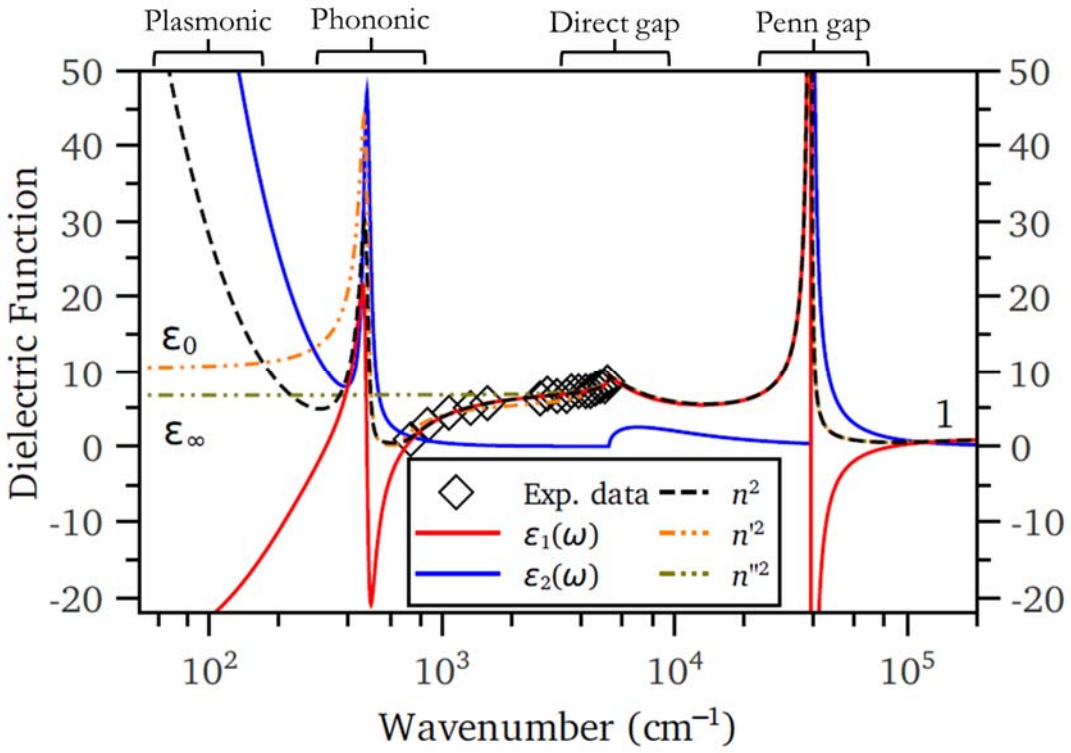

Fig. 3.6. Fit of the measured refractive index (open symbols) with a simplified model that considers four contributions to the DF (dashed black line). The real and imaginary parts of the DF are plotted as solid red and blue lines respectively. The same fit without the plasmonic contribution and without the phononic contribution is shown as dashed orange and green lines respectively.

simplicity of this model it can be seen in Fig. 3.6 that the agreement between the experimental points and the fitted lineshape is excellent.

Once the adjustable parameters are fitted and the lineshape of the DF is known, it is possible to calculate the high frequency dielectric constant ε_∞. As it can be seen in Fig. 3.6 (green dashed line), ε_∞ corresponds to the DF at energies above the LO phonon energy (typically 500 cm^{-1}) and below the first electronic transition (for a low bandgap semiconductor such as InN, below 5000 cm^{-1}). The value of ε_∞ is calculated taking the real part of the DF at zero frequency neglecting the phononic and plasmonic contributions. Note that in optical-response studies ε_∞ is sometimes referred as the "low-frequency dielectric constant, ε_0", this nomenclature will not be used in this thesis.[101]

On the other hand, the static dielectric constant, ε_0 can also be fitted using this model. This parameter is also called relative permittivity or "ε_S", and is the dielectric response arising from the electronic and lattice contributions to the

dielectric response at zero frequency. For a linear, isotropic and homogeneous medium (LIH), the dielectric constant relates the electric displacement field at zero frequency, $\boldsymbol{D}(0)$, with and external constant electric field, $\boldsymbol{E}(0)$, by $\boldsymbol{D}(0) = \varepsilon_0 \boldsymbol{E}(0)$. The value of ε_0 can be calculated extrapolating the DF to zero frequency but neglecting only the plasmonic contribution (see the orange dashed line of Fig. 3.6).

Within the model presented in this section it has been possible to extract the relative pressure coefficient of the high-frequency dielectric constant from the refractive index of InN in the 1000–8000 cm^{-1} spectral region. The relative pressure coefficient is $(1/\varepsilon_\infty)d\varepsilon_\infty/dP = -8.8{\cdot}10^{-3}$ GPa^{-1} for the wurtzite structure and $(1/\varepsilon_\infty)d\varepsilon_\infty/dP = -14.8{\cdot}10^{-3}$ GPa^{-1} for the rocksalt structure in the 12–20 GPa pressure range.

Relating the high-frequency dielectric constant with the ionicity

So far, a model used to obtain the high-frequency dielectric constant from experimental data of the refractive index in the high-frequency range has been described. Now, we focus on the pressure dependence of the high-frequency dielectric constant from a fundamental point of view. For the case of heteropolar semiconductor crystals such as InN, the pressure dependence of the high-frequency dielectric constants can be used to evaluate the degree of ionicity on the chemical bonding. In order to better understand the role of ionicity on the high-frequency dielectric constant, a brief introduction on the concept of ionicity is presented together with related parameters such as the Born effective charge, the polarizability or the Phillips ionicity.

In general, the ionicity of a semiconductor compound can be regarded as the transfer of electronic charge from the cation to the anion as a consequence of a sizable difference in electronegativity between the ions. This results in an increased Coulomb interaction of the crystal bonding,[103] which affects the optical, electronic and vibrational properties. For instance, in ionic semiconductors the fundamental bandgap tends to be larger than in covalent semiconductors.[59]

Regarding the vibrational properties, the degeneracy of the transversal optical phonon modes (known as TO modes) is broken as a consequence of the presence of a long-range electric field created from the (electrically charged) ions when the phonon propagates along the oscillation direction of the ions. This gives rise to the so-called longitudinal optical phonon modes (LO modes). Because the long-range electric field adds increased restoring force to the bonding, the frequency of the LO modes, ω_L, is larger than that of the TO modes, ω_T. This effect is known as LO-TO phonon splitting and its magnitude is related with the static (ε_0) and high-frequency (ε_∞) dielectric constants through the Lydanne-Sacks-Teller relation (LST-relation),

$$\frac{\varepsilon_0}{\varepsilon_\infty} = \frac{\omega_{\mathrm{L}}^2}{\omega_{\mathrm{T}}^2} \,. \qquad [3.57]$$

This relation is obtained from Eq. [3.54] taking $\varepsilon_l(0) = \varepsilon_0$ and $Re\big(\varepsilon_l(\omega_L)\big) = 0$.

The long range electric field responsible for the LO-TO splitting can be regarded to be generated by the so-called Born effective charge or simply transverse charge. The Born effective charge, e^*, is related to the charge transfer between ions in a polar compound and is defined as the change in polarization with respect an ionic displacement,

$$e^* = \frac{\Omega}{|e|}\frac{\partial P}{\partial r} \,, \qquad [3.58]$$

where Ω is the unit cell volume and $|e|$ is the elementary charge. The transverse charge can be related to the phonon splitting through a polarization model consisting of multiple simple harmonic oscillators (SHO),[59,103]

$$e^* = \left(\frac{\mu(\omega_{\mathrm{L}}^2 - \omega_{\mathrm{T}}^2)\varepsilon_\infty}{4\pi k_{\mathrm{e}} N}\right)^{1/2} , \qquad [3.59]$$

where each harmonic oscillator is formed by an anion and a cation, μ is the reduced mass, k_{e} is the Coulomb force constant and N the density of the SHO (i.e. the inverse of the volume of the unit cell). Note that, the phonon frequencies, ω_L and ω_T, and the high-frequency dielectric constant, ε_∞, can be measured from a simple

Raman and optical reflectivity experiment. Combining Eqs. [3.57] and [3.59] it can be shown that the transverse charge is related with the dielectric constants by,

$$e^* = \left(\frac{\mu(\varepsilon_0 - \varepsilon_\infty)}{4\pi k_e N}\right)^{1/2} \omega_T \ . \qquad [3.60]$$

On the other hand, the polarizability of the SHO, α_P, which is the ratio of the induced dipole moment $\boldsymbol{p}$ to the local electric field $\boldsymbol{E}_{loc}$, $\boldsymbol{p} = \alpha_P \boldsymbol{E}_{loc}$, can be obtained from the transverse charge. For the case of III-V semiconductors,[104]

$$e^* = (20\alpha_P - 8\alpha_P^2 - 3)/(3\sqrt{k_e}) \ . \qquad [3.61]$$

From the generalization of the Clausius-Mossotti formula it is possible to connect the high-frequency dielectric constant, which is a macroscopic quantity with the microscopic polarizability

$$4\pi k_e \gamma N \alpha_P = \frac{\varepsilon_\infty - 1}{\varepsilon_\infty + (\gamma^{-1} - 1)} \ , \qquad [3.62]$$

where γ is a parameter which depends on the nature of the chemical bonding. For strongly localized polarization centers such as ionic crystals (with typically cubic structures) $\gamma = 1/3$ (which leads to the Lorentz-Lorentz relation), while for crystals with delocalized electrons (which applies to partially covalent tetrahedral crystals) $\gamma = 0$. The later results in the Sellmeier formula,[101]

$$\varepsilon_\infty = 1 + 4\pi k_e N \alpha_P . \qquad [3.63]$$

From the microscopic description of ε_∞ (see Eq. [3.63]), it follows that the pressure derivative of ε_∞ is governed by two competing mechanisms: On one hand, $\mathrm{d}\varepsilon_\infty/\mathrm{d}P$ will depend on the increase of the polarization centers per unit of volume (higher density N), and on the other hand, on the increase of the polarizability of the electronic bonds with pressure. This can be shown by deriving Eq. [3.63] with respect the pressure,

$$\frac{\varepsilon_\infty}{\varepsilon_\infty - 1}\frac{\partial \ln \varepsilon_\infty}{\partial P} = \kappa - \kappa \frac{\partial \ln \alpha_P}{\partial \ln V} \ , \qquad [3.64]$$

where κ is the compressibility, $\kappa = -\partial \ln V / \partial P$. The two terms in Eq. [3.64] are the compressibility, which is a positive term, and the volume derivative of the polarizability.

Following Eq. [3.64] it is possible to express $d\varepsilon_\infty/dP$ as a function of the Phillips Van-Vechten definition of the fractional degree of ionic bonding, $f_\mathrm{i} = C^2/E_0^2$.[101,105] The Penn gap E_0 has two contributions $E_0^2 = E_h^2 + C^2$, the homopolar and ionic, respectively.[106] Within this approach, Eq. [3.64] can be rewritten as[101]

$$\frac{d\ln\varepsilon_\infty}{dP} \approx \frac{5(\varepsilon_\infty - 1)}{3B}(f_i - 0.9)\ , \qquad [3.65]$$

where B is the bulk modulus. Therefore, highly ionic crystals will exhibit $d\varepsilon_\infty/dP > 0$ (for these systems, the increase of ε_∞ with pressure is mostly a consequence of the increase of polarization centers, N) while in covalent crystals $d\varepsilon_\infty/dP < 0$. The Eq. [3.65] can be used to compare the experimental value of $d\ln\varepsilon_\infty/dP$ found in this thesis (see Article 3.2) for InN with calculated f_i in other works. Taking f_i = 0.859,[35] B = 143[42] and ε_∞ = 6.7[107] Eq. [3.65] yields $dln\varepsilon_\infty/dP \approx -3{\cdot}10^{-3}$, which is in the same order of magnitude of the experimental result obtained in this thesis (see Article 3.2), $dln\varepsilon_\infty/dP \approx -9{\cdot}10^{-3}$.

3.3. Results and list of published works

The work performed in this thesis dealing with the high-pressure optical properties of InN has given rise to two publications, Articles 3.1 and 3.2, which have been attached in the following pages:

- Article 3.1: *High-pressure optical absorption in InN: Electron density dependence in the wurtzite phase and reevaluation of the indirect bandgap of rocksalt InN.,* by J. Ibáñez, A. Segura, B. García-Domene, R. Oliva, F. J. Manjón, T. Yamaguchi, Y. Nanishi and L. Artús. Published in Physical Review B (2012), vol. 86, p. 035210.

In this work, we reported high-pressure optical absorption measurements on the InN epilayers of Table 3.1, with free-electron concentrations in the 5×10^{17} – 1.6×10^{19} cm^{-3} range, with the aim of investigating the effect of free carriers on the pressure coefficient of the optical bandgap of wurtzite InN. With increasing carrier concentration, a reduction of the absolute value of the optical bandgap pressure coefficient of wurtzite InN was observed. An analysis of the experimental data based on the $k \cdot p$ model, as discussed in Section 3.2, allowed us to determine the pressure coefficient for the fundamental bandgap of intrinsic wurtzite InN: 32 meV/GPa. High-pressure optical absorption measurements on sample C of Table 3.1 (a 5.7-μm-thick InN epilayer) above the wurtzite-to-rocksalt transition allowed us to obtain an accurate determination of the indirect bandgap energy of rocksalt InN as a function of pressure: 0.7 eV around the phase transition (~15 GPa), with a pressure coefficient of ~23 meV/GPa.

- Article 3.2: *Pressure dependence of the refractive index in wurtzite and rocksalt indium nitride,* by R. Oliva, A. Segura, J. Ibáñez, T. Yamaguchi, Y. Nanishi and L. Artús. Published in Applied Physics Letters (2014), vol. 105, p. 232111.

In this manuscript, we presented high-pressure Fourier transform infrared reflectance measurements on freestanding InN (sample C of Table 3.1) in order to

determine the pressure dependence of the refractive index of both wurtzite and rocksalt InN. From a fit to the experimental refractive-index curves including the effect of the high-energy optical gaps, phonons, free carriers, and the direct (fundamental) bandgap in the case of wurtzite InN (i.e., by using the theoretical framework discussed in the previous section), we were able to measure the pressure coefficients of the high frequency dielectric constant ε_∞ of wurtzite and rocksalt InN: negative pressure coefficients of $-8.8 \cdot 10^{-3}$ GPa^{-1} and $-14.8 \cdot 10^{-3}$ GPa^{-1} were obtained for the wurtzite phase and the high-pressure polymorph, respectively.

PHYSICAL REVIEW B **86**, 035210 (2012)

High-pressure optical absorption in InN: Electron density dependence in the wurtzite phase and reevaluation of the indirect band gap of rocksalt InN

J. Ibáñez,[1,*] A. Segura,[2] B. García-Domene,[2] R. Oliva,[1] F. J. Manjón,[3] T. Yamaguchi,[4] Y. Nanishi,[4] and L. Artús[1]
[1]*Institut Jaume Almera, Consell Superior d'Investigacions Científiques (CSIC), 08028 Barcelona, Catalonia, Spain*
[2]*Departament de Física Aplicada-ICMUV-MALTA Consolider Team, Universitat de València, 46100 Burjassot (València), Spain*
[3]*Instituto de Diseño para la Fabricación y Producción Automatizada, MALTA Consolider Team-Universitat Politècnica de València, 46022 València, Spain*
[4]*Faculty of Science and Engineering, Ritsumeikan University, Shiga 525-8577, Japan*
(Received 11 June 2012; published 24 July 2012)

We report on high-pressure optical absorption measurements on InN epilayers with a range of free-electron concentrations (5×10^{17}–1.6×10^{19} cm^{-3}) to investigate the effect of free carriers on the pressure coefficient of the optical band gap of wurtzite InN. With increasing carrier concentration, we observe a decrease of the absolute value of the optical band gap pressure coefficient of wurtzite InN. An analysis of our data based on the $\boldsymbol{k}\cdot\boldsymbol{p}$ model allows us to obtain a pressure coefficient of 32 meV/GPa for the fundamental band gap of intrinsic wurtzite InN. Optical absorption measurements on a 5.7-μm-thick InN epilayer at pressures above the wurtzite-to-rocksalt transition have allowed us to obtain an accurate determination of the indirect band gap energy of rocksalt InN as a function of pressure. Around the phase transition (∼15 GPa), a band gap value of 0.7 eV and a pressure coefficient of ∼23 meV/GPa are obtained.

DOI: 10.1103/PhysRevB.86.035210 PACS number(s): 78.66.Fd, 78.40.Fy, 71.20.Nr

I. INTRODUCTION

InN and related group-III nitride alloys such as InGaN and InAlN have enormous potential to develop novel applications for optoelectronics, photovoltaics, or high-frequency electronics. The revision of the band gap energy of wurtzite InN (w-InN) to a value of only $E_G \approx 0.7$ eV gave rise to renewed interest in these compounds, because their band gap energy may be tuned over a wide spectral range, from the near infrared to the ultraviolet. This remarkable property could be exploited to fabricate high-efficiency solar cells and light emitting diodes.[1]

Despite much effort to investigate the structural, electronic, optical, and vibrational properties of w-InN at ambient pressure, relatively little is known about the properties of this material as a function of pressure. X-ray diffraction (XRD) and Raman scattering studies showed that the wurtzite-to-rocksalt phase transition takes place at ∼14 GPa.[2–5] From these structural and lattice-dynamic investigations, values for the bulk modulus and mode Grüneisen parameters of both phases were obtained. In turn, several works have studied the pressure dependence of the fundamental band gap of w-InN and InGaN.[6–10] In general, the pressure dependence of the optical-emission peak energy in InN and InGaN is weaker than that of the absorption edge.[6,10] The observed differences have been attributed to a sizable contribution of impurity states to the optical emission of the samples. Other authors, however, by direct comparison of PL data with pressure coefficients obtained with *ab initio* calculations, conclude that the PL emission from w-InN and InGaN has a mainly band-to-band character.[11]

Kamińska *et al.*[8] showed that conduction-band filling has a clear effect on the photoluminescence (PL) peak pressure coefficient dE_{PL}/dP of w-InN. This effect can be attributed to a reduction of the Fermi energy with increasing pressure as a consequence of the increasing electron effective mass. However, with the PL data alone, it is not possible to rule out that the experimental dE_{PL}/dP values are further reduced by impurity emission. Bearing in mind the different pressure coefficients measured so far in InN and InGaN with PL and absorption techniques, the determination of the absorption-edge pressure coefficients dE_{abs}/dP as a function of the free-carrier concentration could be highly informative with regard to the localized/band-to-band character of the PL emission.

It has been recently shown that rocksalt InN (rs-InN) is an indirect semiconductor with a band gap energy of ∼1 eV around the transition pressure.[12] However, in that work, the very low absorbance of the sample investigated (an InN epilayer with a thickness of 500 nm) allowed only the determination of the higher energy direct transition at the Γ point. Therefore, an accurate determination of the energy of the indirect band gap of rs-InN and its pressure dependence is necessary.

In the present work, we carry out high-pressure optical absorption measurements in w-InN and rs-InN. We investigate the effect of free carriers on the pressure coefficient of the optical band gap of w-InN. For this purpose, different samples with carrier concentrations in the 5×10^{17}–1.6×10^{19} cm^{-3} range are employed. Optical measurements on the thickest epilayer available (5.7 μm) allow us to study in detail the wurtzite-to-rocksalt transition and to obtain an accurate determination of the energy of the indirect band gap of rs-InN and its pressure behavior.

II. EXPERIMENT

Four nominally undoped c-face w-InN epilayers were grown by molecular beam epitaxy on sapphire substrates. The background electron concentration (thickness) of these samples was 5×10^{17} cm^{-3} (5.7 μm), 2×10^{18} cm^{-3} (500 nm), 6.5×10^{18} cm^{-3} (400 nm), and 1.6×10^{19} cm^{-3} (400 nm).[13,14] Flakes containing InN were detached from the substrates and

loaded, together with several ruby chips, into a 200-μm-diameter hole drilled on a 50-μm-thick Inconel gasket. The gasket was placed between the two diamond anvils of a membrane-type diamond anvil cell. Methanol–ethanol–water (16:3:1) was used as a pressure-transmitting medium, and pressure was determined from the fluorescence of ruby chips.[15] Room-temperature optical absorption of the flakes was measured as a function of pressure using a tungsten lamp, spatial filters, and reflective objectives. For the mid-infrared spectral range, the measurements were performed using a single-grating monochromator and PbS or InAs detectors with lock-in amplification. For near-infrared and visible measurements, a multichannel spectrophotometer was employed.

III. RESULTS AND DISCUSSION

A. Wurtzite InN

Optical absorption measurements were carried out to investigate the electron density dependence of the band gap pressure coefficients of w-InN. Figure 1 shows the absorption coefficient α at different pressures for the two w-InN epilayers with low and high electron densities ($n = 5 \times 10^{17}$ and 1.6×10^{19} cm^{-3} in Fig. 1(a) and 1(b), respectively). Both figures show the expected blueshift of the absorption edge with increasing P and the effect of conduction-band filling. The latter is evidenced in Fig. 1(b) by the higher energy of the absorption edge in the absorption spectra, i.e., in the spectra of the sample with $n = 1.6 \times 10^{19}$ cm^{-3}. From an analysis of the absorption coefficient at ambient

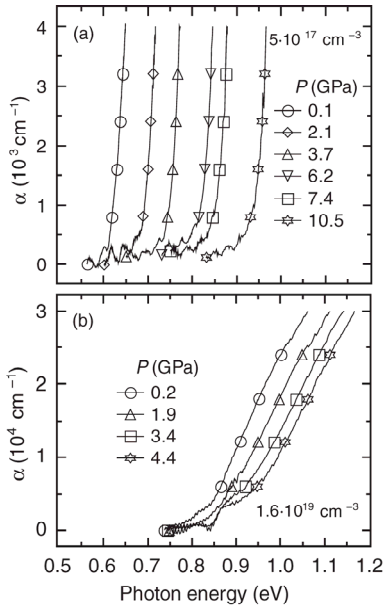

FIG. 1. Optical absorption spectra at different hydrostatic pressures of two InN epilayers with free-electron concentrations of (a) 5×10^{17} cm^{-3} (thickness 5.7 μm) and (b) 1.6×10^{19} cm^{-3} (thickness 400 nm).

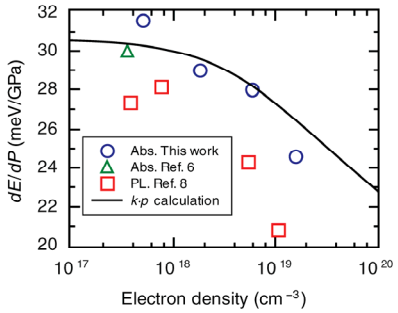

FIG. 2. (Color online) Pressure coefficient of the optical band gap of InN as a function of electron concentration. The data obtained in this work with high-pressure optical absorption measurements are plotted with circles. Data reported in Refs. 6 (triangle) and 8 (squares), obtained with optical absorption and PL measurements, respectively, have also been included in the plot. The curve is the calculated dependence based on the $\boldsymbol{k}\cdot\boldsymbol{p}$ model. For the calculation, a band gap pressure coefficient of 32 meV/GPa at a zero electron concentration has been used.

pressure based on a sigmoidal dependence on photon energy,[16] we extract for the sample with $n = 5 \times 10^{17}$ cm^{-3} a band gap energy value of 0.65 eV. This value is in excellent agreement with that obtained with the same procedure for samples with similar electron densities (0.64 eV, see Ref. 16). With increasing n, we find that the band gap energy monotonically increases up to ~0.8 eV for $n = 1.6 \times 10^{19}$ cm^{-3}, in very good agreement with published values.[17,18]

Figure 2 shows the pressure coefficient of the absorption edge $dE_{\rm abs}/dP$, as a function of n, as extracted from the pressure-dependent optical absorption measurements on the different samples studied in this work. Data from Ref. 6 also obtained with optical absorption experiments have been included in the plot for comparison. As can be seen in the figure, $dE_{\rm abs}/dP$ is reduced from 30–32 meV/GPa for the samples with the lowest electron densities down to ~24 meV/GPa for $n = 1.6 \times 10^{19}$ cm^{-3}. A similar observation was obtained by low-temperature PL measurements in Ref. 8 and attributed to conduction-band-filling effects. Data points from this work can also be found in Fig. 2. However, the $dE_{\rm PL}/dP$ values reported in that work were consistently lower than those obtained with the present optical absorption measurements (e.g., 27.3 meV/GPa at $n = 3.6 \times 10^{17}$ cm^{-3} and 20.8 meV/GPa at $n = 1.1 \times 10^{19}$ cm^{-3}; see Ref. 8). This observation seems to confirm that the pressure dependence of the PL emission in InN is in general weaker than that of the absorption edges. In Refs. 6 and 10, the difference between the pressure coefficients obtained with emission and absorption techniques was related to the possible participation of impurity states (i.e., of highly localized states with low-pressure coefficients) in the PL emission of InN and InGaN.

The solid line in Fig. 2 shows the result of a calculation of the pressure coefficient of the optical band gap as a function of n in w-InN. This calculation was performed using an approximation of the two-band $\boldsymbol{k}\cdot\boldsymbol{p}$ Kane model in the small effective mass limit to take into account the nonparabolicity

of the conduction band of InN.[18] Following Ref. 8, it was assumed that the pressure coefficient of the optical band gap (dE_{abs}/dP) has two contributions: one from the band gap pressure coefficient in the intrinsic semiconductor dE_G/dP and a second one arising from the pressure dependence of the Fermi energy dE_F/dP. The latter is a consequence of the flattening of the conduction band (i.e., of the increasing electron effective mass) with increasing pressure; therefore, it has a negative value. To calculate the derivative of E_F as a function of n and obtain the curve of Fig. 2, the Fermi energy was numerically calculated for different n and P values at room temperature by taking a zone-center electron effective mass value equal to $m_e^* = 0.07m_e$ at ambient pressure.[1] Pressure-dependent $m_e^*(P)$ values were obtained using the expression $m_e^*(P) \approx m_e^* E_G(P)/E_G$ from $\boldsymbol{k}\cdot\boldsymbol{p}$ theory, where $E_G = 0.65$ eV is the band gap of InN at ambient pressure and $E_G(P)$ is assumed to vary linearly with pressure, i.e., $E_G(P) = E_G + (dE_G/dP)P$, where dE_G/dP is left as an adjustable parameter.

Within this approach, we find that a value of $dE_G/dP = 32$ meV/GPa yields the best agreement between the theoretical and the experimental data over a large range of electron densities (Fig. 2). This pressure coefficient value is in very good agreement with the predictions of many-body perturbation theory in the G_0W_0 approximation.[19] Such calculations, which provide excellent E_G values for w-InN at ambient pressure (0.69 eV), yield dE_G/dP values in the range of 28–33 meV/GPa.[19]

In the range of low electron densities ($n < 10^{18}$ cm^{-3}), where conduction-band-filling effects are expected to be small, the dE_{abs}/dP curve calculated using $dE_G/dP = 32$ meV/GPa falls between the two data points obtained with optical absorption measurements plotted in Fig. 2 (one of them from Ref. 6). When n goes to zero, the Fermi energy exhibits some pressure dependence arising from the pressure dependence of m_e^* in the intrinsic semiconductor. As a consequence, for low electron densities, the calculated dE_{abs}/dP values in Fig. 2 tend not to $dE_G/dP = 32$ meV/GPa but to a somewhat lower value (∼30.5 meV/GPa).

As can be seen in Fig. 2, the reduction of dE_{abs}/dP predicted by the $\boldsymbol{k}\cdot\boldsymbol{p}$ calculation agrees well with the experimental data obtained by optical absorption measurements for the samples with higher electron densities, thus confirming that conduction-band filling is responsible for the reduction of dE_{abs}/dP with increasing n. Our data and analysis suggest that the true value of dE_G/dP in intrinsic w-InN is 32 meV/GPa, in the upper limit of the calculations of Ref. 19. By using the bulk modulus ($B_0 = 125.5$ GPa) obtained by means of XRD in Ref. 2, we obtain a volume deformation potential for w-InN of $dE_G/d\ln V = -4.0$ eV.

For sufficiently high electron concentrations, band gap renormalization effects arising from electron–electron interactions and carrier–ion correlations are expected to yield reduced band gap energies.[18] These many-body effects partially compensate for the magnitude of the band gap increase arising from conduction-band filling and result in energy redshifts of ∼150 meV per decade of change of n above 10^{19} cm^{-3} in w-InN.[18] Here, to evaluate the role of band gap renormalization on dE_{abs}/dP, we calculated the pressure coefficients for the conduction-band shifts resulting from electron–electron interaction (ΔE_{e-e}) and electron–ion interaction (ΔE_{e-i}) as a function of n. For this purpose, we used the expressions given in Ref. 18 for both ΔE_{e-e} and ΔE_{e-i} and we obtained their pressure derivatives by numerical methods. Below 5×10^{18} cm^{-3}, our calculations yield pressure coefficients for $\Delta E_{e-e} + \Delta E_{e-i}$ lower than 1 meV/GPa. For electron concentrations close to that of our most heavily doped sample (1.6×10^{19} cm^{-3}), we find that $d(\Delta E_{e-e} + \Delta E_{e-i})/dP \sim 2$ meV/GPa. Given that this value is still comparable to the experimental error of the pressure-dependent optical measurements, it can be assumed that band gap renormalization effects play a minor role in the results of Fig. 2. In contrast, in the ultra-heavily-doped regime ($n \sim 10^{20}$ cm^{-3}), we obtain pressure coefficients for the band gap renormalization shifts that are higher than 4 meV/GPa. Such values are expected to compensate for the reduced dE_{abs}/dP values predicted by the $\boldsymbol{k}\cdot\boldsymbol{p}$ calculations for high electron densities (Fig. 2). However, the $\boldsymbol{k}\cdot\boldsymbol{p}$ model is expected to fail in the ultra-heavily-doped range. Additional work would be desirable to ascertain the role of conduction-band filling and band gap renormalization on the high-pressure optical properties of ultra-heavily-doped w-InN.

B. Rocksalt InN

Rs-InN is an indirect semiconductor with a band gap energy of ∼1 eV.[12] In this work, we perform a detailed study of the pressure dependence, up to 30 GPa, of the indirect band gap of rs-InN using a thick InN epilayer (5.7 μm). Figure 3 shows three absorption spectra obtained on the upstroke at 12.1, 15.3, and 17.4 GPa for this sample. The wurtzite-to-rocksalt phase transition is clearly observed as a change in the shape of the absorption edge with increasing pressure. At 15.3 GPa, the profile at higher photon-energy values of the spectrum still resembles that of the wurtzite phase. In contrast, from the absorption curve at 17.4 GPa, it can be concluded that the phase transition is complete. As discussed in Ref. 12, the pressure values at which the wurtzite-to-rocksalt phase transition is observed in InN by means of optical absorption measurements tend to be higher than those obtained with XRD or Raman-scattering measurements. This discrepancy may be attributed

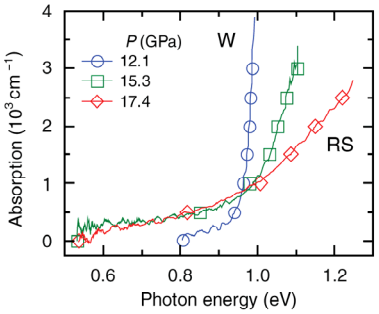

FIG. 3. (Color online) Optical absorption spectra at different hydrostatic pressures around the wurtzite-to-rocksalt transition of a 5.7-μm-thick InN epilayer with a free-electron concentration of 5×10^{17} cm^{-3}.

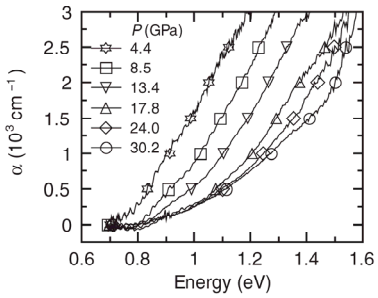

FIG. 4. Optical absorption spectra at different hydrostatic pressures (downstroke cycle) of rs-InN. Measurements were performed on a 5.7-μm-thick InN epilayer with free-electron concentration of 5×10^{17} cm^{-3}.

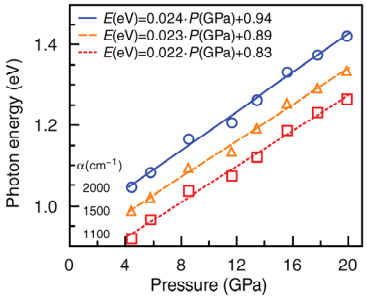

FIG. 6. (Color online) Pressure dependence of the absorption edge of rs-InN at three (constant) absorption-coefficient values. A linear fit to the data allows us to evaluate the pressure coefficient of the indirect band gap of rs-InN.

to the presence of remaining, highly absorbing w-InN domains in the flakes around (or just above) the transition pressure.

High-pressure absorption measurements were obtained in the upstroke cycle up to 30 GPa and then in the downstroke cycle down to ambient pressure. Figure 4 shows the absorption spectra of rs-InN obtained in the downstroke cycle, from 30.2 GPa down to 4.4 GPa. The expected redshift of the absorption edge with decreasing pressure is observed. The absorption spectra of rs-InN obtained in the upstroke cycle ($P > 17.4$ GPa) yielded similar profiles and have not been included in the subsequent analysis. The characteristic shape of the indirect absorption edge is observed in the figure down to 4 GPa. Thus, a clear hysteresis effect is observed. As in Ref. 12 for the case of a much thinner epilayer, we find that for $P < 4$ GPa, the rocksalt-to-wurtzite backtransformation occurs (not shown).

The quadratic dependence of the low-energy tail of the absorption edge of rs-InN confirms the indirect nature of this semiconductor compound. In Fig. 5, we plotted the square root of the absorption coefficient of rs-InN for two pressure values (downstroke cycle). In both cases, a clear linear dependence arising from an indirect transition is observed. For a pressure of 13.4 GPa, close to the pressure at which the wurtzite-to-rocksalt transformation occurs, the low-energy tail can be assigned to an indirect band gap with an energy

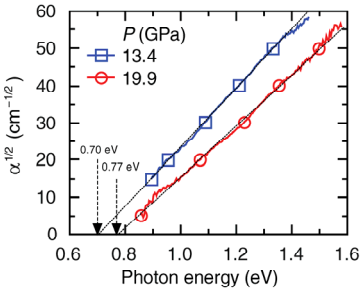

FIG. 5. (Color online) Square root of the room-temperature absorption coefficient of rs-InN measured at two hydrostatic pressure values. From a linear fit to the data, energy values for the indirect band gaps are evaluated.

of 0.70 $\pm$ 0.05 eV. This value is lower than that previously measured in thinner epilayers (1 eV at 15.7 GPa, see Ref. 12). While in Ref. 12 the small thickness of the sample prevented the clear observation of the indirect absorption edge, since the transmittance was dominated by the allowed higher-energy direct transition at the Γ point, the present measurements provide a more accurate determination of the indirect band gap energy of rs-InN.

Previous theoretical works predicted a range of possible indirect band gap values for rs-InN,[20–23] from 0.5[21,23] to 1.9 eV.[20] The present measurements indicate that the indirect band gap energy of rs-InN lies in the lower range of the theoretical calculations, i.e., in agreement with the results of Refs. 21 and 23. These two works predict that the lowest band gap of rs-InN corresponds to a $L - \Gamma$ transition.

From the spectra of Fig. 4, a pressure coefficient for the indirect band gap of rs-InN can be estimated from the shifts at constant absorption coefficient. We show in Fig. 6 the pressure dependence of the energy shift of the absorption edge at three values: 1100, 1500, and 2000 cm^{-1}. A pressure coefficient of 23 meV/GPa is extracted from a linear fit to the data of Fig. 6. This value, slightly lower than that of the direct band gap in the wurtzite phase (32 meV/GPa), allows us to obtain the volume deformation potential for the indirect transition in rs-InN. By using the bulk modulus of rs-InN ($B_0 = 170$ GPa[3]), we obtain a value of $dE_G/d\ln V = -3.9$ eV, only slightly below the deformation potential of the direct fundamental band gap of w-InN.

IV. CONCLUSION

Conduction-band-filling yields reduced optical band gap pressure coefficients in w-InN with increasing carrier concentration. The experimental pressure coefficients in w-InN, measured with optical absorption experiments, are found to be higher than those obtained by PL measurements in previous works. A $\boldsymbol{k}\cdot\boldsymbol{p}$ calculation allows us to reproduce the weakening of the experimentally determined band gap pressure coefficients with increasing electron density. We conclude that the best value for the band gap pressure coefficient in intrinsic w-InN is 32 meV/GPa. The wurtzite-to-rocksalt phase transformation is observed at ~15 GPa. Around the

transition pressure, a band gap of 0.7 eV is obtained for the rocksalt phase. From the high-pressure optical measurements, the pressure coefficient for the indirect band gap of rs-InN is obtained: 23 meV/GPa.

ACKNOWLEDGMENTS

This work was supported by the Spanish Ministry of Science and Innovation through Project No. MAT2010-16116.

*jibanez@ictja.csic.es

[1]J. Wu, J. Appl. Phys. **106**, 011101 (2009).
[2]M. Ueno, M. Yoshida, A. Onodera, O. Shimomura, and K. Takemura, Phys. Rev. B **49**, 14 (1994).
[3]S. Uehara, T. Masamoto, A. Onodera, M. Ueno, O. Shimomura, and K. Takemura, J. Phys. Chem. Solid. **58**, 2093 (1997).
[4]C. Pinquier, F. Demangeot, J. Frandon, J.-C. Chervin, A. Polian, B. Couzinet, P. Munsch, O. Briot, S. Ruffenach, B. Gil, and B. Maleyre, Phys. Rev. B **73**, 115211 (2006).
[5]J. Ibáñez, F. J. Manjón, A. Segura, R. Oliva, R. Cuscó, R. Vilaplana, T. Yamaguchi, Y. Nanishi, and L. Artús, Appl. Phys. Lett. **99**, 011908 (2011).
[6]S. X. Li, J. Wu, E. E. Haller, W. Walukiewicz, W. Shan, H. Lu, and W. J. Schaff, Appl. Phys. Lett. **83**, 4963 (2003).
[7]G. Franssen, I. Gorczyca, T. Suski, A. Kamińska, J. Pereiro, E. Muñoz, E. Iliopoulos, A. Georgakilas, S. B. Che, Y. Ishitani, A. Yoshikawa, N. E. Christensen, and A. Svane, J. Appl. Phys. **103**, 033514 (2008).
[8]A. Kamińska, G. Franssen, T. Suski, I. Gorczyca, N. E. Christensen, A. Svane, A. Suchocki, H. Lu, W. J. Schaff, E. Dimakis, and A. Georgakilas, Phys. Rev. B **76**, 075203 (2007).
[9]W. Shan, W. Walukiewicz, E. E. Haller, B. D. Little, J. J. Song, M. D. McCluskey, N. M. Johnson, Z. C. Feng, M. Schurman, and R. A. Stall, J. Appl. Phys. **84**, 4452 (1998).
[10]M. Millot, Z. M. Geballe, K. M. Yu, W. Walukiewicz, and R. Jeanloz, Appl. Phys. Lett. **100**, 162103 (2012).
[11]G. Franssen, T. Suski, P. Perlin, H. Teisseyre, A. Khachapuridze, L. H. Dmowski, J. A. Plesiewicz, A. Kamińska, M. Kurouchi, Y. Nanishi, H. Lu, and W. Schaff, Appl. Phys. Lett. **89**, 121915 (2006).
[12]J. Ibáñez, A. Segura, F. J. Manjón, L. Artús, T. Yamaguchi, and Y. Nanishi, Appl. Phys. Lett. **96**, 201903 (2010).
[13]R. Cuscó, J. Ibáñez, E. Alarcón-Lladó, L. Artús, T. Yamaguchi, and Y. Nanishi, Phys. Rev. B **79**, 155210 (2009).
[14]R. Cuscó, E. Alarcón-Lladó, J. Ibáñez, T. Yamaguchi, Y. Nanishi, and L. Artús, J. Phys. Condens. Matter **21**, 415801 (2009).
[15]K. Syassen, High Press. Res. **28**, 75 (2008).
[16]J. Wu, W. Walukiewicz, W. Shan, K. M. Yu, J. W. Ager, S. X. Li, E. E. Haller, H. Lu, and W. J. Schaff, J. Appl. Phys. **94**, 4457 (2003).
[17]J. Wu, W. Walukiewicz, S. X. Li, R. Armitage, J. C. Ho, E. R. Weber, E. E. Haller, H. Lu, W. J. Schaff, A. Barcz, and R. Jakiela, Appl. Phys. Lett. **84**, 2805 (2004).
[18]J. Wu, W. Walukiewicz, W. Shan, K. M. Yu, J. W. Ager, E. E. Haller, H. Lu, and W. J. Schaff, Phys. Rev. B **66**, 201403 (2002).
[19]P. Rinke, M. Winkelnkemper, A. Qteish, D. Bimberg, J. Neugebauer, and M. Scheffler, Phys. Rev. B **77**, 075202 (2008).
[20]J. Furthmüller, P. H. Hahn, F. Fuchs, and F. Bechstedt, Phys. Rev. B **72**, 205106 (2005).
[21]J. Serrano, A. Rubio, E. Hernández, A. Muñoz, and A. Mujica, Phys. Rev. B **62**, 16612 (2000).
[22]N. E. Christensen and I. Gorczyca, Phys. Rev. B **50**, 4397 (1994).
[23]M.-Y. Duan, L. He, M. Xu, M.-Y. Xu, S. Xu, and K. K. Ostrikov, Phys. Rev. B **81**, 033102 (2010).

APPLIED PHYSICS LETTERS **105**, 232111 (2014)

Pressure dependence of the refractive index in wurtzite and rocksalt indium nitride

R. Oliva,[1,2] A. Segura,[2] J. Ibáñez,[1,a)] T. Yamaguchi,[3] Y. Nanishi,[3] and L. Artús[1]
[1]*Institut Jaume Almera, Consell Superior d'Investigacions Científiques (CSIC), Lluís Solé i Sabarís s.n., 08028 Barcelona, Catalonia, Spain*
[2]*MALTA-Consolider Team, Departament de Física Aplicada, ICMUV, Universitat de València, c/Dr. Moliner 50, 46100 Burjassot, València, Spain*
[3]*Faculty of Science and Engineering, Ritsumeikan University, Shiga 525-8577, Japan*

(Received 15 October 2014; accepted 28 November 2014; published online 10 December 2014)

We have performed high-pressure Fourier transform infrared reflectance measurements on a free-standing InN thin film to determine the refractive index of wurtzite InN and its high-pressure rocksalt phase as a function of hydrostatic pressure. From a fit to the experimental refractive-index curves including the effect of the high-energy optical gaps, phonons, free carriers, and the direct (fundamental) band-gap in the case of wurtzite InN, we obtain pressure coefficients for the low-frequency (electronic) dielectric constant ε_∞. Negative pressure coefficients of $-8.8\times10^{-2}\,\mathrm{GPa}^{-1}$ and $-14.8\times10^{-2}\,\mathrm{GPa}^{-1}$ are obtained for the wurtzite and rocksalt phases, respectively. The results are discussed in terms of the electronic band structure and the compressibility of both phases.
 [http://dx.doi.org/10.1063/1.4903860]

Group-III nitride semiconductors (GaN, InN, and AlN) and their alloys (InGaN, AlGaN, and InAlN) exhibit unique properties that are already being exploited to design and fabricate high-performance electronic and optoelectronic devices. In particular, after the discovery of the low band-gap of InN (0.65 eV at room temperature) and the associated small electron effective mass and large electron mobility, In-rich InGaN alloys emerged as promising active materials to develop numerous device applications, including high-frequency transistors or optoelectronic devices working in the near-infrared spectral range. In spite of much work dealing with the fundamental properties of the group-III nitrides, many questions regarding the electronic structure, bonding properties, or optical response of these compounds remain to be investigated.

High-pressure experiments provide valuable information about the fundamental properties and structural stability of semiconductor materials. In particular, the data obtained with high-pressure optical measurements allow one to test the results of theoretical calculations dealing with their electronic or lattice-dynamical properties. Besides the energy gaps, the dielectric constants are among the most relevant quantities that characterize the electronic properties and optical response of semiconductors. The pressure dependence of the dielectric constants can be linked to the pressure behavior of the polar phonon frequencies and the critical points in the electronic band structure, and also to the stability of the material.

Pressure coefficients for the refractive index n or the low-frequency (electronic) dielectric constant ε_∞ have been obtained in the past by means of *ab initio* calculations for both wurtzite[1–3] and zinc-blende[2,4,5] InN. The values reported in those studies exhibit significant discrepancies, with differences of more than one order of magnitude in some cases. Thus, experimental work dealing with the determination of the pressure coefficients of the refractive index and/or dielectric constants of InN would be highly desirable, and it would provide additional insight into the pressure behavior of other optical phenomena such as the TO-LO splitting[6–8] and LO-plasmon coupling.[8]

In the present work, we carry out Fourier transform infrared (FTIR) reflectance measurements to investigate the pressure behavior of the (ordinary) refractive index of wurtzite InN (w-InN) and its high-pressure (rocksalt) polymorph (rs-InN) in the transparency region. An analysis of the refractive index is performed by using a single Lorentz-oscillator model to account for high-energy critical points plus an M_0-type critical-point model of the dielectric function to include the contribution from the direct band-gap of the wurtzite phase. Phonons and free-carrier effects are also included in the model. Relative pressure coefficients for ε_∞, $(1/\varepsilon_\infty)d\varepsilon_\infty/dP$, equal to $-8.8\times10^{-3}\,\mathrm{GPa}^{-1}$ and $-14.8\times10^{-3}\,\mathrm{GPa}^{-1}$, are obtained for w-InN and rs-InN, respectively. In the case of the wurtzite phase, the experimental value is in good agreement with the lowest range of values predicted theoretically.[2,5] From our data and analysis, the pressure dependence of the high-energy critical points in the electronic structure of w-InN and rs-InN is also evaluated.

For the present work, we used an InN epilayer grown by plasma-assisted molecular beam epitaxy (MBE) on sapphire. Hall-effect measurements revealed a background electron density $n_e < 2\times10^{18}\,\mathrm{cm}^{-3}$. A free-standing InN flake was mechanically extracted from the sapphire substrate and selected for the present experiments. A preliminary optical measurement of the flake revealed that the initial thickness of the InN layer was $d_0 \sim 3.4\,\mu\mathrm{m}$. Gold was subsequently deposited by evaporation on the back side of the flake in order to enhance the reflectivity signal. The gold layer also serves to isolate the sample Fabry-Perot (FP) cavity in order to avoid modulations of the sample interference fringes by other FP cavities within the diamond anvil cell (DAC) sample space. The flake was then loaded into a gasketed

a)Author to whom correspondence should be addressed. Electronic mail: jibanez@ictja.csic.es

membrane-type DAC, with powdered KBr as pressure transmitting medium. The applied pressure was measured with the ruby fluorescence method.

FTIR reflectivity measurements were performed with a TEO-400 FTIR spectrometer equipped with a thermal source (globar), KBr beam-splitter, and a liquid nitrogen-cooled MCT detector.[9] The modulated infrared beam was focused on the sample by using a gold-coated Cassegrain-type reflective microscope objective (15× magnification). With these objectives, the spot size on the DAC pressure chamber is lower than 70 μm.

Figure 1 shows typical reflectance spectra acquired at different hydrostatic pressure values. Several orders of interference can be seen in all the spectra. Around 2000 cm^{-1}, signal corresponding to absorption by the diamond anvils has been removed for clarity. In the high-energy range of the figure, the observed interferences smear out due to direct absorption by the fundamental band-gap of w-InN (around 5300 cm^{-1} at 0.4 GPa, corresponding to a photon energy of 0.66 eV). With increasing pressure, all the interference bands are blueshifted and new orders of interference progressively show up. At 12 GPa, the interference bands in Fig. 1 display an abrupt blueshift in relation to the spectra acquired at lower pressures. This observation can be attributed to the wurtzite-to-rocksalt phase transition, which in InN is known to occur around 13.5 GPa.[6,8,10] The abrupt displacement of the interference bands to higher wavenumbers is a consequence of the sudden reduction of the sample thickness due to the ~16.4% volume collapse after the wurtzite-to-rocksalt phase transformation.[10]

Below 800 cm^{-1}, the curves of Fig. 1 show an abrupt increase of reflectivity that can be attributed to the polar phonon modes of the InN lattice most likely coupled to the background free electrons typical of as-grown InN. Specific far-infrared measurements in this spectral region would be necessary in order to study in detail the pressure dependence of the vibrational and free carrier contributions to the reflectivity spectra.

In the present work, the pressure-dependence of the (ordinary) refractive index of InN at different wavenumbers has been determined by accurate indexation of the interference maxima and minima of the reflectance spectra. At zero pressure ($P = 0$ GPa) and taking into account the measured thickness of the epilayer ($d_0 \sim 3.4$ μm), a refractive index equal to $n \sim 2.6$ well below the fundamental band-gap of w-InN is obtained, in agreement with the previous experimental determinations.[11,12] The pressure dependence of the sample thickness was evaluated with a Murnaghan equation of state, using a zero-pressure bulk modulus of $B_0 = 143$ GPa (186 GPa) and its corresponding first derivative $B_0' = 4.6$ GPa (6 GPa) for the wurtzite (rocksalt) phase.[8] This treatment does not take into account the pressure dependence of the c/a crystallographic axes ratio in w-InN, which can be shown to have a negligible effect on the resulting $n(\lambda)$ values. To obtain the refractive index of the rocksalt phase, the effect of the 16.4% volume collapse arising from the phase transition on the epilayer thickness was also taken into account.

Figure 2(a) shows the wavenumber dependence of the refractive index thus obtained (open symbols) for the wurtzite phase at different pressure values. The solid lines correspond to the results of a theoretical fit that will be discussed below. As can be seen in the figure, the refractive index of w-InN decreases with increasing pressure, implying a negative pressure coefficient ($dn/dP < 0$). Given that from a microscopic point of view the refractive index is expected to increase (decrease) with density (electronic polarizability), the negative sign of dn/dP in w-InN, which is characteristic of tetrahedrally bonded semiconductors, is mainly determined by the partly covalent character of the bonds (see the discussion in Ref. 13; the Phillips ionicity of w-InN is ~0.578, see Ref. 2) together with its relatively small compressibility. Under these conditions, the positive contribution to dn/dP of the electronic density increase with pressure cannot compensate the strong negative contribution arising from the pressure reduction of the electronic polarizability arising from the blueshift of the optical gaps.[13]

As expected, above the phonon region and below its fundamental band-gap, the refractive index of w-InN is more or less constant and takes a value around 2.6 at ambient

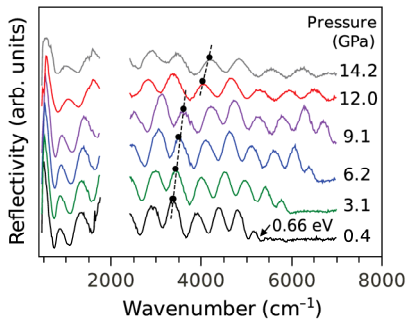

FIG. 1. Reflectance spectra of wurtzite InN at different pressure values (curves up to 9.1 GPa) and of rocksalt InN (curve at 14.2 GPa). The curve at 12 GPa is close to the wurtzite-to-rocksalt transition. In all the spectra, the sixth order of interference has been marked with a black dot.

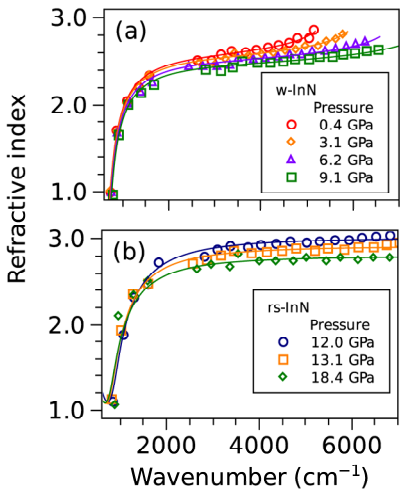

FIG. 2. Experimental refractive index at different pressures for wurzite (a) and rocksalt (b) InN as obtained by indexing of the interference maxima and minima observed in the reflectance spectra (open symbols). The solid curves are the results of a fitting model that includes the high-energy optical gaps, the polar lattice, free-carrier effects, and the direct fundamental band-gap in the case of w-InN.

pressure (Fig. 2), consistent with the $n = 2.54$ value published in the literature.[11] In contrast, stronger dispersion of the experimental refractive index is observed in the vicinity of its direct fundamental band gap. In the low wavenumber region (below 2000 cm^{-1}), the contributions of the polar lattice and the free carriers to the optical response yield a sudden decrease of the measured refractive index.

Figure 2(b) shows the corresponding experimental refractive index data points obtained for rs-InN as a function of wavenumber and for different pressure values. As in the case of the wurtzite phase, we observe that $dn/dP < 0$, which, in part, can be explained by the even lower compressibility of the rocksalt polymorph. Note that in the low wavenumber region the abrupt reduction of n as a consequence of phonons and free-carrier effects is still evident. In contrast, as expected for an indirect band-gap compound like rs-InN,[14,15] the refractive index barely depends on wavenumber well above the polar phonon/plasma edge (>3000 cm^{-1}).

Given the narrow fundamental band-gap of w-InN and the presence of residual free carriers in this compound, for the analysis of the wavenumber dependence of $n(1/\lambda)$ plotted in Fig. 2, one cannot assume that this compound is fully transparent. The effect of the polar lattice, free carriers, and the fundamental absorption edge has to be taken into account to model the optical response of the material. For the present analysis, we calculate the real (ε_r) and imaginary (ε_i) parts of the dielectric function $\varepsilon(\omega) = \varepsilon_r + i\varepsilon_i = (n + i\kappa)^2$, where κ is the imaginary part of the complex refractive index (i.e., the extinction coefficient), as follows:

$$\varepsilon_r(\omega) = \varepsilon_{\text{gap}}(\omega) + \left(1 + \frac{\omega_{PBV}^2(P)}{\omega_0^2(P)}\right) + 4\pi(\chi_{r,l} + \chi_{r,e}), \quad \text{(1a)}$$

$$\varepsilon_i(\omega) = 4\pi(\chi_{i,l} + \chi_{i,e}), \quad \text{(1b)}$$

where $\varepsilon_{\text{gap}}(\omega)$ and $1 + \omega_{PBV}^2(P)/\omega_0^2(P)$ include contributions of the fundamental band gap and high-energy transitions (see below), while $\chi_l(\omega) = \chi_{r,l}(\omega) + i\chi_{i,l}(\omega) = (\varepsilon_\infty/4\pi)(\omega_{LO}^2 - \omega_{TO}^2)/(\omega_{TO}^2 - \omega^2 - i\gamma\omega)$ and $\chi_e(\omega) = \chi_{r,e}(\omega) + i\chi_{i,e}(\omega) = -(\varepsilon_\infty/4\pi)\omega_{pe}^2/(\omega^2 + i\omega\Gamma_e)$ correspond to the susceptibilities of the polar lattice and the free carriers, respectively. For w-InN, the polar lattice susceptibility includes the pressure-dependence of the E_1(TO) and E_1(LO) phonon frequencies, ω_{TO} and ω_{LO}, which have been studied in detail elsewhere.[7,8] For the rocksalt phase, the polar lattice contribution was neglected. Additional measurements in the far-infrared region should be performed to obtain the pressure behavior of the optical phonon modes (see, for instance, Ref. 16 for the case of MgO). The free-electron density n_e, which enters the calculation of the plasma frequency of the background free carriers ω_{pe}, is left as a free adjustable parameter. To reduce the number of adjustable parameters, we take constant phononic and electronic damping parameters of $\gamma = 25$ cm^{-1} and $\Gamma_e = 250$ cm^{-1}, respectively. These values are somewhat larger than those typically observed in as-grown w-InN (for instance, $\gamma \sim 5$ cm^{-1} and $\Gamma_e \sim 125$ cm^{-1} in Ref. 12), which allows us to take into account the expected lifetime reduction of phonons and plasmons with increasing pressure. The use of different combinations of γ and Γ_e values that are much smaller than the photon wavevector in the spectral range of interest does not significantly modify the conclusions of the present analysis. In the real part of the dielectric function, Eq. (1a), besides the lattice and free carrier contributions, two additional terms have been included. First, a contribution arising from the direct fundamental gap of w-InN, $\varepsilon_{\text{gap}}(\omega) = C_0 x^{-2}[2 - (1+x)^{1/2} - (1-x)^{1/2}]$, corresponding to an M_0-type 3D critical point with parabolic bands,[16] with $x = \hbar\omega/E_g(P)$; for the calculations, we use the pressure dependent band gap energy, $E_g(P)$ (given in Ref. 15). The absorption strength of the critical point, C_0, which can be assumed to be independent of pressure,[17] is obtained from a fit to the ambient pressure spectrum ($C_0 = 7.8$). Note that below the fundamental band-gap ($x < 1$) the imaginary part of $\varepsilon_{\text{gap}}(\omega)$ is zero. Second, the contribution from the high-energy critical points in the electronic band structure of InN has been included through the second term of Eq. (1a). The high-energy critical points are modeled in terms of an average band-gap value, ω_0, and the contribution of valence-band electrons is taken into account with a Drude-like dielectric function with plasma frequency ω_{PBV}. For the fits, the quotient $K(P) = \omega_{PBV}^2(P)/\omega_0^2(P)$ is left as a free adjustable parameter. Thus, taking the $\omega \to 0$ limit of Eq. (1a), ε_∞ is simply given by the expression $\varepsilon_\infty = 1 + C_0/4 + K(P)$.

In the particular case of the rocksalt polymorph, the above model is valid (with $C_0 = 0$ due to the indirect bandgap), since the contribution of all the direct optical gaps is included in the single Lorentz oscillator of energy ω_0. In this case, the energy of the oscillator is equivalent to the Penn gap of the semiconductor.

The solid curves in Fig. 2 show the results obtained with the above model, where only the free electron density and $K(P) = \omega_{PBV}^2(P)/\omega_0^2(P)$ were left as free adjustable parameters. In all cases, values around $n_e = 10^{18}$ cm^{-3}, consistent with the Hall measurements performed on the sample, provided good agreement between calculated and experimental curves in the low wavenumber spectral range. This can be seen in Fig. 2, which shows that the theoretical and experimental curves compare well for both w-InN and rs-InN at different pressure values and throughout the whole spectral range considered in this work. Figure 3 shows the pressure dependence of the calculated refractive index at two different photon energies (400 and 600 meV) as obtained from the fits

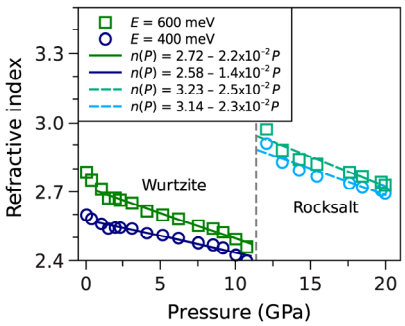

FIG. 3. The refractive index at two selected frequencies (expressed in energy units) is plotted as a function of pressure for both phases, wurtzite and rocksalt. A discontinuity of the refractive index at the transition pressure is also illustrated with a vertical dashed line.

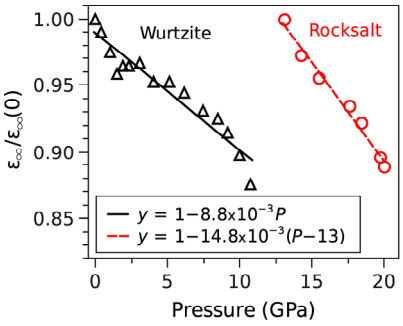

FIG. 4. The relative low-frequency dielectric constant obtained from the fits is plotted as a function of pressure. The relative pressure coefficient is obtained with a linear regression.

of Fig. 2. This figure clearly reflects the negative pressure coefficient of the refractive index in both phases. Just above the transition pressure, the refractive index exhibits an abrupt increase, which can be mostly attributed to the density increase after the phase transition from w-InN to rs-InN. As can be seen in the figure, the experimental pressure coefficient of w-InN is sizably larger at 600 meV, close to the direct band-gap, in relation to the value at 400 meV. This observation is a consequence of the large dispersion of the refractive index close to the direct fundamental band-gap of the wurtzite phase. In contrast, the pressure coefficient of rs-InN barely depends on photon energy, since in this case the pressure behavior of the refractive index is determined by the high-energy critical points.

We show in Fig. 4 the pressure dependence of the low-frequency dielectric constant that is obtained from the fits to the experimental results of Fig. 2 for both phases. From a linear fit to the data of Fig. 4, we obtain relative pressure coefficients $(1/\varepsilon_\infty)d\varepsilon_\infty/dP$ of $-8.8\times10^{-3}\,\mathrm{GPa}^{-1}$ and $-14.8\times10^{-3}\,\mathrm{GPa}^{-1}$ for w-InN and rs-InN, respectively. These values, together with theoretical results from different works,[1,2,4,5] are displayed in Table I. As can be seen in the table, for w-InN, our experimental $(1/\varepsilon_\infty)d\varepsilon_\infty/dP$ values agree well with the lowest range of reported theoretical values (Ref. 2, and also Refs. 2 and 5 for the case of zb-InN). Unfortunately, there is no theoretical data to confront the much larger absolute value of the (negative) pressure coefficient measured in rs-InN ($-14.8\times10^{-3}\,\mathrm{GPa}^{-1}$).

TABLE I. Experimental (expt.) and calculated (calc.) values of the low-frequency dielectric constant and its relative pressure coefficient, $(1/\varepsilon_\infty)d\varepsilon_\infty/dP$, in wurtzite (w), rocksalt (rs), and zincblende (zb) InN. The experimental values obtained for rs-InN in the present work, marked with an asterisk, were obtained at pressures above 12 GPa.

Phase	ε_∞	$(1/\varepsilon_\infty)d\varepsilon_\infty/dP$ ($10^{-3}\,\mathrm{GPa}^{-1}$)	Method
w	6.7	−8.8(8)	Expt. (this work)
w	7.16	−8.6	Calc. (Ref. 2)
w	8.26	−68	Calc. (Ref. 1)
rs*	7.7	−14.8(8)*	Expt. (this work)
zb	8.56	−52	Calc. (Ref. 4)
zb	6.15	−7.8	Calc. (Ref. 2)
zb	6.72	−7.4	Calc. (Ref. 5)

From the pressure dependence of $K(P) = \omega^2_{PBV}(P)/\omega^2_0(P)$ as obtained from the fits to the experimental data of Fig. 2, and taking into account that the pressure behavior of ω^2_{PBV} is determined by the increase of density, we obtain relative pressure coefficients for the high-energy optical gaps of both phases through the expression

$$\frac{1}{K}\frac{dK(P)}{dP} = \frac{1}{B} - \frac{2}{\omega_0}\frac{d\omega_0}{dP}. \quad (2)$$

For w-InN, we find from our fits that $(1/\omega_0)d\omega_0/dP = 0.011\ \mathrm{GPa}^{-1}$, which is only slightly higher than the value that can be inferred from the first maximum of $\varepsilon_i(\omega)$ at around 5.3 eV calculated by Duan *et al.*[3] at 0 and 13.4 GPa ($0.0085\,\mathrm{GPa}^{-1}$). For the rocksalt phase, the value that we obtain from the fits is very similar ($0.0096\,\mathrm{GPa}^{-1}$). Bearing in mind Eq. (2), these similar values indicate that the more negative value of $(1/\varepsilon_\infty)d\varepsilon_\infty/dP$ in rs-InN can be mostly attributed to the lower compressibility (lower $1/B$) of the rocksalt polymorph, i.e., to a lower positive contribution of the pressure-induced increase of the density of polarizable units in the material.

The $(1/\varepsilon_\infty)d\varepsilon_\infty/dP$ value obtained in the present work for w-InN is sizably more negative than those obtained in w-GaN and w-AlN (see, for instance, the recent results by Goñi *et al.*,[18] who have measured $(1/\varepsilon_\infty)d\varepsilon_\infty/dP = -6\times10^{-3}\ \mathrm{GPa}^{-1}$ and $-1.6\times10^{-3}\ \mathrm{GPa}^{-1}$ for w-GaN and w-AlN, respectively). As can be inferred from Eq. (2), the less negative pressure coefficients of $\varepsilon_\infty \sim 1+K(P)$ in these two compounds cannot be attributed to a compressibility effect, since they have lower $1/B$ values ($5\times10^{-3}\,\mathrm{GPa}^{-1}$ in w-GaN and $4.8\times10^{-3}\,\mathrm{GPa}^{-1}$ in w-AlN, see Ref. 17). Thus, our results and analysis suggest that the pressure-induced blueshift of the high-energy optical band-gaps in w-InN must be sizably larger than those in w-GaN or w-AlN, giving rise to a more pronounced (negative) pressure dependence of the dielectric constants.

In conclusion, we have studied the pressure behavior of the refractive index of w-InN and its high-pressure polymorph rs-InN. In the low wavenumber region ($<1000\,\mathrm{cm}^{-1}$), the refractive index of both phases is strongly affected by free carrier effects. For the analysis of the refractive index curves as a function of pressure, dispersion due to the fundamental direct band-gap of the wurtzite phases has to be taken into account. From a fit to the experimental data including the high-energy electronic transitions through a single Lorentz oscillator plus lattice vibrations, free carriers, and the direct (fundamental) band-gap in the case of wurtzite InN, we have obtained pressure coefficients for ε_∞. In the case of the w-InN, our experimental $(1/\varepsilon_\infty)d\varepsilon_\infty/dP$ values ($-8.8\times10^{-2}\,\mathrm{GPa}^{-1}$) agree well with the lowest range of theoretical values reported in the literature. A much larger absolute value of the (negative) pressure coefficient is measured in the case of rs-InN ($-14.8\times10^{-2}\,\mathrm{GPa}^{-1}$), which is a consequence of the lower compressibility of the high-pressure polymorph.

The work was supported by the Spanish Ministry of Economy and Competitiveness (MINECO) under Project Nos. MAT2010-16116, MAT2012-38664-C02-2, and MALTA-CONSOLIDER INGENIO 2010 CSD2007-00045.

[1]B. Abbar, B. Bouhafs, H. Aourag, G. Nouet, and P. Ruterana, Phys. Status Solidi B **228**, 457 (2001).
[2]N. E. Christensen and I. Gorczyca, Phys. Rev. B **50**, 4397 (1994).
[3]M.-Y. Duan, L. He, M. Xu, M.-Y. Xu, S. Xu, and K. K. Ostrikov, Phys. Rev. B **81**, 033102 (2010).
[4]S. Berrah, H. Abid, and A. Boukortt, Semicond. Phys. Quantum Electron. Optoelectron. **9**, 12 (2006).
[5]S. Q. Wang and H. Q. He, J. Phys. Condens. Matter **17**, 4475 (2005).
[6]C. Pinquier, F. Demangeot, J. Frandon, J. C. Chervin, A. Polian, B. Couzinet, P. Munsch, O. Briot, S. Ruffenach, B. Gil, and B. Maleyre, Phys. Rev. B **73**, 115211 (2006).
[7]J. Ibáñez, F. J. Manjón, A. Segura, R. Oliva, R. Cuscó, R. Vilaplana, T. Yamaguchi, Y. Nanishi, and L. Artús, Appl. Phys. Lett. **99**, 011908 (2011).
[8]J. Ibáñez, R. Oliva, F. J. Manjón, A. Segura, T. Yamaguchi, Y. Nanishi, R. Cuscó, and L. Artús, Phys. Rev. B **88**, 115202 (2013).
[9]V. Panchal, A. Segura, and J. Pellicer-Porres, High Pressure Res. **31**, 445 (2011).
[10]S. Uehara, T. Masamoto, A. Onodera, M. Ueno, O. Shimomura, and K. Takemura, J. Phys. Chem. Solids **58**, 2093 (1997).
[11]T. Inushima, T. Shiraishia, and V. Yu. Davydov, Solid State Commun. **110**, 491 (1999).
[12]A. Kasic, M. Schubert, Y. Saito, Y. Nanishi, and G. Wagner, Phys. Rev. B **65**, 115206 (2002).
[13]A. R. Goñi, K. Syassen, and M. Cardona, Phys. Rev. B **41**, 10104 (1990).
[14]J. Ibáñez, A. Segura, F. J. Manjón, L. Artús, T. Yamaguchi, and Y. Nanishi, Appl. Phys. Lett. **96**, 201903 (2010).
[15]J. Ibáñez, A. Segura, B. García-Domene, R. Oliva, F. J. Manjón, T. Yamaguchi, Y. Nanishi, and L. Artús, Phys. Rev. B **86**, 035210 (2012).
[16]J. Pellicer-Porres, A. Segura, Ch. Ferrer-Roca, J. A. Sans, and P. Dumas, J. Phys.: Condens. Matter **25**, 505902 (2013).
[17]A. R. Goñi and K. Syassen, in *High Pressure in Semiconductor Physics I*, edited by T. Suski and W. Paul (Academic Press, 1998).
[18]A. R. Goni, F. Käss, J. S. Reparaz, M. I. Alonso, M. Garriga, G. Callsen, M. R. Wagner, A. Hoffmann, and Z. Sitar, Phys. Rev. B **90**, 045208 (2014).

3.4. References

[1] R. Juza and H. Hahn, Z. Für Anorg. Allg. Chem. **239**, 282 (1938).
[2] T.L. Tansley and C.P. Foley, J. Appl. Phys. **59**, 3241 (1986).
[3] Q. Guo and A. Yoshida, Jpn. J. Appl. Phys. **33**, 2453 (1994).
[4] T. Yodo, T. Nakamura, T. Kouyama, and Y. Harada, Phys. Status Solidi C **2**, 2305 (2005).
[5] C. Stampfl, C.G. Van de Walle, D. Vogel, P. Krüger, and J. Pollmann, Phys. Rev. B **61**, R7846 (2000).
[6] J. Wu, W. Walukiewicz, W. Shan, K.M. Yu, J.W.A. Iii, S.X. Li, E.E. Haller, H. Lu, and W.J. Schaff, J. Appl. Phys. **94**, 4457 (2003).
[7] V.Y. Davydov, A. a. Klochikhin, R. p. Seisyan, V. v. Emtsev, S. v. Ivanov, F. Bechstedt, J. Furthmüller, H. Harima, A. v. Mudryi, J. Aderhold, O. Semchinova, and J. Graul, Phys. Status Solidi B **229**, r1 (2002).
[8] T. Matsuoka, H. Okamoto, M. Nakao, H. Harima, and E. Kurimoto, Appl. Phys. Lett. **81**, 1246 (2002).
[9] V.Y. Davydov, A. a. Klochikhin, V. v. Emtsev, S. v. Ivanov, V. v. Vekshin, F. Bechstedt, J. Furthmüller, H. Harima, A. v. Mudryi, A. Hashimoto, A. Yamamoto, J. Aderhold, J. Graul, and E. e. Haller, Phys. Status Solidi B **230**, R4 (2002).
[10] J. Wu, W. Walukiewicz, K.M. Yu, J.W.A. Iii, E.E. Haller, H. Lu, W.J. Schaff, Y. Saito, and Y. Nanishi, Appl. Phys. Lett. **80**, 3967 (2002).
[11] V.Y. Davydov, A. a. Klochikhin, V. v. Emtsev, D. a. Kurdyukov, S. v. Ivanov, V. a. Vekshin, F. Bechstedt, J. Furthmüller, J. Aderhold, J. Graul, A. v. Mudryi, H. Harima, A. Hashimoto, A. Yamamoto, and E. e. Haller, Phys. Status Solidi B **234**, 787 (2002).
[12] Y. Saito, H. Harima, E. Kurimoto, T. Yamaguchi, N. Teraguchi, A. Suzuki, T. Araki, and Y. Nanishi, Phys. Status Solidi B **234**, 796 (2002).
[13] T. Miyajima, Y. Kudo, K.-L. Liu, T. Uruga, T. Honma, Y. Saito, M. Hori, Y. Nanishi, T. Kobayashi, and S. Hirata, Phys. Status Solidi B **234**, 801 (2002).
[14] M. Hori, K. Kano, T. Yamaguchi, Y. Saito, T. Araki, Y. Nanishi, N. Teraguchi, and A. Suzuki, Phys. Status Solidi B **234**, 750 (2002).
[15] V.Y. Davydov and A.A. Klochikhin, Semiconductors **38**, 861 (2004).
[16] A. Kamińska, G. Franssen, T. Suski, I. Gorczyca, N.E. Christensen, A. Svane, A. Suchocki, H. Lu, W.J. Schaff, E. Dimakis, and A. Georgakilas, Phys. Rev. B **76**, 075203 (2007).
[17] A.G. Bhuiyan, A. Hashimoto, and A. Yamamoto, J. Appl. Phys. **94**, 2779 (2003).
[18] R. Cuscó, J. Ibáñez, E. Alarcón-Lladó, L. Artús, T. Yamaguchi, and Y. Nanishi, Phys. Rev. B **79**, 155210 (2009).
[19] R. Cuscó, E. Alarcón-Lladó, J. Ibáñez, T. Yamaguchi, Y. Nanishi, and L. Artús, J. Phys. Condens. Matter **21**, 415801 (2009).
[20] S.K. O'Leary, B.E. Foutz, M.S. Shur, and L.F. Eastman, Appl. Phys. Lett. **87**, 222103 (2005).
[21] H. Jin, G.L. Zhao, and D. Bagayoko, J. Appl. Phys. **101**, 033123 (2007).
[22] W.Z. Shen, X.D. Pu, J. Chen, H. Ogawa, and Q.X. Guo, Solid State Commun. **137**, 49 (2006).

[23] N. Domènech-Amador, R. Cuscó, L. Artús, T. Stoica, and R. Calarco, Nanotechnology **23**, 085702 (2012).
[24] S. Gwo, C.L. Wu, C.H. Shen, W.H. Chang, T.M. Hsu, J.S. Wang, and J.T. Hsu, Appl. Phys. Lett. **84**, 3765 (2004).
[25] T. Kehagias, G.P. Dimitrakopulos, A.O. Ajagunna, T. Koukoula, K. Tsagaraki, A. Adikimenakis, P. Komninou, and A. Georgakilas, J. Appl. Phys. **114**, 163519 (2013).
[26] C.H. Swartz, R.P. Tomkins, T.H. Myers, H. Lu, and W.J. Schaff, Phys. Status Solidi C **2**, 2250 (2005).
[27] J.M.M. Montes, R.V. Barroso, F.A. Menéndez, J.M.R. Muñiz, and F. Aguado, *Materia a alta presión Fundamentos y aplicaciones*, Edición: 1 (Servicio de Publicaciones de la Universidad de Oviedo, Oviedo; Santander, 2011).
[28] J. Ibáñez, A. Segura, F.J. Manjón, L. Artús, T. Yamaguchi, and Y. Nanishi, Appl. Phys. Lett. **96**, 201903 (2010).
[29] C.-L. Hsiao, T.-W. Liu, C.-T. Wu, H.-C. Hsu, G.-M. Hsu, L.-C. Chen, W.-Y. Shiao, C.C. Yang, A. Gällström, P.-O. Holtz, C.-C. Chen, and K.-H. Chen, Appl. Phys. Lett. **92**, 111914 (2008).
[30] H.A. S. Berrah and A. Boukortt, Semicond. Phys. Quantum Electron. Optoelectron. **6**, 12 (2006).
[31] S.Q. Wang and H.Q. Ye, J. Phys. Condens. Matter **17**, 4475 (2005).
[32] N. Bouarissa, Eur. Phys. J. B - Condens. Matter Complex Syst. **26**, 153 (2002).
[33] A. Munoz and K. Kunc, J. Phys. Condens. Matter **5**, 6015 (1993).
[34] P. Perlin, I. Gorczyca, S. Porowski, T. Suski, N.E. Christensen, and A. Polian, Jpn. J. Appl. Phys. **32**, 334 (1993).
[35] N.E. Christensen and I. Gorczyca, Phys. Rev. B **50**, 4397 (1994).
[36] J. Serrano, A. Rubio, E. Hernández, A. Muñoz, and A. Mujica, Phys. Rev. B **62**, 16612 (2000).
[37] S. Saib and N. Bouarissa, Phys. B Condens. Matter **387**, 377 (2007).
[38] Q. Xia, H. Xia, and A.L. Ruoff, Mod. Phys. Lett. B **08**, 345 (1994).
[39] S. Uehara, T. Masamoto, A. Onodera, M. Ueno, O. Shimomura, and K. Takemura, J. Phys. Chem. Solids **58**, 2093 (1997).
[40] C. Pinquier, F. Demangeot, J. Frandon, J.-C. Chervin, A. Polian, B. Couzinet, P. Munsch, O. Briot, S. Ruffenach, B. Gil, and B. Maleyre, Phys. Rev. B **73**, 115211 (2006).
[41] J. Ibáñez, A. Segura, B. García-Domene, R. Oliva, F.J. Manjón, T. Yamaguchi, Y. Nanishi, and L. Artús, Phys. Rev. B **86**, 035210 (2012).
[42] J. Ibáñez, R. Oliva, F.J. Manjón, A. Segura, T. Yamaguchi, Y. Nanishi, R. Cuscó, and L. Artús, Phys. Rev. B **88**, 115202 (2013).
[43] W. Wang and G. Zhao, Phys. B Condens. Matter **407**, 4313 (2012).
[44] H. Ahn, C.-H. Shen, C.-L. Wu, and S. Gwo, Thin Solid Films **494**, 69 (2006).
[45] B. Abbar, B. Bouhafs, H. Aourag, G. Nouet, and P. Ruterana, Phys. Status Solidi B **228**, 457 (2001).
[46] W.B. Pearson, *A Handbook of Lattice Spacings and Structures of Metals and Alloys*, Pergamon Press (Oxford, London, 1967).
[47] A.P. Lima, A. Tabata, J.R. Leite, S. Kaiser, D. Schikora, B. Schöttker, T. Frey, D.J. As, and K. Lischka, J. Cryst. Growth **201–202**, 396 (1999).
[48] J. Tauc, Mater. Res. Bull. **3**, 37 (1968).

[49] P.Y. Yu and M. Cardona, *Fundamentals of Semiconductors* (Springer Berlin Heidelberg, Berlin, Heidelberg, 2010).
[50] E. Hecht, *Optics* (Addison-Wesley, 2002).
[51] J. Wu, J. Appl. Phys. **106**, 011101 (2009).
[52] W. Walukiewicz, Appl. Phys. Lett. **54**, 2094 (1989).
[53] W. Walukiewicz, Phys. B Condens. Matter **302–303**, 123 (2001).
[54] M. Feneberg, S. Osterburg, K. Lange, C. Lidig, B. Garke, R. Goldhahn, E. Richter, C. Netzel, M.D. Neumann, N. Esser, S. Fritze, H. Witte, J. Bläsing, A. Dadgar, and A. Krost, Phys. Rev. B **90**, 075203 (2014).
[55] B. Arnaudov, T. Paskova, E.M. Goldys, S. Evtimova, and B. Monemar, Phys. Rev. B **64**, 045213 (2001).
[56] T. Makino, Y. Segawa, S. Yoshida, A. Tsukazaki, A. Ohtomo, and M. Kawasaki, Appl. Phys. Lett. **85**, 759 (2004).
[57] E.O. Kane, J. Phys. Chem. Solids **1**, 249 (1957).
[58] J. Wu, W. Walukiewicz, W. Shan, K.M. Yu, J.W. Ager, E.E. Haller, H. Lu, and W.J. Schaff, Phys. Rev. B **66**, 201403 (2002).
[59] P.Y. Yu and M. Cardona, *Fundamentals of Semiconductors* (Springer Berlin Heidelberg, Berlin, Heidelberg, 2010).
[60] M.D. McCluskey and E.E. Haller, *Dopants and Defects in Semiconductors* (CRC Press, 2012).
[61] W. Walukiewicz, Phys. Rev. B **41**, 10218 (1990).
[62] A. Kasic, M. Schubert, Y. Saito, Y. Nanishi, and G. Wagner, Phys. Rev. B **65**, 115206 (2002).
[63] S.X. Li, J. Wu, E.E. Haller, W. Walukiewicz, W. Shan, H. Lu, and W.J. Schaff, Appl. Phys. Lett. **83**, 4963 (2003).
[64] G. Franssen, I. Gorczyca, T. Suski, A. Kamińska, J. Pereiro, E. Muñoz, E. Iliopoulos, A. Georgakilas, S.B. Che, Y. Ishitani, A. Yoshikawa, N.E. Christensen, and A. Svane, J. Appl. Phys. **103**, 033514 (2008).
[65] W. Shan, W. Walukiewicz, E.E. Haller, B.D. Little, J.J. Song, M.D. McCluskey, N.M. Johnson, Z.C. Feng, M. Schurman, and R.A. Stall, J. Appl. Phys. **84**, 4452 (1998).
[66] M. Millot, Z.M. Geballe, K.M. Yu, W. Walukiewicz, and R. Jeanloz, Appl. Phys. Lett. **100**, 162103 (2012).
[67] G. Franssen, T. Suski, P. Perlin, H. Teisseyre, A. Khachapuridze, L.H. Dmowski, J.A. Plesiewicz, A. Kamińska, M. Kurouchi, Y. Nanishi, H. Lu, and W. Schaff, Appl. Phys. Lett. **89**, 121915 (2006).
[68] I. Gorczyca, J. Plesiewicz, L. Dmowski, T. Suski, N.E. Christensen, A. Svane, C.S. Gallinat, G. Koblmueller, and J.S. Speck, J. Appl. Phys. **104**, 013704 (2008).
[69] P. Rinke, M. Winkelnkemper, A. Qteish, D. Bimberg, J. Neugebauer, and M. Scheffler, Phys. Rev. B **77**, 075202 (2008).
[70] J.R. Chelikowsky, Phys. Rev. B **35**, 1174 (1987).
[71] M. Ueno, M. Yoshida, A. Onodera, O. Shimomura, and K. Takemura, Phys. Rev. B **49**, 14 (1994).
[72] M.-Y. Duan, L. He, M. Xu, M.-Y. Xu, S. Xu, and K. (Ken) Ostrikov, Phys. Rev. B **81**, 033102 (2010).
[73] J. Crain, G.J. Ackland, and S.J. Clark, Rep. Prog. Phys. **58**, 705 (1995).
[74] G.J. Ackland, Rep. Prog. Phys. **64**, 483 (2001).

[75] N.E. Christensen, S. Satpathy, and Z. Pawlowska, Phys. Rev. B **36**, 1032 (1987).
[76] J.E. Jaffe, R. Pandey, and A.B. Kunz, Phys. Rev. B **43**, 14030 (1991).
[77] A. Segura, J.A. Sans, F.J. Manjón, A. Muñoz, and M.J. Herrera-Cabrera, Appl. Phys. Lett. **83**, 278 (2003).
[78] S. Ves, U. Schwarz, N.E. Christensen, K. Syassen, and M. Cardona, Phys. Rev. B **42**, 9113 (1990).
[79] W. Andreoni and K. Maschke, Phys. Rev. B **22**, 4816 (1980).
[80] R. Khenata, A. Bouhemadou, M. Sahnoun, A.H. Reshak, H. Baltache, and M. Rabah, Comput. Mater. Sci. **38**, 29 (2006).
[81] D. Ginley, H. Hosono, and D.C. Paine, *Handbook of Transparent Conductors* (Springer Science & Business Media, 2010).
[82] C.E. Ekuma, J. Moreno, and M. Jarrell, J. Appl. Phys. **114**, 153705 (2013).
[83] S.W.W. Liu and S. Rabii, Phys. Rev. B **13**, 1675 (1976).
[84] Y.Z. Zhu, G.D. Chen, H. Ye, A. Walsh, C.Y. Moon, and S.-H. Wei, Phys. Rev. B **77**, 245209 (2008).
[85] S.H. Tolbert, A.B. Herhold, C.S. Johnson, and A.P. Alivisatos, Phys. Rev. Lett. **73**, 3266 (1994).
[86] N.E. Christensen and O.B. Christensen, Phys. Rev. B **33**, 4739 (1986).
[87] H.S. Güder, S. Gilliland, J.A. Sans, A. Segura, J. González, I. Mora, V. Muñoz, and A. Muñoz, Phys. Status Solidi B **235**, 509 (2003).
[88] X. Zhang, Z. Chen, S. Zhang, R. Liu, H. Zong, Q. Jing, G. Li, M. Ma, and W. Wang, J. Phys. Condens. Matter **19**, 425231 (2007).
[89] M.Y.L. Z. W. Chen, Thin Solid Films **515**, 2433 (2006).
[90] L. Pedesseau, J. Even, A. Bondi, W. Guo, S. Richard, H. Folliot, C. Labbe, C. Cornet, O. Dehaese, A.L. Corre, O. Durand, and S. Loualiche, J. Phys. Appl. Phys. **41**, 165505 (2008).
[91] S. Froyen and M.L. Cohen, Phys. Rev. B **28**, 3258 (1983).
[92] M. Merabet, S. Benalia, D. Rached, R. Khenata, A. Bouhemadou, S. Bin Omran, A.H. Reshak, and M. Rabah, Superlattices Microstruct. **49**, 132 (2011).
[93] N.C. Iza Gorczyca, Phys. Rev. B Condens. Matter **39**, 7705 (1989).
[94] W.M. Yim, J. Appl. Phys. **42**, 2854 (1971).
[95] H.S. Daniel Fritsch, Appl. Phys. Lett. **88**, 134104 (2006).
[96] S. Shokhovets, R. Goldhahn, G. Gobsch, S. Piekh, R. Lantier, A. Rizzi, V. Lebedev, and W. Richter, J. Appl. Phys. **94**, 307 (2003).
[97] V.Y. Davydov, A.A. Klochikhin, A.N. Smirnov, I.Y. Strashkova, A.S. Krylov, H. Lu, W.J. Schaff, H.-M. Lee, Y.-L. Hong, and S. Gwo, Phys. Rev. B **80**, 081204 (2009).
[98] N. Domènech-Amador, R. Cuscó, L. Artús, T. Yamaguchi, and Y. Nanishi, Phys. Rev. B **83**, 245203 (2011).
[99] V.Y. Davydov, V.V. Emtsev, I.N. Goncharuk, A.N. Smirnov, V.D. Petrikov, V.V. Mamutin, V.A. Vekshin, S.V. Ivanov, M.B. Smirnov, and T. Inushima, Appl. Phys. Lett. **75**, 3297 (1999).
[100] J.T. Foley and U. Landman, Phys. Rev. B **14**, 1597 (1976).
[101] Suski, Tadeusz and Paul, William, *High Pressure Semiconductor Physics I*, Semiconductors and semimetals (Academic Press, 1998).
[102] G. Burns, *Solid State Physics* (Academic Press, Boston U.a., 1985).
[103] J.C. Phillips, Rev. Mod. Phys. **42**, 317 (1970).

[104] W.A. Harrison and Physics, *Electronic Structure and the Properties of Solids: The Physics of the Chemical Bond* (Dover Publications, New York, NY, 1989).
[105] J.C. Phillips, Chem. Phys. Lett. **3**, 286 (1969).
[106] C.R.A. Catlow and A.M. Stoneham, J. Phys. C Solid State Phys. **16**, 4321 (1983).
[107] R. Oliva, A. Segura, J. Ibáñez, T. Yamaguchi, Y. Nanishi, and L. Artús, Appl. Phys. Lett. **105**, 232111 (2014).

CHAPTER 4

Vibrational properties of InN

4.1. Introduction

As already discussed in the previous chapters, and on account of its remarkable electronic properties, InN is a very promising semiconductor material to design a wide range of novel optoelectronic devices.[1] Among the numerous characterization tools that researchers have at their disposal, vibrational techniques are highly useful to study and characterize new advanced materials. In particular, Raman scattering is now a standard analytical tool to evaluate different properties of semiconductor compounds and structures such as their crystal quality, composition, or strain state. With regard to the latter, one must recall that in III-nitrides, lattice mismatch and the different thermal expansion coefficients between the epilayers and the substrate are known to induce large biaxial strains and high densities of dislocations, which may significantly reduce device performances.

The parameters that relate the components of the strain tensor with the shifts in the phonon frequencies are called *phonon deformation potentials*, and these can be determined with Raman scattering by combining experiments on thin films under biaxial stress and hydrostatic pressure.[2–4] In particular, the experiments at high hydrostatic pressures allow one to determine the so-called *mode Grüneisen parameters*. Their relation with other thermodynamic parameters will be described later in this chapter.

On the other hand, high-pressure Raman scattering measurements are very useful to test lattice-dynamical calculations in semiconductors. In particular, *ab initio* calculations based on the density functional theory (DFT) within the local density approximation (LDA) bear some difficulties to predict the frequencies of longitudinal modes. In turn, the calculated phonon dispersion curves can be used to assign second-order Raman modes, which is particularly relevant in the case of crystal phases whose first-order modes are Raman silent, such as the rocksalt

structure.[5] Similarly, the theoretical one-phonon density of states can be used to assign Raman features measured from low-crystalline samples. While linking the first and second order phonon modes with features in the Raman spectra is not always easy, the combined use of high-pressure measurements and DFT calculations provides valuable information (for instance, the pressure coefficient of the first and second order modes) which may facilitate the phonon assignments.

Some studies of the vibrational properties of wurtzite InN have relied on Raman measurements[6,7] as well as on IR spectroscopy.[8,9] The phonon dispersion curves have also been studied by means of inelastic X-ray scattering (IXS)[10] as well as lattice-dynamics calculations.[6,11] To the date, many works have investigated the vibrational and structural properties of InN under high-pressure. Pinquier et al.[12,13] studied the E_{2h}, A_1(TO) and A_1(LO) optical modes of a freestanding w-InN flake (with a residual electron density as high as 2.3 x 10^{19} cm^{-3}) and determined the pressure coefficients and the corresponding mode Grüneisen parameters; the other Raman active optical modes (i.e. E_{2l}, E_1(TO) and E_1(LO) modes) were not reported by these authors. While the scattering geometry of high-pressure measurements using a diamond anvil cell (DAC) is limited to the back-scattering configuration, it is still possible to detect these phonon modes by measuring InN samples grown along an orientation different than the *c*-direction.

On the other hand, the pressure coefficients of the measured E_{2h} and LO modes published in the literature for InN are rather disperse. These discrepancies could be partially accounted for by residual strains in the studied samples. Thus, high-pressure Raman experiments on different epilayers grown on different substrates and strain conditions could help to identify and/or evaluate strain effects on the pressure coefficient of these modes.

With regard to the high-pressure phase of InN, Pinquier et al.[12,13] observed the phase transition (at P_t = 13.5(5) GPa) from the wurtzite to the rocksalt structure by means of Raman-scattering. These authors reported intense Raman features up to 50 GPa that were attributed to disorder-activated modes, arising from Raman scattering at $k \neq 0$ wave vectors. In order to confirm the assignments of these features, it would be highly desirable to calculate the phonon density of states

(PDOS) in rs-InN across the entire Brillouin zone (BZ) as a function of pressure. Such calculations could also provide information about the mode Grüneisen parameters of the high-pressure phase of InN.

Despite the high amount of work in the literature dealing with the vibrational properties of InN, some additional issues should be considered for the analysis of the longitudinal optical modes. In particular, Davydov et al.[14] showed that the Raman frequency of the A_1(LO) and E_1(LO) modes in w-InN is highly sensitive to the excitation wavelength employed to excite the Raman measurements. These authors hypothesized that the wave vector of the excited phonon is determined by a double-resonance impurity-induced excitation mechanism, in which the wavenumber of the phonon for a given excitation energy is defined by the electronic band dispersion of the material. This double-resonance process results in a decrease of the phonon frequency of $\Delta\omega \approx 5$ cm^{-1} with respect the frequency of the phonon at the centre of zone (gamma point, Γ) if the 514.5-nm line is used as excitation source. Thus, it might occur that this phenomenon affects the experimental pressure coefficients of the LO mode owing to the fact that the electron-hole dispersion and the electronic bandgap energy change with pressure, thus varying the wave vector of the first-order modes as pressure is increased. Additional work to study and analyse the extent of this effect as a function of pressure is thus required.

On the other hand, the study of the pressure dependence of the phonon-plasmon coupled mode (LOPCMs) that shows up in the Raman spectra of heavily doped, *n*-type InN could allow one to probe other fundamental aspects of the electronic structure of this compound, since the frequency of LOPCMs is determined not only be the frequency of vibrational excitations (LO modes) but of free-electron excitations (plasmons). As will be discussed later in this chapter, the pressure behaviour of the LOPCMs is affected by the pressure dependence of the effective electronic mass and the high-frequency dielectric constant.

In this chapter, we perform a comprehensive high-pressure Raman-scattering study on a series of high-quality w-InN epilayers grown by plasma-assisted MBE. The samples have different thickness, orientations and residual electron concentrations, which allows us to investigate the pressure behaviour of all the

optical modes of w-InN and to assess the effect of residual strains on the experimental pressure coefficients. Particular attention is paid to the pressure behaviour of the LO and LOPCM modes in w-InN, and to the optical modes in the rocksalt polymorph. The experimental results are complemented with *ab initio* lattice dynamical calculations, which are performed over the entire BZ for both the wurtzite and rocksalt structures of InN; the one-phonon PDOS of both compounds is also calculated as a function of pressure. Finally, and for comparison purposes, we present a Raman-scattering study of CdO under high pressure, which exhibits the rocksalt structure at ambient conditions.[5] This study allows us to compare the procedure to assign, with the aid of DFT lattice-dynamical calculations, the Raman features in the case of rs-InN with that of a rocksalt compound that is already stable at room pressure.

Goals of this chapter

- To measure the pressure-dependence of all the Raman-active modes of w-InN and report the corresponding mode Grüneisen parameters.
- To discuss the effect of thin film thickness and residual strain on the pressure coefficient of the phonon modes of w-InN.
- To discuss the pressure behaviour of the LO Raman band of w-InN, following the results of Davydov et al.[14]
- To report the frequency of the L^- LOPCM at different pressures and to evaluate the pressure dependence of the effective mass of w-InN.
- To discuss the relationship between the lattice-dynamics and phase stability of InN.
- To assign the features that appear in the Raman spectra of rs-InN as well as those in the spectra of backtransited w-InN (and report their pressure coefficients).
- To study the Raman spectrum of rocksalt CdO as a function of pressure and assign, with the aid of *ab initio* lattice-dynamical calculations, the Raman peaks (and compare with the case of rs-InN).

List of samples used in this chapter

In this chapter, high-pressure Raman-scattering measurements are performed on the same set of high-quality InN epilayers, grown by PA-MBE on sapphire (Al_2O_3) substrates or GaN/Al_2O_3 templates, which were studied in Chapter 3. Information about all these samples can thus be found in Table 3.1 of the preceding chapter. Note that all samples have different epilayer thicknesses, which has allowed us to compare the experimental phonon pressure coefficients of samples with different degrees of strain. In turn, sample D (Table 3.1) was grown along the *a*-direction, which has enabled the detection and study of Raman modes that are symmetry-forbidden in the rest of epilayers, grown along the *c*-direction. Note also the large electron density in sample B2, which has permitted the detection of a fairly intense LOPCM peak for the study of the pressure behavior of this mode.

On the other hand, and for the sake of comparison with the case of rs-InN, a 900-nm thick CdO/sapphire epilayer grown by MOVPE has also been investigated in the present chapter. Hall-effect measurements revealed that the as-grown CdO epilayer displayed high *n*-type conductivity, with an electron density and mobility around 1.8×10^{18} cm^{-3} and 50 $cm^2V^{-1}s^{-1}$, respectively.

4.2. Theoretical framework

Raman scattering by phonons

The Raman effect consists in the inelastic scattering of a photon by an elementary excitation, and was theoretically predicted in 1923 by A. Smekal[15]. Later it was experimentally discovered by C. V. Raman and K. S. Krishnan in liquids,[16] and by G. Landsberg and L. I. Mandelstam in crystals.[17] Here we are concerned with the Raman scattering by phonons in semiconductor crystals.

Phonons are defined as the collective excitation of the atoms within a crystal, which results in $3N$ normal modes, where N is the number of atoms per unit cell (3 modes correspond to acoustic modes, and $3N$-3 correspond to optical modes). In the quantum-mechanical approach, a phonon can be viewed as a quasiparticle that represents the elementary excitation of the normal modes of vibration of a crystal, with momentum $\boldsymbol{q}$ and energy $\hbar\omega_p(\boldsymbol{q})$.

In a first-order Raman process, a phonon can be either created (Stokes) or annihilated (anti-Stokes) by the incoming photons, which are inelastically scattered. The energy of the phonon (i.e., the Raman shift) is given by

$$\Delta\omega = \left(\frac{1}{\lambda_{exc}} - \frac{1}{\lambda_s}\right) , \qquad [4.1]$$

where λ_{exc} is the wavelength of the excitation light and is λ_s the wavelength of the scattered light (expressed in cm units). In the Raman process, the momentum and energy are conserved, so that

$$\hbar\boldsymbol{k}_s = \hbar\boldsymbol{k}_i \pm \hbar\boldsymbol{q} , \qquad [4.2]$$

$$\hbar\omega_s = \hbar\omega_i \pm \hbar\omega_p \qquad [4.3]$$

where the subscripts *i* and *s* refer to the incident and scattered photons, respectively. The negative sign corresponds to a Stokes process (phonon creation) and the positive sign to an anti-Stokes process (phonon annihilation). From Eq. [4.2] it can be readily seen that, for Raman experiments using infrared and visible light, the phonon wave vector is much smaller than the border of the BZ for most crystals.

Therefore, the wave vector of the phonon may be assumed to be zero (dipolar approximation).

Semiclassical approach to the Raman effect

Classically, the Raman process in crystals can be described as the emission of electromagnetic waves (scattered light) by oscillating dipoles within the quasistatic approximation (the phonon frequencies are small compared to the electronic transitions that determine the electric susceptibility of the crystal). The polarization, $\boldsymbol{P}$, of the dipoles has been induced from an external electric field (incident light), $\boldsymbol{E}_i$, and are related by

$$\boldsymbol{P} = \varepsilon_0 \chi E_i \hat{\boldsymbol{e}}_i \ , \qquad [4.4]$$

where χ is the susceptibility of the crystal, defined by its electronic structure. The electric field of the incident light can be taken as: $E_i = E_0 \cos(\boldsymbol{k}_i \boldsymbol{r} - \omega_i t)$. Owing to the fact that the ionic vibrations change the electronic susceptibility, this can be expanded in terms of the normal coordinates of oscillations

$$\chi(\xi, \omega_i, \boldsymbol{k}_i) = \chi + \frac{d\chi}{d\xi}\xi + \cdots \ , \qquad [4.5]$$

where the motion of the ionic vibrations is given by $\xi = \xi_0 \cos(\boldsymbol{q}\boldsymbol{r} - \omega_p t)$. Taking the first-order term of Eq. [4.5], the resulting polarization of the medium along the $\hat{\boldsymbol{e}}_i$ direction is given by,

$$P = E_0 \cos(\boldsymbol{k}_i \boldsymbol{r} - \omega_i t)\chi + E_0 \xi_0 \cos(\boldsymbol{k}_i \boldsymbol{r} - \omega_i t)\cos(\boldsymbol{q}\boldsymbol{r} - \omega_p t)\frac{d\chi}{d\xi} \ . \qquad [4.6]$$

The first term of Eq. [4.6], namely P_0, is the induced polarization oscillating in phase with the external electric field, and corresponds to the elastic scattering (Rayleigh scattering). The second term can be rearranged so that,

$$\begin{aligned} P = P_0 + \frac{E_0 \xi_0}{2}\frac{d\chi}{d\xi}\{&\cos[(\boldsymbol{k}_i + \boldsymbol{q})\boldsymbol{r} - (\omega_i + \omega_p)t] \\ &+ \cos[(\boldsymbol{k}_i - \boldsymbol{q})\boldsymbol{r} - (\omega_i - \omega_p)t]\} \ . \end{aligned} \qquad [4.7]$$

From Eq. [4.7] it can be seen that the second term of the polarization is sinusoidal with two frequencies and wave vectors that correspond to the frequency and wave vector of the scattered photon (see Eq. [4.2] and Eq. [4.3]). Taking higher order terms in Eq. [4.5], one obtains sinusoidal terms with $\boldsymbol{k}_i \pm n\boldsymbol{q}$ wave vectors and $\omega_i \pm n\omega_p$ frequencies; these correspond to higher-order Raman scattering processes.

The intensity of the scattered light polarized in the $\hat{\boldsymbol{e}}_s$ direction is given by[5]

$$I \sim \langle |\hat{\boldsymbol{e}}_s \cdot \boldsymbol{P}|^2 \rangle \ , \qquad [4.8]$$

where the brackets represent the average in time. Taking the susceptibility as a second-rank tensor, it is possible to expand Eq. [4.4] in the normal displacement terms so that the intensity results,

$$I \sim \left| \hat{\boldsymbol{e}}_s \cdot \frac{\partial \chi}{\partial \xi} \cdot \hat{\boldsymbol{e}}_i \right|^2 \langle \xi \xi^* \rangle \ , \qquad [4.9]$$

for the Stokes component. For the anti-Stokes component, the normal displacement terms are exchanged and the partial derivative of the susceptibility is performed over ξ^*. From second quantization arguments, Eq. [4.9] can be evaluated by replacing the normal displacements by the creation, η and annihilation, $\eta^\dagger$, operators.[18] The Stokes and anti-Stokes components are then

$$\langle \eta \eta^\dagger \rangle = \frac{\hbar(n+1)}{2\omega_p} \ , \qquad \langle \eta^\dagger \eta \rangle = \frac{\hbar n}{2\omega_p} \ , \qquad [4.10]$$

respectively, where n is the Bose-Einstein occupation factor

$$n = \frac{1}{e^{\hbar\omega_p / k_B T} - 1} \ , \qquad [4.11]$$

where k_B is the Boltzmann constant and T the temperature. It can be seen that the intensity of the anti-Stokes component vanishes for $T \to 0$ and reaches the Stokes component only in the limit $T \to \infty$. For this reason, most Raman experiments are performed on the Stokes component of the spectra, where the scattering cross section is higher.

Quantum-mechanical approach to the Raman effect

Owing to the large energetic difference between photons (~ 2 eV) and phonons (~ 50 meV), a direct photon-phonon interaction does not actually occur. Instead, the electronic structure has to act as an intermediary in any Raman-scattering process. From time-dependent perturbation theory, the first-order Raman process can be understood as a three-step process, as shown in Fig. 4.1. The Feynman diagrams shown in Fig. 4.1 represent a Stokes (panel A) and anti-Stokes (panel B) process. Sequentially, 1- an incident photon creates a virtual electron-hole pair (or exciton), 2- the virtual electron (or hole) interacts with a phonon creating (Stokes) or absorbing (anti-Stokes) it, and 3- the electron-hole pair recombines emitting a photon. In total there are six possible Feynman diagrams that correspond to a Stokes process. These can be obtained by the permutations of the vertices in Fig. 4.1-A.[19] The most probable one is that shown in Fig. 4.1-A, the probability of which can be derived by using the Fermi Golden Rule,

$$W_{fi} = \frac{2\pi}{\hbar}\left|\sum_{n,n'}\frac{\langle i|\mathcal{H}_{e-R}|n\rangle\langle n|\mathcal{H}_{e-ph}|n'\rangle\langle n'|\mathcal{H}'_{e-R}|f\rangle}{(\hbar\omega_i - E_n + E_i)(\hbar\omega_i - \hbar\omega_p + E_f - E_{n'})}\right|^2 \delta(\omega_i - \omega_p - \omega_s)\ , \qquad [4.12]$$

where $\langle i|$ and $|f\rangle$ represent the initial and final energy states E_i and E_f respectively. Intermediate electronic states with energies E_n and $E_{n'}$ are represented by $\langle n|$ and $|n'\rangle$, respectively. Note that, from the denominator terms of Eq. [4.12], a resonance (i.e. an enhanced scattering probability) takes place for some intermediate electronic states. In particular, resonant Raman scattering takes place when these energies are close to electronic transitions in the band structure that exhibit high joint density of states. Thus, this happens when the energy of the incident or scattered light coincide with an interband transition. The electron-photon Hamiltonian is given by

$$\mathcal{H}_{e-R} = \frac{e}{mc}\mathbf{A}\cdot\mathbf{p}\ , \qquad [4.13]$$

where $\mathbf{A}$ is the vector potential of the electromagnetic field and $\mathbf{p}$ is the quasi-momentum of the intermediate electron or hole.

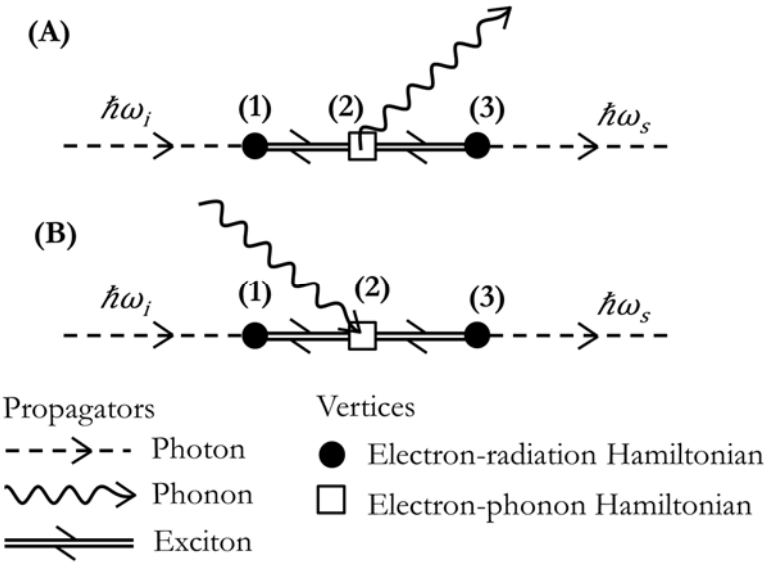

Fig. 4.1. Feynman diagram for the Stokes (upper panel, A) and anti-Stokes (lower panel, B) first-order Raman processes.

For the electron-phonon interaction there are two important scattering interactions: the deformation potential mechanism and the Fröhlich interaction. The deformation potential mechanism can be understood as a modulation of the electronic band structure by the oscillation of ions in the crystal lattice. Within the Born-Oppenheimer approximation, it is possible to write the Hamiltonian as an expansion of the total electronic Hamiltonian, in terms of the ionic displacements

$$\mathcal{H}_{e-ph} \sim \frac{\partial E}{\partial \xi} \cdot \xi \ , \qquad [4.14]$$

where E is the energy of the electronic states.

On the other hand, the Fröhlich electron-phonon interaction is the Coulomb interaction between the long-range electric field associated to the longitudinal optical modes and the electronic structure. This mechanism only takes place for longitudinal phonon modes in a polar semiconductor. For longitudinal phonons with q~0, the Hamiltonian of the interaction is,[19,18]

$$\mathcal{H}_{e-ph} \sim -\frac{iC_F}{q^2 V^{\frac{1}{2}}} (\mathbf{q} \cdot \hat{\mathbf{e}}_{\mathrm{LO}})(\eta^\dagger + \eta) \exp(i\mathbf{q} \cdot \mathbf{r}) \ , \qquad [4.15]$$

where V is the volume of the unit cell and C_F is the Fröhlich constant;

$$C_F^2 = 2\pi k_e e^2 \hbar \omega_{LO} \left(\frac{1}{\varepsilon_\infty} - \frac{1}{\varepsilon_0} \right) , \qquad [4.16]$$

where ε_∞ and ε_0 are the high and low frequency dielectric constants of the material, respectively, k_e is the Coulomb constant and ω_{LO} the phonon frequency of the LO mode.

Phonons in the wurtzite and rocksalt structures

The wurtzite structure

The wurtzite crystal structure, named after the mineral wurtzite (Zn,Fe)S, is of special interest because it is the most stable phase of many binary semiconductor compounds, including AlN, GaN, InN and their alloys.

The corresponding space group is 186 in the International Union of Crystallography classification, $P6_3mc$ in the international short symbol, or C_{6v}^4 in the Schöenflies notation. The structure can be regarded as two interpenetrating hexagonal close-packed type sublattices, one for each atomic species. As it can be seen in the panel A of Fig. 4.2, the wurtzite structure belongs to the hexagonal lattice system and is non-centrosymmetric (i.e. lacks inversion symmetry). This latter characteristic is important because it confers piezoelectric and pyroelectric character to wurtzite materials.

As it is shown in the panel A of Fig. 4.2, the unit cell contains four atoms, with primitive vectors $\vec{a}_1 = a(1/2, -\sqrt{3}/2, 0)$, $\vec{a}_2 = a(1/2, \sqrt{3}/2, 0)$ and $\vec{a}_3 = c(0,0,1)$, where a and c are the lattice parameters. The atomic positions in the unit cell can be taken as $\vec{u}_1 = (2/3, 1/3, 0)$, $\vec{u}_2 = (1/3, 2/3, 1/2)$ for the first atom-type and $\vec{u}_1 = (2/3, 1/3, u)$, $\vec{u}_2 = (1/3, 2/3, 1/3 + u)$ for the second one, where u is an internal lattice parameter around $u \approx 3/8$. Each ion is strictly tetraedrically coordinated only for the ideal case of $u = 3/8$ and $c/a = 2\sqrt{6}/3$. The arrangement of this structure gives polar symmetry along the c axis, which is a key factor for the crystal growth, etching and defect generation.

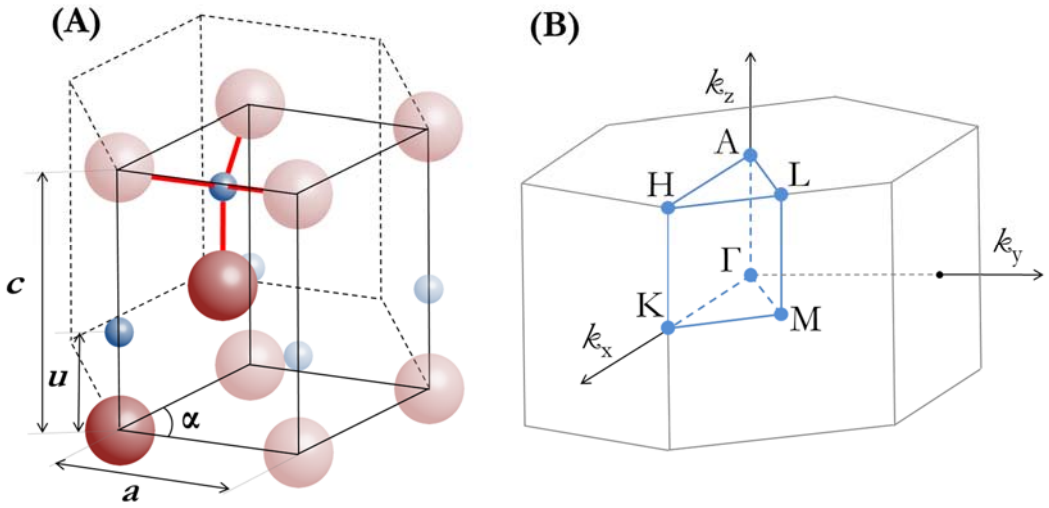

Fig. 4.2. Panel A: The unit cell (solid lines) of the wurtzite structure is shown inside the conventional hexagonal cell (in dotted lines). All the atoms around the corners of the unit cell are shown, and the four atoms of the unit cell are colourful; the tetrahedral coordination is shown with red lines. **Panel B:** First BZ of the wurtzite lattice; the high symmetry points and lines are shown.

With regard the wurtzite reciprocal lattice, it is characterized by the reciprocal primitive vectors, $\vec{b}_1 = 2\pi/a \cdot (1, -1/\sqrt{3}, 0)$, $\vec{b}_2 = 2\pi/a \cdot (-1,1/\sqrt{3}, 0)$ and $\vec{b}_3 = 2\pi/c \cdot (0,0,1)$. The first BZ is shown in the panel B of Fig. 4.2, where the most important high symmetry points and lines are shown. The Γ point, which corresponds to $\vec{k} = (0,0,0)$, is the point with highest symmetry of the structure and in the case of phonon modes, corresponds to long-wavelengths phonon vibrations.

Because first-order Raman experiments only probe small k values, here we will focus on the symmetries associated with Γ. For the wurtzite structure, this point has twelve symmetry operations that coincide with the symmetries of the real space. Following the Schnönflies notation the symmetry operations can be classified in six conjugacy classes (in the direct space)

- The identity; $\{E|0\}$.
- Two six-fold rotations (a rotation of 60º) along the c-axis followed by a $\vec{a}_3/2$ translation; $\{C_6|\vec{a}_3/2\}$ and $\{C_6^{-1}|\vec{a}_3/2\}$.
- Two three-fold rotation (rotation by 120º) along the c-axis; $\{C_3|0\}$ and $\{C_3^{-1}|0\}$.

C_{6v}	$\{E\}$	$2\{C_6\}$	$2\{C_3\}$	$\{C_2\}$	$3\{\sigma_d\}$	$3\{\sigma_v\}$	Basis
A_1	1	1	1	1	1	1	z, z^2, x^2+y^2
A_2	1	1	1	1	−1	−1	
B_1	1	−1	1	−1	1	−1	
B_2	1	−1	1	−1	−1	1	
E_1	2	1	−1	−2	0	0	$(zx, yz), (x, y)$
E_2	2	−1	−1	2	0	0	(x^2-y^2, xy)

Table 4.1. Table of characters of the C_{6v} point group. The linear and quadratic functions of the basis are included.

- A two-fold rotation (rotation by 180º) along the c-axis followed by a $\vec{a}_3/2$ translation; $\{C_2|\vec{a}_3/2\}$.
- Three reflections about the planes defined by the Miller indices: (1,0,0), (0,1,0) and $(1,\bar{1},0)$, followed by a $\vec{a}_3/2$ translation; $\{\sigma_{d1}|\vec{a}_3/2\}$, $\{\sigma_{d2}|\vec{a}_3/2\}$ and $\{\sigma_{d3}|\vec{a}_3/2\}$.
- Three reflections about the planes parallel to the c-axis and perpendicular to the three σ_d planes; $\{\sigma_{v1}|0\}$, $\{\sigma_{v2}|0\}$ and $\{\sigma_{v3}|0\}$.

Symmetry operations of the type $\{R|\vec{a}\}$ transform all the atoms of the unit cell into another of the same type where R stands for a point symmetry and $\vec{a}$ is the translation vector. The symmetry operations are arranged by the conjugacy classes in the columns of Table 4.1 for the C_{6v} point group. The corresponding basis functions are also displayed in the table. It can be seen that the A_1, E_1 and E_2 modes are Raman active because the degree of the bases is two (when the degree is one the mode is infrared active). On the other hand, it can be seen that other modes such as the B_1 is a silent mode.[19]

The wurtzite structure has four atoms in the unit cell (N = 4), and therefore $3 \times N = 12$ phonon modes are expected. From group theory, the total representations at the Γ point can be decomposed into

$$\Gamma = 2A_1 + 2B_1 + 2E_1^{(2)} + 2E_2^{(2)}, \qquad [4.17]$$

where the (2) superscript indicates the double degeneracy of the representations $E_1^{(2)}$ and $E_2^{(2)}$ (see Table 4.1). The three acoustic modes correspond to one set of A_1

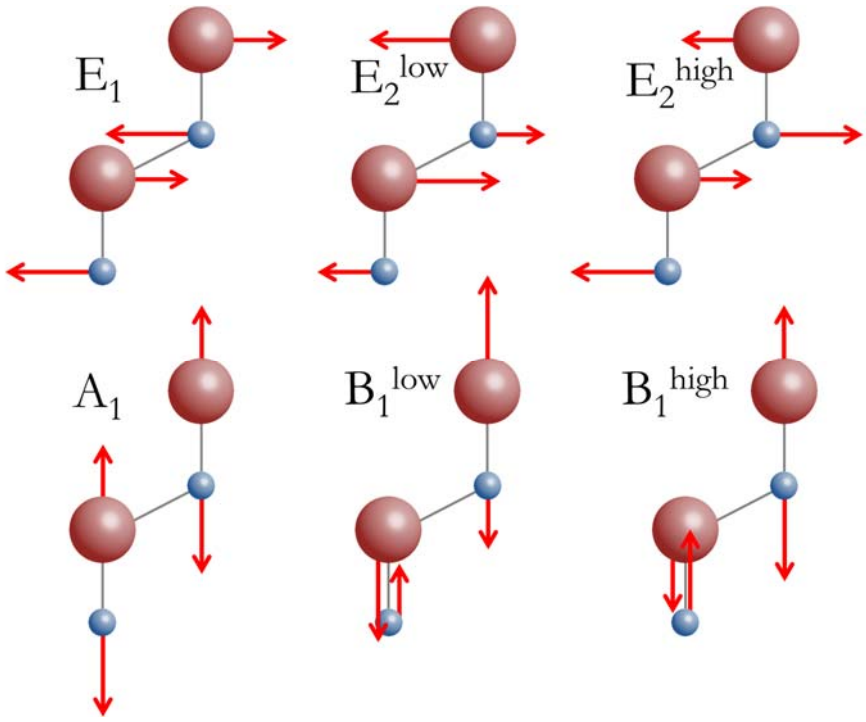

Fig. 4.3. Atomic displacements for the optical phonon modes of the wurtzite structure.

and $E_1^{(2)}$ modes. As can be seen in Fig. 4.3, the atoms of the E_1 and E_2 (A_1) optical modes oscillate in the $x-y$ (z) plane.

The Raman tensors that transform like the set of functions as obtained for each Raman-active basis are

$$\mathrm{A}_1(z)=\begin{pmatrix} a & 0 & 0\\ 0 & a & 0\\ 0 & 0 & b\end{pmatrix},\mathrm{E}_1(x)=\begin{pmatrix} 0 & 0 & c\\ 0 & 0 & 0\\ c & 0 & 0\end{pmatrix},\mathrm{E}_1(y)=\begin{pmatrix} 0 & 0 & 0\\ 0 & 0 & c\\ 0 & c & 0\end{pmatrix},$$
$$\mathrm{E}_2^{(1)}=\begin{pmatrix} d & 0 & 0\\ 0 & -d & 0\\ 0 & 0 & 0\end{pmatrix},\mathrm{E}_2^{(2)}=\begin{pmatrix} 0 & d & 0\\ d & 0 & 0\\ 0 & 0 & 0\end{pmatrix}. \qquad [4.18]$$

Table 4.2 shows the selection rules for first-order Raman-scattering for the wurtzite structure for different scattering configurations. These are readily obtained by using Eq. [4.9] and the Raman tensors in Eq. [4.18].

Scattering configuration	E_{2l}	$A_1(\mathrm{TO})$	$E_1(\mathrm{TO})$	E_{2h}	$A_1(\mathrm{LO})$	$E_1(\mathrm{LO})$
$z(xx)\bar{z}$	✓			✓	✓	
$z(xy)\bar{z}$	✓			✓		
$x(yy)\bar{x}$	✓	✓		✓		
$x(yz)\bar{x}$			✓			
$x(zz)\bar{x}$		✓				
$x(yz)y$			✓			✓
$x(yy)x$	✓	✓		✓		
$x(yy)z$	✓	✓		✓	✓	

Table 4.2. Selection rules for first-order Raman-scattering measurements in the wurtzite structure through the deformation potential mechanism. The scattering configuration is expressed with Porto's notation.

The rocksalt structure

The rocksalt structure, named after the name of the common mineral halite (NaCl), is a usual phase for alkali halides and many divalent metal oxides, sulfides, selenides, and tellurides. In general, this structure is more likely to be formed when the cation is somewhat smaller than the anion.[20] Also, the rocksalt structure is the most stable phase of III-group nitrides at high pressure and appears in the phase diagrams of all II-VI compounds.[21]

The space group of the rocksalt structure is 225 in the International Union of Crystallography classification, $Fm\bar{3}m$ in the Hermann–Mauguin notation belonging to the O_h point group. The structure can be regarded as two interpenetrating face-centered cubic sublattices. The structure belongs to the cubic lattice system and is centrosymmetric.

As shown in the panel A of Fig. 4.4, the unit cell contains two atoms, and the primitive vectors are $\vec{a}_1 = a/\sqrt{2}\cdot(1,1,0)$, $\vec{a}_2 = a/\sqrt{2}\cdot(1,0,1)$ and $\vec{a}_3 = a/\sqrt{2}\cdot(0,1,1)$ where a is the lattice parameter. The atomic positions in the unit cell are given by $\vec{u}_1 = (0,0,0)$ and $\vec{u}_2 = (1/2,1/2,1/2)$. Each ion is 6-coordinated (shown with red lines in the panel A of Fig. 4.4) and has a local octahedral coordination.

The reciprocal lattice of the rocksalt structure is characterized by the reciprocal primitive vectors $\vec{b}_1 = \sqrt{2}\pi/a\cdot(1,1,-1)$, $\vec{b}_2 = \sqrt{2}\pi/a\cdot(1,-1,1)$ and

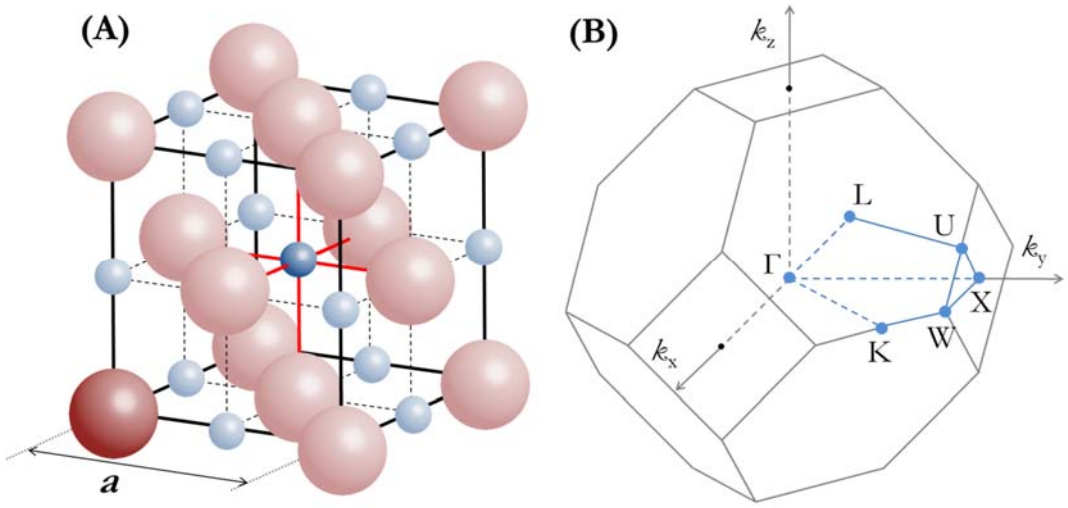

Fig. 4.4. Panel A: Conventional cell of the rocksalt structure. The two atoms of the unit cell are shown with full colour. The 6-coordination is shown with red lines. **Panel B:** First BZ for the rocksalt structure; the high symmetry points and lines are shown.

$\vec{b}_3 = \sqrt{2}\pi/a \cdot (-1,1,1)$. The first BZ is shown in the panel B of Fig. 4.4, where the most important high symmetry points and lines are shown.

The rocksalt structure exhibits higher symmetry than the wurtzite structure and has 48 symmetry operations classified in the following conjugacy classes:

- The identity; $\{E\}$.
- Three two-fold rotations about each of the equivalent [100] axes; $\{3C_2\}$.
- Two four-fold improper rotations about each of the three equivalent [100] axes; $\{6S_4\}$.
- Six reflections, one for each equivalent (110) planes; $\{6\sigma_d\}$.
- Eight three-fold rotations, two for each of the four equivalent [111] axes; $\{8C_3\}$.
- The inversion; $\{i\}$.
- Three reflections, one for each of the three equivalent [110] axes; $\{3\sigma_h\}$.
- Six four-fold rotations, two for each of the three equivalent [100] axes; $\{6C_4\}$.
- Six two-fold rotations about each of the six equivalent [110] axes; $\{6C_2'\}$.

O_h	$\{E\}$	$6\{C_4\}$	$3\{C_2\}$	$8\{C_3\}$	$6\{C_2'\}$	$\{i\}$	$6\{S_4\}$	$3\{\sigma_h\}$	$8\{S_6\}$	$6\{\sigma_d\}$	Basis
A_{1g}	1	1	1	1	1	1	1	1	1	1	$x^2+y^2+z^2$
A_{1u}	1	1	1	1	1	−1	−1	−1	−1	−1	
A_{2g}	1	−1	1	1	−1	1	−1	1	1	−1	
A_{2u}	1	−1	1	1	−1	−1	1	−1	−1	1	
E_g	2	0	2	−1	0	2	0	2	−1	0	
E_u	2	0	2	−1	0	−2	0	−2	1	0	$(2z^2-x^2-y^2, x^2-y^2)$
T_{2u}	3	−1	−1	0	1	−3	1	1	0	−1	
T_{2g}	3	−1	−1	0	1	3	−1	−1	0	1	(xy, xz, yz)
T_{1u}	3	1	−1	0	−1	−3	−1	1	0	1	(x, y, z)
T_{1g}	3	1	−1	0	−1	3	1	−1	0	−1	

Table 4.3. Table of characters of the O_h point group. The linear and quadratic functions of the basis are included.

- Eight six-fold improper rotations, two about each of the four equivalent [111] axes; $\{8S_6\}$.

The rocksalt structure has two atoms in the unit cell, and therefore $3 \times 2 = 6$ phonon modes are expected at each wave vector. As it can be seen in the character table of the O_h point group (Table 4.3), there are ten irreducible representations. From inspection of the corresponding basis it can be seen that only one is infrared-active. From group theory, the total representations at the Γ point can be decomposed into

$$\Gamma = 2T_{1u}^{(3)} \ , \qquad [4.19]$$

where the subscript (3) indicates the triply degeneracy of the representation (as it can be seen from the character of the identity class for this representation). The T_{1u} mode is polar and splits into two TO and one LO modes. As it can be seen from the basis functions of T_{1u} (Table 4.3), this mode is IR-active and Raman silent. Note that this mode transforms like a vector as a consequence of the cubic symmetry of the rocksalt structure. Hence, the three acoustic modes also exhibit the same symmetry.

Vibrational properties and its relation with the phase stability

Pressure dependence of the phonon modes

The vibrational properties of a crystalline solid depend on the restoring forces that bind the atoms within the crystal lattice, which in turn depend on the electronic structure of the material. The electronic potential of the whole system (ions plus electronic cloud) has two contributions, one which is repulsive and arises from the Coulomb interaction between the ions, V_i, and another which is originated by the electronic cloud, V_e. The total energy of the system, U_{e+i}, is a function of the atomic positions in real space, as the displacement of an ion will modify the electronic structure. In general, applying pressure on a crystalline solid (i.e., reducing interatomic distances) yields an increase of both the energy and its second derivative around the stability position. The second derivative of the total energy is known as the interatomic force constant (IFC) which is

$$C_{\alpha,\beta}(lk,l'k') = \frac{\partial^2 U_{e+i}(\boldsymbol{u})}{\partial \boldsymbol{u}_\alpha(lk)\partial \boldsymbol{u}_\beta(l'k')}\ , \qquad [4.20]$$

where the subscripts of the spatial coordinates, $\boldsymbol{u}_\alpha(lk)$, denote the position of the ion k in the unit cell l within the crystal. The phonon frequencies, ω, can be calculated by solving the dynamical equation, which reads

$$\left|\frac{C_{\alpha,\beta}}{\sqrt{M_k M_{k'}}} - \omega^2 \delta_{\alpha\beta}\delta_{kk'}\right| = 0\ , \qquad [4.21]$$

where the first term is known as *dynamical matrix*, and M_k is the mass of the k^{th} ion.

An increase of the IFCs results in an increase of the phonon frequencies in the whole BZ. Therefore, it can be expected that the pressure dependence of the each phonon frequency, w_i, is positive with pressure. This dependency is usually linear at low pressure values,

$$w_i(P) = w_i(0) + a_i \cdot P, \qquad [4.22]$$

where $w_i(0)$ is the phonon frequency of the i^{th} phonon at zero pressure and a_i is the corresponding phonon pressure coefficient.

When the crystal phase is around the phase transition or outside its range of stability (i.e., when the phase is in a metastable state), the phonon frequencies do not show the pressure behaviour given by Eq. [4.22], but exhibit anomalies such an abrupt decrease of the frequency of some phonon modes. The decreased phonon frequencies are a consequence of a rapidly decrease of some IFCs. For instance, some calculations on non-stable phases have found negative IFCs for acoustic and low-frequency optical modes,[22–25] implying imaginary phonon energies as can be inferred from Eq. [4.21]. In this case, the phase cannot exist at the corresponding pressure. On the other hand, the frequency of a given phonon mode may decrease with increasing pressure. Such modes are called *soft modes*. At first, the soft modes were observed by means of temperature-dependent experiments and their relation with phase transitions was described by the Landau theory of phase transitions.[22] The presence of soft modes evidences that the interatomic bonding is weakening for that particular phonon symmetry. In practice, soft modes indicate that the phase is losing stability so that the compound will end up in a distorted phase (after a second-order transition), or in a high-pressure polymorph (after a first-order transition).

Next, the pressure-dependence of the InN lattice dynamics is discussed. For this purpose, *ab initio* lattice-dynamical calculations have been performed. We show that the wurtzite structure of InN exhibits a soft mode, while the rocksalt high-pressure phase only exhibits phononic anomalies at pressure values below its stability range.

High-pressure lattice-dynamics of the wurtzite phase of InN

Theoretical phonon-dispersion curves of w-InN at 0 and 25 GPa obtained with DFT-LDA calculations are shown in Fig. 4.5. It can be seen that, above the optical gap, the A_1, E_1, B_{1h} and E_{2h} modes exhibit positive pressure coefficients (i.e. the curves calculated at high pressure are blueshifted). This is observed for any other III-V or II-VI group compounds with the wurtzite structure. Note that the E_1(LO) phonon mode at the Γ-point has a lower frequency than the A_1(LO) mode. This incorrect ordering has also been observed in previous calculations (for instance

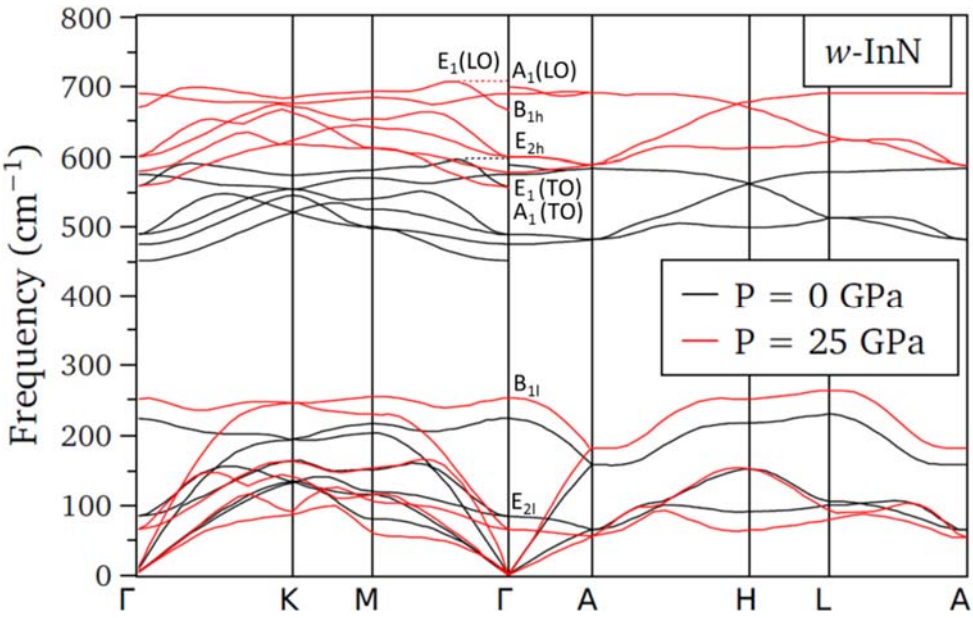

Fig. 4.5. Calculated phonon dispersion curves of the wurtzite structure of InN at two different pressures, 0 GPa (black lines) and 25 GPa (red lines). The eight optical phonon modes at Γ are named. The E_1(LO) frequency around Γ has been corrected with dashed lines.[11] These calculations have been performed using a plane-wave pseudopotential approach to DFT as implemented in the ABINIT package. The energy functionals for the exchange-correlation term has been calculated within the LDA. An 8×8×4 Monkhorst-Pack *k*-point sampling has been used. The kinetic cut-off energy is 65 mHa.

InN[6] or ZnO[26]; in Fig. 4.5 it has been manually corrected with a dotted line). These types of errors have been attributed to the overestimation of the high-frequency dielectric constant due to the well-known bandgap problem of LDA-based calculations, which lead to an underestimation of the longitudinal optical mode frequency. Concerning the low frequency phononic branches, it can be seen in Fig. 4.5 that the TA and E_{2l} modes exhibit a soft mode character along the whole BZ. Other anomalies such as imaginary (or negative) frequencies are not found in these calculations. Nevertheless, the TA modes at the K point of the BZ significantly decrease their frequency. This result contrasts with the fact that the frequency of such mode barely varies at 10 GPa (see the results section of this chapter, Article 4.3). On the other hand, the calculations show that the zone-center frequency of the E_{2l} mode rapidly decreases at pressures above 10 GPa. We find that for this mode $\omega(P) = 83.9 - 0.55P - 7.6 \cdot 10^{-3}P^2$. Note that, taking into account that the bulk modulus is expected to increase with pressure, the negative sign of the quadratic term is somewhat surprising.

As discussed later in this section, the soft mode behavior of the E_{2l} mode evidences a phase instability that results in the wurtzite to rocksalt phase transition.

High-pressure lattice-dynamics of the rocksalt phase of InN

The wurtzite-to-rocksalt phase transition that occurs in InN upon compression can be easily detected in Raman-scattering experiments (see Article 4.3 in the results section of this chapter). The broad Raman features arising from the rocksalt structure evidence that the crystal is highly disordered. As described in Article 4.3, the rocksalt phase remains metastable down to $P_{bt} \approx 2$ GPa, when a back-transition to the wurtzite phase takes place.[27]

In Fig. 4.6, calculated phonon dispersion curves for rs-InN in the stability regime (for the case of 25 GPa) and in the instability regime (at 0 GPa, much lower than the transition pressure around 13 GPa) are shown. It can be seen that at 25 GPa the phonon dispersion curves exhibit a set of well-separated phononic branches. The optical branches exhibit a larger frequency than the acoustic branches over the whole BZ, with a phononic gap around 50 cm^{-1}.

On the other hand, the phononic dispersion calculated at 0 GPa is found to exhibit some anomalies. Firstly, note that the frequency of the TO(L) mode abruptly drops in relation to that corresponding to $P = 25$ GPa.[28] Secondly, the phononic gap is closed. Indeed, the LA phononic branch increases in frequency and mixes with the optical branches at the L-X-W region of the BZ. The fact that the phonon frequency of the TO(L) mode is below that of the LA(L) mode can be attributed to the phase instability of rs-InN. It is also important to note that for most rocksalt semiconductors the phononic gap is open (larger than zero). Exceptional cases where the LA(L) mode is at higher frequency than the optical TO(L) mode are ZnO, GaN or ScN.[26,29] Amongst these, only the rocksalt phase of ScN is stable at ambient pressure.

Comparing the phononic dispersion of rs-InN calculated at 0 and 25 GPa (Fig. 4.6), it can be seen that all the phononic branches blueshift with pressure. The absence of softening behaviour is what can be expected given that the rocksalt phase is stable up to pressures well above 25 GPa. Indeed, first-principles

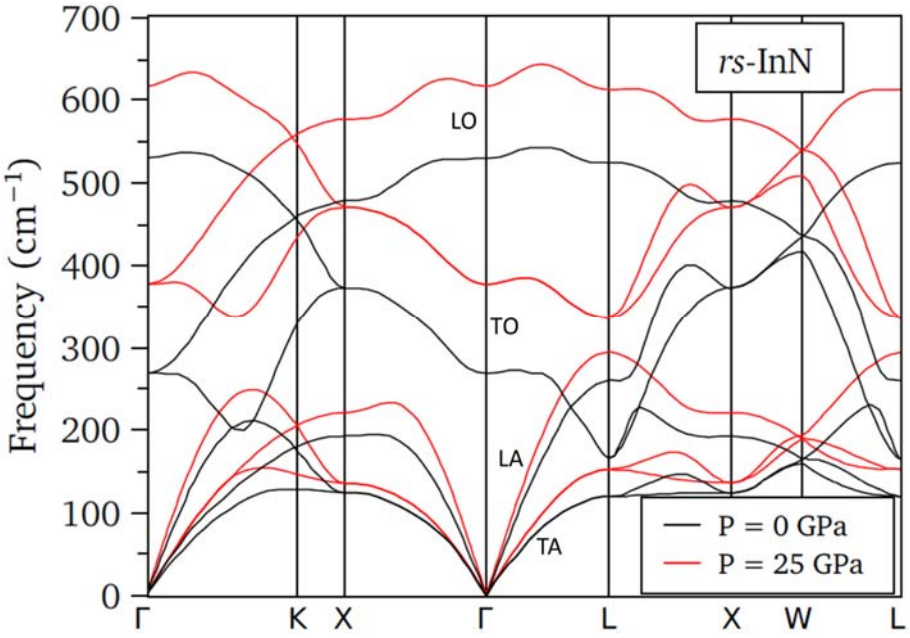

Fig. 4.6. Calculated phonon dispersion curves of the rocksalt structure of InN at two different pressures, 0 GPa (black lines) and 25 GPa (red lines). The optical and acoustic branches are named. These calculations have been performed using a plane-wave pseudopotential approach to DFT as implemented in the ABINIT package. The energy functionals for the exchange-correlation term has been calculated within the LDA. An 8×8×8 Monkhorst-Pack *k*-point sampling has been used. The cutoff energy used for the plane-wave basis is of 100 Ha.

calculations for group-III nitride compounds show that the rocksalt structure is the most stable phase at least up to 200 GPa.[30]

The mode Grüneisen parameters

The pressure coefficient of the phonon modes is related to the so-called mode Grüneisen parameters.[31,32] These parameters can be related to the (macroscopic) Grüneisen parameter, which is dimensionless and approximately constant over pressure and temperature. The Grüneisen parameter is relevant in materials science to evaluate the role played by phonons on different thermodynamic properties such as thermal expansion or heat capacity. The mode Grüneisen parameter of minerals is particularly important in geophysics, where it is used to set limitations on the pressure and temperature dependencies of thermodynamical properties of the mantle as well as to constrain the adiabatic temperature gradient.[33] In this thesis, the mode Grüneisen parameters of wurtzite

and rocksalt InN have been measured by high-pressure Raman-scattering measurements (see Articles 4.1 and 4.3 in the results section of this chapter).

For a given phonon mode, the microscopic definition of the mode Grüneisen parameters is

$$\gamma_i = \frac{\partial ln\omega_i}{\partial lnV} = \frac{B_0 a_i}{\omega_i} , \qquad [4.23]$$

where B_0 is the bulk modulus at zero pressure, a_i is the phonon pressure coefficient and ω_i the phonon energy (frequency) at zero pressure. Assuming that all γ_i take the same value, it can be shown that the thermal expansion coefficient, α, is related to the Grüneisen parameter of the crystal γ (which can be taken as $\gamma = \gamma_i$), through the following expression:

$$\gamma = \frac{\alpha B_0}{\rho C_V} , \qquad [4.24]$$

where C_V is the heat capacity at constant volume. This approximation holds fairly well for semiconductors. The mode Grüneisen parameter of the optical modes for IV and III-V group crystals is $\gamma \approx 1$;[34] for II-VI group crystals $\gamma \approx 2$, and $\gamma \approx 3$ for the alkali halides.[35] Nevertheless, this approximation is not valid for molecular crystals where the pressure dependence of the intramolecular bonding differs significantly from the intermolecular bonding. For a more accurate description of the crystal, the macroscopic value of the mode Grüneisen parameter must be obtained by weighting all the phononic contributions:

$$\gamma(T) = \frac{\sum_i \gamma_i C_V(\omega_i, T)}{\sum_i C_V(\omega_i, T)} , \qquad [4.25]$$

where the contribution to the heat capacity of each phonon mode can be derived from the Bose-Einstein distribution of phonons in a crystal lattice,

$$C_V(\omega_i, T) = \left(\frac{dU}{dT}\right)_V = k_B \left(\frac{\hbar\omega_i}{k_B T}\right)^2 \frac{exp(\hbar\omega_i / k_B T)}{(exp(\hbar\omega_i / k_B T) - 1)^2} . \qquad [4.26]$$

Note that Eq. [4.25] and [4.26] should be integrated throughout the entire BZ. These equations only apply within the quasi-harmonic approximation (QHA), which implies that discrepancies could arise between the calculated thermal expansion coefficient from Eq. [4.24] and the measured values from macroscopic variables, especially at high temperatures (temperatures higher than the Debye temperature) where the phonon-phonon interaction is important. Further analysis on this topic can be found elsewhere.[22]

While the mode Grüneisen parameters can be used to study the thermodynamical properties of a semiconductor crystal, they can also be used to evaluate the phase stability of a crystal at different pressures. This is introduced in the next section for the case of the wurtzite, zinc blende and diamond structures.

The mode Grüneisen parameter and the transition pressure

In 1988 John Maddox evidenced a problem about the knowledge of phase diagrams stating the famous quote "One of the continuing scandals in the physical sciences is that it remains in general impossible to predict the structure of even the simplest crystalline solids from a knowledge of their chemical composition".[36] Ever since large progress has been made in the field of predicting the crystalline stable structures as a consequence of improvements in first principle calculations.[37] The existing models (such as DFT) have been tested by the use of experimental techniques such as high-pressure X-ray diffraction or Raman scattering measurements. These techniques provide valuable information regarding the phase diagrams of crystalline compounds. Here we focus on the particular case of semiconductor materials belonging to the A^NB^{8-N} group. For this kind of compounds it has been proposed that their phase transition is hinted by negative mode Grüneisen parameters.[34,35,38]

The most stable phase of semiconductor compounds belonging to the A^NB^{8-N} group are wurtzite, zinc-blende or diamond. These phases exhibit similarities in their lattice-dynamical behaviour under pressure. For instance, for the case of zinc-blende and diamond structures the transversal acoustic (TA) modes are typically soft modes. For the case of the wurtzite structure, the zone centre E_2^{low} is

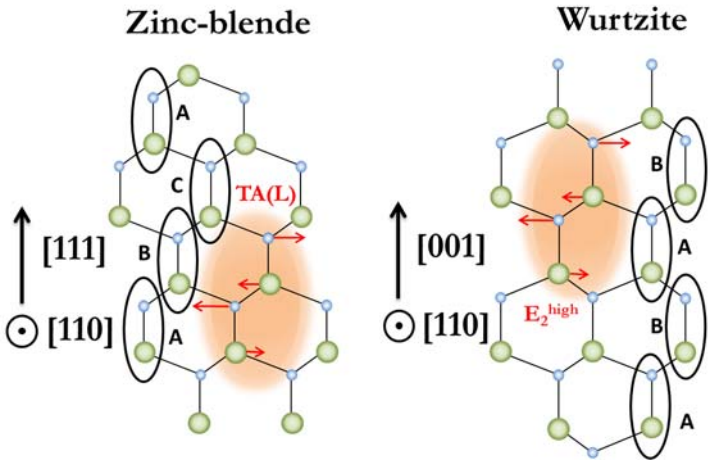

Fig. 4.7.

Comparison of the atomic arrangement in the zinc blende (ABCA…) and wurtzite (ABAB…) structures along the [111] and [001] directions, respectively. Lattice vibrations corresponding to phonon modes are shown in red lines.

almost the equivalent to the TA mode at the L-point of the zinc-blende structure. This can be seen in Fig. 4.7 where the atomic arrangement of these structures in the crystalline planes (110) are compared. The arrangement of the tetrahedral is said to be *staggered* in the zinc-blende structure and *eclipsed* in the wurtzite structure.[39] As it can be in the figure, the stacking order of the ions is of the type ABCABCAB… for the zinc-blende structure and ABABA… for the wurtzite structure. For each structure, four ions have been shaded, and the motion of the corresponding phononic mode (i.e. TA(L) and E_{2h} for the zinc-blende and wurtzite structures, respectively) is shown in red arrows (larger arrows indicate larger amplitude of oscillation). Note that the phononic symmetries are not equivalent but very similar.

The equivalence of the E_{2h} mode of the wurtzite structure with the TA(L) mode of the zinc-blende structure can be understood if the wurtzite structure is regarded as the unfolding (doubling the unit cell) of the zinc-blende structure along its [111] direction (Γ→L). Indeed, the number of atoms of the wurtzite structure in the unit cell is the double (four) than that of the zinc blende structure (two). The phononic dispersion curves along the [111] direction of the zinc-blende structure as calculated elsewhere[40] have been plotted in Fig. 4.8. It can be seen that the folding at the A-point of the wurtzite structure yields six phonon modes at the Γ point of the wurtzite structure (along this direction). Note that doubling the unit cell corresponds to dividing the BZ in half. The frequencies obtained by using this method are remarkably similar to those calculated in this thesis for the wurtzite structure (see Article 4.3).

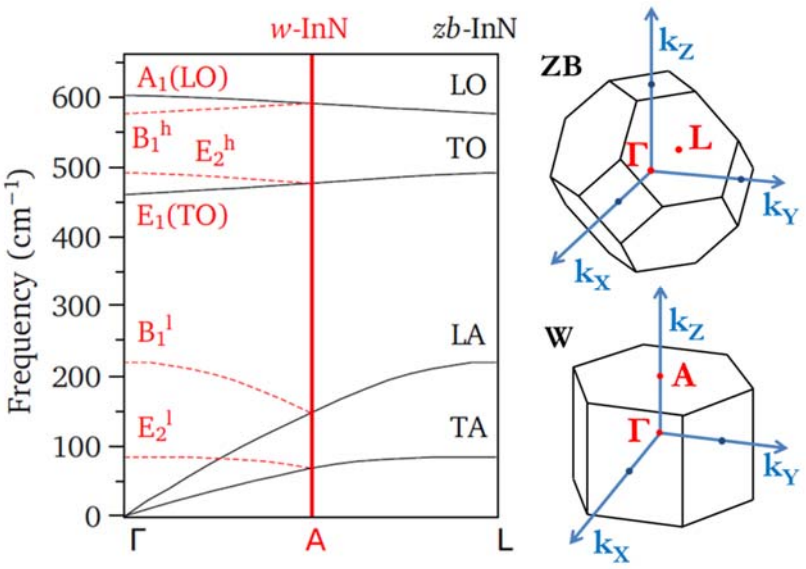

Fig. 4.8.

Phonon dispersion curves along the [111] direction in the zinc blende structure of InN. Folding at the A-point approximate the wurtzite structure of InN along the [001] direction.

Experimental results in many II-VI and III-V group semiconductors[34,35,38] lead to the conclusion that the transition pressure could be proportional to the mode Grüneisen parameter of the purely bond bending TA(X) mode. This conjecture was supported by the fact that the TA mode softening is indicative of the weakening of non-central forces of long-range origin needed to stabilize the tetrahedral lattice against the short-wavelength shear distortion.[41] However, later experiments[35] found that this rule would not hold for all zinc blende and diamond structures. The TA(X) or E_2^{low} mode Grüneisen parameters and their corresponding first-order transition pressure is plotted in Fig. 4.9 for many semiconductor compounds belonging to the A^NB^{8-N} group, with hexagonal,[42,43] zinc blende,[35,44] or diamond[35,45] structures at ambient conditions. As it can be seen in the figure, a general trend is found: lower mode Grüneisen parameters correspond to lower transition pressures. Considering the extreme cases, it can be seen that, on one side, diamond exhibits a positive Grüneisen parameter.[45] On the other, GaSb is found to exhibit a very negative Grüneisen parameter as well as a low transition pressure.[44] Other authors have reported similar trends by using an empirical formula with only one free adjustable parameter which relates, for a given binary compound, the transition pressure with the bulk modulus.[46]

The case of InN and ZnO is particularly interesting because both wurtzite compounds have very similar bulk modulus (B_0 ≈ 140 GPa). Still, the phase transition of InN (P_t ≈ 13 GPa) is higher than that of ZnO (P_t ≈ 9 GPa). The lower

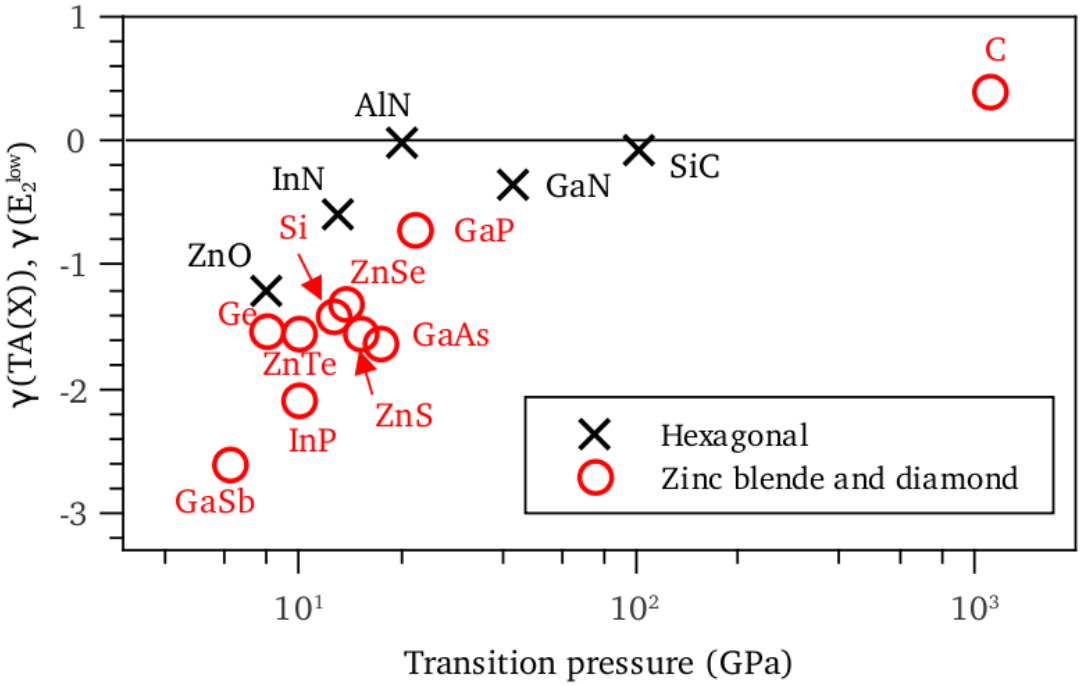

Fig. 4.9. Mode Grüneisen parameters plotted versus the first phase transition pressure for different crystal structures. Hexagonal structures are represented with a cross symbol, and include 6H-SiC and the wurtzite structures ZnO, InN, AlN, and GaN. For these compounds, the mode Grüneisen parameter corresponds to the E_2^{low} mode. Zinc blend structures include a variety of III-V and II-VI semiconductors. The diamond structures include silicon, germanium and diamond. For these structures the corresponding mode Grüneisen parameter is TA(X).

structural stability of ZnO is then evidenced by its lower (more negative) mode Grüneisen parameter (see Fig. 4.9). Nevertheless, results for AlN seem to break the general tendency of Grüneisen parameter versus transition pressure. For this case, different experiments[42] have found $\gamma \approx 0$ while the phase transition takes place at relatively low pressures. This latter result evidences that further investigation is needed to fully understand the mechanisms that govern the mode Grüneisen parameter of the acoustic modes. Ionicity[47] or anharmonicity[38] effects have been proposed to explain differences in the observed trend.

First principle calculations of the phase stability

The transition pressure between two crystal phases can be predicted by means of first principle calculations. This is done using a well stablished thermodynamic theorem originating from the definition of the Gibbs energy

$$G = E_{total} + P\Omega - TS \ . \qquad [4.27]$$

Any system will minimize its Gibbs free energy for a given pressure and temperature. Hence, the transition pressure between two phases (namely 1 and 2) corresponds to the pressure that satisfies $G_1 = G_2$. Here, E_{total} represents the total internal energy of the system at a given volume Ω (e.g. the volume of the unit cell). Under the adiabatic approximation, which assumes that the atoms are fixed at specific positions and thermal vibrations are neglected (i.e. the calculation simulates the system at T = 0 K), the entropic term in Eq. [4.27] is zero. Therefore, the phase transition for a system at zero temperature will take place when the enthalpy

$$H = E_{total} + P\Omega \qquad [4.28]$$

is equal in both phases. Now, the only terms left to be computed are the total energy and the volume for a certain pressure. The pressure is calculated from the definition of the stress tensor,

$$\sigma_{ij} = \frac{dE_{total}(\Omega_{ij})}{\mathrm{d}\Omega_{ij}} \ . \qquad [4.29]$$

For the case of hydrostatic pressure, $\sigma_{ij} = -P\delta_{ij}$. For a given input pressure, the volume of the system is found to be the one that satisfies Eq. [4.29].

Now it is possible to calculate the enthalpy *vs* pressure curves, or the total energy versus volume. This is illustrated in Fig. 4.10 for the case of InN. Calculations here performed are based on the DFT[48] within the LDA[49] using the Quantum ESPRESSO code.[50] Theory is applied in plane-wave basis employing norm-conserving pseudopotentials of the Troullier-Martins type.[51] The plane-wave cutoff energy is 80 Ry. The reciprocal space sampling is performed on a Monkhorst-Pack mesh[52] of 8×8×8 (for the rocksalt phase) and 8×8×4 (for the wurtzite phase).

The total energy, enthalpy and volume values shown in Fig. 4.10 correspond to a four atom system. It is important to remark that the comparison of all these magnitudes between different crystal phases only make sense if they are referred to the same amount of atoms. Note that the energy, enthalpy and volume quantities are extensive (this is, proportional to the size of the system, or number of atoms).

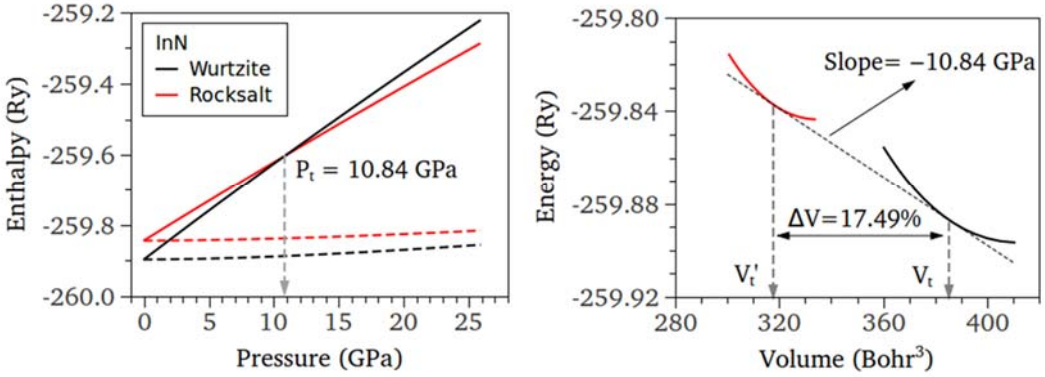

Fig. 4.10. First principles calculations for InN in the wurtzite and rocksalt structures. **Left panel:** Enthalpy is plotted versus pressure in solid lines for each phase, at pressures above 10.84 GPa the rocksalt structure displays lower enthalpy values. The dashed lines correspond to the total energy at different pressure values. **Right panel:** Total energy versus volume curves for the wurtzite (black solid line) and rocksalt phases (red solid line). The transition pressure can be calculated by the tangent method, the collapsing volume can be then inferred.

Here the number four has been chosen because there are four atoms in the unit cell of the wurtzite structure.

As it can be seen in Fig. 4.10, the transition pressure can be calculated in two equivalent ways. Firstly, as displayed in the left panel of Fig. 4.10, the transition pressure corresponds to the crossing between the $H(P)$ curves. Hence,

$$H(P_t) = H'(P_t) \Rightarrow E_{total} + P_t V_t = E_{total}{}' + P_t V_t' \ , \qquad [4.30]$$

then,

$$E_{total} = E_{total}{}' + P_t(V_t' - V_t) \ . \qquad [4.31]$$

The common tangent method consists in plotting a tangent line to one $E(V)$ curve at a certain point (volume of transition) at which it coincides with the $E'(V')$ curve of the other structure. The slope of this common tangent corresponds (with a negative sign) to the transition pressure (see Eq. [4.29]). Thus, two conditions must hold. Firstly, the volume derivatives of the $E(V)$ curves must be the same at the respective transiting volume. This can be shown from Eq. [4.29], owing to the fact that the transition pressure value is (obviously) unique,

$$P_t = -\frac{dE}{dV} = -\frac{dE'}{dV'} = P_t' \ . \qquad [4.32]$$

Secondly, the tangent line must be common (should connect) to both $E(V)$ curves, this is a consequence of Eq. [4.31], where the $P_t(V_t' - V_t)$ term takes into account the difference of total energy between both structures (see right panel of Fig. 4.10).

The here calculated transition pressure for InN is in excellent agreement with the 10.83 GPa and 11.1 GPa values calculated by K. Kunc[28] and J. Serrano,[30] respectively. Nevertheless, these values are lower than those reported experimentally around 13 GPa.[53,13,27,54] It has been observed that LDA-based calculations systematically underestimate the pressure transition value, as discussed in detail elsewhere.[55] On the other hand, the calculated volume difference at the transition pressure, $\Delta V/V = 17.49\%$, as shown in Fig. 4.10, is in very good agreement with the results of high-pressure X-ray diffraction measurements: $\Delta V/V = 17.6\%$,[53] and $\Delta V/V = 17.88\%$.[56]

One and two-phonon Raman processes

First-order disorder-activated modes

Due to wave vector conservation, first-order Raman scattering processes in a perfect crystal involve phonon wave vector close to the center of the BZ. For a Raman measurement with visible light in the backscattering configuration the phonon wave vector $q = 4\pi n/\lambda_{exc}$ is of the order of 10^6 cm^{-1}, which is around 1% of the BZ. However, defects and disorder can cause the breakdown of the wave vector selection rule because the coherence length of the crystal is reduced, and phonons with long wave vector can participate in first-order Raman processes. For instance, it has been shown that the Raman spectra of microcrystals can be related to the crystallite size using the spatial correlation model, also referred to as the phonon confinement model.[57–59] This model assumes that the phonon wave vector participating in the Raman scattering process is not well defined and is exponentially damped.[60] Within this framework the line shape of the first-order Raman spectra can be modelled as

$$\frac{d\sigma}{d\Omega}(x) \sim d_c^3 \int_{BZ} d\boldsymbol{q} \frac{exp(-d_c^2 q^2)}{[\omega - \omega(\boldsymbol{q})]^2 + \Gamma^2} \ , \qquad [4.33]$$

where Γ is the full-width at half maximum (FWHM) of the Raman line shape for a perfect crystal, $\omega(\boldsymbol{q})$ the wavevector-dependent phonon frequencies and d_c is the Gaussian correlation length. This model has been used to evaluate the effect of nano-columnar structures of InGaN thin films on the broadening of the E_{2h} mode.[61] For the case of amorphous materials, where the correlation length is much smaller (of the order of a few bond lengths), the Raman scattering spectrum reflects the PDOS of the entire BZ.[62]

We would like to recall that the PDOS, $g(\omega)$, is defined as the density of normal vibrational modes per unit of volume, and $g(\omega)d\omega$ is the number of modes with frequencies in the $(\omega, \omega + d\omega)$ range. This is calculated by adding the contributions of each phononic branch, s, after integration along the entire BZ for a given frequency:

$$g(\omega) = \sum_s \int_{BZ} \frac{d\boldsymbol{k}}{(2\pi)^3} \delta(\omega - \omega_s(\boldsymbol{k})) \ . \qquad [4.34]$$

Alternatively, one can change the integration over a surface defined by $\omega_s(\boldsymbol{k}) \equiv \omega$. This is, from the condition of constant frequency, one can write $d^3k = dSdk_\perp$, where $k_\perp$ is a direction proportional to the surface of constant frequency. On the other hand, $d\omega = |\boldsymbol{\nabla}_{\boldsymbol{k}}\omega| dk_\perp$. This yields

$$g(\omega) = \sum_s \int \frac{d\boldsymbol{S}}{(2\pi)^3} \frac{1}{|\boldsymbol{\nabla}_{\boldsymbol{k}}\omega_s(\boldsymbol{k})|} \ . \qquad [4.35]$$

Eq. [4.35] helps us to illustrate that the density of states is important for those frequencies where the phononic dispersion is flat. Calculated PDOS for the wurtzite and rocksalt phases of InN at different pressures can be found in the results section (see Article 4.3). In Aticle 4.2, lattice-dynamical calculations for CdO, which exhibits the rocksalt phase at ambient pressure, are also presented.

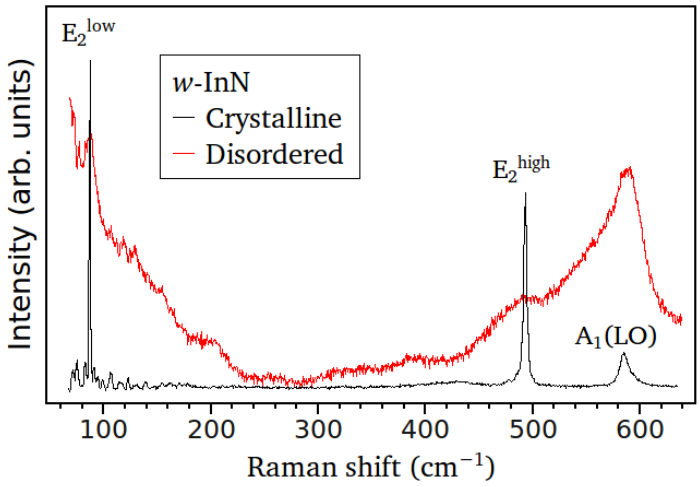

Fig. 4.11.

Comparison between Raman spectra of w-InN acquired at room pressure in the back-scattering configuration for a highly crystalline sample (black line) and the same sample after undergoing two phase transitions (red line).

The first-order disorder-activated modes reflecting the PDOS are only observed on highly disordered systems. Such high disorder can be induced, for instance, by damaging the crystal lattice with ion bombardment.[63] In this thesis, amorphization is observed after pressure-induced phase transitions; this is the case of InN after the wurtzite-to-rocksalt phase transition, where first-order disorder-activated modes show up in the Raman spectra. Intense Raman features of disorder activated modes of rs-InN at high pressure were initially reported by Pinquier et al.[13] In this thesis (see Article 4.3 for details), we also find that that the wurtzite structure is recovered after the downstroke. The Raman spectrum of a recovered sample at room pressure is shown in Fig. 4.11 together with the spectrum of the same as-grown sample before starting the high-pressure experiments. The disordered material has been obtained after two phase transitions, one from the wurtzite to the rocksalt structure in the upstroke cycle (around 13 GPa) and a second one after the downstroke cycle, from the rocksalt back to the wurtzite structure, which occurs around 2-3 GPa. It can be seen that the Raman spectrum of InN after two phase transitions exhibits broad bands at frequencies above 450 cm^{-1} and below 250 cm^{-1}, which can be attributed to first-order disorder-activated modes of the wurtzite structure and which can be compared with the PDOS calculated for w-InN.

Second-order Raman scattering

The first acquired second-order Raman spectra was taken for halite (rocksalt, NaCl) in 1931.[64] The rocksalt structure is Raman-silent, which implies that only second-order Raman features should be observed. The nature of the second-order spectrum became highly controversial in the decade of 40's between C. V. Raman[65] and M. Born[66]. The former defended that the second order scattering could be described by doubling the linear dimension of the unit cell and considering only the discrete frequencies at the Γ-point of the BZ, in contradiction with the classical or quantum mechanics lattice-dynamical theory which predicted a continuous spectrum, as supported by M. Born. Further measurements found a continuous Raman spectrum for many rocksalt crystals, in agreement with Born's theory.[67] Hence, phonons with large wave vectors participate in the second-order Raman process as long as the overall momentum of the process is conserved.

The second-order Raman spectra have been the subject of research for many decades. For an appropriate interpretation of the spectrum, the selection rules of the second order modes must be taken into account.[68] Also, the line shape of the Raman spectra can be calculated from the phononic branch contribution[69] that include the temperature-dependent phonon occupation terms.[70] Burstein et al.[68] showed, for the case of the rocksalt structure, that the second-order Raman spectrum can be successfully interpreted from the phonon dispersion curves as a combination of phonon pairs at specific high-symmetry points in the BZ.

In order that a second-order Raman scattering process takes place the only condition is that the global energy and momentum are conserved. Hence, the Raman shift (i.e. $\omega_i^l - \omega_s^l$) is related to the two-phonon frequencies, namely, ω^p and $\omega^{p'}$ by

$$\omega^p(\boldsymbol{q}) \pm \omega^{p'}(\boldsymbol{q}') = \omega_i^l(\boldsymbol{k}_i) - \omega_s^l\ (\boldsymbol{k}_s)\ , \qquad [4.36]$$

where the momentum of each phonon $\boldsymbol{q}$ and $\boldsymbol{q}'$ must satisfy

$$\boldsymbol{q} + \boldsymbol{q}' = \boldsymbol{k}_i - \boldsymbol{k}_s \approx 0\ . \qquad [4.37]$$

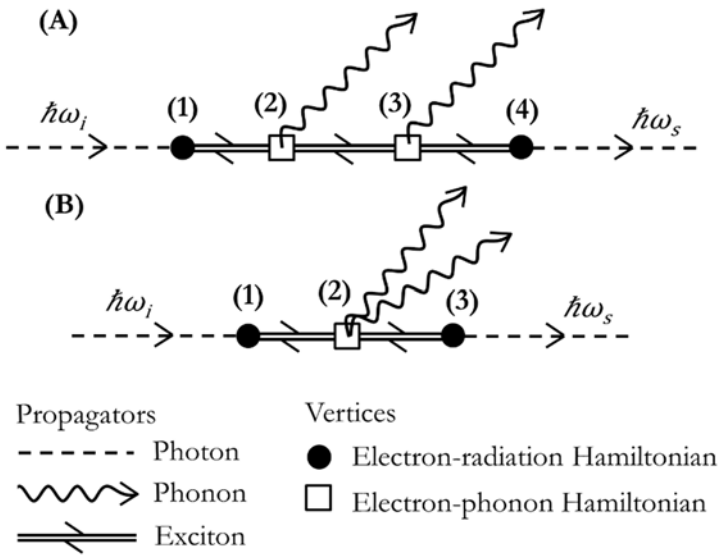

Fig. 4.12.

Feynman diagram for the two-phonon creation processes in the second-order Raman-scattering mechanism.
Panel A: Two phonons are created successively with the intermediation of an exciton.
Panel B: Two phonons are simultaneously created.

The phonon sum and difference options of Eq. [4.36] are referred as *combination* and *difference modes* respectively. When the two phonons are identical, these are called *overtones* and, from Eqs. [4.36] and [4.37] these obey

$$2\omega^p(\boldsymbol{q}) = \omega_i^l - \omega_s^l \ , \qquad [4.38]$$

and

$$\boldsymbol{q} \approx -\boldsymbol{q}' \ . \qquad [4.39]$$

Hence, if the frequency in the Raman spectrum corresponding to the overtone modes alone is divided by two, the resulting spectrum corresponds to the PDOS (as defined in Eq. [4.34]) after correcting for a phonon occupancy term and for the scattering efficiency. Similarly, and neglecting the Raman selection rules, the combination and difference modes correspond to the sum and difference density of states.[39,60]

From a quantum mechanical approach, the second-order Raman scattering processes can be understood in terms of quasi-particle interactions. Two of the most probable combination scattering processes are depicted in Fig. 4.12 by using the corresponding Feynman diagrams. In the panel A of Fig. 4.12, two phonons are created successively by the intermediation of a virtual electron. Up to three electronic bands may participate in this process. In contrast, the Feynman diagram depicted in the panel B only allows the participation up to two bands in the

scattering process. The distinction between these two mechanisms can be found under resonant conditions in a polar semiconductor.[60]

In this thesis (Article 4.2, see the results section), and for the sake of comparison with the case of rs-InN, the high-pressure behaviour of the second-order modes of rs-CdO has been investigated. In this case, the joint experimental and theoretical work that we have performed has allowed us to assign the second-order features that show up in the Raman spectra of this compound.

Longitudinal optical plasmon coupled modes

So far, the inelastic scattering of light by optical phonons in a crystal has been presented in terms of different scattering mechanisms (deformation potential, Fröhlich). For the case of extrinsic polar semiconductors other excitations can participate in the Raman-scattering process. In particular, electron-density waves, known as *volume plasmons,* interact with the longitudinal optical phonons because both have a long-range longitudinal electric field that couples with each other.[71] The resulting modes are known as LOPCM's.[72] LO-plasma coupling yields two LOPCMs, known as the L^+ and L^- modes, which have a mixed phononic and plasmonic character. The frequency of these modes depends on the electronic density. In particular, the frequency of the L^+ mode in degenerate semiconductors is highly sensitive to N_e. For this reason, Raman scattering has proven to be a very useful technique for the evaluation of the electron density in polar semiconductors.[72] In the particular case of InN the evaluation of N_e by means of optical techniques such as Raman spectroscopy is particularly interesting because these allow to probe the bulk electronic density in a contactless and non-destructive way.[73]

There exists a large variety of models with different levels of complexity to calculate the frequency and line shape of the LOPCMs as a function of carrier density. The simplest approach is based on the Drude susceptibility, so that the dielectric function including phononic (from Eq. [3.54]) and plasmonic (from Eq. [3.56]) contributions reads

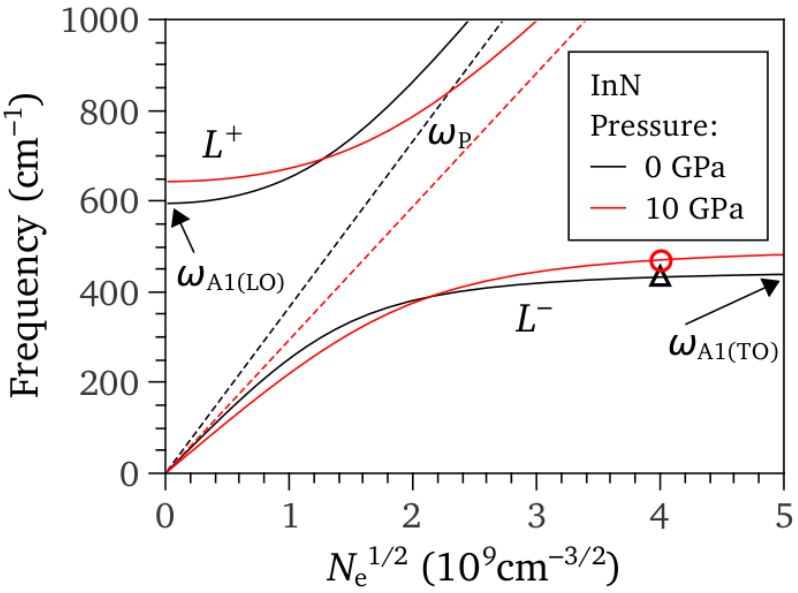

Fig. 4.13. The frequencies of the L^- coupled mode of an *n*-type ($1.6 \cdot 10^{19}$ cm^{-3}) w-InN epilayer measured at ambient pressure and 10 GPa (open symbols) are plotted versus the electronic density. The lower branch, L^-, has been fitted to the experimental data within the Drude model approach. From the fitting, the electron effective mass has been adjusted. The L^+ coupled mode (solid line) and the plasma frequency ω_P (dashed line) are also represented.

$$\varepsilon(\omega) = \varepsilon_\infty + \frac{\varepsilon_\infty(\omega_L^2 - \omega_T^2)}{\omega_T^2 - \omega^2 - i\omega\gamma_l} - \frac{\varepsilon_\infty\omega_P^2}{\omega^2 + i\omega\gamma_p} \,. \qquad [4.40]$$

Neglecting the phononic and electronic damping factors, γ_l and γ_p, the zeroes of the real part of the dielectric function yield the frequencies of the LOPCMs

$$\omega_\pm^2 = \frac{1}{2}\left[(\omega_L^2 + \omega_P^2) \pm \sqrt{(\omega_L^2 + \omega_P^2\omega_L^2)^2 - 4\omega_P^2\omega_T^2}\right] \,. \qquad [4.41]$$

There are two real and positive solutions, $\omega_\pm$ corresponding to the L^+ and L^- modes, respectively. The dependency of the LOPCMs on the electron charge density, N_e, is plotted in Fig. 4.13 for w-InN. As it can be seen in this figure, at low (large) electron charge densities, the frequency of the L^+ (L^-) mode approaches the frequency of the A_1(LO) (A_1(TO) mode) phonon mode. In this case, it is clear that the LOPCM exhibits *phonon-like* character. In contrast, at large (low) electron charge densities, the L^+ (L^-) behave like the uncoupled free plasmons, and therefore the respective coupled modes clearly exhibit *plasmon-like* character.

It is worth mentioning that another classical model, the hydrodynamical model (HD), is widely employed to evaluate N_e from the LOPCM spectra because it includes the wave vector dispersion of the plasmon modes, as well as temperature effects.[74,75] For a degenerate semiconductor, the free-carrier susceptibility in the HD approach can be expanded in terms of (q/ω)[76] yielding

$$\varepsilon^{HD}(\omega,q) \approx \varepsilon_\infty - \frac{\varepsilon_\infty \omega_p^2}{\omega^2 + i\omega\gamma_p}\left[1 + \frac{3}{5}v_F^2\left(\frac{q}{\omega}\right)^2\right], \qquad [4.42]$$

which corresponds to the Drude model when

$$q \ll \frac{\omega^2 m^*}{\hbar k_F}\sqrt{\frac{5}{3}} \quad . \qquad [4.43]$$

It should also be noted that both the Drude and HD model do not include Landau damping effects. When the plasmon and Fermi wavenumbers are similar, the LOPCMs can interact with the free electrons. The wave vector range at which this interaction takes place is called single particle excitation (SPE) regime. The line shape of the LOPCMs in the SPE regime can be calculated with the Lindhard-Mermin (LM) susceptibility, which includes quantum-mechanical effects within the random-phase approximation (RPA).[77]

In this thesis, the pressure-dependence of the electronic effective mass of w-InN has been evaluated from the pressure behaviour of the L^- mode of sample B2 (see the results section, Article 4.3). As it can be seen in Fig. 4.13, two frequency values of the L^- mode measured at 0 and 10 GPa are plotted. The LOPCM exhibits a negative (positive) pressure coefficient when its character is plasmon-like (phonon-like). In the strong coupling region (this is, an intermediate electron density of the two extreme cases), the pressure coefficient of the LOPCMs diminishes. The negative pressure coefficient of the plasmon-like (and plasma) frequency is due to the fact that electron effective mass increases with pressure. In the results section (Article 4.3), a detailed analysis of the pressure behaviour of the L^- mode is presented. Such analysis allows us to obtain the pressure coefficient for the electron effective mass of w-InN: $dm^*/dP = 3{\cdot}10^{-3}\ m_e$ GPa^{-1}; as discussed in detail in Article 4.3, this value is in good agreement with the $\boldsymbol{k}\cdot\boldsymbol{p}$ theory.

Martin's double resonance mechanism on the LO modes

During the last few years, extensive research has been carried out on highly-crystalline InN samples by means of Raman scattering. The frequency of the non-polar modes (i.e. E_{2l} and E_{2h}) and transversal polar modes E_1(TO) and A_1(TO) has been measured both in strained and unstrained samples.[6,78] Nevertheless, sizably different values have been reported for the case of the longitudinal optical modes. For the case of *n*-type samples, one would expect to measure Raman signal arising only from the two modes of the LOPCMs and non-polar modes, but many authors reported a narrow feature in the region of the LO modes 580 – 596 cm^{-1}.[8,11,78–81] Some authors proposed that the observed feature corresponds to the A_1(LO) mode arising from the surface depletion layer that exists in doped InN.[78] Other authors proposed that this mode arises from the large-wavevector LOPCMs with a frequency not far from that of the A_1(LO) mode.[82,83,84] The dependency of these modes with electron density was found to be compatible with high Landau damping regimes. Later, Cuscó et al.[85] found that the frequency of this feature is highly dependent on the excitation source (the LO feature blueshifts up to 5 cm^{-1} from using the 514.5-nm to the 780.0-nm laser lines), and the feature was attributed to the resonant E_1(LO) mode arising from the relaxation of the selection rules owing to the presence of defects in the crystal lattice. More recently, Davydov et al.[14] reported a systematic study of the dependence of the A_1(LO) and E_1(LO) modes with excitation energy. They reported a decrease of the phonon frequency as high as 10 cm^{-1} with increasing excitation energy from 1.17 eV to 2.81 eV.[14,86] This result was attributed to a Martin's double resonance mechanism.[87] Such process presumably takes place for small bandgap semiconductors with a sharp, deep electronic dispersion of the conduction-valence bands (typically near the center of the BZ, Γ) for excitation energies larger than the bandgap energy, and typically covering a wide range of the wave vector electronic dispersion. This mechanism has been observed for GaAs,[88] graphite,[89,90] and more recently graphene.[91,92]

A Feynman diagram of the Martin's double resonance process is shown in Fig. 4.14. This consists in a fourth-order process in which the scattering mechanism is mediated by a charged ion.[83] It can be seen that an incoming photon creates an

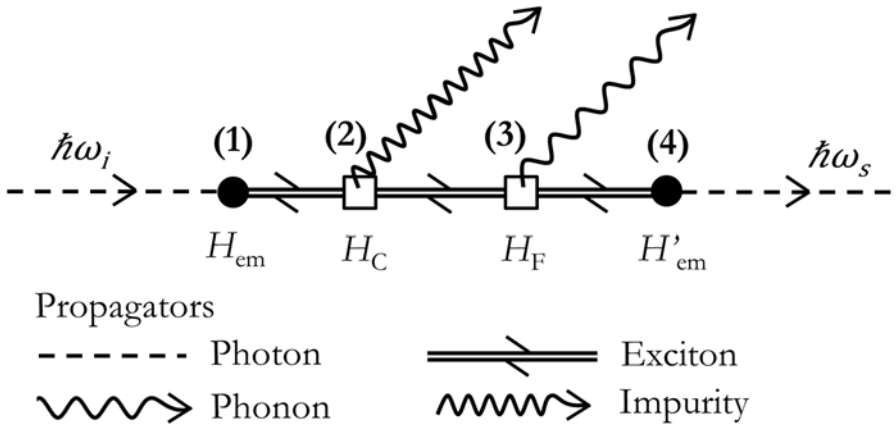

Fig. 4.14. Feynman diagram of the Martin's double-resonance mechanism. This process takes place in InN for the large wave vector LO phonon modes. The dashed lines represent photons, the wavy line (2) and the solid lines electron-hole pairs. A photon with initial energy $\hbar\omega_i$ scatters inelastically in a fourth order process, the scattered phonon $\hbar\omega_s$ has a decreased energy corresponding to that of the created (for the Stokes case) phonon with a wave vector $k = 2q$, where q is the wave vector at which the exciton has been created. The global momentum of the interaction is conserved.

electron-hole pair (1), the energy of the excited pair corresponds to that of the photon, and the associated wave vector, q, is defined by the electronic dispersion of the valence and conduction band of the semiconductor which is represented in Fig. 4.15, panel A. Following the Feynman's diagram, the electron is then elastically scattered by a charged impurity (2), and the momentum of the electron-hole pair changes arbitrarily to an allowed state of the conduction band at the same energy. Then, the electron-hole pair scatters inelastically and excites an LO phonon via the Fröhlich mechanism. The phonon acquires the necessary momentum so that the electron-hole pair returns to its initial wave vector (3), recombining and emitting the outgoing photon (4). Note that the ordering of the (2) and (3) processes can be interchanged. The double-resonance process takes place only when electrically charged defects are present in the crystal lattice. For the case of InN, Cuscó et al.[93] reported an important increase of the Raman intensity of the longitudinal modes in magnesium-doped InN samples. Measurements with different polarizations revealed that the A_1(LO) and E_1(LO) forbidden modes were observed in highly doped samples. All these results are consistent with the impurity-assisted, wave vector non-conservation nature of the Martin's mechanism.[87,94]

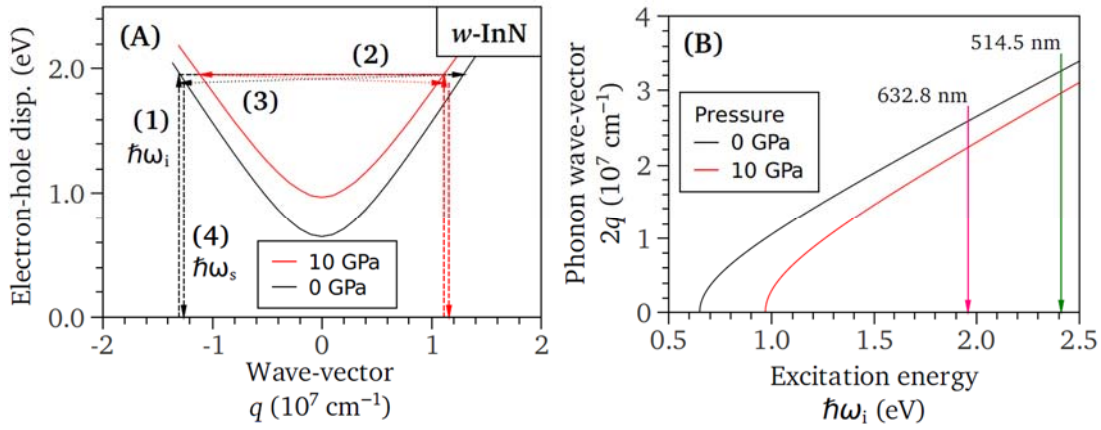

Fig. 4.15. Panel A (left panel): Electronic dispersion of the electron-hole pairs (only light-holes considered) for wurtzite InN at room pressure (black line) and 10 GPa (red line). The black dashed arrows indicate the different steps of the Martin's mechanism: sequentially, (1) an electron-hole pair is formed from an incident photon ($\hbar\omega_i$ corresponding to the 633-nm laser line energy), (2) the electron scatters elastically with a charged impurity changing its momentum, (3) the electron scatters inelastically with a phonon, recovering its original wave vector, and (4) the electron-hole recombines emitting a photon ($\hbar\omega_s$). Red arrows show the same process for the dispersion curve at 10 GPa. **Panel B** (right panel): The resulting phonon wave vector ($2q$) is plotted as a function of laser excitation energy for 0 and 10 GPa (black and red solid lines, respectively).

The scattering cross-section of the interaction can be calculated from perturbation theory including the four Hamiltonians (see Fig. 4.14) for the photon-exciton interaction (H_{em} and H'_{em}), the Coulomb interaction of the free electron with the charged impurity (H_C) and the inelastic scattering of the free electron with a phonon via the Fröhlich interaction (H_F). As discussed elsewhere,[88] the cross section of this process is higher than third order processes (where the phonon wave vector $k \approx 0$) because the cross section of the impurity-induced Fröhlich process is proportional to $\sim k^2$ (thus, important for long wave vectors) and the momentum-conservation is relaxed. In the Martin's double resonance mechanism the wave vector of the process is $k = 2q$ (see Fig. 4.15).

The role of pressure on Martin's mechanism can be analyzed with the aid of Fig. 4.15. Here, the electron-hole dispersion has been plotted for InN at two selected pressures (0 and 10 GPa). The electronic dispersion has been calculated using a $\boldsymbol{k} \cdot \boldsymbol{p}$ approach that takes into account nonparabolicity effects,[14]

$$E_{eh}(k,P) = E_e\left(\sqrt{\frac{\hbar^2k^2}{2m_e^*(P)E_e}+\frac{1}{4}}-\frac{1}{2}\right) + E_{lh}\left(\sqrt{\frac{\hbar^2k^2}{2m_{lh}^*(P)E_{lh}}+\frac{1}{4}}-\frac{1}{2}\right), \quad [4.44]$$

where E_e (0.4 eV for InN) and E_{lh} (0.8 eV for InN)[14] are nonparabolicity coefficients which are assumed to be pressure-independent for simplicity. The effective masses (for InN, m_e^*=0.07 and m_{lh}^*=0.035) can be assumed to depend linearly on the bandgap energy at a given pressure (see Eq. [3.45]). In the panel A of Fig. 4.15, Martin's process is represented with arrows on the electronic dispersion. Following the figure, the exciton is created (1) with an energy corresponding to the particular case of the 632.8-nm line of an He-Ne laser, then the free electron scatters elastically (2) with an impurity, recovers its initial wave vector with an inelastic scattering with a phonon (3) and recombines emitting the outgoing photon (4). The same process has been plotted in red arrows for the bands at 10 GPa, and it can be seen that in the latter, the momentum of the excited phonon has been reduced. This can be better seen in the panel B of Fig. 4.15, where the wave vector of the phonon ($2q$) is represented as a function of excitation energy for two pressures. As the pressure increases, the phonon wave vector is reduced for a given excitation energy. The change of wave vector with pressure is clearly more important for excitation energies in the vicinity of the direct bandgap energy.

Owing to the fact that the wave vector of the phonon is selected via the electronic dispersion of the material, and that the electron-hole dispersion changes with pressure, one can expect that the pressure coefficient of LO modes with large wave vector will be effected by the pressure-induced changes in wave vector. In fact, the LO phonon frequency decreases with increasing wave vector (see, for instance, the phonon dispersion curves as calculated for InN in Article 4.3). This means that pressure will modify the frequency of the phonons by two mechanisms: (a) the expected increase in frequency of the LO branches in the BZ, and (b) the decrease of the wave vector of the LO modes as pressure increase. This effect has been evaluated in this thesis (see Article 4.3 for details). For the case of InN, it has

been observed that the pressure coefficient of the A_1(LO) mode is expected to increase only ~0.5 $cm^{-1}GPa^{-1}$ either using red (632.8-nm) or green (514.5-nm) laser light as excitation source as a consequence of the Martin's double resonance mechanism. It is interesting to note that (see the panel B of Fig. 4.15), sizable pressure-induced changes in the double-resonance mechanism might occur for excitation energies near the direct bandgap of w-InN.

4.3. Results and list of published works

In this thesis, high-pressure Raman-scattering measurements have been performed on the wurtzite and rocksalt crystal structures of InN. For this purpose, a number of different samples, listed in Table 3.1, have been investigated. Also, and for the sake of comparison, an epilayer of rocksalt CdO has also been studied. The work carried out for this thesis has given rise to three publications, Articles 4.1, 4.2, and 4.3, which can be found attached in the following pages:

- Article 4.1: *High-pressure Raman scattering in wurtzite indium nitride*, by J. Ibáñez, F. J. Manjón, A. Segura, R. Oliva, R. Cuscó, R. Vilaplana, T. Yamaguchi, Y. Nanishi and L. Artús. Published in Applied Physics Letters (2011), vol. 99, p. 01190.

In this work, we presented Raman-scattering measurements at high hydrostatic pressures on c-face and a-face InN layers. The aim of this work was to perform a preliminary investigation of the high-pressure behavior of the zone-center optical phonons of wurtzite InN. This work allowed us to obtain the linear pressure coefficients and mode Grüneisen parameters of w-InN. The experimental results were compared with theoretical values obtained from *ab initio* lattice-dynamical calculations based on DFT-LDA. Good agreement was found between the experimental and calculated results. In Article 4.3, a more comprehensive study of the pressure behavior of the phonons of w-InN and rs-InN is presented.

- Article 4.2: *High-pressure Raman scattering of CdO thin films grown by metal-organic vapor phase epitaxy*, by R. Oliva, J. Ibáñez, L. Artús, R. Cuscó, J. Zúñiga-Pérez, and V. Muñoz Sanjosé. Published in Journal of Applied Physics (2013), vol. 113, p. 053514

The aim of this work was to study the pressure behavior of the phonons in a compound exhibiting the rocksalt structure at ambient pressure, and to compare with the case of rs-InN, which is only stable above 13 GPa. For this purpose, we performed Raman-scattering measurements under high hydrostatic pressure on high-quality CdO thin films grown by metal-organic vapor phase epitaxy on

sapphire substrates. The pressure dependence of the second-order Raman bands was discussed in terms of DFT-LDA lattice-dynamical calculations, which also allowed us to obtain the mode Grüneisen parameters for the zone-center TO and LO modes of CdO. Our experiments and calculations allowed us to conclude that at low pressures (<4 GPa) the Raman spectra of CdO are dominated by second-order modes, while at higher pressures (>4 GPa) the spectra mainly display contributions from disorder-activated first-order modes. This is in contrast with the case of rs-InN after the wurtzite-to-rocksalt transition. In this case, the Raman spectra are dominated by first-order disorder activated modes, probably due to the fact that the samples are amorphized after the phase transition.

- Article 4.3*: High-pressure lattice dynamics in wurtzite and rocksalt indium nitride investigated by means of Raman spectroscopy*, by J. Ibáñez, R. Oliva, F. J. Manjón, A. Segura, T. Yamaguchi, Y. Nanishi, R. Cuscó, and L. Artús. Published in Physical Review B (2013), vol. 88, p. 115202.

The aim of this work was to extend the knowledge on the high-pressure vibrational properties of InN gained in Article 4.1. We carried out a comprehensive experimental and theoretical (DFT-LDA) lattice-dynamical study of InN at high hydrostatic pressures. For this purpose, we performed Raman scattering measurements on five w-InN epilayers, with different residual strain and free electron concentrations. We also performed *ab initio* lattice-dynamical calculations on both wurtzite InN (w-InN) and rocksalt InN (rs-InN) as a function of pressure, in order to interpret the experimental results. We compared the experimental and theoretical pressure coefficients of the optical modes in w-InN, and we analyzed the role of residual strain on the measured pressure coefficients of the wurtzite phase. In the case of the LO band, we analyzed in detail its pressure behavior considering the double-resonance mechanism that is thought to be responsible for the selective excitation of LO phonons with large wave vectors in w-InN. The pressure behavior of the L^- coupled mode observed in heavily doped *n*-type w-InN (sample B2 of Table 3.1) also allowed us to estimate the pressure dependence of the electron

effective mass in w-InN. The results thus obtained were found to be in good agreement with $\boldsymbol{k \cdot p}$ theory. The wurtzite-to-rocksalt phase transition on the upstroke cycle, and the rocksalt-to-wurtzite backtransition on the downstroke cycle were investigated, and the Raman features that show up in the respective spectra were interpreted in terms of the DFT lattice-dynamical calculations. In both cases, we concluded that the Raman spectra of both phases after the corresponding phase transitions arise from highly disordered material, i.e., the Raman spectra are dominated by first-order disorder activated modes.

APPLIED PHYSICS LETTERS **99**, 011908 (2011)

High-pressure Raman scattering in wurtzite indium nitride

J. Ibáñez,[1,a)] F. J. Manjón,[2] A. Segura,[3] R. Oliva,[1] R. Cuscó,[1] R. Vilaplana,[4] T. Yamaguchi,[5] Y. Nanishi,[5] and L. Artús[1]
[1]*Institut Jaume Almera, Consell Superior d'Investigacions Científiques, 08028 Barcelona, Catalonia, Spain*
[2]*Instituto de Diseño para la Fabricación y Producción Automatizada, MALTA Consolider Team-Universitat Politècnica de València, 46022 València, Spain*
[3]*Departamento de Física Aplicada-ICMUV-MALTA Consolider Team, Universitat de València, 46100 Burjassot, València, Spain*
[4]*Centro de Tecnologías Físicas, MALTA Consolider Team-Universitat Politècnica de València, 46022 València, Spain*
[5]*Faculty of Science and Engineering, Ritsumeikan University, Shiga 525-8577, Japan*

(Received 2 May 2011; accepted 20 June 2011; published online 7 July 2011)

We perform Raman-scattering measurements at high hydrostatic pressures on *c*-face and *a*-face InN layers to investigate the high-pressure behavior of the zone-center optical phonons of wurtzite InN. Linear pressure coefficients and mode Grüneisen parameters are obtained, and the experimental results are compared with theoretical values obtained from *ab initio* lattice-dynamical calculations. Good agreement is found between the experimental and calculated results. © *2011 American Institute of Physics*. [doi:10.1063/1.3609327]

Over the last few years, indium nitride (InN) has received intensive research interest because of its great potential to develop a wide variety of applications such as high-frequency electronic devices, high-efficiency tandem solar cells, or infrared light-emitting devices.[1] Although the growth of high quality InN is still challenging, bulk material with residual electron densities lower than 5×10^{17} cm^{-3} and electron mobilities higher than 2000 cm^2 V^{-1} s^{-1} has been achieved by molecular beam epitaxy (MBE).[2] In spite of the great interest of InN from both fundamental and applied points of view, many material properties of this compound remain to be investigated. The production of high-quality InN layers and the discovery of the 0.7 eV fundamental band gap of wurtzite InN (w-InN) made necessary to revise many material parameters of InN and InN-based alloys, including their high-pressure behavior.[3,4]

While the available experimental data on the vibrational properties of InN stem mainly from Raman spectroscopy (see for instance Ref. 5 and references therein), a deeper understanding of the lattice dynamics in InN has only been accomplished very recently by means of grazing incidence inelastic x-ray scattering (IXS) measurements on high-quality InN epilayers.[6] Regarding the high-pressure vibrational properties of InN, Pinquier *et al.*[7,8] used Raman scattering to study the pressure dependence of the E_{2h}, A_1 (TO), and A_1 (LO) phonon modes of w-InN in a layer with a high background electron concentration (2.3×10^{19} cm^{-3}). These authors observed the wurtzite-to-rocksalt transition and studied the pressure dependence, up to 50 GPa, of broad bands arising from the rocksalt phase.[8] However, the pressure dependence of the long-lived E_{2l} mode and of the E_1 modes of w-InN was not reported in those works. Recently, Yao and co-workers employed Raman scattering to investigate the structural stability of poorly crystalline w-InN nanowires under high pressure.[9] The pressure coefficients and mode Grüneisen parameters obtained by these authors for the A_1 (TO), E_{2h}, and A_1 (LO) modes were sizably lower than those reported in Refs. 7 and 8.

In this letter, we present Raman-scattering measurements under high hydrostatic pressure on high-quality *c*-face and *a*-face InN epilayers grown by MBE. Experiments on both types of samples have allowed us to study the pressure behavior of the non-polar E_{2l} and E_{2h} optical phonons and of the polar A_1 (TO), E_1 (TO), and LO phonons of w-InN. The linear pressure coefficients and mode Grüneisen parameters of these modes have been determined and found to be in good agreement with the results of *ab initio* lattice-dynamical calculations based on density functional theory (DFT).

For the present study, we used two different w-InN epilayers, with thicknesses of 5.7 μm (*c*-face) and 500 nm (*a*-face). Both samples were grown by plasma assisted MBE on sapphire substrates. The background electron concentration of the samples was $\sim 1 \times 10^{18}$ cm^{-3} (*c*-face) and $\sim 4 \times 10^{18}$ cm^{-3} (*a*-face). Flakes of w-InN containing some residual sapphire were detached from the substrate and loaded in a gasketed membrane-type diamond anvil cell (DAC) with 400 μm culet-size diamonds. Methanol-ethanol-water (16:3:1) was employed as pressure transmitting medium, and the ruby fluorescence method was used to determine the applied pressure. Confocal micro-Raman measurements at room temperature were acquired with a HORIBA Jobin-Yvon LabRam-HR spectrometer. To reduce the Rayleigh radiation and to detect the low-frequency E_{2l} mode of w-InN by means of a single-grating spectrometer such as the LabRam-HR system, we used the 632.8-nm line of a He-Ne laser as excitation radiation. A 50× objective was employed to focus the laser beam and to collect the scattered radiation. In the case of the *c*-face sample, the measurements were carried out up to the transition pressure, which was observed to begin at $\sim$ 12 GPa in this sample. For the *a*-face sample, the experiments were performed up to a pressure of $\sim$ 10 GPa.

Figures 1 and 2 show selected Raman spectra at different pressures for the *c*-face and the *a*-face epilayers, respectively. As expected from the selection rules for Raman experiments in backscattering geometry on a *c* face of

a)Author to whom correspondence should be addressed. Electronic mail: jibanez@ictja.csic.es.

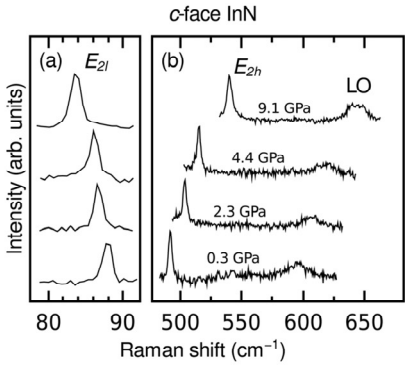

FIG. 1. Room-temperature Raman spectra of a *c*-face InN layer at different hydrostatic pressures in the up-stroke (a) in the low-frequency region and (b) in the high-frequency region.

wurtzite crystals, the spectra of Fig. 1 are dominated by the non-polar E_{2l} and E_{2h} modes of w-InN [Figs. 1(a) and 1(b), respectively]. The weak band that appears in the high-frequency region of the spectra in Fig. 1(b) contains contributions of both A_1 (LO) and E_1 (LO) modes. Note that, at ambient pressure, the Raman spectra of as-grown *c*-face epilayers display the expected A_1 (LO) mode and also some weaker signal arising from the forbidden E_1 (LO) mode. The observation of E_1 (LO) signal through impurity-induced Fröhlich interaction in the spectra of *c*-face InN layers is attributed to the relaxation of the selection rules induced by defects.[10] When the InN material is loaded into the DAC, the LO band is found to broaden and shift to higher frequencies, while the dominant E_{2h} peak remains basically unchanged. This suggests that sample misorientation and/or disorder generated during the sample loading give rise to a further enhancement of the E_1 (LO) signal. Similarly, in the case of the *a*-face epilayer both the A_1 (LO) and E_1 (LO) modes are symmetry forbidden and they become visible through impurity scattering [Fig. 2(b)]. The spectra of the *a*-face sample also exhibit the A_1 (TO) and E_1 (TO) modes, which show up as weak features below the E_{2h} peak [Fig. 2(a)]. Among all the modes observed in this work, the low-intensity TO peaks yield the highest error in the frequency measurement, which we estimate is lower than 2 cm^{-1}. The E_{2l} peaks detected in the case of the *a*-face epilayer (not shown) were fairly weak, superimposed to a relatively strong background signal.

Both Figs. 1 and 2 show the expected frequency increase for all phonon modes with increasing pressure, with the exception of the E_{2l} mode, which displays a pressure-induced softening. This behavior is typical of shear phonon modes, i.e., zone-edge transverse acoustic (TA) modes in zincblende and diamond semiconductors.[11] In general, it is found that the mode Grüneisen parameter of the soft mode linearly correlates to the transition pressure of the material.[12,13] In the case of wurtzite compounds, the E_{2l} mode corresponds to the TA(L) mode of the zincblende structure due to the folding of the zone-edge TA modes along the Γ-L direction of the Brillouin zone. The softening of the E_{2l} mode has been observed in many different wurtzite compounds, including ZnO (Ref. 14) and GaN (Ref. 15). Only AlN (Refs. 13 and 16) and BeO (Ref. 17) seem not to exhibit this softening behavior. While the positive pressure coefficient for the E_{2l} mode of BeO is probably linked with its high pressure stability, the case of AlN is somewhat puzzling, since the wurtzite-to-rocksalt transition occurs at a relatively low pressure (~20 GPa). The observation of positive pressure coefficients for the E_{2l} mode of AlN might be related to the special balance between ionic and covalent restoring forces in this compound.[11] In the case of InN, following the discussion of Ref. 12, the observed softening of the E_{2l} mode is consistent with the observed transition pressures, around 12–14 GPa.[8,18]

In Fig. 3, we have plotted the pressure dependence of the measured optical phonon frequencies. Data obtained for the two samples studied in this work have been included in the figure. Note the similar pressure behavior observed for the E_{2h} and LO modes in both samples. Table I displays the linear pressure coefficients (a_i) extracted with a linear fit to all the experimental data, i.e., employing the expression $\omega_i(P) = \omega_i(0) + a_i P$, where $\omega_i(P)$ is the frequency of the *i*th mode at a pressure P. Mode Grüneisen parameters for the *i*th mode, γ_i, are subsequently deduced by using the expression $\gamma_i = B_0 a_i/\omega_i(0)$, where B_0 is the bulk modulus of the material. Here, we use a value of $B_0 = 143$ GPa, which we obtain from DFT *ab initio* calculations (see details in Ref. 5). This value

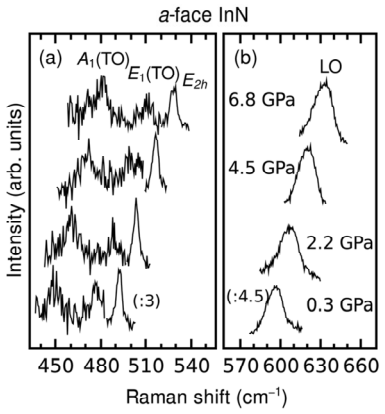

FIG. 2. Room-temperature Raman spectra of a *a*-face InN layer at different hydrostatic pressures in the up-stroke (a) in the middle-frequency region and (b) in the high-frequency region.

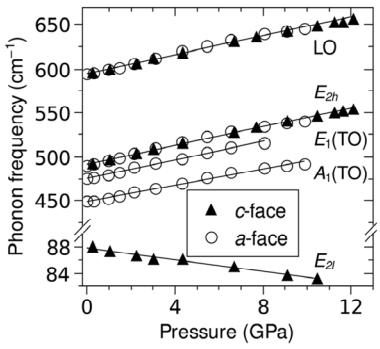

FIG. 3. Pressure dependence of the optical phonon frequencies of w-InN measured in the up-stroke in *c*-face InN (solid triangles) and in *a*-face InN (open circles). The lines are the results of linear fits to the experimental data.

TABLE I. Results of the linear fits to the pressure behavior of the optical phonons of w-InN. $\omega_i(0)$ and a_i are the zero-pressure frequency and the linear pressure coefficient for the ith mode, respectively. A bulk modulus of 143 GPa was used to obtain the mode Grüneisen parameters (γ_i). Values in parentheses are the results of *ab initio* lattice-dynamical calculations. Theoretical values for the LO mode correspond to the A_1 (LO) phonon.

Phonon mode i	$\omega_i(0)$ (cm^{-1})	a_i (cm^{-1} GPa^{-1})	γ_i
E_{2l}	88 (83.9)	−0.4 (−0.63)	−0.65 (−1.07)
A_1 (TO)	449 (450.4)	5.3 (4.69)	1.69 (1.49)
E_1 (TO)	476 (474.5)	5.3 (4.88)	1.59 (1.47)
E_{2h}	492 (488.4)	5.2 (5.18)	1.51 (1.52)
LO	595 (591.8)	5.1 (4.87)	1.22 (1.17)

is in close agreement to that obtained recently with grazing incidence IXS measurements ($B_0 = 152$ GPa).[6] We plot in Fig. 3 the results of linear fits to the experimental data (solid lines). The resulting mode Grüneisen parameters for the different phonons are displayed in the last column of Table I.

The a_i values obtained with our high-pressure Raman experiments for the TO, E_{2h}, and LO modes of InN are lower than those reported in InN films with much higher residual electron densities.[7,8] In contrast, the a_i values obtained by Yao *et al.*[9] on InN nanowires are even lower than those measured here. Given that several possible sources of unintentional doping have been reported in InN, the origin of the different pressure behavior observed in samples with different electron densities cannot be established. More work would be necessary in order to clarify this issue.

From the experimental data obtained with the present measurements (Table I), it can be seen that the pressure behavior of the A_1 (TO) phonons of w-InN (ionic vibrations along the c-axis) is similar to that of the E_{2h} and E_1 (TO) modes (vibrations perpendicular to the c-axis). GaN exhibits a similar behavior.[19] This is in contrast, for instance, to the case of w-AlN, where the measured pressure coefficients for the E_1 and E_{2h} modes are much larger than for the A_1 modes.[16]

To gain further insight into the pressure behavior of the phonons of w-InN, we have performed *ab initio* lattice-dynamical calculations of the linear pressure coefficients (a_i) and mode Grüneisen parameters (γ_i) for the zone-center optical phonons of this compound. The calculations, based on DFT within the local density approximation (LDA), were carried out with the ABINIT package.[20] Calculations were performed at different pressures, and a_i and γ_i values were obtained with a linear fit to the data. Details of the calculations at ambient pressure can be found elsewhere.[5] Since the ABINIT code fails to correctly predict the dispersion of the E_1 (LO) mode in wurtzite materials,[5] the calculated values for the LO phonon given in Table I correspond to the A_1 (LO) phonon. The resulting a_i and γ_i values are displayed in parentheses in Table I. Good agreement is found between the experimental data obtained in the present work and the calculated values for the TO and the non-polar modes. In contrast, the theoretical a_i values are systematically lower than those previously measured in bulk w-InN.[7,8] Remarkably, the DFT-LDA calculations predict the softening of the E_{2l} mode, as observed with the present measurements. Note also that the DFT calculations predict a very small increase of the A_1 (LO)−A_1 (TO) splitting (∼0.18 cm^{-1} GPa^{-1}). Instead, we observe a small decrease of ∼−0.2 cm^{-1} GPa^{-1} for the LO band in relation to both the A_1 (TO) and the E_1 (TO) modes. Within the experimental error of the present measurements, this result confirms that only a very small pressure dependence of the LO-TO splitting may be expected in w-InN. Finally, we would like to remark that, leaving aside the soft E_{2l} mode, the *ab initio* calculations predict a very similar pressure behavior for all the Raman-active modes of w-InN regardless of the direction of the ionic vibrations, which is in agreement with the experimental results.

In conclusion, we have performed high-pressure Raman measurements on c-face and a-face layers to investigate the pressure behavior of the zone-center optical phonons of wurtzite InN. The linear pressure coefficient and mode Grüneisen parameters of the E_{2l}, A_1 (TO), E_1 (TO), E_{2h}, and LO modes of w-InN have been obtained. Good agreement between the experimental data and theoretical values obtained with *ab initio* lattice-dynamical calculations has been found.

Work supported by the Spanish MICINN (Projects MAT2010-16116, MAT2008-06873-C02-02, MAT2010-21270-C04-04, and CSD2007-00045), the Catalan Government (BE-DG 2009), and the Spanish Council for Research (PIE2009-CSIC).

[1]*Indium Nitride and Related Alloys*, edited by T. D. Veal, C. F. McConville, and W. J. Schaff (CRC/Taylor and Francis, Boca Raton, 2009).
[2]C. S. Gallinat, G. Koblmller, J. S. Brown, S. Bernardis, J. S. Speck, G. D. Chern, E. D. Readinger, H. Shen, and M. Wraback, Appl. Phys. Lett. **89**, 032109 (2006).
[3]S. X. Li, J. Wu, E. E. Haller, W. Walukiewicz, W. Shan, H. Lu, and W. J. Schaff, Appl. Phys. Lett. **83**, 4963 (2003).
[4]I. Gorczyca, J. Plesiewicz, L. Dmowski, T. Suski, N. E. Chistensen, A. Svane, C. S. Gallinat, G. Koblmueller, and J. S. Speck, J. Appl. Phys. **104**, 013704 (2008).
[5]N. Domènech-Amador, R. Cuscó, L. Artús, T. Yamaguchi, and Y. Nanishi, Phys. Rev. B **83**, 245203 (2011).
[6]J. Serrano, A. Bosak, M. Krisch, F. J. Manjón, A. H. Romero, N. Garro, X. Wang, A. Yoshikawa, and M. Kuball, Phys. Rev. Lett. **106**, 205501 (2011).
[7]C. Pinquier, F. Demangeot, J. Frandon, J. W. Pomeroy, M. Kuball, H. Hubel, N. W. A. van Uden, D. J. Dunstan, O. Briot, B. Malcyrc, S. Ruffenach, and B. Gil, Phys. Rev. B **70**, 113202 (2004).
[8]C. Pinquier, F. Demangeot, J. Frandon, J. C. Chervin, A. Polian, B. Couzinet, P. Munsch, O. Briot, S. Ruffenach, B. Gil, and B. Maleyre, Phys. Rev. B **73**, 115211 (2006).
[9]L. D. Yao, S. D. Luo, X. Shen, S. J. You, L. X. Yang, S. J. Zhang, S. Jiang, Y. C. Li, J. Liu, K. Zhu, Y. L. Liu, W. Y. Zhou, L. C. Chen, C. Q. Jin, R. C. Yu, and S. S. Xie, J. Mater. Res. **25**, 2330 (2010).
[10]R. Cuscó, J. Ibáñez, E. Alarcón-Lladó, L. Artús, T. Yamaguchi, and Y. Nanishi, Phys. Rev. B **79**, 155210 (2009).
[11]J. M. Wagner and F. Bechstedt, Phys. Status Solidi B **235**, 464 (2003).
[12]B. A. Weinstein, Solid State Commun. **24**, 595 (1977).
[13]E. V. Yakovenko, M. Gauthier, and A. Polian, JETP **98**, 981 (2004).
[14]J. S. Reparaz, L. R. Muniz, M. R. Wagner, A. R. Goñi, M. I. Alonso, A. Hoffmann, and B. K. Meyer, Appl. Phys. Lett. **96**, 231906 (2010).
[15]P. Perlin, C. Jauberthie-Carillon, J. P. Itié, A. San Miguel, I. Grzegory, and A. Polian, Phys. Rev. B **45**, 83 (1992).
[16]F. J. Manjón, D. Errandonea, A. H. Romero, N. Garro, J. Serrano, and M. Kuball, Phys. Rev. B **77**, 205204 (2008).
[17]A. P. Jephcoat, R. J. Hemley, H. K. Mao, R. E. Cohen, and M. J. Mehl, Phys. Rev. B **37**, 4727 (1988).
[18]J. Ibáñez, A. Segura, F. J. Manjón, L. Artús, T. Yamaguchi, and Y. Nanishi, Appl. Phys. Lett. **96**, 201903 (2010).
[19]A. R. Goñi, H. Siegle, K. Syassen, C. Thomsen, and J.-M. Wagner, Phys. Rev. B **64**, 035205 (2001).
[20]The ABINIT code is a common project of the Universitié Catholique de Louvain, Corning Incorporated, and other contributors (http://www.abinit.org).

JOURNAL OF APPLIED PHYSICS 113, 053514 (2013)

High-pressure Raman scattering of CdO thin films grown by metal-organic vapor phase epitaxy

R. Oliva,[1] J. Ibáñez,[1] L. Artús,[1] R. Cuscó,[1] J. Zúñiga-Pérez,[2,3] and V. Muñoz-Sanjosé[2]
[1]*Institut Jaume Almera, Consell Superior d'Investigacions Científiques (CSIC), Lluís Solé i Sabarís s.n., 08028 Barcelona, Catalonia, Spain*
[2]*Departament de Física Aplicada i Electromagnetisme, Universitat de València, Dr Moliner 50, València, 46100 Burjassot, Spain*
[3]*Centre de Recherche sur l'Hétéro-Epitaxie et ses Applications, CNRS, Valbonne, France*

(Received 19 November 2012; accepted 22 January 2013; published online 6 February 2013)

We have performed Raman-scattering measurements under high hydrostatic pressure on CdO thin films grown by metal-organic vapor phase epitaxy on sapphire substrates. The pressure dependence of the second-order Raman bands is discussed in terms of *ab initio* lattice-dynamical calculations, which allow us to obtain mode Grüneisen parameters for the zone-center TO and LO modes of CdO. Our experiments and calculations suggest that at low pressures (<4 GPa) the Raman spectra are dominated by second-order modes, while at higher pressures (>4 GPa) the spectra mainly display contributions from disorder-activated first-order modes. © *2013 American Institute of Physics*. [http://dx.doi.org/10.1063/1.4790383]

I. INTRODUCTION

Unintentionally-doped cadmium oxide (CdO) is an *n*-type semiconductor that crystallizes in the rocksalt structure. The direct band-gap energy of intrinsic CdO has recently been shown to lie around 2.2 eV at room temperature.[1,2] CdO exhibits remarkable properties such as low resistivity, high transparency, and high refractive index, which make this compound an excellent candidate for next-generation transparent conducting-oxide layers that could be exploited in photovoltaic cells or flat-panel displays. CdO is also interesting both from applied and fundamental points of view because alloying of CdO with ZnO might allow one to extend the optical emission of ZnO-based structures to longer wavelengths.

Several works have been devoted to investigate the structural and optical properties of CdO.[2–4] However, the vibrational properties of CdO have been comparatively less investigated, which can be partly attributed to the fact that CdO crystallizes in the rocksalt structure and, as a consequence, the first-order Raman modes are symmetry forbidden. Early infrared measurements suggested that the zone-center transverse-optical (TO) and longitudinal-optical (LO) phonon modes of CdO are located at 262 and 523 cm^{-1}, respectively.[5] A first Raman study on polycrystalline CdO showed that the second-order Raman bands of CdO strongly depend on electron density.[6] Recently, we have reported Raman scattering studies on CdO epilayers exhibiting strong second-order modes that were assigned on the basis of *ab initio* calculations of the phonon dispersion curves.[7]

Pressure-induced frequency shifts of the Raman bands strongly depend on the nature (optical or acoustic) and number of phonons involved in the Raman-scattering processes. Thus, the application of high hydrostatic pressures to study the vibrational properties of CdO may provide further information about the assignments of the second-order Raman bands. The high-pressure vibrational properties of rocksalt compounds have been scarcely investigated so far.

Here, we present a high-pressure Raman-scattering investigation of CdO. We use high-quality CdO epilayers grown by metal-organic vapor phase epitaxy (MOVPE) on sapphire. The pressure dependence of the Raman spectra obtained experimentally up to ~16 GPa is discussed in terms of *ab initio* lattice-dynamical calculations at different hydrostatic pressures of the full phonon band structure. From the calculations, bulk modulus and mode Grüneisen parameters for the zone-center TO and LO modes of CdO are obtained. The combined analysis of the experimental results and the calculations allow us to identify the different contributions that dominate the Raman spectrum of CdO at different pressure ranges.

II. EXPERIMENT

High-quality, MOVPE-grown CdO/sapphire epilayers with a thickness of ≈900 nm were used in the present work. Details on the growth conditions and structural properties of these epilayers can be found elsewhere.[8,9] Hall-effect measurements revealed that the as-grown CdO thin films display high *n*-type conductivity, with free-electron densities as high as 1.8×10^{20} cm^{-3} and electron mobilities around 50 $cm^2 V^{-1} s^{-1}$.

For the high-pressure Raman experiments, flakes of CdO/sapphire were loaded into a gasketed membrane-type diamond-anvil cell (DAC). Methanol-ethanol-water (16:3:1) was used as pressure-transmitting medium, and the applied pressure was measured with the ruby fluorescence method.[10] Confocal, unpolarized micro-Raman measurements were performed at room temperature by using the triple subtractive configuration of a Jobin-Yvon T64000 spectrometer equipped with a LN_2-cooled charge coupled device (CCD) detector. The 514.5-nm line of an Ar^+ laser was employed as excitation source. A 50× objective was used to focus the laser beam and to collect the back-scattered light. At ambient pressure, the energy of the absorption edge of the heavily

doped CdO samples used in this work[1] is larger than that of the excitation radiation used to perform the Raman experiments (2.41 eV for the 514.5-nm line of the Ar^+ laser). Thus, it is expected that CdO will remain transparent throughout the high-pressure measurements.

III. RESULTS AND DISCUSSION

A. *Ab initio* lattice-dynamical calculations

Ab initio calculations of the vibrational properties of CdO as a function of hydrostatic pressure were performed with the ABINIT package,[11] which relies on a plane-wave pseudopotential approach to density functional theory (DFT) in the local density approximation (LDA) using the Teter-Pade parametrization of the exchange-correlation functionals.[12] For the calculations, Trouiller-Martins pseudopotentials were used.[13] In the case of the Cd pseudopotential, 4*d* electrons were included as valence states. A $6 \times 6 \times 6$ Monkhorst–Pack *k*-point sampling and a plane wave basis set with an energy cutoff of 60 hartree were considered, giving rise to a convergence of the total energy better than 1 mhartree. The lattice parameter for CdO at ambient pressure obtained after a full structural relaxation of the rocksalt lattice yielded a lattice parameter of $a = 4.6939$ Å, in agreement with reported experimental values (4.6942 Å in Ref. 8). Structural relaxation of the CdO rocksalt lattice as a function of pressure allowed us to determine the bulk modulus at zero pressure ($B_0 = 157.7$ GPa) and its first derivative ($B_0' = 4.8$). These data agree well with high-pressure structural studies which obtained B_0 values around 150 GPa, with $B_0' \approx 4$.[14,15]

For the response-function calculations, the dynamical matrices were obtained at different pressure values on a mesh of 28 *k*-points using the density-functional linear-response approach, and the interatomic force constants were generated by a Fourier transformation, which allows the dynamical matrices to be interpolated for arbitrary wave vectors. The full phonon dispersion curves are obtained after diagonalization of the dynamical matrices,[16,17] and one-phonon and two-phonon density of states (2PDOS) are subsequently extracted. To obtain smooth profiles for the density-of-states curves, a Gaussian-like smearing technique was employed.

Figure 1 shows the phonon dispersion curves and PDOS of CdO at two different pressures, $P = 0$ and $P = 10$ GPa. The corresponding PDOS is plotted in the right panel of Fig. 1. As can be seen in the figure, the lattice-dynamical calculations predict a very small frequency gap at ambient pressure between the acoustic and optical branches. At $P = 10$ GPa the calculations predict a considerable opening of the phonon gap, which is particularly evident at the L point. On the other hand, the calculated PDOS exhibits an overall upward frequency shift with increasing pressure. From the pressure-induced frequency shifts of the zone-center TO phonon (266.5 cm^{-1}) and the LO phonon (429.6 cm^{-1}), the mode Grüneisen parameters, γ_i, for these two modes were obtained. For the TO(Γ) mode, we obtain a pressure coefficient of 4.9 cm^{-1}/GPa ($\gamma_{TO} = 2.90$). For the LO(Γ) mode, in spite of the similar pressure coefficient (4.6 cm^{-1}/GPa), the calculated mode Grüneisen parameter is much lower

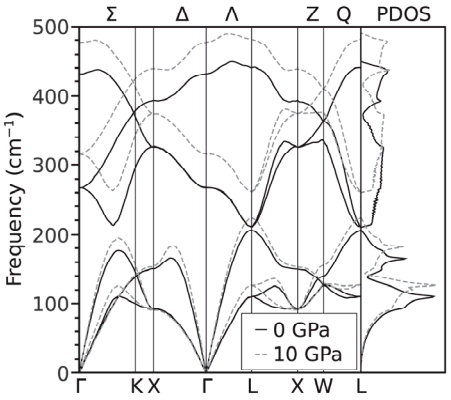

FIG. 1. Calculated phonon dispersion curves at 0 GPa (solid line) and 10 GPa (dashed line). The corresponding one-phonon density of states for both pressure values is shown on the right panel of the figure.

($\gamma_{LO} = 1.69$), which is a consequence of the large TO-LO splitting in CdO. These data can be found in Table I. Note, however, that the LDA calculations tend to fail for the calculation of LO frequencies. The intrinsic limitations of the calculations based on the LDA functional, which can be particularly important in strongly correlated systems such as transition-metal oxides, yield a substantial overestimation of the high-frequency dielectric constant, giving rise to large underestimations of the LO-TO splitting.

The Raman spectrum of rocksalt CdO and its pressure dependence are expected to reflect the 2PDOS. Figure 2 shows the calculated two-phonon sum and difference 2PDOS curves for $P = 0$ and 10 GPa. While the contribution of different modes at ambient pressure extends below 400 cm^{-1} and dominates the low-frequency spectral range (<150 cm^{-1}), the sum 2PDOS extends over a wide frequency range, from 200 cm^{-1} up to 900 cm^{-1}. Upon increasing pressure, the DFT calculations predict sizable upward frequency shifts for most of the features with high-density of states that appear in both the sum and difference 2PDOS. Only in the 50–80 cm^{-1} range the difference 2PDOS exhibits a maximum that barely shifts with pressure, and which can be attributed to LA-TA or LO-TO difference modes as will be discussed below. In the next sections, the calculated pressure coefficients will be used to assess the assignment of the second-order Raman bands that appear in the Raman spectrum of CdO.

B. High-pressure Raman spectrum of CdO

Figure 3 shows Raman spectra of CdO at different hydrostatic pressure values. A smooth background signal attributed to diffused light within the DAC was subtracted from the Raman spectra. Several broad features are observed

TABLE I. Calculated pressure coefficients and mode Grüneisen parameters for the zone-center LO and TO modes of CdO.

CdO phonons	dω/dP (cm^{-1}/GPa)	Grüneisen parameter
TO (Γ)	4.9	2.90
LO (Γ)	4.6	1.69

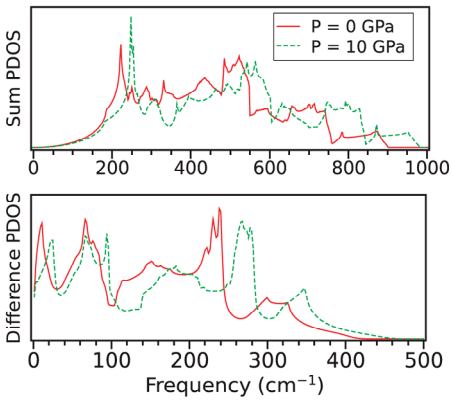

FIG. 2. Sum (upper panel) and difference two-phonon density of states at pressures values of 0 GPa (solid line) and 10 GPa (dashed line).

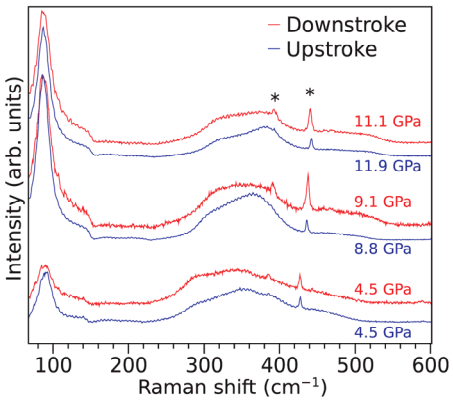

FIG. 4. Comparison of Raman spectra of CdO at different hydrostatic pressures obtained in the upstroke and downstroke cycles. Peaks from the sapphire substrate have been marked with an asterisk.

in the Raman spectra of Fig. 3. The different bands have been labeled from A to F. The A_{1g} mode ($\omega \approx 420\,\text{cm}^{-1}$ at $P = 0$) and E_g mode ($\omega \approx 750\,\text{cm}^{-1}$ at $P = 0$) of sapphire are also visible in all the spectra, showing that the CdO layers remain mostly transparent throughout the whole experiment. The obtained pressure dependence of these two modes (not shown) was in good agreement with previous Raman scattering measurements on bulk sapphire.[18] In Fig. 3, the peaks from sapphire are marked with an asterisk. In some of the spectra, weak Raman features corresponding to the methanol-ethanol-water (16:3:1) mixture can also be distinguished in the high-frequency spectral range at ≈ 880, 1033, and 1065 cm^{-1}.

The reproducibility of these experiments was checked by repeating the high-pressure Raman measurements on a second CdO/sapphire flake. The results thus obtained were highly coincident with the first set of experiments, with equivalent number and shape of Raman features as a function of pressure. As can be seen in Fig. 4, the high-pressure Raman spectra are also well reproduced in the downstroke cycle. In particular, as can be seen in the figure, the intensity ratio between the low-frequency (A) and medium-frequency (B to E) features is clearly recovered after the downstroke cycle, which suggests that the crystal lattice of CdO has not suffered any irreversible damage during the upstroke cycle.

In the low frequency region, a broad feature labeled A_1 shows up in the spectra acquired at low hydrostatic pressures (Fig. 3). This band, which barely shifts with increasing pressure, can be distinguished from the A_2 peak, which displays a strong intensity enhancement and a very small negative pressure coefficient. As can be seen in Fig. 5, the zero pressure frequency extrapolated for these two peaks is different, which suggests that they are originated by different Raman modes.

In the 200–500 cm^{-1} range, a broad band is observed at ambient pressure.[7] This band can be decomposed in 4 contributions, which in Fig. 3 are labeled as B_1, C_1, D, and E. The pressure behavior of the features is plotted in Fig. 5. Feature B_1, located at 265 cm^{-1} at $P = 0$, is the sharpest feature in the Raman spectrum of CdO at ambient pressure and was tentatively assigned as a 2TA(L) mode in Ref. 7. With

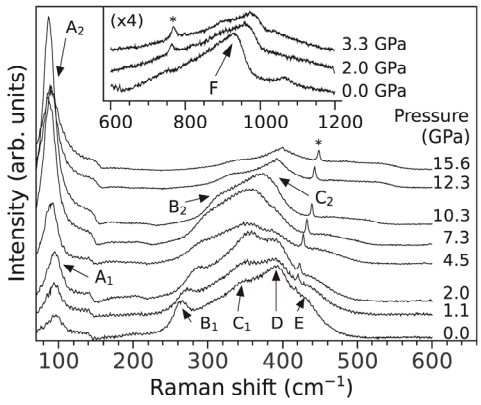

FIG. 3. Raman spectra of CdO at different hydrostatic pressures. The inset shows the Raman signal observed in the high-frequency region of the spectrum. Peaks from the sapphire substrate have been marked with an asterisk.

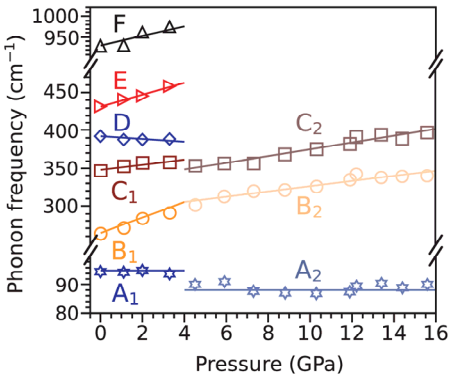

FIG. 5. Phonon frequency of the different features observed in the Raman spectrum of CdO as a function of hydrostatic pressure.

increasing P, this feature displays a sizable upward frequency shift of $8.5 \pm 2\,\mathrm{cm}^{-1}$/GPa and a clear loss of intensity. This high pressure coefficient already indicates that optical modes probably contribute to this feature, as will be discussed below. Above 4.5 GPa this band has completely smeared out. Similarly, features D and E rapidly weaken and disappear at intermediate pressures. On the contrary, feature C_1 seems to gain intensity in relation to the rest of features in the low pressure regime, from ambient pressure up to 2 GPa. At higher pressure values this band smears out completely. In the same frequency region, a new feature (C_2) emerges for $P > 5$ GPa. While the pressure behavior exhibited by bands C_1, D, and E is fairly weak, this feature exhibits a relatively large blueshift of around $4.4 \pm 1\,\mathrm{cm}^{-1}$/GPa with increasing pressure. Similarly, above 5 GPa a broad feature emerges on the low-frequency shoulder around 300 cm^{-1} (feature B_2). Although the large width of band B_2 makes it very difficult to accurately determine its pressure coefficient, this feature displays a sizable blueshift with increasing P, not lower than $3.5\,\mathrm{cm}^{-1}$/GPa. As will be discussed below, the appearance of bands B_2 and C_2 might be related to disorder activated TO modes.

C. Assignment of the Raman modes

In order to assign the different features (A to F) observed experimentally, we have compared their pressure behavior with that of first-order and second-order (sum and difference) phonon modes at high-symmetry points of the Brillouin zone obtained with *ab initio* lattice-dynamical calculations. In Table II, we show a tentative assignment performed for some of these bands together with the pressure coefficient measured experimentally (see Fig. 5) and the corresponding frequency extrapolated to $P = 0$ GPa. For comparison, the calculated pressure coefficient and zero-pressure frequency of the assigned modes can be found in the table in parentheses. Next, we proceed to discuss on the assignments performed for the observed features:

(i) The lattice dynamical calculations reveal that the frequency and pressure behavior of LA-TA difference modes around the L point are very similar to those of feature A_1. On the other hand, the temperature behavior of this band indicates that it arises from a phonon-difference second-order mode.[7] Thus, this band can be assigned to a LA-TA(L) mode.

(ii) Regarding the A_2 band observed at higher pressures in the same frequency range as feature A_1, we first note that in the 90–120 cm^{-1} region the calculated one-phonon PDOS (Fig. 1) exhibits sharp features arising from TA modes. On the other hand, and bearing in mind the large errors expected for the LDA calculations of the LO frequencies, the *ab initio* calculations reveal that LO-TO modes as well as LA-TA modes may also be expected in this spectral region. We conclude that the A_2 band most probably reflects the large difference PDOS at different points of the Brillouin zone, although it cannot be ruled out that this feature displays an important contribution from disorder-activated transverse acoustic (DATA) modes.

(iii) Our measurements reveal that the B_1 peak displays a large pressure coefficient, as high as $8.5 \pm 2\,\mathrm{cm}^{-1}$/GPa. This large value suggests that this feature cannot be attributed to first order modes or to combination modes involving only acoustic phonons, as for instance a 2TA combination. Here we tentatively assign this band to a TA+TO mode at the L point, for which the lattice-dynamical calculations predict a relatively large pressure coefficient ($6.6\,\mathrm{cm}^{-1}$/GPa, see Table I). Although this value is sizably lower than the experimental one, it should be noted that the error of the measurement is large as the B_1 band rapidly smears out with increasing pressure (see Fig. 3).

(iv) As discussed in Ref. 7, features C_1, D, and E arise from second-order combinations in the region of 330–450 cm^{-1}. The pressure behavior of bands C_1 and E, plotted in Fig. 5, is compatible with the expected qualitative behavior of second-order modes in this spectral region (see Fig. 2). In the case of band D, however, a negative pressure coefficient is observed (not included in Table II). We speculate that this behavior and also the pressure-induced shifts displayed by features C_1 and E is the consequence of strong band overlapping of a large number of second-order combinations around this particular frequency region, giving rise to the observed pressure dependence of the observed features.

(v) The broad B_2 and C_2 bands emerge at pressures higher than ~4 GPa and display sizable pressure coefficients which cannot be accurately measured because

TABLE II. Experimental pressure coefficient (third column) and phonon frequency at zero pressure (second column) as obtained from the data of Fig. 5 for the different features that appear in the high-pressure Raman spectra of CdO. In parentheses, theoretical values obtained with *ab initio* calculations for first- and second-order phonon modes at different high-symmetry points of the Brillouin zone. The last column displays the phonon mode considered for such calculations.

Feature	Zero pressure frequency (cm^{-1})	$d\omega/dP$ (cm^{-1}/GPa)	Pressure range (GPa)	Phonon mode
A_1	95 ± 1 (95.7)	0.0 ± 0.5 (0.1)	0 4	LA TA(L)
A_2	88 ± 1 (83.4, 93.1)	0.0 ± 0.5 (−0.4,−0.2)	5–16	LO-LO(K),TA(X)
B_1	264 ± 2 (322.7)	8.5 ± 2 (6.6)	0–4	TA+TO(L)
C_1, E	300–450	3.5 ± 1	0–4	Second orders
B_2	292 ± 2 (291.3)	>3.5 (4.8)	5–16	TO(K)
C_2	331 (325.8, 333.6)	4.4 ± 1 (4.8, 4.3)	5–16	TO(X), TO(W)
F	930 ± 3 (859.2, 882.4)	11 ± 1 (9.2, 8.0)	0–4	2LO(Γ), 2LO(L)

of the large width of these two bands. According to our lattice-dynamical calculations, the pressure-induced shift of these bands is compatible with the pressure behavior of TO modes (see Table II). We speculate that this spectral region is dominated at low pressure values (<4 GPa) by second-order modes, while at higher pressures (>4 GPa) it is dominated by TO modes, which might be activated by pressure-induced disorder.

(vi) As occurs with the rest of second-order bands, feature F vanishes at pressures higher than 4 GPa. This band, attributed in Ref. 7 to second-order optical modes, exhibits a high pressure coefficient of $11 \pm 1\ cm^{-1}$/GPa. This result confirms that this band corresponds to longitudinal optical second-order modes, probably arising from the L or Γ points. Note that, as already mentioned, the difference between the experimental and calculated data for this band (see Table II) can be attributed to the typical underestimation of the TO-LO splitting of LDA calculations. In any case, the agreement between our experimental pressure coefficients and the calculations is better than 8%, thus confirming that feature F arises from 2LO combinations. The intensity loss observed for this band at higher pressures supports the previous discussion, i.e., that second-order modes (disorder-activated first-order modes) tend to disappear (dominate) at higher applied pressures.

IV. CONCLUSION

We have performed Raman-scattering measurements of CdO at high hydrostatic pressures. The experimental results have been analyzed in terms of *ab initio* lattice-dynamical calculations of the full phonon band structure of CdO as a function of pressure. All features in the Raman spectra of CdO at pressures below 4 GPa are assigned to second-order modes. In contrast, our experimental results and calculations suggest that at higher pressures the Raman spectrum is dominated by disorder-activated first order modes. From the lattice-dynamical calculations, Grüneisen parameters of 2.90 and 1.69 were obtained for the zone-center TO and LO modes, respectively.

ACKNOWLEDGMENTS

This work was supported by the Spanish Government under projects MAT2010-16116 and TEC2011-28076-C02-02 and by Generalitat Valenciana under projects Prometeo/2011-035 and ISIC/2012/008.

[1]P. H. Jefferson, S. A. Hatfield, T. D. Veal, P. D. C. King, C. F. McConville, J. Zuniga-Perez, and V. Munoz-Sanjose, Appl. Phys. Lett. **92**, 022101 (2008).
[2]A. Segura, J. F. Sánchez-Royo, B. García-Domene, and G. Almonacid, Appl. Phys. Lett. **99**, 151907 (2011).
[3]S. K. V. Farahani, T. D. Veal, P. D. C. King, J. Zúñiga-Pérez, V. Muñoz-Sanjosé, and C. F. McConville, J. Appl. Phys. **109**, 073712 (2011).
[4]S. G. Choi, J. Zúñiga-Pérez, V. Muñoz-Sanjosé, A. G. Norman, C. L. Perkins, and D. H. Levi, J. Vac. Sci. Technol. B **28**, 1120 (2010).
[5]H. Finkenrath, N. Uhle, and W. Waidelich, Solid State Commun. **7**, 11 (1969).
[6]G. Schaack and N. Uhle, Solid State Commun. **19**, 315 (1976).
[7]R. Cuscó, J. Ibáñez, N. Domenech-Amador, L. Artús, J. Zúñiga-Pérez, and V. Muñoz-Sanjosé, J. Appl. Phys. **107**, 063519 (2010).
[8]J. Zúñiga-Pérez, C. Munuera, C. Ocal, and V. Muñoz-Sanjosé, J. Cryst. Growth **271**, 223 (2004).
[9]J. Zuñiga-Pérez, C. Martínez-Tomás, and V. Muñoz-Sanjosé, Phys. Status Solidi C **2**, 1233 (2005).
[10]G. J. Piermarini, S. Block, J. D. Barnett, and R. A. Forman, J. Appl. Phys. **46**, 2774 (1975).
[11]X. Gonze *et al.*, Comput. Phys. Commun. **180**, 2582 (2009).
[12]S. Goedecker, M. Teter, and J. Hutter, Phys. Rev. B **54**, 1703 (1996).
[13]N. Troullier and J. L. Martins, Phys. Rev. B **43**, 1993 (1991).
[14]H. Z. Liu, H. K. Mao, M. Somayazulu, Y. Ding, Y. Meng, and D. Häusermann, Phys. Rev. B **70**, 094114 (2004).
[15]J. Zhang, Phys. Chem. Miner. **26**, 644 (1999).
[16]X. Gonze and C. Lee, Phys. Rev. B **55**, 10355 (1997).
[17]S. Baroni, S. de Gironcoli, A. Dal Corso, and P. Giannozzi, Rev. Mod. Phys. **73**, 515 (2001).
[18]G. H. Watson, W. B. Daniels, and C. S. Wang, J. Appl. Phys. **52**, 956 (1981).

PHYSICAL REVIEW B **88**, 115202 (2013)

High-pressure lattice dynamics in wurtzite and rocksalt indium nitride investigated by means of Raman spectroscopy

J. Ibáñez,[1,*] R. Oliva,[1] F. J. Manjón,[2] A. Segura,[3] T. Yamaguchi,[4] Y. Nanishi,[4] R. Cuscó,[1] and L. Artús[1]

[1]*Institut Jaume Almera, Consell Superior d'Investigacions Científiques, 08028 Barcelona, Catalonia, Spain*

[2]*Instituto de Diseño para la Fabricación y Producción Automatizada, MALTA Consolider Team-Universitat Politècnica de València, 46022 València, Spain*

[3]*Departamento de Física Aplicada-ICMUV-MALTA Consolider Team, Universitat de València, 46100 Burjassot, València, Spain*

[4]*Faculty of Science and Engineering, Ritsumeikan University, Shiga 525-8577, Japan*

(Received 11 July 2013; published 5 September 2013)

We present an experimental and theoretical lattice-dynamical study of InN at high hydrostatic pressures. We perform Raman scattering measurements on five InN epilayers, with different residual strain and free electron concentrations. The experimental results are analyzed in terms of *ab initio* lattice-dynamical calculations on both wurtzite InN (w-InN) and rocksalt InN (rs-InN) as a function of pressure. Experimental and theoretical pressure coefficients of the optical modes in w-InN are compared, and the role of residual strain on the measured pressure coefficients is analyzed. In the case of the LO band, we analyze and discuss its pressure behavior considering the double-resonance mechanism responsible for the selective excitation of LO phonons with large wave vectors in w-InN. The pressure behavior of the L^- coupled mode observed in a heavily doped n-type sample allows us to estimate the pressure dependence of the electron effective mass in w-InN. The results thus obtained are in good agreement with $\mathbf{k}\cdot\mathbf{p}$ theory. The wurtzite-to-rocksalt phase transition on the upstroke cycle and the rocksalt-to-wurtzite backtransition on the downstroke cycle are investigated, and the Raman spectra of both phases are interpreted in terms of DFT lattice-dynamical calculations.

DOI: 10.1103/PhysRevB.88.115202 PACS number(s): 78.66.Fd, 78.20.−e, 78.30.−j

I. INTRODUCTION

Over the last decade, InN has attracted much research interest from both fundamental and applied points of view. The renewed attention on this compound and on the entire III-nitride alloy system was boosted after the revision of the fundamental band-gap energy of InN from 1.9 to 0.65 eV, extending the expected emission range of III-nitride alloys from deep-UV (AlN) down to the near-IR region (InN).[1,2] InN also exhibits unique transport properties, such as a small electron effective mass, a surface accumulation layer with ultra-high electron density, and very high saturation and peak drift velocities.[1,2] All these unique properties make InN a promising candidate to fabricate a wide range of devices such as tandem solar cells, IR emitters, and high-speed and high-frequency electronic devices. As a consequence of the great potential of InN for device applications, a great deal of effort has been devoted to improve the crystal quality of InN layers and numerous studies dealing with the optical and electrical properties of InN can be found in the literature.

High-pressure optical measurements are widely employed in semiconductor physics to obtain detailed information about the band structure and the lattice dynamics of semiconductors.[3] In particular, high-pressure techniques provide a highly useful benchmark to test existing models (for instance, density functional theory) for the calculation of the electronic and vibrational properties of semiconductors.

Several high-pressure Raman-scattering studies of wurtzite InN (w-InN) have been published so far.[4–7] Pinquier and coworkers[4,5] investigated the pressure dependence of the E_{2h}, A_1(TO), and LO phonons of w-InN. Pressure coefficients and mode Grüneisen parameters were obtained for these phonon modes, and the wurtzite-to-rocksalt transition was found to lie in the 12–14 GPa range, in agreement with x-ray diffraction measurements[8] and with the predictions of *ab initio* calculations.[9] In Ref. 5 the pressure dependence of several broad features attributed to rocksalt InN (rs-InN) was investigated up to 50 GPa. However, it would be highly desirable to perform lattice-dynamical calculations as a function of pressure in order to support the assignment of the features that appear in the Raman spectra of rs-InN. In turn, Yao and coworkers[6] carried out high-pressure Raman-scattering measurements to study the structural stability of poorly crystalline w-InN nanowires. Recently the softening of the E_{2l} mode has been observed, and the pressure behavior of the E_1(TO) mode has been investigated on a-face layers,[7] with good agreement between the experimental data and *ab initio* calculations relying on density functional theory.

Despite these previous investigations, there are still open questions with regard to the high-pressure vibrational properties of InN. On the one hand, it has been shown that longitudinal optical (LO) modes with large wave vectors defined by the incoming photon energies are selectively excited in Raman-scattering experiments on w-InN.[10] The selective excitation of LO modes with large wave vectors, attributed to a double-resonance excitation process in which the phonon wave vector (q) depends on the electron-hole dispersion,[10] may strongly affect the pressure behavior of the LO modes in w-InN through pressure-induced changes of the electronic structure. On the other hand, a relatively large dispersion of pressure coefficients and mode Grüneisen parameters for both the polar and nonpolar modes of w-InN and w-GaN can be found in the literature. Given that the observed discrepancies could be in part related to residual strains in epilayer material, high-pressure Raman experiments on layers grown on different substrates and/or with different levels of residual strain could be highly informative.

In the case of heavily doped n-type samples, LO-plasmon coupling gives rise to long-wavelength ($q \simeq 0$) L^- modes.[11] While the number of studies dealing with the investigation of the pressure behavior of LO-plasmon coupled modes (LOPCMs) in III–V semiconductors is scarce,[12–14] the pressure dependence of the LOPCMs could be used to gain information about the electronic structure of these compounds.

Here we report Raman-scattering measurements under high hydrostatic pressure on five different w-InN epilayers grown on sapphire substrates. The experimental results are discussed in the light of *ab initio* lattice-dynamical calculations on both w-InN and rs-InN at different pressures. Good agreement is found between the experimental and calculated pressure coefficients of the zone center E_{2l}, E_{2h}, A_1(TO), and E_1(TO) phonons of w-InN. The role of residual strain on the measured pressure coefficients is shown to be negligible within the experimental error of these type of high-pressure measurements. The analysis of the pressure behavior of the LO band in w-InN, taking into account the double-resonance mechanism responsible for the selective excitation of LO phonons with large wave vectors in this material, indicates that the experimental pressure coefficients obtained under visible excitation are barely affected by pressure-induced changes of the electronic structure of w-InN. The pressure behavior of the L^- LOPCM that shows up in heavily doped n-type w-InN is investigated, and the frequency of the L^- band is used to evaluate the electron effective mass of w-InN as a function of hydrostatic pressure. The effective mass values thus obtained turn out to agree well with $\mathbf{k}\cdot\mathbf{p}$ theory. The wurtzite-to-rocksalt phase transition and the subsequent rocksalt-to-wurtzite backtransition are observed in the upstroke and downstroke cycles, respectively. The lattice-dynamical calculations are used to assign the different Raman features that appear in the spectra of both rs-InN and backtransited, poorly crystalline w-InN.

II. EXPERIMENT

For the present work, we used one a-face and four c-face InN epilayers grown by plasma-assisted MBE on sapphire substrates. The background electron density of the samples was obtained with Hall-effect measurements and ranges from $n_e \sim 1 \times 10^{18}$ to 1.6×10^{19} cm^{-3}. Table I shows the thickness and background electron concentration of the samples.

Flakes of w-InN containing residual sapphire were detached from the substrates by mechanical polishing and subsequent cutting. The flakes, together with a few ruby chips, were placed in a gasketed membrane-type diamond anvil cell (DAC) with 400 μm culet-size diamonds. Methanol-ethanol-water (16:3:1) was used as pressure transmitting medium, and the applied pressure was determined with the ruby fluorescence method.

TABLE I. List of samples studied in this work, including data about the residual electron concentration (n_e) and thickness of the w-InN epilayers. All samples are c-face material except sample D, which is a-face.

Sample	Structure	n_e ($\times 10^{18}$ cm^{-3})	Thickness (μm)
A	InN/GaN/sapphire	2	0.5
B1	InN/sapphire	6.5	0.4
B2	InN/sapphire	16	0.4
C	InN/sapphire	<2	5.7
D	InN/sapphire (a-face)	4	0.5

Confocal micro-Raman measurements at room temperature were performed with a HORIBA Jobin-Yvon LabRam-HR spectrometer. The measurements were excited with the 632.8-nm line of a He-Ne laser, since this excitation wavelength allowed us to reduce the Rayleigh radiation and detect the low-frequency E_{2l} mode of w-InN. A 50× objective was employed to focus the laser beam and to collect the backscattered radiation.

III. *AB INITIO* CALCULATIONS

Ab initio lattice-dynamical calculations for w-InN and rs-InN were carried out at different hydrostatic pressures. The calculations were performed using a plane-wave pseudopotential approach to DFT as implemented in the ABINIT package.[15] The calculations were performed within the local density approximation (LDA) by using the Teter parametrization of the exchange-correlation functional[16] and Troullier-Martins pseudopotentials.[17] For the In pseudopotential, 4d electrons were included as valence states. An $8 \times 8 \times 4$ Monkhorst-Pack k-point sampling and a plane-wave basis set with energy cutoffs ranging from 65 to 100 Ha were considered.

A full structural relaxation of the w-InN crystal lattice at zero pressure yielded the following lattice parameters: $a = 3.520$ Å and $c = 5.691$ Å. These values are in very good agreement with those measured by high-resolution x-ray diffraction measurements.[18] Structural relaxation of the w-InN lattice as a function of pressure allowed us to determine the zero-pressure bulk modulus ($B_0 = 143$ GPa). This value is in good agreement with experimental measurements[19] and with previous first-principles calculations.[20] In the case of rs-InN, the full structural relaxation yielded a lattice parameter of $a = 4.523$ Å at ambient pressure and a zero-pressure bulk modulus of $B_0 = 186$ GPa, only slightly higher than the value measured by Uehara *et al.* (170 ± 16 GPa).[8] For hydrostatic pressures of $p = 15$ GPa, just above the transition pressure, we find a bulk-modulus value of $B_{15} = 255$ GPa. The resulting first pressure derivative of $B_0(p)$ is around 4.6, which is in good agreement with the value measured by Uehara *et al.* ($B_0' = 5 \pm 0.9$).[8]

To obtain the phonon dispersion and phonon density of states over the whole Brillouin zone, the ABINIT code computes the dynamical matrix on a mesh of k points using the perturbation theory linear-response approach.[21,22] Interatomic force constants are generated at arbitrary wave vectors by a Fourier transformation, and the dynamical matrices and phonon frequencies are then interpolated for the whole Brillouin zone. Lattice-dynamical calculations were performed at different pressure values, and linear pressure coefficients (a_i) for the zone-center phonons of w-InN and rs-InN were thus obtained.

Figure 1 displays the calculated phonon dispersion along high-symmetry directions at pressure values $p = 0$ and 10 GPa for w-InN. Similarly, Fig. 2 shows the phonon dispersion at $p = 15$ and 25 GPa for rs-InN. The corresponding one-phonon

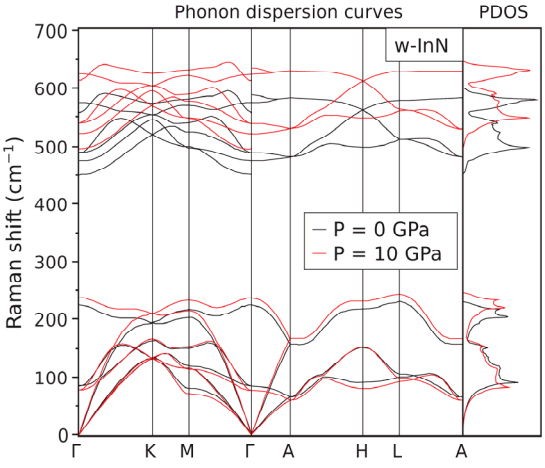

FIG. 1. (Color online) *Ab initio* calculation of the phonon band structure of wurtzite InN along the main lines of symmetry at 0 and 10 GPa. The right panel shows the corresponding phonon density of states (PDOS).

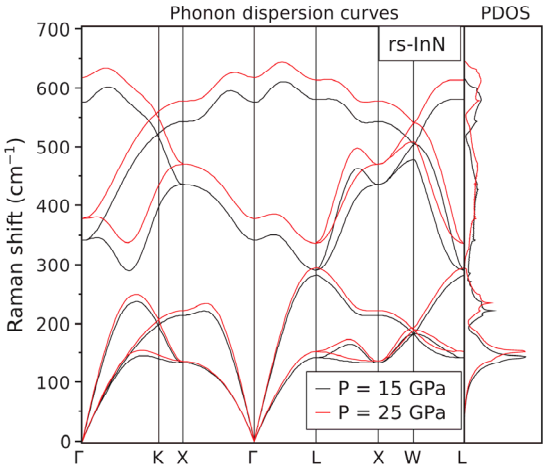

FIG. 2. (Color online) *Ab initio* calculation of the phonon band structure of rocksalt InN along the main lines of symmetry at 15 and 25 GPa. The right panel shows the corresponding phonon density of states (PDOS).

density-of-states (1-PDOS) curves are displayed in the right panel of both figures. As expected, the phonon branches and the calculated PDOS exhibit an overall upward frequency shift with increasing pressure, with the exception of the E_{2l} and transverse acoustic (TA) branches of w-InN, for which the DFT calculations predict a downward frequency shift with increasing pressure. The softening of these modes has been related to the stability of tetrahedral structures under pressure.[23,24] Conversely, the present DFT calculations do not predict any softening of the TA branches of rs-InN. The phonon frequencies at 0 GPa (ω_{i0}), linear pressure coefficients (a_i), and mode Grüneisen parameters ($\gamma_i = B_0 a_i/\omega_{i0}$) for the zone-center optical modes of w-InN and rs-InN as obtained from the present DFT calculations are displayed in Tables II and III, respectively. In the case of rs-InN, the calculations were also performed around $p = 15$ GPa to obtain the corresponding pressure coefficients and Grünesisen parameters around the phase transition pressure (Table III). Note that, although structural techniques show that the phase transition in InN starts around 12 GPa, optical experiments show that the transition is complete only above 15 GPa.[25] The Grüneisen parameters at 15 GPa were computed by using the bulk modulus at this pressure value ($B_{15} = 255$ GPa). As can be seen in Table III, the calculated a_i values around 15 GPa for rs-InN are sizably lower than those obtained at 0 GPa, reflecting the decreasing compressibility of the material with increasing p.

As discussed elsewhere,[26] the ABINIT code provides a good convergence of the phonon frequencies except for the LO modes. This limitation, which may be related to uncertainties in the values of the dielectric constant arising from the LDA band-gap problem, yields an incorrect ordering of the A_1(LO) and E_1(LO) phonon frequencies in w-InN and also a spurious

TABLE II. Best values for the zero-pressure frequency (ω_{i0}), linear pressure coefficient ($a_i = d\omega_i/dp$), relative pressure coefficient ($d \ln \omega_i/dp = a_i/\omega_{i0}$), and mode Grüneisen parameters ($\gamma_i = a_i B_0/\omega_{i0}$) for the zone center TO and E_2 optical phonons and the LO band of w-InN as obtained from high-pressure Raman scattering measurements on different w-InN samples. For comparison, values obtained with *ab initio* lattice-dynamical calculations are also given. Theoretical data for the LO band correspond to the zone-center A_1(LO) mode. A zero-pressure bulk modulus of 143 GPa was used to obtain the γ_i values.

Phonon mode (i)	ω_{i0}(cm^{-1})	a_i(cm^{-1}GPa^{-1})	$d \ln \omega_i/dp$(GPa^{-1})	γ_i
E_{2l} (theor.)	83.9	−0.63	−0.0075	−1.07
E_{2l} (expt.)	88	−0.35 ± 0.05	−0.004 ± 0.0006	−0.6 ± 0.09
A_1(TO) (theor.)	450.4	4.69	0.0104	1.49
A_1(TO) (expt.)	449	5.3 ± 0.5	0.012 ± 0.001	1.69 ± 0.16
E_1(TO) (theor.)	474.5	4.88	0.0103	1.47
E_1(TO) (expt.)	476	5.3 ± 0.5	0.011 ± 0.001	1.59 ± 0.16
E_{2h} (theor.)	488.4	5.18	0.0106	1.52
E_{2h} (expt.)	489	5.1 ± 0.3	0.0104 ± 0.0006	1.49 ± 0.09
A_1(LO) (theor.)	591.8	4.87	0.0082	1.18
LO (expt.)	595	4.8 ± 0.4	0.0081 ± 0.0007	1.15 ± 0.1

TABLE III. Theoretical values for the zero-pressure frequency (ω_{i0}), linear pressure coefficient (a_i) at 0 GPa and the corresponding mode Grüneisen parameters (γ_i) for the zone-center optical phonons of rs-InN as obtained with *ab initio* lattice-dynamical calculations. Values around 15 GPa, corresponding to hydrostatic pressures just above the transition pressure, are also given. Bulk modulus values of 186 and 255 GPa at 0 and 15 GPa obtained from the present DFT calculations were used to calculate the γ_i values.

Phonon mode (i)	ω_{i0}	a_i(cm^{-1})	γ_i(cm^{-1}GPa^{-1})
TO (0 GPa)	268.7	5.78	4.00
TO (15 GPa)	340.0	3.99	3.00
LO (0 GPa)	530.4	5.35	1.88
LO (15 GPa)	597.5	3.80	1.62

dispersion of the E_1(LO) branch along the Γ-M and Γ-K high-symmetry lines. Similarly, as also reported in the case of other rocksalt compounds like CdO,[27] large errors for the frequency and dispersion of the LO mode of rs-InN may be expected. These errors pose some limits to the accuracy of the calculated 1-PDOS and will have to be borne in mind for the discussion of the high-pressure Raman data presented later.

IV. RESULTS AND DISCUSSION

In Raman-scattering experiments on w-InN material, three types of excitations may be expected to appear in the first-order spectra: (1) zone-center ($q \simeq 0$) nonpolar (E_{2l} and E_{2h}) modes and polar (A_1 and E_1) TO modes, excited through the deformation potential mechanism; (2) polar (A_1 and E_1) LO modes with large wave vectors ($q \neq 0$) defined by the exciting photon energies through a double-resonance excitation process;[10] (3) the long-wavelength ($q \sim 0$) L^- branch of the LOPCMs.[11,28,29]

The pressure behavior of all these modes might be affected by residual strains in the epilayers. In addition, the pressure dependence of non-Γ LO modes may be modified by pressure-induced changes of the electronic structure of w-InN. In the case of the L^- modes, the pressure dependence is expected to reflect pressure-induced changes of both the bare phonon frequencies and of the electron effective mass.

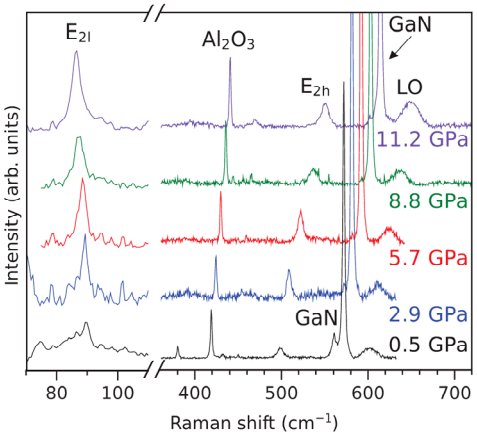

FIG. 3. (Color online) Raman spectra acquired at different hydrostatic pressure values from a high-quality w-InN epilayer grown on a GaN template (sample A).

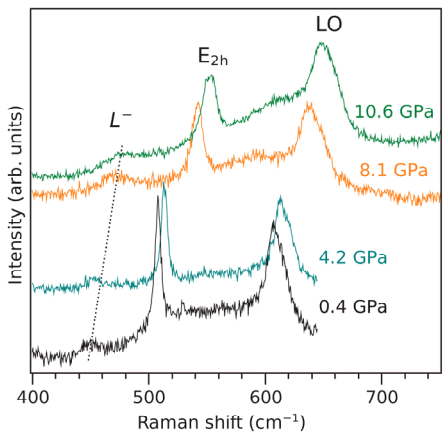

FIG. 4. (Color online) Raman spectra acquired at different hydrostatic pressure values from a heavily doped n-type w-InN epilayer grown on sapphire (sample B2).

Figures 3–5 show selected high-pressure Raman spectra of InN. The spectra of Fig. 3 correspond to a high-quality InN epilayer grown on a GaN template (sample A). The Raman spectra of Fig. 4 were obtained from a heavily doped n-type epilayer directly grown on sapphire (sample B2), while those of Fig. 5, measured up to 19.6 GPa (i.e., beyond the wurtzite-to-rocksalt transition), correspond to a 5.7-μm-thick (relaxed) InN epilayer (sample C). In Ref. 7 Raman spectra below 10 GPa were reported for this sample and also for the a-face InN epilayer (sample D).

As expected from the Raman selection rules for c-face wurtzite crystals, below the wurtzite-to-rocksalt phase transition all the spectra of w-InN are dominated by the nonpolar E_{2l}

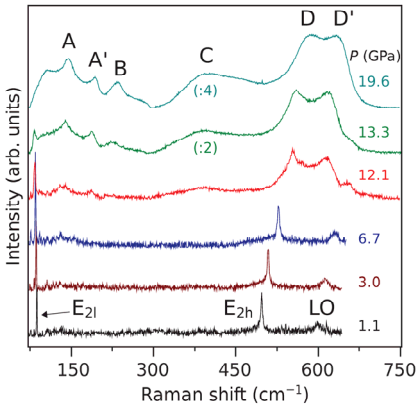

FIG. 5. (Color online) Raman spectra acquired at different hydrostatic pressure values, up to 20 GPa, from a 5.7-μm-thick epilayer grown on sapphire (sample C).

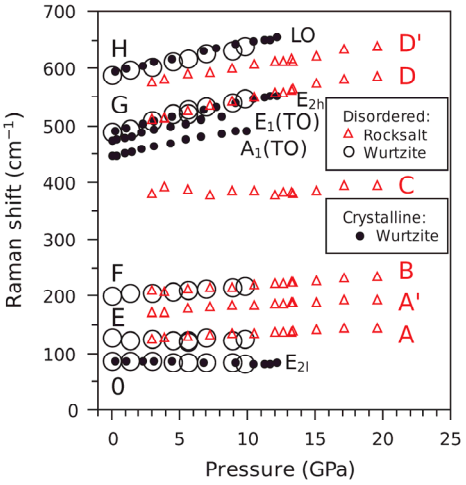

FIG. 6. (Color online) Pressure dependence of the optical phonon frequencies of crystalline wurtzite InN measured in the up-stroke cycle in c-face InN and a-face InN (solid dots). The triangles show the pressure dependence of the disorder-activated first-order bands that appear in the Raman spectrum of rocksalt InN in the up-stroke and in the down-stroke cycles (bands A to D′). The open circles show the corresponding data points for the disorder-activated first-order bands that show up in the Raman spectra after the rocksalt-to-wurtzite backtransition (bands O and E to H).

and E_{2h} phonons (Figs. 3–5). In the case of sample A, grown on GaN/sapphire, strong peaks from GaN are also observed (Fig. 3). In the high-frequency region, a weak band arising from the $q \neq 0$ A_1-E_1 LO phonons of w-InN is also observed in all samples. As discussed in Ref. 7, the Raman spectra of the InN flakes loaded into the DAC contain contributions of both A_1 and E_1 symmetries, which is attributed to symmetry-forbidden enhancement of the E_1(LO) signal due to the impurity-induced Fröhlich interaction mechanism.[11] In the case of a-face material (sample D), the Raman spectra also exhibit weak features corresponding to the zone-center A_1(TO) and E_1(TO) modes (not shown here; see Ref. 7).

The pressure dependence of the phonon modes that is typically obtained in w-InN is illustrated in Fig. 6 (plotted with solid dots). The figure shows the pressure dependence of the E_{2l}, E_{2h}, and LO frequencies as obtained during the upstroke cycle for the thick (relaxed) InN epilayer (sample C). As will be discussed below, a virtually equivalent pressure behavior was observed for the rest of samples. For completeness, the figure also shows the pressure dependence of the TO modes measured on the a-face epilayer (sample D). From a linear fit to the data, zero-pressure frequencies, ω_{i0}, and hydrostatic linear pressure coefficients, $a_i = (d\omega_i/dp)_{p=0}$, can be extracted for the ith phonon mode. The values obtained throughout this work (see below) are summarized in Table II.

A. Zone-center phonons: E_{2l}, E_{2h}, and TO modes

The pressure behavior of the zone-center E_{2l}, E_{2h}, and TO modes was previously investigated in Ref. 7, where the

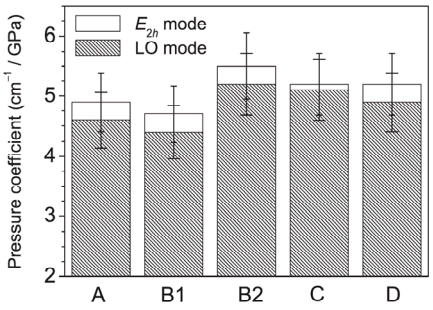

FIG. 7. Pressure coefficients for the E_{2h} and LO bands as obtained with high-pressure Raman measurements on all the samples investigated in this work. Error bars have been added to both plots.

softening of the E_{2l} was observed and the pressure coefficients of the TO modes were measured. However, the experimental pressure coefficients of the zone-center phonon modes of w-InN could be strongly affected by strain-related phenomena. Indeed, InN epilayers grown on sapphire or GaN/sapphire substrates usually display different degrees of compressive strain.[28,30] Also, the compressibility of the sapphire substrate is markedly lower than that of InN or GaN. As a consequence, the application of pressure on the InN epilayers could partly compensate the built-in compressive strains and give rise to reduced phonon pressure coefficients in comparison to relaxed material. In order to investigate the effect of built-in strains on the high-pressure Raman spectra of w-InN epilayers, we have investigated five different InN samples (see Table I). These measurements were partly motivated by the fact that, in spite of the small number of works dealing with the high-pressure vibrational properties of w-InN[4–7] and of w-GaN,[31–34] the dispersion of reported pressure-coefficient values in these two compounds is relatively high. For instance, in the case of the E_{2h} mode of w-InN, pressure coefficients ranging from 4.74 cm^{-1} GPa^{-1} (Ref. 6) up to 5.56 cm^{-1} GPa^{-1} (Ref. 4) have been reported.

Figure 7 shows the linear pressure coefficients measured for the zone-center E_{2h} modes in all the samples investigated in this work. Data for the LO modes (see discussion below) are also given. As can be seen in the figure, slightly different values are obtained in these epilayers. The observed variations, however, do not seem to display any clear trend with regard to the sample thickness and/or the residual strain of the epilayers (the latter can be readily evaluated from the zero-pressure E_{2h} frequency).[28,30] This can be seen by comparing the pressure coefficient of sample A, which exhibits the highest degree of compressive strain among all the samples investigated, with that of samples B1 and B2, with similar degrees of strain relaxation. Similarly, in spite of their sizably different degrees of strain, the pressure coefficients of the 5.7-μm-thick (relaxed) epilayer (sample C) and that of the a-face epilayer (sample D) are very similar. The observed variations are in all cases lower than the expected error of this type of measurements, which may be taken around $\sim$10%. Typical sources of error in these experiments may arise from pressure gradients within the gasket, which may be particularly important when the sample is located at a relatively large

distance from the ruby chips. Thus, we conclude that within the experimental error of the technique, the measured pressure coefficients are not affected by built-in compressive strains in the epilayers.

In the case of the w-InN epilayer grown on GaN/sapphire (sample A), strong peaks corresponding to the A_{1g} mode of sapphire and the E_{2h} and E_1(TO) modes of GaN also show up in the Raman spectra (see Fig. 3). We obtain a pressure coefficient of 2.0 ± 0.2 cm^{-1} GPa^{-1} for the A_{1g} mode of sapphire, in good agreement with previous results (2.1 cm^{-1} GPa^{-1} in Ref. 35). In the case of GaN, we measure a linear pressure coefficient of 3.7 and 3.9 cm^{-1} GPa^{-1} for the E_1(TO) and E_{2h} modes of GaN, respectively. These values agree well with the data published in the literature: for the E_1(TO) mode, values of 3.68 cm^{-1} GPa^{-1} (Ref. 31) and 3.94 cm^{-1} GPa^{-1} (Ref. 34) were measured on GaN single crystals and on 50-μm-thick GaN crystals grown on SiC, respectively. In the latter reference, a value of 3.3 cm^{-1} GPa^{-1} obtained with DFT calculations was also given. In the case of the E_{2h} mode of w-GaN, somewhat larger experimental pressure coefficients have been reported (4.17 cm^{-1} GPa^{-1} in Ref. 31 and 4.24 cm^{-1} GPa^{-1} in Ref. 34). In this case, the *ab initio* lattice-dynamical calculations predict a value of 3.6 cm^{-1} GPa^{-1},[34] only slightly lower than our experimental value. As in the case of the E_{2h} mode of w-InN discussed above, the present results seem to confirm that the dispersion of the pressure coefficients that can be found in the literature for w-GaN is not a consequence of strain but of the intrinsic experimental error of this type of measurements.

From the set of data obtained from all our measurements for the E_{2h} of w-InN, collected in the histogram of Fig. 7, and also from the measurements for the E_{2l} mode, we obtain best values for the linear pressure coefficients (a_i) and the corresponding mode Grüneisen parameters, $\gamma_i = B_0 a_i/\omega_{i0}$, of these two modes. Table II summarizes the values thus obtained. A value of $B_0 = 143$ GPa as obtained from the DFT calculations has been used to calculate γ_i. The table also shows data for the TO phonons as measured on the a-face epilayer (sample D). In addition, Table II displays ω_{i0} values for the different zone-center modes of w-InN. For the E_{2l} and E_{2h}, the data correspond to strain-free w-InN material (sample C). In the case of the TO phonons, the ω_{i0} values displayed in the table were obtained from a compressively strained epilayer (sample D). Thus, these values are somewhat larger than the experimental values expected in strain-free w-InN.

For comparison, Table II also shows the corresponding results of the DFT-LDA lattice-dynamical calculations described in Sec. III. As can be seen in the table, overall good agreement is found between the experimental and calculated a_i values for the E_2-symmetry modes. In particular, as discussed in Ref. 7, the DFT calculations predict the softening of the E_{2l} mode in w-InN. On the other hand, the calculated a_i values for the TO modes are only slightly lower than those obtained experimentally.

The relative pressure coefficients of the zone-center phonons, $d \ln \omega_i(p)/dp$, can be linked to those of the nearest-neighbor bond lengths involved in the different vibrations.[36] For instance, the relative pressure coefficients of E_1(TO) and E_{2h} phonons in w-InN are very similar (see Table II) because both modes involve vibrations in the hexagonal plane.

A direct comparison of the $d \ln \omega_i(p)/dp$ values obtained from the present measurements with those of w-GaN and w-AlN (see data in Ref. 36) confirms that, owing to the higher compressibility of w-InN, $d \ln \omega_i(p)/dp$ is sizable larger in this compound. In the particular case of the A_1(TO) mode, the higher $d \ln \omega_i(p)/dp$ value in w-InN in relation to w-GaN and w-AlN arises from the higher relative pressure coefficient of the bonds along the c axis.[36] In the case of the E_1(TO) and E_{2h} modes, the higher relative pressure coefficient of the bond lengths of w-InN within the hexagonal plane also gives rise to higher $d \ln \omega_i(p)/dp$ values in comparison to w-GaN and w-AlN.

Both the measured and calculated pressure coefficients for the A_1(TO) and the E_1(TO) modes, with ionic vibrations in nonequivalent directions, turn out to be very similar (see Table II). This result can be interpreted in terms of a small structural anisotropy in w-InN, i.e., a small deviation of the axial ratio c/a of the hexagonal cell in relation to its ideal value (1.633). This is in contrast to the case of w-AlN, which displays sizable degrees of structural anisotropy, as shown by DFT calculations and confirmed by the relatively large pressure dependence of the A_1-E_1 TO splitting.[36] In the case of w-InN, the fact that the A_1-E_1(TO) splitting barely depends on p points to a small pressure dependence of the structural anisotropy in this compound. This is in agreement with the structural data of Ueno *et al.*, who found a very small decrease of the c/a ratio in w-InN below 10 GPa.[19]

B. LO phonons with large wave vectors

Davydov *et al.*[10] showed that in Raman-scattering experiments on w-InN, A_1(LO) and E_1(LO) modes with large wave vectors are selectively excited. This observation, also reported in w-InN nanowires,[37] was attributed to a double-resonance excitation process that occurs due to the unusual conduction band of w-InN. Within this interpretation, the wave vector conservation law is broken due to scattering of electrons and holes from charged impurity centers. The wave vectors of the phonons are defined by the exciting photon energies, $E_{\rm exc}$, so that the magnitude of the phonon wave vector (q) is given by twice the wave vector in the electron-hole dispersion corresponding to an energy equal to $E_{\rm exc}$, i.e., $q = 2k$, with

$$E_{\rm exc} = E_g(p) + E_e(k) - E_h(k), \tag{1}$$

where $E_g(p)$ is the pressure-dependent band-gap energy of w-InN, and $E_e(k)$ [$E_h(k)$] is the conduction (light-hole or heavy-hole) band dispersion. According to the results of Ref. 10, the q values for A_1(LO) modes are determined by the electron-light hole dispersion, while those of E_1(LO) phonons are given by electron-heavy hole transitions.

One important implication of this model is that the LO phonon wave vector should be modified by pressure-induced changes of the electronic structure, which should have a bearing on the experimental pressure coefficients of the LO modes of w-InN. With regard to this, it can be realized that the pressure coefficient of the LO modes with large q values can be separated into two different contributions,

$$a_{\rm LO} = \frac{d\omega_{\rm LO}}{dp} + \delta a_{\rm DR}, \tag{2}$$

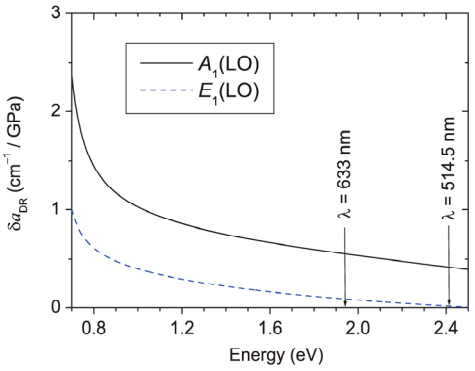

FIG. 8. (Color online) Change of the LO-phonon pressure coefficient, δa_{DR}, as a function of the excitation energy for A_1(LO) and E_1(LO) phonons. δa_{DR} takes into account pressure-induced variations of the frequency of LO modes with large wave vectors as a consequence of the double-resonance excitation of these modes.

where $d\omega_{LO}/dp$ refers to the conventional pressure dependence expected for optical phonons as a consequence of the compression of the lattice, while δa_{DR} takes into account pressure-induced variations of the LO frequency as a consequence of the wave-vector change induced by the double-resonance excitation.

Figure 8 illustrates the excitation energy dependence of δa_{DR} that predicts the model of Ref. 10 for the A_1(LO) and E_1(LO) phonons. Note that these curves have been obtained within a simplified framework, and, as a consequence, they should be taken only as a qualitative guide to illustrate the pressure behavior of the LO phonons of w-InN that might be expected from the selective excitation mechanism proposed in that work. To calculate the curves of Fig. 8 we first obtained the pressure-induced phonon wave-vector variation for a given E_{exc} value by taking pressure derivatives of the resonance condition Eq. (1). The pressure-induced wave-vector variation, dk/dp, was numerically evaluated, and the corresponding pressure derivatives for the A_1(LO) and E_1(LO) modes were subsequently calculated by using the numerical phonon dispersions obtained in Ref. 10. Note that pressure yields an overall uniform frequency increase of the optical phonon frequencies along the whole Brillouin zone, equivalent to that of zone-center phonons [i.e., $d\omega_{LO}(\Gamma)/dp$], with no important wave-vector dispersion variations. This can be seen in Fig. 1 by comparing the dispersion of optical phonons at 0 and 10 GPa. Note that, in contrast, the acoustic modes display sizable changes in the phonon dispersion as expected due to the stiffening of the elastic constants with increasing pressure.

Following Ref. 10, the electron and the light-hole band dispersions were calculated within a $\mathbf{k}\cdot\mathbf{p}$ approach that includes nonparabolicity effects, i.e., $E_e(k) = E_e\{\sqrt{\hbar^2k^2/2m_e^*(p)E_e + 1/4} - 1/2\}$ and $E_{lh}(k) = -E_{lh}\{\sqrt{\hbar^2k^2/2m_{lh}^*(p)E_{lh} + 1/4} - 1/2\}$, where E_e and E_{lh} are nonparabolicity coefficients and $m_e^*(p)$ and $m_{lh}^*(p)$ are pressure-dependent electron and light-hole effective masses at the Γ point. As in Ref. 10, a parabolic heavy-hole dispersion was assumed. For these calculations, pressure-induced changes of the light-hole and heavy-hole effective masses were neglected for simplicity. The pressure dependence of m_e^* can be modeled within a $\mathbf{k}\cdot\mathbf{p}$ formalism as

$$\frac{m_e^*(p)}{m_e^*(0)} = \frac{E_g(p)}{E_g(0)}, \tag{3}$$

where $m_e^*(0) = 0.07m_e$ is the ambient-pressure effective electron mass at Γ (Ref. 2), $E_g(p) = E_g(0) + a_g p$ is the pressure-dependent fundamental band-gap energy of w-InN, $E_g(0)$ is the ambient-pressure band-gap energy, and a_g is the pressure coefficient of the fundamental band-gap. In the case of undoped w-InN, $E_g(0) = 0.65$ eV and $a_g = 32$ meV/GPa,[25] which yields a relative pressure coefficient for the electron effective mass, $\gamma_m = (d\ln m_e^*(p)/dp)_{p=0}$, equal to 0.0492 GPa^{-1}. According to Eq. (3) and using the band-gap pressure coefficients obtained in Ref. 25 as a function of n_e, γ_m decreases to 0.0312 GPa^{-1} for $n_e = 1.6\times10^{19}$ cm^{-3} as in our most heavily doped sample. These values are similar to those determined with pressure-dependent mobility measurements on w-InN.[38]

According to the above considerations, the dk/dp changes arise from the pressure-induced increase of both the band-gap energy and the effective masses. The opening of the band-gap with hydrostatic pressure implies a reduction of the corresponding phonon-wave vector for a fixed photon energy, and, as a consequence, it yields positive δa_{DR} values. The increase in the electron effective mass yields the opposite effect. This is reflected in Fig. 8 for the case of undoped material, which shows that δa_{DR} is clearly larger around the fundamental band gap of w-InN, i.e., where nonparabolicity effects are less important. With increasing excitation energy, the reduction of δa_{DR} induced by the increase of effective mass counteracts the effect arising from the pressure-induced band-gap opening.

As can be seen in Fig. 8, the predicted variation of the linear pressure coefficients of the A_1(LO) and E_1(LO) phonons of w-InN induced by the doubly resonant selective excitation of both modes, $d\omega_{DR}/dp$, is larger for the A_1(LO) phonon. This occurs as a consequence of the lower magnitude of the wave vectors involved in the selective excitation of this mode.[10] As can be seen in the figure, this model predicts δa_{DR} values of around 1 and 2.5 cm^{-1} GPa^{-1} for the E_1(LO) and A_1(LO) modes, respectively, for excitation energies around the fundamental band gap of InN. With increasing excitation energy, the effect on the phonon pressure coefficients is rapidly reduced. For the photon energies corresponding to the wavelength employed in the present work (632.8 nm), the model predicts that $\delta a_{DR} \sim$ 0.5 cm^{-1} GPa^{-1} for the A_1(LO) mode and a value close to zero for the E_1(LO) phonon.

Bearing in mind the A_1-E_1 character of the LO bands, it can be concluded that the experimental pressure coefficients of the large wave-vector LO modes measured in this work are barely affected by the double-resonance mechanism, i.e., $a_{LO} \approx d\omega_{LO}/dp$. However, the present calculations do suggest that high-pressure Raman measurements on w-InN samples excited with markedly different wavelengths (for instance, longer wavelengths vs UV excitations) could give rise to sizable changes in the measured LO-phonon pressure

coefficients. Thus, this type of experiments could be highly informative with regard to the selective excitation of LO modes with large wave vectors in w-InN.

As in the case of the E_{2h} phonons, from the set of data obtained from all our measurements for the LO band (see Fig. 7) we obtain the average value for the linear pressure coefficient (a_i) and the corresponding mode Grüneisen parameter, $\gamma_i = B_0 a_i/\omega_{i0}$, of this mode. The value thus obtained is shown in Table II. Following the previous considerations, we conclude that the effect of the double-resonance mechanism on this value, measured with 632.8 nm radiation, is within the experimental error of this type of high-pressure experiments.

C. Long-wavelength L^- coupled modes

In polar semiconductors, free carriers couple with LO phonons and give rise to the L^+ and L^- LO-plasmon coupled modes (LOPCMs). Numerous studies have been reported on inelastic light scattering by LOPCMs in III–V semiconductors, and different models have been developed to analyze the LOPCM behavior.[39–41] The analysis of the LOPCM peaks is widely employed to evaluate in a contactless and nondestructive manner the free-carrier density of the samples. However, only a few reports have been devoted to investigate the pressure dependence of the LOPCMs.[12,13]

In the case of the heavily doped, n-type w-InN sample studied in this work (sample B2), in addition to the E_2 and LO modes, a peak corresponding to the L^- LOPCM also shows up in the Raman spectra (see Fig. 4). It has been shown that wave vector is conserved in Raman scattering by the L^- coupled-modes in high-quality w-InN. These modes exhibit the usual behavior of the low-energy branch of the long-wavelength ($q \sim 0$) LOPCMs, i.e., they increase in frequency and phononlike character with increasing electron density.[11,29] The dependence of the L^- mode on carrier concentration can be satisfactorily described with the standard dielectric model,[39,40] and line-shape fits to the L^- peak allow one to extract free-electron density values in good agreement with Hall-effect measurements.[11,28] In contrast, L^+ bands do not show up in the Raman spectra, which may be attributed to the low Raman-scattering efficiencies of this mode in the III-nitrides as well as to electron density inhomogeneities.[11] It should be noted that in the last decade there was some controversy with regard to the simultaneous observation of LO phonons and L^- coupled modes in w-InN. In fact, some authors tentatively explained the appearance of the LO peaks in doped samples through $q \neq 0$ LOPCMs excited by breakdown of the Raman selection rules[42–44] or by a Fano-type interference between the LO mode and the continuum electronic states.[45] According to the results of Refs. 10 and 11, the simultaneous observation of LO and L^- modes in doped material is a consequence of the different wave vectors involved: large wave vectors in the case of the A_1-E_1 LO modes due to the double-resonance excitation, and $q \sim 0$ wave vectors for the L^- coupled modes.

The aim of this section is to study the pressure dependence of the long-wavelength L^- mode in sample B2 ($n_e = 1.6 \times 10^{19}$ cm^{-3}) in order to evaluate the electron effective mass of w-InN as a function of pressure. Figure 9 shows the frequency

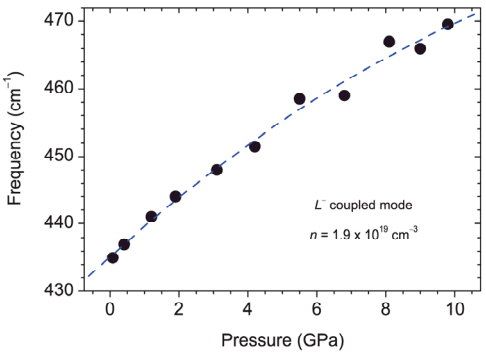

FIG. 9. (Color online) Frequency of the L^- coupled mode (solid dots) as obtained with high-pressure Raman measurements on a heavily doped n-type w-InN epilayer (sample B2). The dashed line serves as a guide to the eye.

of the L^- peak as a function of applied hydrostatic pressure (solid dots) as obtained from the high-pressure measurements on sample B2. As can be seen in the figure, the L^- mode exhibits the expected blueshift with increasing hydrostatic pressure. In the low-pressure regime, below 4 GPa, the linear pressure coefficient of the L^- is ~4.3 cm^{-1}/GPa, which is markedly lower than that of the TO and LO phonons (see Table II). Thus, it is seen that in spite of its strong phononlike character, the L^- frequency reflects the expected increase of the electron effective mass with increasing pressure. At higher pressures, the figure shows a slight saturation of the linear dependence that we tentatively attribute to a reduction of the free-electron density by compensating defects generated during the pressurization of the sample.

To evaluate the electron effective mass, $m_e^*(p)$, from the Raman spectra we first note that the frequency of the long-wavelength L^- mode at a given pressure depends on the electron density, on the frequency of the zone-center TO and LO phonons and on $m_e^*(p)$. Thus, given that the pressure behavior of the TO and LO modes is already known, $m_e^*(p)$ at a given p value can be obtained from the frequency of the $q \sim 0$ L^- mode by using the expression[39]

$$\omega_-^2 = \tfrac{1}{2}\{(\omega_p^2 + \omega_{\mathrm{LO}}^2) - [(\omega_p^2 - \omega_{\mathrm{LO}}^2)^2 - 4\omega_p^2(\omega_{\mathrm{TO}}^2 - \omega_{\mathrm{LO}}^2)]^{(1/2)}\}, \quad (4)$$

where $\omega_p^2(p) = 4\pi e^2 n_e/\epsilon_\infty m_e^*(p)$ is the pressure-dependent plasma frequency of the free carriers, and $\epsilon_\infty = 6.7$ is the high-frequency dielectric constant of w-InN.[46] For simplicity, we neglect the pressure dependence of ϵ_∞. In Eq. (4) ω_{TO} and ω_{LO} correspond to the zone-center TO and LO frequencies, respectively. The pressure dependence of both modes has been studied in the previous sections.

Then $m_e^*(p)$ values are estimated from the experimental L^- frequencies and Eq. (4) by assuming that n_e does not depend on p. Figure 10 (solid dots) shows the m_e^* values thus obtained. Around ambient pressure, the $m_e^*(p)$ values obtained from the L^- frequency are around $0.1m_e$, only slightly lower than the value extracted from a two-band $\mathbf{k}\cdot\mathbf{p}$ Kane model for w-InN

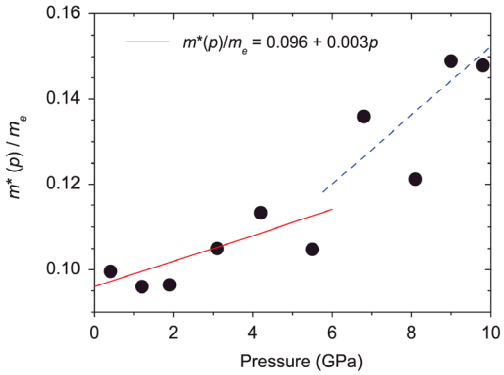

FIG. 10. (Color online) Electron effective mass values obtained from the frequency of the L^- mode as a function of pressure (solid dots). The solid line shows the result of a linear fit to the experimental data below 6 GPa, while the dashed line serves as a guide to the eye to the experimental points obtained at higher hydrostatic pressures.

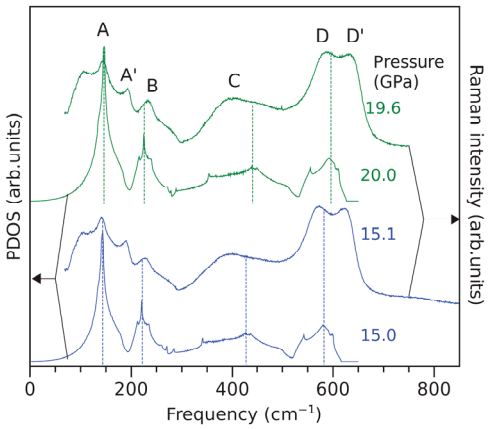

FIG. 11. (Color online) Raman spectra of rocksalt InN at 15.1 and 19.6 GPa. For comparison, calculated one-phonon density of states (PDOS) curves at 15 and 20 GPa for rs-InN are also shown.

with $n_e = 1.6 \times 10^{19}$ cm^{-3} ($m_e^* = 0.12m_e$).[28,47] In Ref. 48, line-shape fits to the L^- coupled mode of w-InN were carried out to estimate the ambient-pressure effective mass in samples with n_e just below 10^{19} cm^{-3}. Whereas the value obtained in that work ($m_e^* = 0.05m_e$) is clearly lower than that expected in heavily doped material, our result seems to better reflect the strong nonparabolicity of w-InN.[47]

As can be seen in Fig. 10, in the low-pressure regime ($p <$ 6 GPa) the values of m_e^* obtained from Eq. (4) tend to increase linearly, in agreement with that expected from a $\mathbf{k}\cdot\mathbf{p}$ approach as discussed above [see Eq. (3)]. In contrast, at larger pressure values the figure shows a superlinear increase that most probably reflects a reduction of n_e in the pressurized sample due to the generation of compensating defects. A linear fit to the m_e^* values obtained below 6 GPa yields $m_e^*(p) = (0.096 + 0.003p)m_e$, which implies a relative pressure coefficient $\gamma_m = 0.031 \pm 0.01$ GPa^{-1}. This value is in excellent agreement with that obtained with Eq. (3) together with the data of Ref. 25 ($\gamma_m = 0.0312$ GPa^{-1} at $n_e = 1.6 \times 10^{19}$ cm^{-3}) and with that expected from the experimental results of Ref. 38, where a slightly larger value of $\gamma_m = 0.034$ GPa^{-1} was measured in samples with lower electron densities ($n_e = 2.4 \times 10^{18}$ cm^{-3}). Note, however, the large error associated to the determination of γ_m from the analysis of the L^- frequencies, suggesting that the nearly perfect match between the derived γ_m value and $\mathbf{k}\cdot\mathbf{p}$ theory may be fortuitous. In addition, it should be borne in mind that the pressure dependence of ϵ_∞ has been neglected for the present analysis. According to DFT-LDA calculations of the refractive index of w-InN as a function of pressure,[49] ϵ_∞ might display a sizable large (negative) pressure coefficient, much larger than that of w-GaN or w-AlN. Such pressure dependence would imply that the m_e^* values obtained from the frequency of the L^- modes have been underestimated. An experimental measurement of the pressure behavior of ϵ_∞ would be necessary in order to obtain a more reliable γ_m value extracted from the analysis of the L^- mode.

D. Raman scattering in rs-InN

Previous high-pressure Raman-scattering investigations have shown that, above ~13 GPa, new bands that can be attributed to the rocksalt phase emerge in the Raman spectra of InN.[5,6] This can be observed in Fig. 5 for the case of sample C. In the spectrum obtained at 12.1 GPa, it can be seen that the phonons of w-InN coexist with new bands that are assigned to rs-InN. Note, however, that, as already mentioned, the phase transition is only complete around 17 GPa as observed by absorption spectroscopy.[25] The new Raman bands, which are labeled A, A′, B, C, D, and D′ in Fig. 5, totally dominate the Raman spectra well above the phase transition pressure. The Raman spectra plotted in the figure are very similar to those of previous works.[5,6] In Ref. 5, were Raman measurements of rs-InN were performed up to 50 GPa, it was found that features D and D′ merge above 30 GPa. It must be noted that similar Raman spectra were also measured in GaN[33] and AlN[36] above 30 and 20 GPa, respectively.

In crystalline materials with rocksalt structure one expects that first-order Raman modes are forbidden due to Raman selection rules. Thus, one would expect relatively weak bands arising from second-order modes. In the case of rs-InN, the frequency position of the observed features suggests that the spectra are dominated by first-order scattering, activated by the relaxation of the selection rules. We plot in Fig. 11 Raman spectra of rs-InN (sample C) at two different pressure values (15.1 and 19.6 GPa), together with calculated one-phonon DOS curves at similar pressure conditions (15 and 20 GPa). As can be seen in the figure, a remarkable qualitative agreement is found between the experimental data and the calculated curves, thus confirming that disorder-activated first-order modes dominate the Raman spectra of rs-InN after the wurtzite-to-rocksalt transformation. It is concluded that poorly crystalline (amorphized) rs-InN is formed after the phase transition.

Following the results of Fig. 11 and the corresponding phonon dispersion curves for rs-InN (see also Fig. 2), features A and A′ can be attributed to disorder-activated transverse

TABLE IV. Zero-pressure frequency (ω_{i0}, linear pressure coefficient ($a_i = d\omega_i/dp$) and mode Grüneisen parameters ($\gamma_i = a_i B_0/\omega_{i0}$) for the different features that show up in the Raman spectra of rs-InN. A bulk modulus of 186 GPa was used to compute γ_i.

Feature (i)	Assignment	ω_{i0} (cm^{-1})	a_i (cm^{-1}GPa^{-1})	γ_i
A	DATA	124.0	1.2	1.8
A′	DATA	169.8	1.3	1.42
B	DALA	204.1	1.6	1.46
C	DATO	380.7	3.9	1.90
D	DALO	498.8	4.7	1.75
D′	DALO	567.2	3.7	1.21

acoustic (DATA) modes, while feature B is assigned to longitudinal acoustic (DALA) modes. On the other hand, the transverse optical branches give rise to a very broad band in the 1-PDOS, centered only slightly above 400 cm^{-1} (Fig. 2). Thus, we assign feature C to disorder-activated transverse optical (DATO) modes. With regard to the LO branch, the *ab initio* lattice-dynamical calculations yield a much narrower feature in the one-phonon DOS which is centered just below 600 cm^{-1} at 15 GPa. The pressure behavior of this feature resembles that of bands D and D′ observed experimentally. Bearing in mind the limitations of the *ab initio* calculations for the determination of LO frequencies, these two bands can be assigned to disorder-activated LO (DALO) modes.

The frequency of features A to D′, as obtained from the Raman spectra of sample C up to 20 GPa, is plotted with triangles in Fig. 6. Data obtained in the subsequent downstroke cycle at pressure values below the wurtzite-to-rocksalt transition pressure have also been included in the figure (see the next section for details). Table IV shows the resulting ω_{i0} and a_i values as obtained from a linear regression to the data of Fig. 6. In the case of bands A, A′, and B, relatively low a_i values are measured (1.2–1.6 cm^{-1} GPa^{-1}), which is a consequence of the acoustic nature of these bands. In the case of the optical features (C, D, and D′), larger a_i values are obtained (3.7–4.7 cm^{-1} GPa^{-1}). These values are consistently higher than those reported in Ref. 5, where a_i values below 3 cm^{-1} GPa^{-1} were measured. We believe that this difference is a consequence of the different pressure ranges investigated in both works, together with the expected reduced compressibility of the material with increasing pressure. In the case of Ref. 5, the wide pressure range investigated, up to 50 GPa, could have yielded underestimated linear pressure coefficients. Note that, in contrast, the a_i values measured in the present work are consistent with the DFT-LDA calculations for the zone-center TO and LO modes of rs-InN at 15 GPa (see Table III). Although the pressure behavior of the DATO and DALO bands is not expected to be exactly coincident with that of the zone-center optical modes, the consistency between the calculated values and the a_i values measured for features C, D, and D′ further suggests that underestimated a_i values were obtained in Ref. 5.

E. Rocksalt-to-wurtzite backtransformation

Raman measurements in the downstroke cycle were also performed on sample C in order to investigate the backtransformation of the rocksalt phase to the wurtzite phase. Figure 12 shows Raman spectra obtained at 5.7, 3.0, and 2.3 GPa in the downstroke cycle and an additional spectrum (upper curve) obtained after increasing the pressure up to 3.0 GPa. The figure clearly shows that the rocksalt phase is metastable down to pressure values as low as 3.0 GPa. At lower pressures (2.3 GPa), the rocksalt-to-wurtzite backtransition is observed, and new features (labeled O, E, F, G, and H) appear in the Raman spectra. In particular, it should be noted that, for similar pressure values, feature H in the backtransited wurtzite phase is located at higher frequencies than feature D′ in the rocksalt phase (see also Fig. 6). Similarly, the relative intensity between features H and G is markedly different to that observed between bands D and D′ in rs-InN (see also the upper curve of Fig. 13 corresponding to backtransited w-InN at 9.8 GPa).

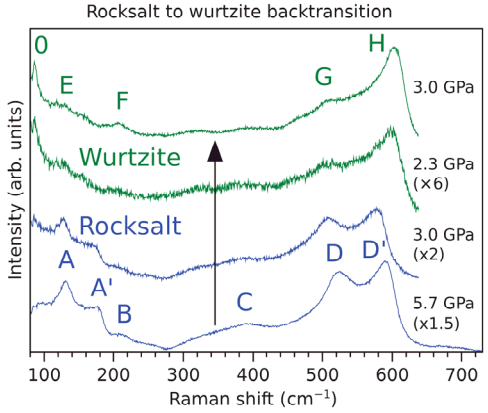

FIG. 12. (Color online) Raman spectra of rs-InN at 5.7 and 3.0 GPa and of w-InN at 2.3 GPa obtained during the down-stroke cycle, and of w-InN at 3.0 GPa after a subsequent up-stroke cycle.

In Fig. 6 we have plotted the frequency position of all the features that show up in the Raman spectra of disordered w-InN as measured in the downstroke cycle and also during a subsequent upstroke cycle up to ∼10 GPa (open circles). As can be seen in the figure, the pressure behavior of features O, G, and H closely follows that of the E_{2l}, E_{2h}, and LO modes of crystalline w-InN, respectively. This is confirmed in Fig. 13, where we have plotted Raman spectra of backtransformed (disordered) w-InN at 0 and 9.8 GPa, together with the calculated 1-PDOS of w-InN at very similar pressure values (0 and 10 GPa, respectively). Similar spectra were observed after a pressure cycle of 20 GPa on InN samples[50] and also in highly disordered material subject to a high-dose ion-beam implantation process.[51] The observed bands can be attributed to first-order modes activated by disorder in poorly crystalline (amorphized) w-InN. As can be seen in Fig. 13, features G and H resemble the 1-PDOS curves at the corresponding frequency regions, which are mainly dominated by E_{2h} modes and LO modes, respectively. In turn, feature O is found to redshift with increasing hydrostatic pressure (see Fig. 13), as occurs in the case of the E_{2l} branch and also of TA modes from high-symmetry and high-wave-vector points of

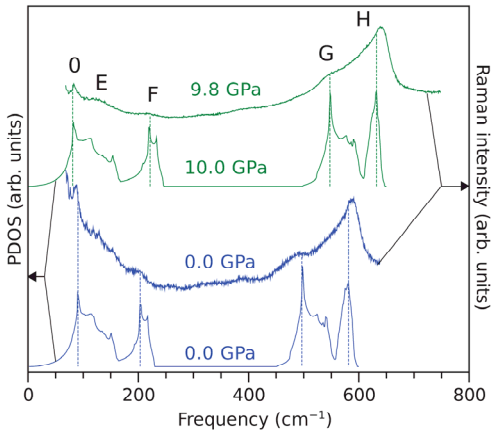

FIG. 13. (Color online) Raman spectra of poorly crystalline wurtzite InN after the rocksalt-to-wurtzite backtransition at ambient pressure and 9.8 GPa. For comparison, calculated one-phonon density of states (PDOS) curves at 0 and 10 GPa for w-InN are also shown.

the Brillouin zone in III–V semiconductors.[23,24] This band probably contains contributions from E_{2l} modes and also from TA modes along the entire Brillouin zone, which are activated by disorder in the backtransformed, poorly crystalline w-InN sample.

As can be seen in Fig. 13, the frequency and pressure behavior of features E and F is fairly reproduced in the calculated 1-PDOS curves. Following the data of this figure and also the phonon dispersion curves for w-InN as a function of pressure (see Fig. 1), it can be concluded that features E and F most likely arise from first-order DATA and DALA modes, respectively. Contributions to these bands from the E_{2l} and the (silent) B_{1l} branches cannot be ruled out.

The Raman-scattering results on backtransformed w-InN are similar to those obtained in AlN,[36] where the rocksalt-to-wurtzite backtransition pressure was found to occur around 1.3 GPa. In that work, taking into account that the wurtzite-to-rocksalt phase transition is completed only above 30 GPa, the return to the disordered wurtzite phase was tentatively attributed to an incomplete transition during the upstroke cycle arising from the nucleation of wurtzite microcrystals still present at the maximum applied pressures (25 GPa). Such an interpretation cannot be directly extrapolated to the present work, since the phase transition is expected to be complete at the maximum applied pressure (~20 GPa). In both cases, it would be highly interesting to investigate whether the backtransition occurs in samples that have been subject to very large hydrostatic pressures, i.e., to pressure values much higher than those corresponding to the wurtzite-to-rocksalt phase transition.

V. SUMMARY AND CONCLUSIONS

We have performed high-pressure Raman-scattering measurements on wurtzite InN (w-InN) epilayers grown by plasma-assisted molecular beam epitaxy. The possible effect of residual strains on the measured pressure coefficients has been evaluated by studying different w-InN epilayers with different levels of built-in residual strain. The observed variation in the measured pressure coefficients for the E_{2h} and LO bands for all the samples investigated has been found to be lower than the typical error associated to this type of measurement. Thus, we conclude that the pressure coefficients extracted from the high-pressure Raman measurements are not affected by strain-related phenomena.

Pressure coefficients and the corresponding Grüneisen parameters have been measured for the zone-center E_{2l}, E_{2h}, A_1(TO), and E_1(TO) phonons of w-InN. The experimental data have been compared with theoretical results obtained from *ab initio* lattice-dynamical calculations as a function of hydrostatic pressure, with good agreement between the experimental and calculated pressure coefficients. The similar pressure coefficients obtained for the A_1(TO) and E_1(TO) modes suggest a small change in the anisotropy of w-InN with increasing pressure.

It has recently been shown that the LO modes of w-InN exhibit a strong wave-vector dependence that has been attributed to a selective resonance effect.[10] Given that the proposed double-resonance mechanism could affect the pressure behavior of the LO band, we have performed a calculation to evaluate the change of the pressure coefficient for the $q \neq 0$ LO modes as a function of the energy of the excitation radiation. The calculations reveal that the LO modes might display increased pressure coefficients for excitation energies close to the band gap of w-InN. High-pressure Raman experiments with different excitation wavelengths could be highly informative with regard to the double-resonance mechanism proposed in Ref. 10. In the case of visible or near-infrared radiation, the calculations suggest that no important pressure coefficient variations may be expected. The experimental pressure coefficients obtained for the A_1-E_1(LO) band with 632.8-nm excitation are in good agreement with the results of *ab initio* calculations for the A_1(LO) band, which confirms that the double-resonance mechanism does not significantly affect the pressure behavior of the LO band at these excitation conditions.

In w-InN samples with high levels of free electron concentration ($n_e = 1.6 \times 10^{19}$ cm^{-3}), the L^- coupled mode shows up in the Raman spectra. We have studied the pressure dependence of this mode, and we have used its frequency to evaluate the electron effective mass in w-InN as a function of pressure in the low-pressure regime. We have found a relative pressure coefficient for the electron effective mass [$\gamma_m = (d \ln m_e^*(p)/dp)_{p=0}$] equal to 0.031 ± 0.01 GPa^{-1}, in very good agreement with $\mathbf{k} \cdot \mathbf{p}$ theory. These results show the usefulness of Raman scattering to probe pressure-induced changes of the electronic structure of polar semiconductors.

For pressures above ~13 GPa, peaks from rocksalt InN (rs-InN) show up in the Raman spectra. The spectra have been interpreted in terms of *ab initio* lattice-dynamical calculations as a function of pressure. We conclude that the features that appear in the Raman spectra of rs-InN can be assigned to disorder-activated first-order modes. Raman measurements in the downstroke cycle reveal that the rocksalt phase is

metastable down to pressure values as low as 3.0 GPa. Around 2.3 GPa, we find that the rocksalt-to-wurtzite backtransition occurs. The Raman spectrum of the backtransformed w-InN phase is dominated by disorder-activated first-order modes, as revealed by comparison of the Raman spectra with the calculated one-phonon density of states of w-InN.

ACKNOWLEDGMENTS

Work was supported by the Spanish Ministerio de Economía y Competitividad through Projects MAT2010-16116, MAT2010-21270-C04-04 and MALTA Consolider Ingenio 2010 (CSD2007-00045).

*Corresponding author: jibanez@ictja.csic.es

[1]T. D. Veal, C. F. McConville, and W. J. Schaff (eds.), *Indium Nitride and Related Alloys* (CRC Press/Taylor Francis, Boca Raton, FL, 2010).
[2]J. Wu, J. Appl. Phys. **106**, 011101 (2009).
[3]T. Suski and W. Paul (eds.), *High Pressure in Semiconductor Physics I and II*, Semiconductors and Semimetals Vols. 54 and 55 (Academic Press, New York, 1998).
[4]C. Pinquier, F. Demangeot, J. Frandon, J. W. Pomeroy, M. Kuball, H. Hubel, N. W. A. van Uden, D. J. Dunstan, O. Briot, B. Maleyre, S. Ruffenach, and B. Gil, Phys. Rev. B **70**, 113202 (2004).
[5]C. Pinquier, F. Demangeot, J. Frandon, J. C. Chervin, A. Polian, B. Couzinet, P. Munsch, O. Briot, S. Ruffenach, B. Gil, and B. Maleyre, Phys. Rev. B **73**, 115211 (2006).
[6]L. D. Yao, S. D. Luo, X. Shen, S. J. You, L. X. Yang, S. J. Zhang, S. Jiang, Y. C. Li, J. Liu, K. Zhu, Y. L. Liu, W. Y. Zhou, L. C. Chen, C. Q. Jin, R. C. Yu, and S. S. Xie, J. Mater. Res. **25**, 2330 (2010).
[7]J. Ibáñez, F. J. Manjón, A. Segura, R. Oliva, R. Cuscó, R. Vilaplana, T. Yamaguchi, Y. Nanishi, and L. Artús, Appl. Phys. Lett. **99**, 011908 (2011).
[8]S. Uehara, T. Masamoto, A. Onodera, M. Ueno, O. Shimomura, and K. Takemura, J. Phys. Chem. Solids **58**, 2093 (1997).
[9]M.-Y. Duan, L. He, M. Xu, M.-Y. Xu, S. Xu, and K. K. Ostrikov, Phys. Rev. B **81**, 033102 (2010).
[10]V. Yu. Davydov, A. A. Klochikhin, A. N. Smirnov, I. Yu. Strashkova, A. S. Krylov, Hai Lu, W. J. Schaff, H.-M. Lee, Y.-L. Hong, and S. Gwo, Phys. Rev. B **80**, 081204(R) (2009).
[11]R. Cuscó, J. Ibáñez, E. Alarcón-Lladó, L. Artús, T. Yamaguchi, and Y. Nanishi, Phys. Rev. B **79**, 155210 (2009).
[12]S. Ernst, A. R. Goñi, K. Syassen, and M. Cardona, J. Phys. Chem. Sol. **56**, 567 (1995).
[13]S. Ernst, A. R. Goñi, K. Syassen, and M. Cardona, Phys. Rev. B **53**, 1287 (1996).
[14]Y. C. Lin, C. H. Chiu, W. C. Fan, C. H. Chia, S. L. Yang, D. S. Chuu, M. C. Lee, W. K. Chen, W. H. Chang, and W. C. Chou, J. Appl. Phys. **102**, 123510 (2007).
[15]ABINIT is a common project of the Université Catholique de Louvain, Corning Incorporated, and other contributors, http://www.abinit.org; X. Gonze, J.-M. Beuken, R. Caracas, F. Detraux, M. Fuchs, G.-M. Rignanese, L. Sindic, M. Verstraete, G. Zerah, F. Jollet *et al.*, Comput. Mater. Sci. **25**, 478 (2002).
[16]S. Goedecker, M. Teter, and J. Hütter, Phys. Rev. B **54**, 1703 (1996).
[17]N. Troullier and J. L. Martins, Phys. Rev. B **43**, 1993 (1991).
[18]M. F. Wu, S. Q. Zhou, A. Vantomme, Y. Huang, H. Wang, and H. Yang, J. Vac. Sci. Technol. A **24**, 275 (2006).
[19]M. Ueno, M. Yoshida, A. Onodera, O. Shimomura, and K. Takemura, Phys. Rev. B **49**, 14 (1994).
[20]J. Serrano, A. Bosak, M. Krisch, F. J. Manjón, A. H. Romero, N. Garro, X. Wang, A. Yoshikawa, and M. Kuball, Phys. Rev. Lett. **106**, 205501 (2011), and references therein.
[21]P. Giannozzi, S. de Gironcoli, P. Pavone, and S. Baroni, Phys. Rev. B **43**, 7231 (1991).
[22]X. Gonze and C. Lee, Phys. Rev. B **55**, 10355 (1997).
[23]B. A. Weinstein, Solid State Commun. **24**, 595 (1977).
[24]E. V. Yakovenko, M. Gauthier, and A. Polian, JETP **98**, 981 (2004).
[25]J. Ibáñez, A. Segura, B. García-Domene, R. Oliva, F. J. Manjón, T. Yamaguchi, Y. Nanishi, and L. Artús, Phys. Rev. B **86**, 035210 (2012).
[26]J. Serrano, A. H. Romero, F. J. Manjón, R. Lauck, M. Cardona, and A. Rubio, Phys. Rev. B **69**, 094306 (2004).
[27]R. Cuscó, J. Ibáñez, N. Domènech-Amador, L. Artús, J. Zúñiga-Pérez, and V. Muñoz-Sanjosé, J. Appl. Phys. **107**, 063519 (2010).
[28]R. Cuscó, E. Alarcón-Lladó, J. Ibáñez, T. Yamaguchi, Y. Nanishi, and L. Artús, J. Phys.: Condens. Matter **21**, 415801 (2009).
[29]R. Cuscó, J. Ibáñez, E. Alarcón-Lladó, L. Artús, T. Yamaguchi, and Y. Nanishi, Phys. Rev. B **80**, 155204 (2009).
[30]X. Wang, S.-B. Che, Y. Ishitani, and A. Yoshikawa, Appl. Phys. Lett. **89**, 171907 (2006).
[31]P. Perlin, C. Jauberthie-Carillon, J. P. Itie, A. San Miguel, I. Grzegory, and A. Polian, Phys. Rev. B **45**, 83 (1992).
[32]P. Perlin, T. Suski, J. W. Ager III, G. Conti, A. Polian, N. E. Christensen, I. Gorczyca, I. Grzegory, E. R. Weber, and E. E. Haller, Phys. Rev. B **60**, 1480 (1999).
[33]M. P. Halsall, P. Harmer, P. J. Parbrook, and S. J. Henley, Phys. Rev. B **69**, 235207 (2004).
[34]A. R. Goñi, H. Siegle, K. Syassen, C. Thomsen, and J.-M. Wagner, Phys. Rev. B **64**, 035205 (2001).
[35]G. H. Watson, W. B. Daniels, and C. S. Wang, J. Appl. Phys. **52**, 956 (1981).
[36]F. J. Manjón, D. Errandonea, A. H. Romero, N. Garro, J. Serrano, and M. Kuball, Phys. Rev. B **77**, 205204 (2008).
[37]N. Doménech-Amador, R. Cuscó, L. Artus, T. Stoica, and R. Calarco, Nanotechnology **23**, 085702 (2012).
[38]I. Gorczyca, J. Plesiewicz, L. Dmowski, T. Suski, N. E. Christensen, A. Svane, C. S. Gallinat, G. Koblmueller, and J. S. Speck, J. Appl. Phys. **104**, 013704 (2008).
[39]M. Cardona and G. Güntherodt, *Light Scattering in Solids IV*, Topics in Applied Physics (Springer-Verlag, Berlin, 1984), Vol. 54.
[40]L. Artús, R. Cuscó, J. Ibáñez, N. Blanco, and G. González-Díaz, Phys. Rev. B **60**, 5456 (1999).
[41]J. Ibáñez, R. Cuscó, and L. Artús, Phys. Status Solidi B **223**, 715 (2001).
[42]A. Kasic, M. Schubert, Y. Saito, Y. Nanishi, and G. Wagner, Phys. Rev. B **65**, 115206 (2002).
[43]F. Demangeot, C. Pinquier, J. Frandon, M. Gaio, O. Briot, B. Maleyre, S. Ruffenach, and B. Gil, Phys. Rev. B **71**, 104305 (2005).
[44]J. S. Thakur, D. Haddad, V. M. Naik, R. Naik, G. W. Auner, H. Lu, and W. J. Schaff, Phys. Rev. B **71**, 115203 (2005).

[45]T. Inushima, M. Higashiwaki, and T. Matsui, Phys. Rev. B **68**, 235204 (2003).
[46]A. Kasic, E. Valcheva, B. Monemar, H. Lu, and W. J. Schaff, Phys. Rev. B **70**, 115217 (2004).
[47]J. Wu, W. Walukiewicz, W. Shan, K. M. Yu, J. W. Ager, E. E. Haller, H. Lu, and W. J. Schaff, Phys. Rev. B **66**, 201403 (2002).
[48]J. G. Kim, Y. Kamei, N. Hasuike, H. Harima, K. Kisoda, K. Sasamoto, and A. Yamamoto, Phys. Satatus Solidi C **7**, 1887 (2010).
[49]N. E. Christensen and I. Gorczyca, Phys. Rev. B **50**, 4397 (1994).
[50]S. V. Ovsyannikov, V. V. Shchennikov, A. E. Karkin, A. Polian, O. Briot, S. Ruffenach, B. Gil, and M. Moret, Appl. Phys. Lett. **97**, 032105 (2010).
[51]V. Yu. Davydov, A. A. Klochikhin, M. B. Smirnov, V. V. Etsev, V. D. Petrikov, I. A. Abroyan, A. I. Titov, I. N. Goncharuk, A. N. Smirnov, V. V. Mamutin, S. V. Ivanov, and T. Inushima, Phys. Status Solidi B **216**, 779 (1999).

4.4. References

[1] J. Wu, J. Appl. Phys. **106**, 011101 (2009).
[2] A. Sarua, M. Kuball, and J.E.V. Nostrand, Appl. Phys. Lett. **81**, 1426 (2002).
[3] F. Demangeot, J. Frandon, P. Baules, F. Natali, F. Semond, and J. Massies, Phys. Rev. B **69**, 155215 (2004).
[4] J. Gleize, M.A. Renucci, J. Frandon, E. Bellet-Amalric, and B. Daudin, J. Appl. Phys. **93**, 2065 (2003).
[5] R. Oliva, J. Ibáñez, L. Artús, R. Cuscó, J. Zúñiga-Pérez, and V. Muñoz-Sanjosé, J. Appl. Phys. **113**, 053514 (2013).
[6] N. Domènech-Amador, R. Cuscó, L. Artús, T. Yamaguchi, and Y. Nanishi, Phys. Rev. B **83**, 245203 (2011).
[7] N. Domènech-Amador, R. Cuscó, L. Artús, T. Stoica, and R. Calarco, Nanotechnology **23**, 085702 (2012).
[8] V.Y. Davydov, V.V. Emtsev, I.N. Goncharuk, A.N. Smirnov, V.D. Petrikov, V.V. Mamutin, V.A. Vekshin, S.V. Ivanov, M.B. Smirnov, and T. Inushima, Appl. Phys. Lett. **75**, 3297 (1999).
[9] Z.G. Qian, W.Z. Shen, H. Ogawa, and Q.X. Guo, J. Phys. Condens. Matter **16**, R381 (2004).
[10] J. Serrano, A. Bosak, M. Krisch, F.J. Manjón, A.H. Romero, N. Garro, X. Wang, A. Yoshikawa, and M. Kuball, Phys. Rev. Lett. **106**, 205501 (2011).
[11] G. Kaczmarczyk, A. Kaschner, S. Reich, A. Hoffmann, C. Thomsen, D.J. As, A.P. Lima, D. Schikora, K. Lischka, R. Averbeck, and H. Riechert, Appl. Phys. Lett. **76**, 2122 (2000).
[12] C. Pinquier, F. Demangeot, J. Frandon, J.W. Pomeroy, M. Kuball, H. Hubel, N.W.A. van Uden, D.J. Dunstan, O. Briot, B. Maleyre, S. Ruffenach, and B. Gil, Phys. Rev. B **70**, 113202 (2004).
[13] C. Pinquier, F. Demangeot, J. Frandon, J.-C. Chervin, A. Polian, B. Couzinet, P. Munsch, O. Briot, S. Ruffenach, B. Gil, and B. Maleyre, Phys. Rev. B **73**, 115211 (2006).
[14] V.Y. Davydov, A.A. Klochikhin, A.N. Smirnov, I.Y. Strashkova, A.S. Krylov, H. Lu, W.J. Schaff, H.-M. Lee, Y.-L. Hong, and S. Gwo, Phys. Rev. B **80**, 081204 (2009).
[15] A. Smekal, Naturwissenschaften **11**, 873 (1923).
[16] C.V. Raman, Nature **121**, 501 (1928).
[17]Naturwissenschaften **16**, 557 (1928).
[18] Cardona, M and Güntherodt, G, *Light Scattering in Solids II: Basic Concepts and Instrumentation* (Springer, New York, 1982).
[19] P.Y. Yu and M. Cardona, *Fundamentals of Semiconductors* (Springer Berlin Heidelberg, Berlin, Heidelberg, 2010).
[20] F. Seitz, *The Modern Theory of Solids* (Dover Pubns, New York, 1987).
[21] G.J. Ackland, Rep. Prog. Phys. **64**, 483 (2001).
[22] R.A. Cowley, Adv. Phys. **29**, 1 (1980).
[23] G. Vaitheeswaran, V. Kanchana, X. Zhang, Y. Ma, A. Svane, and S.N. Kaul, J. Phys. Condens. Matter **24**, 075402 (2012).
[24] M. Marqués, J. Osorio, R. Ahuja, M. Flórez, and J.M. Recio, Phys. Rev. B **70**, 104114 (2004).
[25] J. Pellicer-Porres, D. Martínez-García, A. Segura, P. Rodríguez-Hernández, A. Muñoz, J.C. Chervin, N. Garro, and D. Kim, Phys. Rev. B **74**, 184301 (2006).

[26] J. Serrano, A.H. Romero, F.J. Manjón, R. Lauck, M. Cardona, and A. Rubio, Phys. Rev. B **69**, 094306 (2004).
[27] J. Ibáñez, R. Oliva, F.J. Manjón, A. Segura, T. Yamaguchi, Y. Nanishi, R. Cuscó, and L. Artús, Phys. Rev. B **88**, 115202 (2013).
[28] K. Kunc, A. Polian, F. Demangeot, and O. Briot, Phys. Status Solidi B 1 (2015).
[29] S. Duman, S. Bağcı, H.M. Tütüncü, G. Uğur, and G.P. Srivastava, Diam. Relat. Mater. **15**, 1175 (2006).
[30] J. Serrano, A. Rubio, E. Hernández, A. Muñoz, and A. Mujica, Phys. Rev. B **62**, 16612 (2000).
[31] E. Grüneisen, Ann. Phys. **344**, 257 (1912).
[32] T.H.K. Barron, Ann. Phys. **1**, 77 (1957).
[33] L. Vočadlo, J.P. Poirer, and G.D. Price, Am. Mineral. **85**, 390 (2000).
[34] B.A. Weinstein and G.J. Piermarini, Phys. Rev. B **12**, 1172 (1975).
[35] A. Jayaraman, Rev. Mod. Phys. **55**, 65 (1983).
[36]Nature **335**, 201 (1988).
[37] S.M. Woodley and R. Catlow, Nat. Mater. **7**, 937 (2008).
[38] B.A. Weinstein, Solid State Commun. **24**, 595 (1977).
[39] P.Y. Yu and M. Cardona, *Fundamentals of Semiconductors* (Springer Berlin Heidelberg, Berlin, Heidelberg, 2010).
[40] G.P.S. H. M. Tütüncü, Phys. B-Condens. Matter - Phys. B **316**, 190 (2002).
[41] W. Weber, Phys. Rev. Lett. **33**, 371 (1974).
[42] J.-M. Wagner and F. Bechstedt, Phys. Rev. B **62**, 4526 (2000).
[43] Y. Syono and M.H. Manghnani, *High-Pressure Research: Application to Earth and Planetary Sciences* (American Geophysical Union, 1992).
[44] S. Klotz, M. Braden, J. Kulda, P. Pavone, and B. Steininger, Phys. Status Solidi B **223**, 441 (2001).
[45] C.A. and editors of the volumes III/17A-22A-41A1a, in *Group IV Elem. IV-IV III-V Compd. Part - Lattice Prop.*, edited by O. Madelung, U. Rössler, and M. Schulz (Springer Berlin Heidelberg, 2001), pp. 1–6.
[46] Y. Al-Douri, H. Abid, and H. Aourag, Mater. Lett. **59**, 2032 (2005).
[47] J.-M. Wagner and F. Bechstedt, Phys. Status Solidi B **235**, 464 (2003).
[48] P. Hohenberg and W. Kohn, Phys. Rev. **136**, B864 (1964).
[49] W. Kohn and L.J. Sham, Phys. Rev. **140**, A1133 (1965).
[50] P. Giannozzi, S. Baroni, N. Bonini, M. Calandra, R. Car, and C. Cavazzoni et al., J. Phys. Condens. Matter **21**, 395502 (2009).
[51] N. Troullier and J.L. Martins, Phys. Rev. B **43**, 1993 (1991).
[52] H.J. Monkhorst and J.D. Pack, Phys. Rev. B **13**, 5188 (1976).
[53] M. Ueno, M. Yoshida, A. Onodera, O. Shimomura, and K. Takemura, Phys. Rev. B **49**, 14 (1994).
[54] J. Ibáñez, A. Segura, F.J. Manjón, L. Artús, T. Yamaguchi, and Y. Nanishi, Appl. Phys. Lett. **96**, 201903 (2010).
[55] A. Mujica, A. Rubio, A. Muñoz, and R.J. Needs, Rev. Mod. Phys. **75**, 863 (2003).
[56] L. d. Yao, S. d. Luo, X. Shen, S. j. You, L. x. Yang, S. j. Zhang, S. Jiang, Y. c. Li, J. Liu, K. Zhu, Y. l. Liu, W. y. Zhou, L. c. Chen, C. q. Jin, R. c. Yu, and S. s. Xie, J. Mater. Res. **25**, 2330 (2010).
[57] H. Richter, Z.P. Wang, and L. Ley, Solid State Commun. **39**, 625 (1981).
[58] K.K. Tiong, P.M. Amirtharaj, F.H. Pollak, and D.E. Aspnes, Appl. Phys. Lett. **44**, 122 (1984).

[59] K. Roodenko, I.A. Goldthorpe, P.C. McIntyre, and Y.J. Chabal, Phys. Rev. B **82**, 115210 (2010).
[60]*Light Scattering in Solids I* (Springer Berlin Heidelberg, Berlin, Heidelberg, 1983).
[61] T. Sugiura, Y. Kawaguchi, T. Tsukamoto, H. Andoh, M. Yamaguchi, K. Hiramatsu, and N. Sawaki, Jpn. J. Appl. Phys. **40**, 5955 (2001).
[62] R. Shuker and R.W. Gammon, Phys. Rev. Lett. **25**, 222 (1970).
[63] N. Domènech-Amador, R. Cuscó, R. García-Hernansanz, G. González-Díaz, J. Gandhi, A. Bensaoula, and L. Artús, Semicond. Sci. Technol. **29**, 045013 (2014).
[64] F. Rasetti, Nature **127**, 626 (1931).
[65] R.S. Krishnan, Proc. Indian Acad. Sci. - Sect. A **26**, 419 (1947).
[66] Born, Max and Bradburn, Mary, Nature **156**, 567 (1945).
[67] R. Loudon, Adv. Phys. **13**, 423 (1964).
[68] E. Burstein, F.A. Johnson, and R. Loudon, Phys. Rev. **139**, A1239 (1965).
[69] W. Hayes and R. Loudon, *Scattering of Light by Crystals* (Courier Corporation, 2012).
[70] P. Gallo, V. Mazzacurati, G. Ruocco, and G. Signorelli, Phys. Rev. B **47**, 11830 (1993).
[71] B.B. Varga, Phys. Rev. **137**, A1896 (1965).
[72] G. Abstreiter, M. Cardona, and A. Pinczuk, in *Light Scatt. Solids IV*, edited by P.D.M. Cardona and P.D.G. Güntherodt (Springer Berlin Heidelberg, 1984), pp. 5–150.
[73] R. Cuscó, E. Alarcón-Lladó, J. Ibáñez, T. Yamaguchi, Y. Nanishi, and L. Artús, J. Phys. Condens. Matter **21**, 415801 (2009).
[74] U. Nowak, W. Richter, and G. Sachs, Phys. Status Solidi B **108**, 131 (1981).
[75] S. Ernst, A.R. Goñi, K. Syassen, and M. Cardona, J. Phys. Chem. Solids **56**, 567 (1995).
[76] L. Artus, R. Cusco, J. Ibanez, N. Blanco, and G. Gonzalez-Diaz, Phys. Rev. B **60**, 5456 (1999).
[77] N.D. Mermin, Phys. Rev. B **1**, 2362 (1970).
[78] T. Inushima, T. Shiraishi, and V.Y. Davydov, Solid State Commun. **110**, 491 (1999).
[79] H.-J. Kwon, Y.-H. Lee, O. Miki, H. Yamano, and A. Yoshida, Appl. Phys. Lett. **69**, 937 (1996).
[80] M.-C. Lee, H.-C. Lin, Y.-C. Pan, C.-K. Shu, J. Ou, W.-H. Chen, and W.-K. Chen, Appl. Phys. Lett. **73**, 2606 (1998).
[81] J.S. Dyck, K. Kim, S. Limpijumnong, W.R.L. Lambrecht, K. Kash, and J.C. Angus, Solid State Commun. **114**, 355 (2000).
[82] A. Kasic, M. Schubert, Y. Saito, Y. Nanishi, and G. Wagner, Phys. Rev. B **65**, 115206 (2002).
[83] F. Demangeot, C. Pinquier, J. Frandon, M. Gaio, O. Briot, B. Maleyre, S. Ruffenach, and B. Gil, Phys. Rev. B **71**, 104305 (2005).
[84] J.S. Thakur, D. Haddad, V.M. Naik, R. Naik, G.W. Auner, H. Lu, and W.J. Schaff, Phys. Rev. B **71**, 115203 (2005).
[85] R. Cuscó, J. Ibáñez, E. Alarcón-Lladó, L. Artús, T. Yamaguchi, and Y. Nanishi, Phys. Rev. B **79**, 155210 (2009).
[86] V.Y. Davydov, A.A. Klochikhin, A.N. Smirnov, I.Y. Strashkova, A.S. Krylov, H. Lu, W.J. Schaff, H.-M. Lee, Y.-L. Hong, and S. Gwo, Semiconductors **44**, 161 (2010).
[87] R.M. Martin, Phys. Rev. B **10**, 2620 (1974).
[88] J. Menéndez and M. Cardona, Phys. Rev. B **31**, 3696 (1985).
[89] C. Thomsen and S. Reich, Phys. Rev. Lett. **85**, 5214 (2000).
[90] J. Maultzsch, S. Reich, and C. Thomsen, Phys. Rev. B **70**, 155403 (2004).

[91] P. Venezuela, M. Lazzeri, and F. Mauri, Phys. Rev. B **84**, 035433 (2011).
[92] V. Carozo, C.M. Almeida, B. Fragneaud, P.M. Bedê, M.V.O. Moutinho, J. Ribeiro-Soares, N.F. Andrade, A.G. Souza Filho, M.J.S. Matos, B. Wang, M. Terrones, R.B. Capaz, A. Jorio, C.A. Achete, and L.G. Cançado, Phys. Rev. B **88**, 085401 (2013).
[93] R. Cuscó, N. Domènech-Amador, L. Artús, K. Wang, T. Yamaguchi, and Y. Nanishi, J. Appl. Phys. **112**, 053528 (2012).
[94] D. Olego and M. Cardona, Phys. Rev. B **24**, 7217 (1981).

CHAPTER 5

Optical and vibrational properties of InGaN

5.1. Introduction

$In_xGa_{1-x}N$ thin films were initially synthetized in the mid 70's by means of the electron beam plasma technique.[1,2] But it was not until the late 80's, during the race for the growth of efficient GaN-based blue LEDs, that important efforts were put into the characterization and growth of high-quality InGaN thin films.[3–5] Most remarkably, S. Nakamura et al. demonstrated that InGaN can be used as an active layer to obtain high-brightness blue LEDs.[6–8] Also, as discussed in the previous chapters, improvements in the growth of InN led to the discovery of its fundamental bandgap, around 0.64 eV, much lower than the previously thought ≈1.8 eV value.[9] This finding gave renewed interest to the InGaN alloy because the range of optoelectronic applications of this material system could be extended from the ultraviolet (3.4 eV) to the infrared energies (0.64 eV), covering the whole visible spectral region.[10] Despite the high technological interest of InGaN alloys, the growth of unstrained and homogeneous thin films is still challenging.

A major difficulty in the growth of high-quality InGaN is the lack of compositional homogeneity. For instance, spinodal decomposition has been reported for MBE-grown samples.[11] Also, some authors have reported the existence of indium-rich InGaN nanoclusters that segregate near the surface during the growth process.[12,13] On the other hand, lattice mismatch, and different thermal expansion coefficients between the layer and the substrate result in strain, the relaxation of which results in high densities of dislocations. These can be partly reduced by using GaN buffer layers instead of direct growth on sapphire or 6H-SiC substrates.[5] Nevertheless, the in-plane lattice mismatch between GaN and InGaN can be as high as $\Delta a/a$ = 11% in In-rich samples, which results in importantly strained InGaN layers. During growth, the built-in strain accumulates up to a certain thickness, above which it is relaxed by dislocations and defects. The thickness at which this takes place is

known as critical layer thickness (CLT). At higher thickness the sample grows more relaxed but at the expense of lower crystal quality.[14] Characterizing the effects of compositional fluctuations, strain and defects on the optoelectronic properties of the InGaN active layers is essential in order to improve growth methods and optimize device performances.

The characterization of the structural, vibrational and optoelectronic properties of InGaN as a function of composition is in general not straightforward. For instance, determining the alloy composition of an InGaN epilayer from X-ray diffraction measurements might be misleading because the lattice parameters of InGaN depend on indium concentration and also on the strain caused by the substrate. Thus, it is in general necessary to use a combination of different characterization techniques in order to properly determine the relevant properties of the alloy.

For the determination of the fundamental bandgap of InGaN several effects must be taken into account. Firstly, composition fluctuations of the order of 10-20% indium concentration can take place in different spatial scales, ranging from the sub-micron scale up to the millimeter scale.[15] Hence, the measured bandgap values obtained with optical methods may strongly depend on the particular technique used, as discussed later in this chapter. Secondly, compressive strain arising from the substrate can importantly modify the bandgap. For the case of gallium-rich InGaN samples grown on GaN/Al_2O_3 templates, some authors have reported strain-related blueshifts of the bandgap as high as ~200 meV.[14,16] Other effects, such as high electron concentration or impurity recombination centers, also modify the optical bandgap of InGaN.[17]

It is well known that the compositional dependence of the bandgap of InGaN is not linear, but displays a quadratic dependence as a function of In/Ga content which is usually expressed in terms of a *bowing parameter*, *b*. Early studies found a large bowing parameter of 2.3 eV,[18] 2.5 eV[19] and 2.6 eV[20] but currently accepted values are around b = 1.43 eV.[21] In order to determine the bandgap of InGaN and its compositional dependence, it is clear that all the effects described above must be carefully taken into account. One of the aims of this chapter will be

to evaluate the importance of these effects in high-quality InGaN epilayers grown on GaN/Al_2O_3 templates.

As already mentioned throughout this thesis, the measured (optical) bandgap significantly depends on the characterization technique. As is well known, optical emission (luminescence) techniques tend to report lower energies than absorption experiments; the difference between these two values is called *Stokes shift*.[22] The origin of this difference is mainly related, in the case of InGaN alloys, to the compositional inhomogeneities.

With regard to theoretical calculations of the bandgap of InGaN, *ab initio* methods have been applied with the aim of determining, among many other physical properties, the bowing parameter.[23,24] Nevertheless, it is challenging to calculate the bandgap of any alloy because a supercell consisting of many atoms with different arrangements must be used. This adds to the well-known limitations of some approaches such as density functional theory (DFT), which gives rise to important underestimations of the bandgap values. Recent results using more sophisticated methods have found b = 1.6 eV for InGaN, in fairly good agreement with experiments.[25]

Aside from optical measurements, vibrational techniques such as Raman or Brillouin scattering may be highly informative to characterize the crystal quality and other relevant properties of semiconductor materials. In particular, Raman scattering has proven useful to evaluate the composition,[26–32] bandgap energy,[20,26] morphology,[33–35] homogeneity,[30,32,34,36–41] and strain,[32,35,42–45] of InGaN thin films and heterostructures such as superlattices. A typical near-resonant backscattering measurement of a InGaN thin film grown on its c-axis is dominated by two characteristic Raman bands, the E_{2h} nonpolar mode and the A_1(LO) polar mode, which is Fröhlich resonant. As shown in numerous previous works, these modes exhibit one-mode behavior in the InGaN alloy.

As in the case of the optical bandgaps, the experimental determination of the dependence of the InGaN phonon frequencies with composition is not straightforward and many effects must be taken into account. Firstly, in-plane compressive (tensile) strain arising from the substrate causes the phonon modes to blueshift (red-

shift). As already mentioned, the evaluation of strain and composition with structural techniques such as X-ray diffraction (XRD) is usually difficult, and therefore it may be highly desirable to determine the alloy composition independently (for instance, by means of energy-dispersive X-ray spectroscopy (EDX) or similar methods). Once the strain values are well known, the Raman frequencies corresponding to unstrained material can be calculated by using the corresponding *phonon deformation potentials*. Secondly, the samples may exhibit in-depth compositional variations, and as a consequence the Raman frequencies may depend on the excitation wavelength. Indeed, different regions of the samples are probed with different excitation wavelengths. For instance, the penetration depth varies from ~100 nm using the 325-nm line for an intermediate indium composition up to (ideally) several millimeters in the transparency region.[15] Finally, lateral composition fluctuations broaden the phonon peaks, and in particular, the A_1(LO) polar mode, which is usually resonantly excited through the Fröhlich interaction mechanism.[30] One of the aims of the present chapter will be to understand the role of all these effects on the optical phonon behavior of InGaN.

In turn, some works have studied the lattice-dynamics of InGaN by means of theoretical calculations. This is a very challenging task because the phonon symmetry of the wurtzite structure is lost due to the randomly distributed chemical species (the In and Ga cations) and distorted positions of the ions. Therefore, a large amount of multiple bands may be expected in the phonon dispersion curves of InGaN when supercell calculations are performed. In a more simplistic approach, H. Grille et al.[46] assumed that the symmetry of the alloy is preserved in its wurtzite structure. Interpolating the interatomic force constants and other parameters of the pure compositional end-members, they calculated the frequency of the phonon modes as a function of composition using a method based on the modified random-element isodisplacement (MREI) model and a rigid-ion model. These authors found an almost linear, one-mode dependence of the phonon modes with composition. While calculations for the AlGaN system using this approach are in good agreement with experimental results[47] this is not the case for InGaN, where important deviations from linearity of the A_1(LO) or E_{2h} frequencies are usually found.[32] Other ap-

proaches based in the Born-Huang model, or virtual crystal approximation (VCA), have been used to study the phonons of InGaN.[48] The elastic constants and pressure dependence have been calculated by means of *ab initio* calculations either using alchemical pseudopotential mixing[23] or supercells.[24] Calculations based on supercells showed that the composition-dependence of the elastic constants is highly sensitive to the particular arrangement of the ions inside the unit cell. Therefore, an experimental determination of the elastic constants of InGaN, for instance by means of Brillouin scattering, would be highly desirable in order to confirm the theoretical predictions.

As already seen in the previous chapters, high-pressure optical and vibrational measurements are widely employed to study semiconductor materials, since they provide relevant information about the band structure and the lattice-dynamics of semiconductor compounds. One of the main aims of this chapter will be to revisit the high-pressure optical properties of InGaN and, in particular, to perform a high-pressure Raman study on a set of InGaN epilayers with different In compositions, and grown on different substrates. To our knowledge, this is the first high-pressure Raman investigation on the InGaN alloy.

Thus, in this chapter optical and vibrational measurements are performed at room and high-pressure conditions on a series of InGaN epilayers. The samples used for the different studies on the InGaN alloy are listed in Tables 5.1, 5.2 and 5.3 below. The principal aim of this part of the thesis is to better understand the compositional dependence of the bandgaps and of the optical and acoustic phonons of InGaN and their pressure behaviour. For this purpose, and among others, we employ different analytical techniques such as photoluminescence (PL), optical absorption, Raman scattering or Brillouin spectroscopy.

Goals of this chapter

- To reevaluate the bowing parameter of InGaN with optical techniques by using the available samples.
- To determine the compositional dependence of the A_1(LO) and E_{2h} phonon modes of InGaN.
- To understand the origin of the excitation-wavelength dependence of the frequency of the A_1(LO) Fröhlich resonant mode of InGaN.
- To evaluate the compositional dependence of the acoustic modes and the elastic constants of InGaN by means of Brillouin scattering.
- To study the folded acoustic phonons in InGaN/GaN superlattices by means of Raman scattering.
- To determine the pressure dependence of the A_1(LO) mode of InGaN as a function of composition.

List of samples used in this chapter

For this chapter, three sets of InGaN samples have been used. The first set, listed in Table 5.1, has been employed for Raman, Brillouin and optical-emission studies. These are high-quality InGaN epilayers grown on GaN/Al_2O_3 templates by plasma-assisted molecular beam epitaxy (PAMBE). In these samples, the GaN buffer layer has a thickness of 4 μm and the nominal sample thickness is between 200−1200 nm. Further details of the growth process and characterization of these samples can be found elsewhere.[49]

We would like to mention that high-resolution XRD measurements were performed on these samples to evaluate their composition and strain state, which was obtained from reciprocal space maps (RCMs) around the symmetrical ($\mathbf{00\bar{2}}$) and the asymmetrical ($\mathbf{11\bar{4}}$) and ($\mathbf{01\bar{5}}$) reflections. In order to assess the composition values, EDX measurements were also performed on some of the samples (A1053, A1012 and A1010, see Table 5.1). The residual electron concentration of the InGaN samples was found to be in the range $3\cdot10^{18}$−$1\cdot10^{19}$ cm^{-3}, as determined by Hall-effect measurements on some of the epilayers (A1053, A1012, A1010 and

A1018). These results are similar to those found in samples grown under similar conditions.[19,50]

The second set of samples, used for high-pressure Raman-scattering measurements, is listed in Table 5.2. These samples consist of InGaN epilayers grown on (111)-oriented silicon substrates. The samples were grown by metal-organic chemical vapor deposition (MOCVD), with a small (~10 nm thick) InAlN accommodation layer which was deposited prior to the growth of the InGaN epilayer.

The last set of samples, which have been used to the study the folding of the acoustic modes in InGaN, is listed in Table 5.3. The samples in this set consist of InGaN/GaN superlattices grown by molecular beam epitaxy (MBE) on sapphire substrates with a 5-7 μm thick GaN buffer layer. Each InGaN-GaN bilayer has a thickness between 8 and 18 nm and is sequentially grown 25−90 number of times. Further details of the growth process and characterization of these samples can be found elsewhere.[51]

Sample	Structure	Thickness (nm)	Relaxation (%)	N_e (cm^{-3})
A1053	$In_{17}Ga_{83}N/GaN/Al_2O_3$	650	–	$1.36 \cdot 10^{19}$
A969	$In_{25}Ga_{75}N/GaN/Al_2O_3$	200	68	–
A1012	$In_{28}Ga_{74}N/GaN/Al_2O_3$	1200	48	$3.19 \cdot 10^{18}$
A1004	$In_{33}Ga_{67}N/GaN/Al_2O_3$	960	40	–
A1010	$In_{34}Ga_{66}N/GaN/Al_2O_3$	710	57	$8.58 \cdot 10^{18}$
A1018	$In_{42}Ga_{58}N/GaN/Al_2O_3$	710	~50	$7.16 \cdot 10^{18}$
A1035	$In_{44}Ga_{56}N/GaN/Al_2O_3$	560	50	–
A1177	$In_{68}Ga_{32}N/GaN/Al_2O_3$	500	100	–
A1182	$In_{75}Ga_{25}N/GaN/Al_2O_3$	500	~100	–
S1450	$In_{90}Ga_{10}N/GaN/Al_2O_3$	–	–	–

Table 5.1. List of $InGaN/GaN/Al_2O_3$ samples used in this thesis. The InGaN epilayers have been grown by plasma-assisted molecular beam epitaxy (PAMBE) on GaN/Al_2O_3 templates, the thickness of the buffer layer is of 4 μm.

Sample	Structure	Thickness (nm)
MD8023	$In_{11}Ga_{89}N/In_{35}Al_{65}N/Si(111)$	350
MD8021	$In_{19}Ga_{81}N/In_{35}Al_{65}N/Si(111)$	300
MD7951	$In_{30}Ga_{70}N/In_{35}Al_{65}N/Si(111)$	360
MD7950	$In_{36}Ga_{64}N/In_{35}Al_{65}N/Si(111)$	400
MD7520	$In_{37}Ga_{63}N/In_{37}Al_{63}N/Si(111)$	463
MD7195	$In_{43}Ga_{57}N/In_{38}Al_{62}N/Si(111)$	541
MD7545	$In_{45}Ga_{55}N/In_{35}Al_{65}N/Si(111)$	446

Table 5.2. List of InGaN samples grown by grown by metal-organic chemical vapor deposition (MOCVD) on Si(111) substrates, an InAlN accommodation with a thickness of ~10 nm has been deposited before the epitaxial growth of InGaN.

Sample	Structure (SLs on GaN/Al_2O_3 substrates)	Total thickness (nm)	Thickness InGaN (nm)	Thickness GaN (nm)
A	$In_{30}Ga_{70}N/GaN$	500	3.5	4.5
B	$In_{18}Ga_{82}N/GaN$	800	4.6	4.2
C	$In_{23}Ga_{77}N/GaN$	400	4.5	4.5
D	$In_{15}Ga_{85}N/GaN$	500	4.4	8.1
E	$In_{33}Ga_{67}N/GaN$	500	7.7	7.7
F	$In_{38}Ga_{62}N/GaN$	450	7.5	9.8
G	$In_{19}Ga_{81}N/GaN$	620	4.5	13.3

Table 5.3. List of InGaN/GaN superlattices grown by means of molecular beam epitaxy (MBE). The SL's have been grown on sapphire substrates with 5-7 μm thick GaN buffer layers.

5.2. Theoretical framework

5.2.1. Optical properties

The bandgap and bowing parameter

In general, semiconductor alloys exhibit a nonlinear bandgap dependence with composition. From a fundamental perspective, two effects mainly account for this fact. Firstly, an intrinsic bowing is obtained from virtual-crystal approximation (VCA) calculations. Secondly, the short-range effect of aperiodicity (i.e. disorder) of the potential. The latter statistically increases the available states in the vicinity of the conduction/valence bands, but without altering the shape of the absorption spectrum.[52,53] For the case of ternary alloys with large differences in the lattice constant of the binary compounds (as is the case of InGaN) or with highly-localized states (as is the case of the nitrides), both contributions must be considered.[54]

Generally, an empirical parabolic function is used to fit the composition dependence of the fundamental bandgap. For the case of InGaN

$$E_G^{InGaN}(x) = E_G^{InN}x + E_G^{GaN}(1-x) - bx(1-x)\ , \qquad [5.1]$$

where b is the so-called bowing parameter, and x is the indium molar fraction. It must be noted that studies before 2002 overestimated the bowing parameter because the bandgap of InN was taken larger than the actual, well-stablished value of E_G^{InN} = 0.65 eV.

It has been proposed that group-III nitrides share a common universal bowing parameter, after scaling the bandgap energy of the composition end-members.[55] This conjecture is supported by the hypothesis that the main contribution to the bowing arises from composition disorder.[56] Also, it has been found that the bandgap values of indium-rich InGaN and InAlN match for the same lattice parameter.[10]

Numerous works report bowing-parameter values for the InGaN alloy, obtained with optical measurements. Many of these works focused on the Ga-rich compositional region, since highly crystalline GaN is in general easier to grow than InN and early high-quality InGaN samples were typically Ga-rich.[57,58] From the in-

vestigations in the Ga-rich region it was soon found that the bowing parameter was composition-dependent and decreases with increasing indium concentration.[57,59,60] Using MBE-grown samples, Hori et al.[18] and Davydov et al.[19] estimated a rather large bowing parameter from luminescence measurements of b = 2.3 eV and 2.5 eV, respectively. From the composition dependency of the bandgap of InGaN they concluded that the fundamental bandgap of InN was below 1 eV, around 0.7 eV. Nevertheless, their studies did not take into account important effects on the evaluation of the bandgap such as strain or the Stokes shift, which, as described below, are important for the determination of the fundamental bandgap and bowing parameter of InGaN.

On the other hand, Kurouchi et al.[61] measured a lower bowing parameter, b = 1.8 eV, in fully-relaxed thin films grown directly on sapphire substrates. They performed absorption and PL measurements but only considered the latter because the absorption measurements revealed a fundamental bandgap for InN around 0.9 eV, higher than expected. Considering their reported absorption values for the bandgap of indium-rich InGaN samples, the adjusted bowing parameter would be significantly smaller.[21]

Wu et al.[21] measured a small bandgap bowing parameter, around b = 1.43 eV. For their set of samples these authors reported a large Stokes shift (up to ~0.5 eV at intermediate InGaN composition) by comparing PL and absorption measurements. The b = 1.43 eV value agrees well with most theoretical studies,[25,59,62–70], and is the recommended value reported in several reviews.[10,65,71] Nevertheless, this work did not evaluate the effects of strain or residual electron density, which could importantly modify the optical bandgap as shown later in this chapter.

With regard to theoretical calculations of b, it has to be noted that most of the existing works rely on additional *ad hoc* corrections to properly calculate the bandgap of the composition end-members, which are typically underestimated.[59] For instance, negative values for the bandgap of InN have been reported by GGA- and LDA-based calculations.[54,62–64,68] Newer hybrid functionals allowed to better calculate the fundamental bandgap of InN and GaN, and presumably that of InGaN by means of DFT, employing HSE06 or PBE functionals.[59,72] These latter

studies reported a bowing parameter of b = 1.36 eV. However, using the PBE0 functional other authors found a bowing parameter equal to b = 1.63 eV.[73]

As already mentioned, in order to accurately determine the fundamental bandgap of InGaN by means of optical techniques, one must bear in mind that the emission energy is significantly lower than the absorption edge (*Stokes shift*), which, in the case of alloys, is mostly a consequence of compositional alloy fluctuations. In order to understand the large Stokes shift observed in group-III nitride alloys, many works have performed measurements as a function of temperature and/or power excitation. Here, a general overview on this topic will be presented, with the aim of better understanding the results of PL and CL measurements in the InGaN system. Also, it will be shown that absorption measurements allow one to determine the mean bandgap of an inhomogeneous alloy. Finally, the effect of residual electron density and strain effects will be evaluated in order to obtain an estimation of the bowing parameter of InGaN.

Compositional inhomogeneity and the Stokes shift

As explained in Chapter 3, the optical emission in InN is determined by electronic band filling effects and radiative recombination from shallow impurity levels. For the case of InGaN, composition fluctuations at the nano- and micro-scale are responsible for an important part of the observed Stokes shifts.[74,75] The importance of this mechanism has been confirmed by Huang et al.[74], who showed that the Stokes shift increases up to indium concentrations around 50% and decreases again at higher indium concentrations for samples with similar crystal quality.[76] In general, highly homogeneous samples will exhibit a low Stokes shift, while poorly crystalline InGaN samples with large composition inhomogeneities will exhibit a large Stokes shift, arising from radiative recombination of localized states and from indium-rich clusters.

A scheme of the Stokes shift mechanism in laterally inhomogeneous samples is shown in Fig. 5.1, where the conduction and valence band edges are plotted along different spatial regions of a typical inhomogeneous InGaN sample. Note that the absorption process can take place for any available state between the valence and

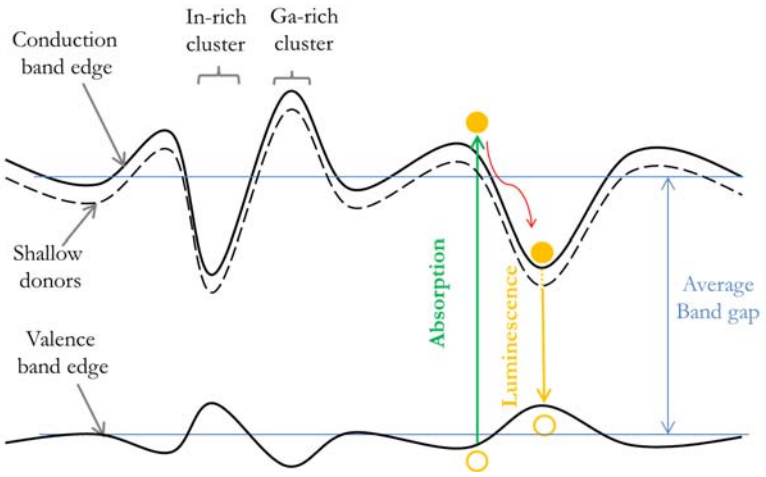

Fig. 5.1. Picture that illustrates the origin of the Stokes shift in InGaN. The valence and conduction band edges are plotted along different spatial regions, where indium-rich nano/micro clusters participate in the emission process.

conduction band. Thus, neglecting electron density or strain effects, optical absorption provides a good measure of the average bandgap of the alloy. Other optical techniques suitable to evaluate the fundamental bandgap of InGaN are photoluminescence excitation (PLE),[19,74] photocurrent (PC)[77,78] or photoreflectance (PR).[79–81] In contrast, the optical emission energy is lower than the average gap. For the luminescence process, the excited carriers tend to decay to the lowest-potential regions.[82] Thus, recombination takes place preferably at indium-rich clusters. As revealed by spatially-resolved cathodoluminescence, emission is enhanced in indium-rich clusters.[77,83]

A typical PL and absorption spectrum of InGaN is shown in Fig. 5.2. These spectra were obtained from sample A1018 (see Table 5.1). As it can be seen in the figure, the line shape of the absorption edge of InGaN is not sharp, in contrast to what would be expected for a direct-bandgap semiconductor, but exhibits a smooth tail near the absorption edge. The origin of this feature can be attributed to defects and composition fluctuations that contribute to the density of states around the fundamental gap. This feature, known as *Urbach tail*,[84,85] is typically observed in disordered materials. For instance, it has been observed that highly-doped GaN exhibits similar tailing effects, comparable to those measured in amorphous silicon.[86] The Urbach tail can be modelled with the expression

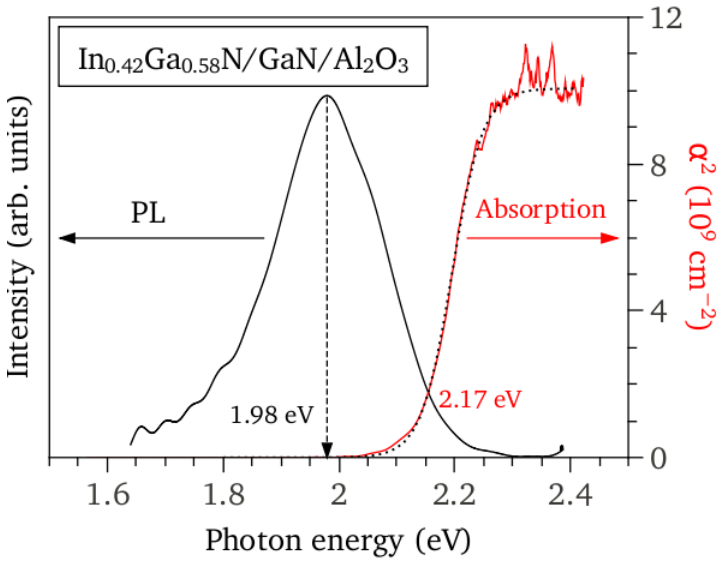

Fig. 5.2. Photoluminescence and absorbance spectra acquired at RT of sample A1018 (see Table 5.1.). The absorption edge has been determined from a sigmoidal fit (dotted line). The PL measurements were excited with a 514.5-nm laser line.

$$\alpha(E) = \alpha_0 \exp\left(\frac{E - E_g}{\Delta E}\right), \qquad [5.2]$$

where E_g is the average bandgap energy and ΔE is known as the Urbach energy.[87] Using this expression, the optical absorption can be used to extract the bandgap of the semiconductor.

With regard to absorption experiments, many works use a sigmoidal function to take into account the absorption edge and the plateau of the absorbance spectra, to determine the "effective bandgap":[22]

$$\alpha(E) = \frac{\alpha_0}{1 + \exp\left(\frac{E_g - E}{\Delta E}\right)}, \qquad [5.3]$$

where α_0 is the absorbance saturation value. Eq. [5.3] has been used to fit the absorbance spectra from the measurements performed on the InGaN samples studied in this work (Table 5.1). An example of fitted spectrum is shown in Fig. 5.2 (dotted line) for the particular case of sample A1018. The fitted bandgap value is 2.17 eV and the resulting Urbach energy is of the order of 50 meV, much lower than most reported values for a similar indium composition (~160 meV). This result may be a consequence of the good sample quality of the set of samples available in this work.

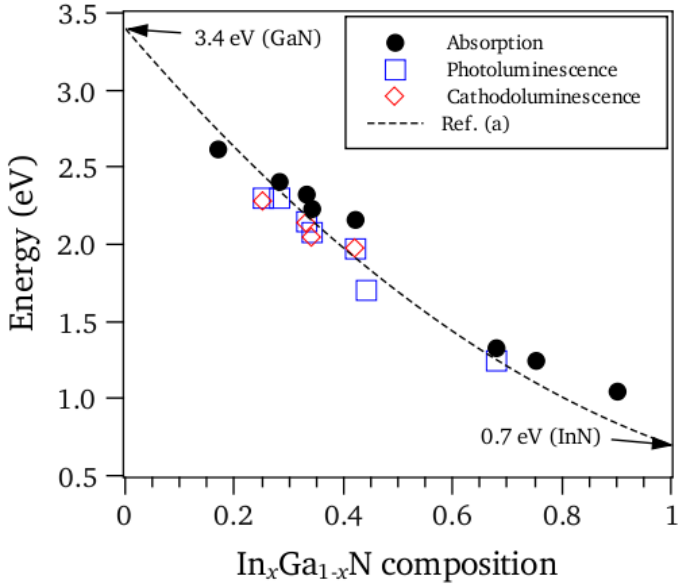

Fig. 5.3. Bandgap energy of InGaN as measured from absorption (full circles), photoluminescence (open squares) and cathodoluminescence (open rhombus, performed at T = 80 K). The bandgap of GaN and InN is also displayed, together with the dependence measured in Ref. (a)[21]. The samples used for the characterization are shown in Table 5.1

As it can be seen in Fig. 5.2, sample A1018 exhibits a Stokes shift of 190 meV. Note that the absorption coefficient reaches $\alpha_0 \sim 10^5$ cm^{-1} above the absorption edge, which is a typical value for direct semiconductors. The Stokes shift here reported is lower than that found by Huang et al.[74], i.e. around 300-500 meV in samples with similar indium concentration. Again, this may be a consequence of the improved crystal quality of the MBE-grown InGaN/GaN/Al_2O_3 samples investigated in this work.

The bandgap energies measured by absorption and luminescence (PL or CL) techniques for all the InGaN/GaN epilayers available in this thesis are shown in Fig. 5.3. As expected, the bandgap energies obtained in all samples from the optical emission are sizably lower than those obtained with absorption measurements. We would like to remark that the absorption bandgaps obtained in this thesis for InGaN (see full circles in Fig. 5.3) are somewhat higher than the largely accepted values reported by Wu et al.[21](see dashed line in Fig. 5.3), giving rise to a lower bowing parameter. Here a bowing parameter of b = 0.9 eV is obtained from the RT absorption measurements. This value is sizably lower than the b = 1.43 eV measured at RT by Wu et al. using the same method. It has to be noted that a more linear de-

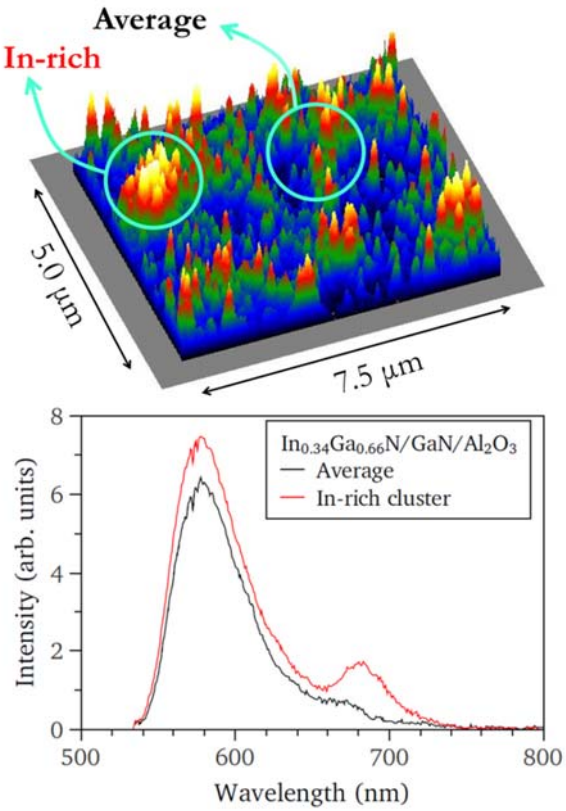

Fig. 5.4.

Cathodoluminescence characterization of the sample A1004 at T = 80 K.
Top: Pancromatic mapping of a selected 5.0 x 7.5 μm² region. The region emitting at higher intensity is labelled as "In-rich" and another typical emission region as "Average".
Bottom: Spectra corresponding to two selected regions of this sample (see upper panel). Both spectra emit at 577 nm which corresponds to a composition of $In_{0.35}Ga_{0.65}N$ (using a bowing parameter of b = 1.5 eV), very similar to the nominal composition of the sample. The most intense region has a secondary peak around 785 nm. This corresponds to a composition of $In_{0.54}Ga_{0.46}N$, therefore this domain is attributed to an indium-rich cluster.

pendence of the bandgap energy with composition is typically associated with increased homogeneity and crystallinity.

In order to evaluate the degree of composition inhomogeneity in the $InGaN/GaN/Al_2O_3$ epilayers studied in this work (Table 5.1), CL mappings from all samples were obtained at 80 K. A panchromatic mapping for the case of sample A1004 is shown in the upper panel of Fig. 5.4, where the bright spots can be attributed to indium-rich micro-clusters. It has to be noted that only a few of our samples exhibited a secondary peak arising from In-rich regions, as is the case of sample A1004. However, as can be seen in the bottom panel of Fig. 5.4, the overall intensity of the long-wavelength emission is much smaller than that of the main band-to-band peak. Thus, in spite of the presence of In-rich domains in some of our epilayers, it can be concluded that the degree of lateral inhomogeneity of these samples is not very high, even lower than that of InGaN layers investigated in previous works.

Effects of the electron density on the optical bandgap

Owing to the fact that the Fermi level of intrinsic In-rich InGaN is below the Fermi stabilization energy (~4.9 eV below the vacuum level[10]), it is expected that InGaN exhibits large residual electron concentrations, giving rise to Burstein-Moss shifts (see Chapter 3). In fact, some authors found that around 50% of the Stokes shift can be attributed to the Burstein-Moss shift for indium-rich samples with high electron density (>$2\cdot10^{18}$ cm^{-3}).[88] For samples with similar residual electron concentrations, Donmez et al.[17] reported a blueshift of the optical bandgap as high as 200 meV after evaluating the effect of bandgap filling, bandgap renormalization and band tailing on the experimental data. As can be seen in Table 5.1, the samples used in this thesis exhibit fairly large electron densities (>$3\cdot10^{18}$ cm^{-3}), which suggests that the free-electron concentration might have a bearing in the determination of the fundamental bandgap of InGaN and of the bowing parameter.

Let's evaluate the effect on the optical bandgap of InGaN of the Burstein-Moss shift and the bandgap renormalization on the samples studied in this work. For electron densities of the order of $N_e \approx 5\cdot10^{18}$ cm^{-3}, as is the case of our epilayers, and assuming parabolic bands, the Burstein-Moss shift is given by

$$\Delta E_{BM} = \frac{\hbar^2 k_F^2}{2\mu^*} , \qquad [5.4]$$

where k_F is the Fermi wave vector which depends on the electron density; $k_F = (3\pi^2 N_e)^{1/3}$, and μ^* is the free-carrier reduced mass. Assuming that momentum conservation takes place between electrons and holes in an absorption process, μ^* is given by[89]

$$\mu^* = \frac{m_e^* m_h^*}{m_e^* + m_h^*} , \qquad [5.5]$$

where m_e^* and m_h^* are the isotropic effective mass of electrons and holes, respectively.[89] Note that $\mu^* \approx m_e^*$ in narrow bandgap semiconductors such as InN ($\mu^* = 0.06m_e$), with a large difference between valence and conduction effective-mass values.[90] For the case of GaN, $\mu^* = 0.16m_e$.[89] Equation [5.4] is equivalent to Eq.

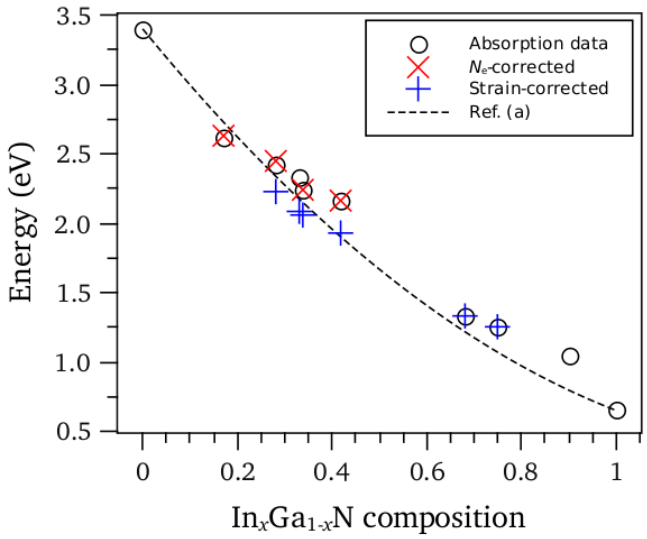

Fig. 5.5.
Bandgap energy versus composition of InGaN. The absorption measurements of the InGaN samples listed in Table 5.1 and Table 3.1 (sample C) are shown as open circles. The electron density effects (red diagonal crosses) and the strain effects (blue vertical crosses) on the bandgap are corrected for those samples that were measured by Hall effect and HRXRD. The bowing dependence of the bandgap as reported by Wu et al., Ref. (a),[21] is shown with a dashed line.

[3.37] in the parabolic limit (see Chapter 3).[10] Indeed, as already discussed in Chapter 3 for the case of InN, the effective electron mass around Γ can be described with $\boldsymbol{k}\cdot\boldsymbol{p}$ theory:

$$\frac{m_e^*}{m_0} = \left(1 + \frac{E_P}{E_G}\right)^{-1}, \qquad [5.6]$$

where E_G is the fundamental bandgap and E_P is the $\boldsymbol{k}\cdot\boldsymbol{p}$ matrix element. This parameter can be estimated as $E_P \approx \frac{8\pi^2\hbar^2}{m_0 a^2} \approx 24$ eV for a typical value of the lattice constant $a \approx 5$ Å.[91,92] For the case of III-V group semiconductors it has been found that a universal $E_P = 12$ eV value successfully describes the effective mass versus bandgap dependency.[10] For the particular case of w-InN, a value of $E_P = 11$ eV and $E_G = 0.65$ eV allows one to reproduce the experimentally determined $m_{InN}^* = 0.055m_0$ value.[90]

Although the effective mass of InGaN has not been experimentally determined, it can be approximated by linearly interpolating between both compositional end members.[93,94,95] Using Eq. [5.6] and taking $E_P = 11.2$ eV the effective masses of InN and GaN can be obtained: $m_{InN}^* = 0.055m_e$ and $m_{GaN}^* \approx 0.23m_e$ (note that the latter is very similar to the experimentally reported value, $m_{GaN}^* = 0.20m_e$[65]). Then, the effective mass of the InGaN alloy system can be estimated by using Eq. [3.45], and Eq. [5.4] can then be employed to evaluate the bandgap filling effects.

With regard to the bandgap renormalization contribution to the optical bandgap, Eqs. [3.40] and [3.41] in Chapter 3 can be used (assuming that the static dielectric constant of InGaN can be linearly interpolated from the compositional end members).[50,96]

Taking into account these two effects (bandgap filling and bandgap renormalization, and neglecting at the moment strain effects for simplicity), a bandgap value can be extracted from the optical measurements on the samples studied in this thesis. The electron-density corrected bandgap values for the samples A1010, A1018, A1012 and A1053 (Table 5.1) are shown with crosses in Fig. 5.5. These are not much larger (from 3 to 26 meV) than the as-obtained values from the absorption edge at room temperature. Thus, electron density effects are not relevant in our samples, and would only be important in the case of much larger carrier concentrations. For instance, an $In_{0.75}Ga_{0.25}N$ sample with $N_e = 5 \cdot 10^{19}$ cm^{-3} would exhibit an optical bandgap 255 meV higher than the fundamental bandgap.

Strain effects on the bandgap

As pointed out in previous sections, the currently accepted bandgap dependence on composition for InGaN was early reported by Wu et al.[21] Nevertheless such measurements could have some important sources of errors because strain effects were neglected in that work. As it has been shown elsewhere,[60,63,97] strain strongly affects the bandgap energy, in particular in the case of samples with low indium concentration. Recent studies have shown that the bowing parameter is importantly affected by the presence or absence of strain in the samples. A very large bowing parameter, around $b = 2.9$ eV,[98] has been reported after correcting the influence of strain on the bandgap for samples with low indium content ($x < 0.25$), in agreement with results obtained in Yan et al.[99]

As discussed above, the strain state of the InGaN/GaN/Al_2O_3 samples studied in this thesis was obtained from HRXRD reciprocal mappings. It was found that the samples with intermediate compositions, $0.25 < x < 0.42$, exhibit large strain values (in the range 1.5 – 2.3 %). Hence, it is clear that strain in these epilayers

might strongly affect the experimental optical gaps. Next, we obtain strain-corrected bandgap values for our samples.

Most works dealing with the composition dependence of the bandgap along the entire composition range relied on XRD measurements for the determination of the alloy composition and neglected the residual strain effects on the bandgap.[17,18,21] For instance, for the case of the samples studied by Wu et al.[21,100] the composition was determined using Vegard's law to analyze the XRD measurements. This implies that the indium concentration would have been overestimated if the samples exhibited sizable degrees of strain, as is usual in the InGaN alloy. Note that the thickness of their samples (around 240 nm) was close to the critical layer thickness[101] (CLT) and that other works systematically reported important strain values for InGaN thin films.[32,57,58,102] Thus, the possible large strain in the samples used in that work would yield overestimated bandgap energies

Next, we review how the bandgap depends on the strain for both the conduction and valence bands. In the case of the conduction band, the dependency on strain is typically given by

$$E_C = E_C(0) + a_1\varepsilon_\perp + 2a_2\varepsilon_\parallel \,, \qquad [5.7]$$

where a_1 and a_1 are the deformation potentials and $E_C(0)$ is the strain-free fundamental conduction band energy. On the other hand, the description of the strain dependence of the valence bands is more complex because the light-hole (LH), heavy-hole (HH) and crystal-field split-off hole bands (CH) vary their energy level with strain independently. The band ordering, and dependence with strain is typically calculated by solving the Bir-Pikus Hamiltonian,[103] based on $\boldsymbol{k}\cdot\boldsymbol{p}$ theory.[104] For the case of wurtzite nitrides, under compressive strain conditions, it can be shown that the valence band maximum barely depends on compressive strain, and therefore the strain dependence of the bandgap is basically given by Eq. [5.7].[104–106]

In this thesis, the as-measured bandgap energies of InGaN, as shown with circles in Fig. 5.5, are expected to be overestimated due to compressive strain arising from the GaN/Al_2O_3 template. For the case of these samples, the large thickness of the epilayers ensures that they are not fully strained but partially relaxed. Indeed, the

thickness of these samples (see Table 5.1) is in all cases larger than the CLT, which in the case of InGaN is below ≈50 nm for In contents higher than 20%.[101] The degree of plastic relaxation (*R*) of the InGaN/GaN/Al_2O_3 epilayers, determined from XRD reciprocal space mappings, is shown in Table 5.1.

Then, the components of the strain tensor that enter Eq. [5.7] can be obtained from the same definition of plastic relaxation (*R*)

$$R(\%) = 100 \cdot \frac{a - a_{GaN}}{a_{InGaN} - a_{GaN}}, \qquad [5.8]$$

where a is the measured lattice parameter of the thin film, and a_{InGaN} is obtained by using Vegard's law

$$a_{InGaN} = x \cdot a_{InN} + (1 - x) \cdot a_{GaN} \ . \qquad [5.9]$$

A plastic relaxation of R = 0% (100%) implies that the epilayer is fully strained (fully relaxed). Note that the validity of Eq. [5.9] has been confirmed in theoretical calculations.[59,107] Finally, the in-plain strain is given by

$$\varepsilon_{\parallel} = \frac{a - a_{InGaN}}{a_{InGaN}} \ . \qquad [5.10]$$

For the case of compressive strain in thin films grown along the c-axis of wurtzite, stress is only applied in the in-plane axis. From the macroscopic theory of elasticity it can be proven that the two strain components are related by

$$\varepsilon_{\perp} = -\frac{2C_{13}}{C_{33}}\varepsilon_{\parallel} \ , \qquad [5.11]$$

where the composition dependence of the elastic constants can be assumed to be parabolic[108] as revealed by Brillouin scattering measurements performed in this thesis (see Article 5.3 for details), so that

$$C_{ij}(x) = xC_{ij}^{InN} + (1 - x)C_{ij}^{GaN} - b_{ij}x(1 - x) \ . \qquad [5.12]$$

Here we use for GaN (InN) C_{13} =114.0 (107.5) GPa, C_{33} = 406.8 (258) GPa and b_{13} = −4.5 and b_{33} = −1.

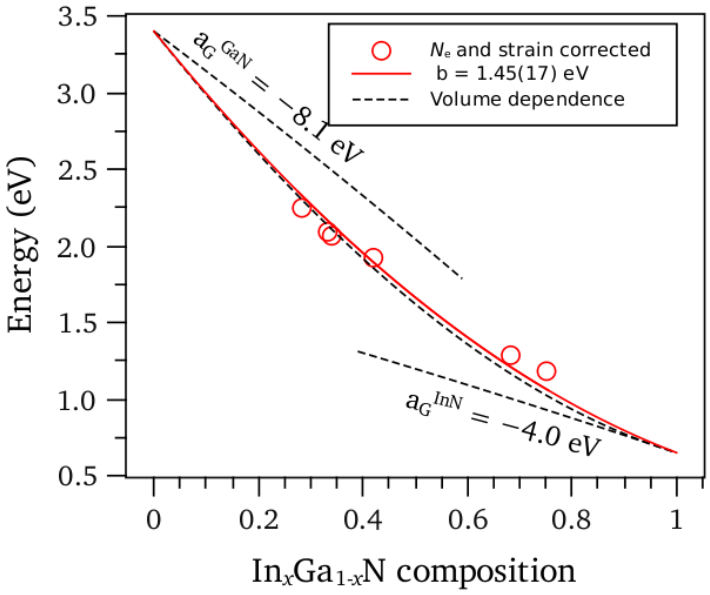

Fig. 5.6.

The bandgap energies of InGaN are shown as a function of composition (circles) after correcting electronic density effects and strain effects on the optical bandgap. All measurements are performed by optical absorption The resulting bowing parameter is b = 1.45(17) eV (solid line). The dashed lines correspond to the energy dependence on volume as extrapolated from the deformation potentials of the compositional end-members.

In order to obtain strain-corrected bandgap energies, the deformation potentials of InGaN as a function of In content should be known. Owing to the fact that the composition dependence of the bandgap of InGaN is not precisely stablished, it is obvious that there are not experimental values for the deformation potentials of the alloy. Early works dealing with this topic used the deformation potentials of GaN in order to correct the measured bandgap energy of Ga-rich InGaN samples.[57,58,109] For intermediate compositions, it is possible to linearly interpolate the deformation potentials of the compositional end members.[110] Here we rely on the deformation potentials of InN and GaN calculated by Yan et al. in order to obtain the corresponding values at intermediate In contents.[111] These are, for GaN (InN), a_1= −5.81 (−3.62) eV and a_2 = −8.92 (−4.6) eV, which are in good agreement with experimental values.[65]

The strain-corrected bandgap values thus obtained (using Eq. [5.7]) and the results of the optical measurements on our samples, is shown in Fig. 5.5. The corrected energies are around 250 meV lower at low and intermediate In contents. This confirms the sizable effect of strain on the optical gaps of the InGaN alloy. As expected, in the case of indium-rich samples, which are almost completely relaxed (R ~ 100%), the experimental bandgap is not affected by strain.

As can be seen in Fig. 5.6, from the strain-corrected bandgap values, we obtain a bowing parameter of b = 1.45(17) eV. This value is in very good agreement with the recommended value, b = 1.43 eV, reported by Wu et al.[21], and is only slightly lower than the strain-corrected bowing parameter, b = 1.65 eV, obtained from spectroscopic ellipsometry experiments.[102] It is worth mentioning that recent LDA-based *ab initio* calculations, with external corrections to the bandgap problem, found a similar bowing parameter, around b = 1.6 eV.[112] Other calculations based on LDA[64] and PBE[73] functional also found similar bowing parameters, b = 1.63 eV and b = 1.67 eV, respectively.

On the other hand, it is interesting to analyze the origin of b from a fundamental perspective. The bandgap of an alloy can be understood to depend separately on the chemical composition and the volume of the unit cell. The combination of size and chemical effects is often referred as the "chemical pressure" as an analogy of the hydrostatic pressure.[113] This is supported in III-group nitrides by the observation that the volume dependence of the bandgap in indium-rich $In_xGa_{1-x}N$ and $In_xAl_{1-x}N$ matches on a wide compositional range.[10] It has been shown[113] that the bowing parameter is a consequence of differences in the volume of the unit cell and the volume deformation potential, which is defined as

$$a_G = \frac{dE_G}{dlnV} = -B\frac{dE_G}{dP} \ . \qquad [5.13]$$

For the case of InGaN, both conditions are satisfied: the differences in the volume of the unit cell between InN and GaN are around ΔV = 25 %,[113] and the volume deformation potential of GaN ($a_G^{GaN} = -8.1$ eV[79]) is twice as large as that of InN ($a_G^{InN} = -4.0$ eV[114]).

From the volume deformation potentials it is possible to express the bandgap of the compositional end member as a function of the volume of the unit cell of InGaN:

$$E_V(V) = E_0 + \frac{V - V_0}{V_0} a_G \ , \qquad [5.14]$$

where E_0 and V_0 are the bandgap and volume values corresponding to the relaxed unit cell, respectively. The projection of the bandgap energy of GaN and InN (E_V^{GaN} and E_V^{InN} respectively) on the volume of the unit cell of InGaN, $V^{InGaN}(x)$, is shown in Fig. 5.6 as a function of composition. The dependency of V^{InGaN} with composition has been calculated assuming that $V^{InGaN}(x) = a^2(x)c(x)\sqrt{3}/2$ and using Vegard's law for the lattice parameters.

The compositional dependence of the InGaN bandgap arising from size effects can be defined as a weighted average of the volume terms corresponding to the compositional end-members[113]

$$E_G^{InGaN}(x) = x \cdot E_V^{InN} + (1-x) \cdot E_V^{GaN} \ . \qquad [5.15]$$

The curve resulting from Eq. [5.15] for InGaN has been plotted in Fig. 5.6 (curved dashed line). The resulting bowing parameter is b = 1.61 eV, somewhat larger that the value that we have obtained on our samples. From this value it can be concluded that the bowing parameter of InGaN is mainly originated by size effects.

Pressure dependence of the fundamental bandgap

High-pressure optical measurements on the bandgap of InGaN are highly valuable for several reasons. Firstly, they allow one to evaluate the bandgap deformation potentials.[115] Secondly, information on the emission mechanism, such as the participation of localized impurity states, can be revealed from the emission energies and its pressure dependence.[76] Finally, high-pressure optical measurements may also provide information about chemical and interatomic size effects,[10] which is useful to deepen on the nature of the bandgap of semiconductor alloys. For the case of InGaN, it is expected that the pressure coefficient of the bandgap decreases for increasing indium composition as a consequence of the larger ionicity of InN with respect GaN. This due to the fact that higher ionicity entails decreased pressure coefficients, as observed in III-V group compounds.[116] For instance, III-group nitrides with large ionicity such as InN and GaN exhibit much lower bandgap pressure coefficients (32 meV/GPa[114] and 38 meV/GPa[79], respectively) than other III-V group compounds such as GaAs (117 meV/GPa[117]).

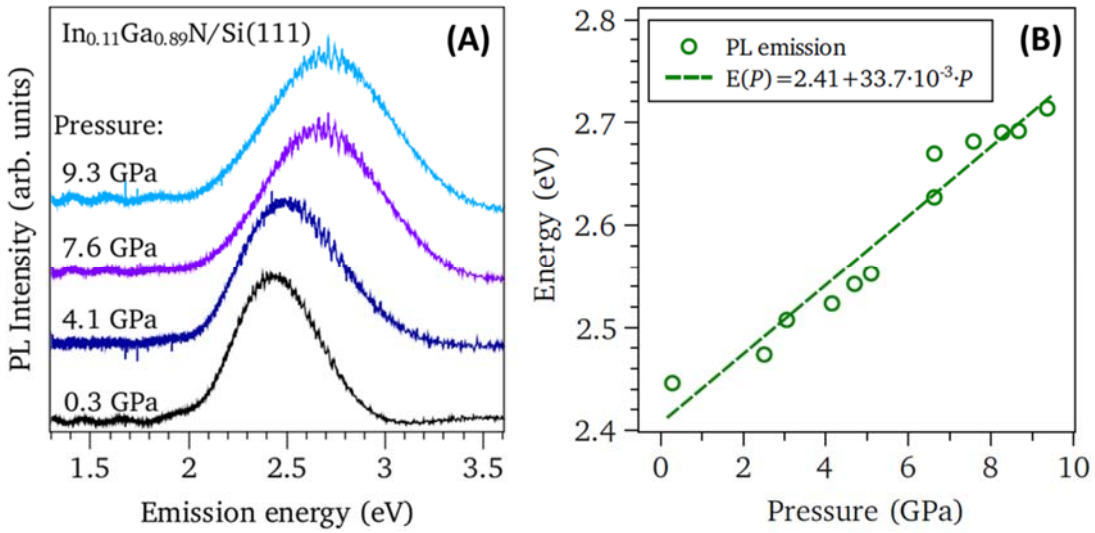

Fig. 5.7. Left panel: Photoluminescence spectra acquired at different pressure values for the sample MD8023 (see Table 5.2). **Right panel:** Linear fit of the emission energy as a function of pressure. A pressure coefficient of 33.7 meV/GPa has been obtained. The measurements have been performed using the 514.5-nm line of an Ar^+ laser and a USB2000+ Ocean spectrometer.

The pressure coefficient of the bandgap of InGaN

For the case of InGaN it has been found that the dependency of the pressure coefficient with composition is sublinear, exhibiting a strong bowing. Moreover, calculations have evidenced that the bowing parameter of the pressure coefficient largely increases if the arrangement of indium atoms is clustered (at a scale lower than 2 nm).[113,118,119] Such a parabolic dependence has been attributed to indium induced changes on the topmost of the valence band.[113,119]

To confirm the strong bowing in the pressure coefficient of the PL emission of InGaN, here we have performed high-pressure PL measurements on the InGaN/Si(111) epilayers (see Table 5.2). The PL spectra and the dependency of the optical gap with pressure for the case of sample MD8023 are shown in Fig. 5.7. As it can be seen by comparing Fig. 5.7 and Fig. 5.2, the PL peak of the InGaN/Si(111) epilayers is ~60% broader than that observed in the samples grown by MBE. This result is likely a consequence of the fact that the samples grown on Si(111) substrates exhibit larger degrees of compositional inhomogeneities. The pressure coefficient for the optical gap measured in sample MD8023 is 33.7 meV/GPa, which, in spite of its poorer optical quality is in agreement with published values.[76] This value has been plotted versus the indium composition in Fig. 5.8 (open red square). In

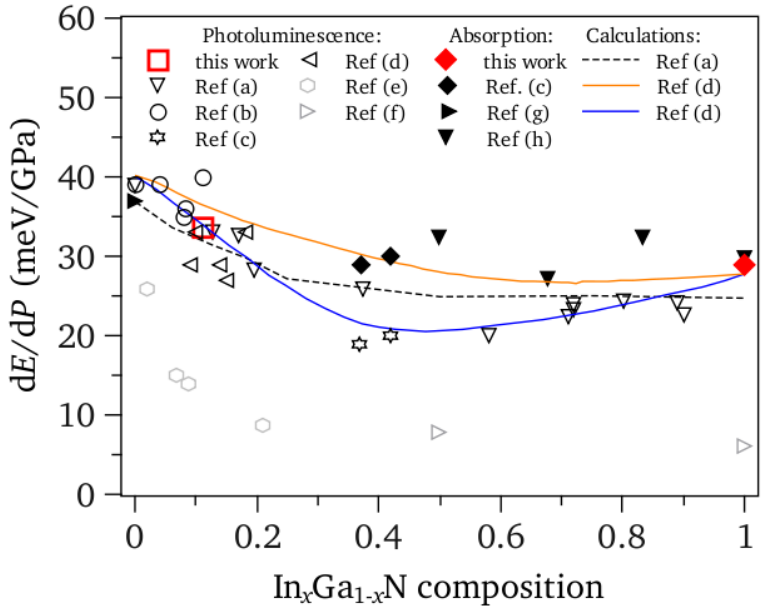

Fig. 5.8. Pressure coefficient of the bandgap of InGaN as a function of composition. Experimental photoluminescence (open symbols), absorption (full symbols) and calculations (dashed and orange lines for an uniform alloy and blue line for a clustered alloy) are compared with the here measured dE/dP of InGaN (red square) and InN (red rhombus). Refs: (a),[76] (b),[79] (c),[125] (d),[118] (e),[120] (f),[121] (g),[123] (h).[121]

this figure other experimental (PL and absorption measurements) and theoretical values published in the literature are also shown. The here obtained pressure coefficient is found to be in good agreement with previous measurements and theoretical calculations.

However, as will become evident below (see Article 5.4 in the results section), the experimental pressure coefficients of the optical phonons in InGaN strongly depend on the substrate material. Thus, it remains to be investigated whether the PL pressure coefficients are also affected by substrate effects. In the case of sample MD8023, the value here obtained could very well be overestimated, and therefore the actual pressure coefficient of the optical emission of this sample could be lower, closer to the samples measured in Ref. (d), as would be expected in more inhomogeneous material. Thus, there is still work to be done in order to understand the role of the substrate and of compositional inhomogeneities on the experimental $\mathrm{d}E_g/\mathrm{d}P$ values of InGaN.

As it can be seen in Fig. 5.8, there is a large dispersion of the pressure coefficient of InGaN in the literature. As a general trend, it can be seen that the pressure

coefficient measured by absorption is higher than the ones measured by luminescence techniques. For the case of PL measurements, three mechanisms may account for the decreased pressure coefficient. Firstly, as observed by Suski et al.[120] the quantum confined Stark effect, responsible for the emission in strained QD's, is almost insensitive to external pressure. Secondly, emission from highly localized (presumably donor-like[76]) states is almost pressure-independent, as observed by Li et al.[121] Indeed, they also measured a composition-independent emission energy (in an absolute energy scale), which allowed them to report deformation potentials for the valence and conduction bands. Finally, as observed for InN from low-temperature PL experiments,[122] band filling effects might decrease the pressure coefficient of the optical bandgap.[123] This latter effect may be expected to occur in absorption experiments likewise.

By comparing calculations and PL measurements, Franssen et al.[76,124] concluded that the origin of the PL emission was band-to-band radiative transitions in their samples, and that the effect of composition fluctuations might not be significant to account for the decreased pressure coefficient measured by PL. In contrast, Millot et al.[125] reported a large reduction of the dE_{PL}/dP with respect dE_{abs}/dP for good quality samples with intermediate In-composition. This was attributed to the existence of highly localized defects which could participate in the emission process. These authors suggest that this mechanism is important at intermedium indium concentration, where the conduction band minimum and the Fermi stabilization energy match.

From the large dispersion in the experimental data and different interpretations, it can be concluded that the measured pressure coefficient is highly dependent on the samples used for the experiments. As suggested by Gorczyca et al.[118] the large scatter of measured values, which typically fall inside the theoretical predictions for two extreme arrangements of atoms (i.e. uniform and clustered), might reflect the degree of indium clustering on samples grown with different conditions.

Regardless the origin of the differences observed between the absorption and PL measurements it seems clear that a large bowing takes place in the pressure coefficient of the fundamental bandgap of InGaN as a function of composition. Such

bowing has been calculated by several authors.[76,118,119,126] The origin of the parabolic dependence of the pressure coefficient of the bandgap can be attributed to the bowing dependence of either; the volume deformation potential, a_G (see Eq. [5.13]), or the bulk modulus, $B = -\mathrm{d}P/\mathrm{d}lnV$. It has been shown that the bulk modulus of InGaN depends almost linearly with composition.[76,118,119,127] Therefore, the decreased pressure coefficient of the alloy is most likely due to an unusual bowing of the deformation potential. It has been proposed that, similarly to the bowing-like dependence of the bandgap, the decreased pressure coefficient may be accounted for by a strong modification of the valence band width, which is more pronounced for a clustered arrangement of the indium atoms.[76,107,118,119]

5.2.2. Vibrational properties

Optical phonons of the alloy

The study of the vibrational properties of InGaN by spectroscopic techniques such as Raman scattering is important from both applied and fundamental perspectives. Raman scattering is a highly valuable technique to obtain information about the strain, the crystal quality and other defect-related phenomena on thin films and nanostructures. In the case of InGaN alloys, Raman scattering measurements allow one to determine the In/Ga content of the films from the compositional dependence of the optical phonon frequencies. For such purpose, it is necessary to understand diverse phenomena related to the lattice dynamics of alloy compounds.

Phonons in alloys

Pseudobinary mixed crystals of the form $A_xB_{1-x}C$ are classified in two classes, the one-mode (or amalgamation type) and two-mode (or persistent type) classes.[128] The one-mode behavior is characterized by a continuous variation of the phonon frequency between those of the composition end-members. For this class, the dependence on molar fraction, x, of the optical phonon modes is typically linear or quasi-linear. On the other hand, in the two-mode behavior two sets of optical modes (each one corresponding to a compositional end-member) coexist in the alloy and may persist until the other compositional end-member. The frequency of these modes in the opposite composition end member is either that corresponding to a local mode (i.e., the frequency of the local vibrational modes, LVM, is that of the impurity modes *AC*:*B* or *BC*:*A)* or a gap mode.[46] It is important to note that some alloys exhibit a mixed mode behavior in which one mode behavior is observed along a particular composition range and a two mode behavior over the remaining composition range.

The two-mode or mixed behavior has been observed in most of the III-V ternary alloys, such as $In_xGa_{1-x}As$,[128] $In_xAl_{1-x}N$,[129] $Al_xGa_{1-x}As$,[130] $In_xAl_{1-x}As$,[131] $Al_xGa_{1-x}P$,[132] $In_xAl_{1-x}P$,[133] $In_xGa_{1-x}P$,[134] $GaAs_{1-x}P_x$,[135] $InAs_xSb_{1-x}$,[136] or $GaAs_xSb_{1-x}$.[137]

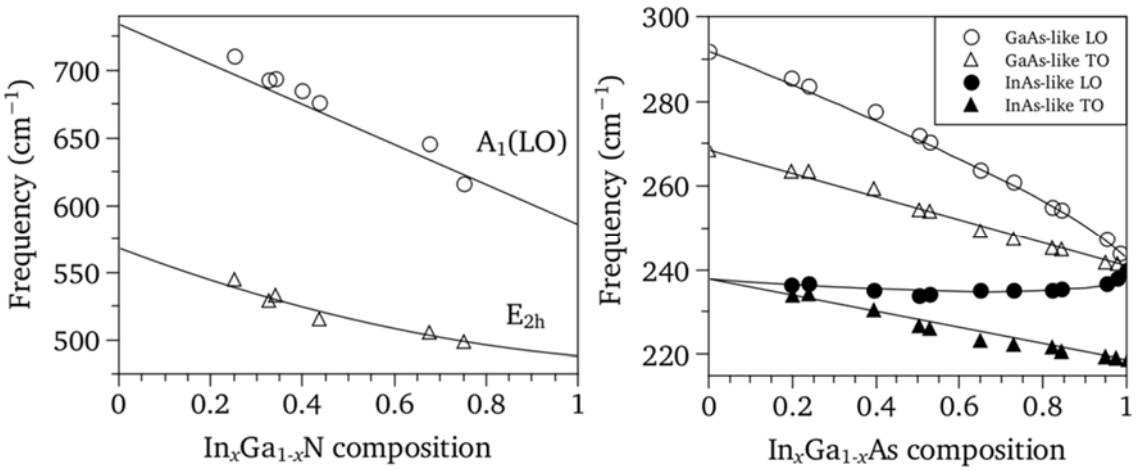

Fig. 5.9. The experimental frequencies of the optical modes of $In_xGa_{1-x}N$[32] (left panel) and $In_xGa_{1-x}As$[128] (right panel) are plotted as a function of composition. The one-mode behavior and two-mode behavior are clear for InGaN and InGaAs, respectively. In the left panel, the straight line for the A_1(LO) phonon mode represents the linear behavior between InN and InGaN while the parabolic line is a fit to the E_{2h} phonon mode. In the right panel, straight lines are interpolated between the composition end-members, and the curved lines are calculated within a model proposed by Groenen et al.[128]

In contrast, the one-mode behavior, which is the case of $In_xGa_{1-x}N$, is much less common.[30,35,46]

In general, two conditions make the two-mode behavior more likely to occur. Firstly, the large difference in frequency of the optical phonon modes at Γ between the composition end members. Secondly, a weak dispersion of the phonon branches along the Brillouin zone (BZ). These conditions are satisfied for ternary systems with a common heavy-mass ion, such as $Al_xGa_{1-x}As$ or $GaAs_{1-x}P_x$. Note that the difference in frequency of the TO mode for GaAs (267 cm^{-1}) in comparison to that of AlAs or GaP (362 cm^{-1} and 364 cm^{-1} respectively) is as large as ~36%. But this is not the case for III-group nitrides where the small reduced mass due to the small mass of the nitrogen anion imply a small optical phonon band width and comparable optical phonon frequencies.[10,46] For instance, the difference in frequency of the A_1(TO) mode between InN and GaN is only around ~19%.

To understand the one-mode behavior of the polar modes of InGaN, it must be recalled that Grille et al.[46] proposed that one-mode behavior is enhanced in highly ionic compounds as a consequence of a strong electrostatic coupling between the *AC*-like and *BC*-like sublattices. Note that AlN, GaN and especially InN are amongst the most ionic III-V compounds. This is in good agreement with the ex-

perimental finding of the one-mode behavior of the polar modes for $In_xGa_{1-x}N$ and $Al_xGa_{1-x}N$ alloys.

In order to illustrate the two classes, the composition dependency of the optical phonon modes of $In_xGa_{1-x}N$ and $In_xGa_{1-x}As$ is shown in Fig. 5.9. The plotted frequencies of the A_1(LO) and E_{2h} modes have been measured using the 325.0-nm line of an He-Cd laser in order to minimize resonance effects on the frequency of the A_1(LO) mode. The dependency of the A_1(LO) mode with excitation energy and strain will be described later in this chapter. Also, strain effects have been corrected for the A_1(LO) and E_{2h} modes. It can be seen that the composition dependency of the A_1(LO) mode is linear, but the E_{2h} mode exhibits a small bowing (b = 46 cm^{-1}). Such a bowing dependence is not typical for the one-mode behavior, and early works interpreted this sublinear dependence to a two-mode dependence of the E_{2h} mode.[28] Later works showed that there exists only one Raman feature around the E_{2h} frequencies along the whole composition range, thus concluding that this mode is one-mode type.[30,32,138]

On the other hand, the optical modes of $In_xGa_{1-x}As$ films (see Fig. 5.9, right panel) have much lower frequencies than those of $In_xGa_{1-x}N$, partly due to the increased mass of the anion. It can be seen that there are two sets of LO and TO modes. These modes shift from the pure member frequencies to those corresponding to the LVMs. In the particular case of the GaAs-like modes, the frequency of the Ga-As LVM virtually matches the frequency of the InAs LO mode, around 240 cm^{-1}. The composition dependency of the TO modes corresponding to each sublattice is linear. In contrast, the LO modes exhibit a pronounced bowling-like dependency. This bowing is accounted for by the coupling of the macroscopic electric field between the LO vibrations of each sublattice.[128]

Insight into the Raman S-band of InGaN

It has been widely reported that the line shape of the A_1(LO) Raman peak of InGaN exhibits an asymmetry. This effect is particularly important when the spectrum is recorded under non-resonant conditions. This is illustrated in Fig. 5.10 for the sample A1035 which is measured in resonant (514.5-nm laser line) and non-resonant (325.0-nm laser line) conditions. As it can be seen in the figure, the spec-

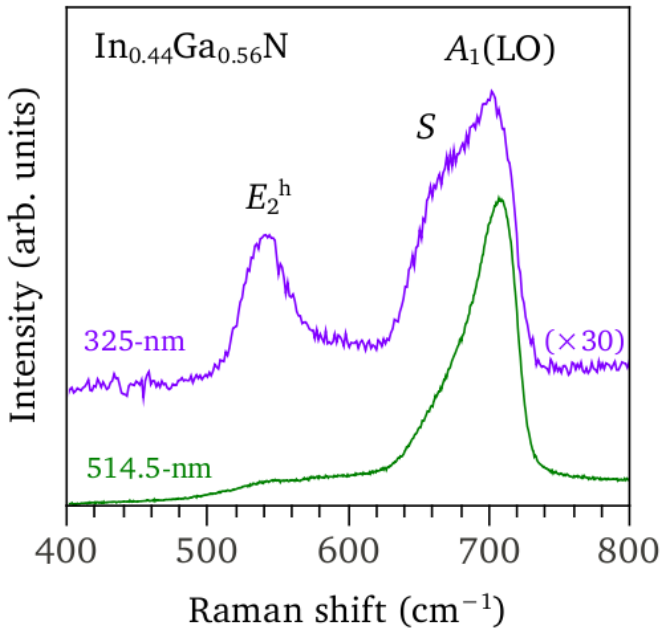

Fig. 5.10.

Raman spectra of the sample A1035 measured with the 325-nm line of an He-Cd laser and the 514.5-nm of an Ar^+ laser. The E_2^h, *S*-band and A_1(LO) Raman modes are clearly visible in the spectrum measured with ultraviolet light (scaled x30). The spectrum measured with green light exhibits a resonant A_1(LO) mode, a large low-frequency shoulder hints the *S*-band. The intensity of the E_2^h mode is very low in comparison the to A_1(LO) mode.

trum measured under resonant conditions is dominated by an intense A_1(LO) slightly-asymmetric peak. In contrast, when the spectrum is recorded in non-resonant conditions, the intensity of the A_1(LO) mode is significantly reduced, an band shows up in the low-frequency region of the A_1(LO) peak (namely "*S* band") and the non-polar E_{2h} Raman mode is observed.

It has been proposed that the *S* band arises from indium-rich regions present as a consequence of phase segregation.[28] But the fact that this low-frequency feature is not observed around the E_{2h} mode indicates that this peak has a different origin. Some authors discussed the asymmetry and shift of the A_1(LO) Raman peak in light of the high electron density naturally present in InGaN epilayers.[26] But their results, which used alpha-irradiated InGaN samples with different N_e concentrations, were not conclusive. It has to be noted that Raman studies on highly doped InGaN samples (N_e = 7−9·10[19] cm^{-3}) of indium concentrations $0.68<x<1$ exhibited a L^- coupled-mode peak around the A_1(TO) mode but any additional feature around the A_1(LO) peak.[139] On the other hand, it has been suggested that this feature arises from the disorder activation of the phonon density of states, which has a maximum slightly below the A_1(LO) frequency.[30,43,140] Finally, some authors attributed the *S*-band to a B_{1h} silent mode.[138] The corresponding phononic branch can be seen in Fig. 4.1 along high-symmetry points in the BZ. At the Γ point, the B_{1h} mode has a frequency ~20 cm^{-1} lower than that of the A_1(LO) mode.[46] Such mode has been

observed in InN[141] and AlGaN.[142] Kontos et al. showed that the stoichiometric-activation of the B_1 silent mode is also responsible for the observation of optical modes in InGaN with forbidden polarization configurations.[35] Owing to the resonant nature of the *S* band, this latter work concluded that the origin of this feature is most likely a B_1 mode rather than a defect-activated phonon mode corresponding to any critical point of the phonon density of states.

Effect of strain on the optical phonon modes

Strain in epilayers

In order to achieve high-quality material with epitaxial growth, substrates with comparable lattice parameters (and thermal expansion coefficients) are usually employed. A schematic picture of an epitaxial thin film grown on a different substrate is shown in Fig. 5.11. It can be seen that the strained in-plane lattice parameter of the epilayer matches that of the substrate. The resulting strain, which influences the optoelectronic properties, must be taken into account in order to understand the performance of double heterostructure or QW-based devices. For the case of thin films grow pseudomorphically on the substrate, strain relaxation by extended defects takes place after a certain thickness. This is because the formation energy of defects becomes lower than the accumulated elastic energy. Thus, at a certain critical thickness (this is, the critical layer thickness, CLT), dislocations, V-type defects and three dimensional growth takes place, partly relieving the in-plane strain.[143–145] This kind of defects propagate along the growth direction. Ultimately these defects act as nonradiative recombination centers, decreasing the performance of optoelectronic devices.[146]

Owing to the fact that $In_xGa_{1-x}N$ is usually grown on GaN/sapphire templates and even on GaN substrates, many works have been devoted to the determination of the CLT(x) for the InGaN/GaN system. Actually there exist a large variety of models for the calculation of this parameter for semiconductors and alloys.[143,147–149] Some of these models have been adapted for the particular case of InGaN/GaN and other hexagonal compounds.[144,145,150,151] Owing to the fact that there is a large difference in lattice parameter and thermal expansion coefficient be-

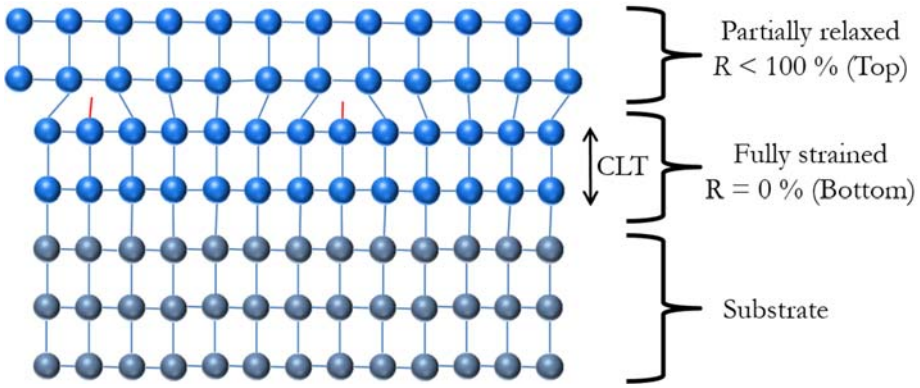

Fig. 5.11. A simple representation of the accommodation of an epilayer on a substrate with a lower lattice parameter is shown. After a critical thickness value, CLT, dislocations appear and the strain is relaxed.

tween InN and GaN, (around 11% and 32%, respectively) the calculations have been focused on InGaN with small indium content (x < 0.3).[152] The large lattice mismatch implies that the CLT(x) is rapidly reduced with increasing In concentration. For instance, indium concentrations higher than 40% correspond to a CLT ~ 1 nm.[43,144]

Experimentally, typical values of the CLT(x) for InGaN/GaN are around CLT ~ 100 nm for 6% indium content, and is decreased to d_{crit} ~ 50 nm for 20% indium content.[101,145,150,153] The experimental determination of the CLT is typically carried out by means of structural,[154,155] optical[101,156] or vibrational techniques such as Raman scattering.[39] Also, morphological changes can be observed in the surface of the InGaN thin films by means of SEM.[43,101,148] Samples grown above the CLT exhibit a rough surface as a consequence of three dimensional growth. This observation confirms the results of recent calculations in which 3D growth is the most important mechanism in releasing strain for InGaN samples with indium concentrations lower than x < 27%. However, the misfit dislocation mechanism becomes important for higher indium concentration values.[43,144]

The phonon deformation potentials

Raman scattering is particularly useful to measure strain in bulk and nanostructured materials.[157] In order to evaluate the strain state of the epilayers from the measured Raman shift of the optical modes, the knowledge of the so-called phonon deformation potentials is necessary. For the case of the wurtzite

ij, *kl*	11	22	33	23, 32	13, 31	12, 21
a, *β*	1	2	3	4	5	6

Table 5.4. Voight notation that relates the components of the fourth order stiffness tensor to a second order simplified tensor.

structure, the relation of the strain-induced Raman shift of the *i*th phonon mode, $\Delta\omega_i$, with the strain, $\boldsymbol{\epsilon}$, or stress, $\boldsymbol{\sigma}$ tensors, is given by the derivation of the linear deformation potential theory,[158,159]

$$\Delta\omega_i = 2a_i\epsilon_{xx} + b_i\epsilon_{zz} = 2\tilde{a}_i\sigma_{xx} + \tilde{b}_i\sigma_{zz} \ , \qquad [5.16]$$

$$a_i = \tilde{a}_i(C_{11} + C_{12}) + \tilde{b}_i C_{13} \ , b_i = 2\tilde{a}_i C_{13} + \tilde{b}_i C_{33} \ . \qquad [5.17]$$

where a_i and b_i are the phonon deformation potentials, PDPs, of each optical mode. It has to be noted that Eq. [5.16] is only valid for the different Raman modes with symmetries A_1, E_1 and E_2 provided that $\epsilon_{xx} = \epsilon_{yy}$ and $\epsilon_{xy} = 0$, which holds for uniaxial, biaxial and hydrostatic measurements. For the case of GaN and InN, the PDPs have been previously determined using samples grown on different substrates, conditions and thickness.[157,160–168] But a_i and b_i can also be obtained with other techniques such as biaxial stress modulation,[169,170] uniaxial pressure measurements,[159] or first principles calculations.[171,172]

The relation between the strain/stress components can be derived from elastic theory. The generalized Hook's law is,

$$\sigma_{ij} = C_{ijkl}\epsilon_{kl} \ . \qquad [5.18]$$

As a consequence of the symmetry of the Cauchy stress tensor ($\sigma_{ij} = \sigma_{ji}$), the stiffness tensor is symmetric, and there are at most six different elements of the stress and strain tensors. Therefore the fourth order tensor C_{ijkl} can be written in a simplified manner as a second order tensor (matrix) $C_{\alpha\beta}$. The relation of the components of both tensors is given by the Voight notation, which is shown in Table 5.4.

The hexagonal C_{6v} structure is transversally isotropic (along the plane perpendicular to the c-axis), and the stiffness tensor has only five independent ele-

ments: C_{11}, C_{12}, C_{13}, C_{33} and C_{44}. For this crystal structure and using the new notation, Eq. [5.18] is expressed as

$$\begin{pmatrix}\sigma_1\\ \sigma_2\\ \sigma_3\\ \sigma_4\\ \sigma_5\\ \sigma_6\end{pmatrix} = \begin{pmatrix}C_{11} & C_{12} & C_{13} & 0 & 0 & 0\\ C_{12} & C_{11} & C_{13} & 0 & 0 & 0\\ C_{13} & C_{13} & C_{33} & 0 & 0 & 0\\ 0 & 0 & 0 & C_{44} & 0 & 0\\ 0 & 0 & 0 & 0 & C_{44} & 0\\ 0 & 0 & 0 & 0 & 0 & C_{66}\end{pmatrix}\begin{pmatrix}\epsilon_1\\ \epsilon_2\\ \epsilon_3\\ \epsilon_4\\ \epsilon_5\\ \epsilon_6\end{pmatrix}, \qquad [5.19]$$

where $C_{66} = \frac{1}{2}(C_{11} - C_{12})$.

For the case of a biaxially strained epilayer on a substrate, $\sigma_i = 0$ for i = 3,4,5,6, and $\sigma_1 = \sigma_2$, $\epsilon_1 = \epsilon_2$. From Eq. [5.19], we obtain the relation

$$\epsilon_3 = \frac{-2C_{13}}{C_{33}}\epsilon_1 \ . \qquad [5.20]$$

For the case of uniaxial strain, $\sigma_1 = \sigma_2 = 0$ and

$$\epsilon_3 = -\frac{C_{11} + C_{12}}{C_{13}}\epsilon_1 = \frac{\epsilon_1}{\nu}\ , \qquad [5.21]$$

where ν is the Poisson's ratio. For the case of hydrostatic pressure, $\sigma_1 = \sigma_2 = \sigma_3 = -P$ and

$$\epsilon_3 = \frac{2C_{13} - C_{11} - C_{12}}{C_{13} - C_{33}}\epsilon_1 \ . \qquad [5.22]$$

For the latter case, some works simply use the expression $\epsilon_3/\epsilon_1 = -2\nu/(1-\nu)$.[163,168,173] While this relation works fairly well for the case of GaN,[172] this is only valid for cubic systems and will not be considered in this thesis.

From the previous expressions it can be seen that it is not possible to obtain a_i and b_i separately using any of this three experiments alone (i.e. applying biaxial strain, uniaxial strain or hydrostatic pressure). Thus, at least two sets of measurements should be performed for such purpose. In order to calculate the PDPs, most works dealing with uniaxial or biaxial experiments stem on the hydrostatic pressure coefficients of the optical modes measured in the literature.[159,167–170]

Effect of excitation wavelength on the A_1(LO) frequency

It is well known that the frequency of the A_1(LO) phonon mode in InGaN is highly dependent on the excitation wavelength. This fact has been discussed in terms of in-depth composition or strain gradients,[30,35,39,40,174] selective resonance excitation,[36,37,45,174] or disorder-induced breakdown of the wave vector conservation.[20,26] Considering the later effect, it has to be noted that decreased phonon frequencies should be observed as a consequence of the participation of phonons with large wave vector. This has not been observed in many works,[30,32,35,37,45] which reported an increase of the A_1(LO) frequency with increasing excitation energy (hence, wave vector). Thus, it can be ruled out that the participation of phonons with large wave vectors is the most important mechanism for the dependence of the A_1(LO) mode with excitation energy. This effect will not be considered in this thesis.

In order to clarify the origin of the dependence of the A_1(LO) frequency on the excitation wavelength, it is important to study a large set of samples with different composition values and degrees of composition inhomogeneity. Also, the measure of the non-resonant modes such as the non-polar E_{2h} mode is highly informative. Nevertheless, the strong signal arising from the resonant A_1(LO) mode and background luminescence, make it difficult to measure the E_{2h} mode near resonant conditions. On the other hand, measuring the A_1(LO) mode well away from the resonant condition is difficult because the *S* band exhibits a similar intensity around the same frequency,[138] such is the case for the Sample A1182 (see Fig. 5.10). In this section, the impact of in-depth gradients of composition and strain will be discussed, and a model for the resonant selective excitation will be proposed. The validity of this model will be contrasted with experimental results reported in the literature and a wide range of experimental data from the samples of Table 5.1 and 5.2 measured under different excitation conditions.

The resonant profile of the A_1(LO) mode

Resonance Raman-scattering (RRS) takes place when the exciting energy coincides with the interband electronic transitions of the material, thus yielding an

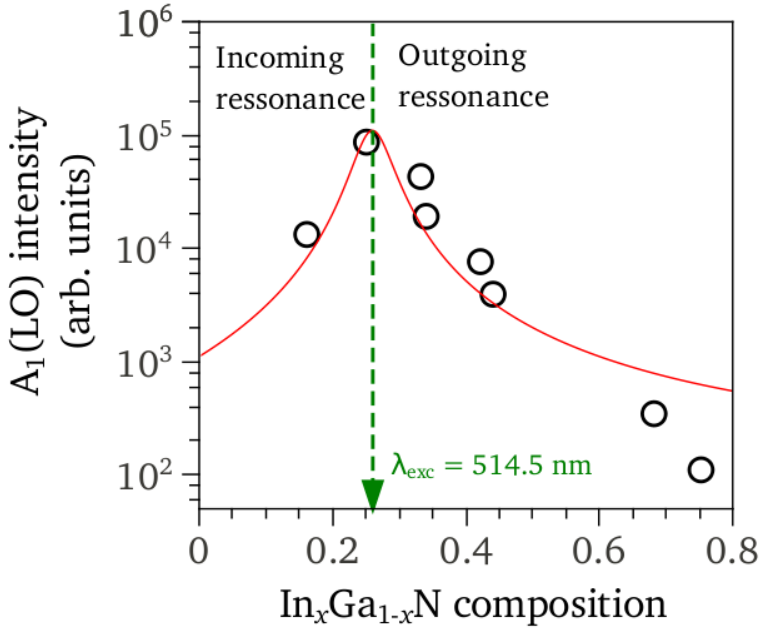

Fig. 5.12. Integrated intensity of the A_1(LO) mode of InGaN as a function of composition. The excitation source was the 514.5-nm line of an Ar^+ laser. For this excitation energy, the resonant condition corresponds to an indium composition of [x] = 26%. The red line is a fitted Lorentzian that represents the resonance profile of the Fröhlich interaction, as used in this thesis.[32]

increased Raman signal. For the case of polar semiconductors, the LO-phonons exhibit a strong enhancement of light scattering when the excitation energy is close to the bandgap due to the electron-phonon Fröhlich interaction mechanism. RRS has been widely employed for group III-V alloys,[36] and is particularly useful for the study of small dimensionality structures. For instance, RRS has been used to study the effect of strain and composition on the phonon frequencies of MQWs[45] as well as the effects of piezoelectric fields in QWs.[44] For the case of thin films, the RRS has been used to evaluate phase separation in wurtzite[38] and cubic InGaN.[175] Also, RRS allows to observe multiphoton processes, which have been studied up to the 5th-LO-mode for the sample A1053.[176] The determination of the bandgap of InGaN by means of RRS has been demonstrated for thin films[20] and heterostructures.[37] In this thesis the resonant profile of InGaN is evaluated in order to provide a possible explanation for the dependence of the A_1(LO) frequency on excitation energy.

Owing to the fact that the A_1(LO) Raman peak is very intense even for excitation energies away from the bandgap energy (around $\Delta E \sim 250$ meV), it has been

suggested that the phonon scattering resonance profile of this mode is broad and strong.[26,30] This is illustrated in Fig. 5.12 for the samples of Table 5.1 measured with the 514.5-nm line of an Ar^+ laser. In this figure it can be seen that the intensity of the A_1(LO) mode increases up to five orders of magnitude as the bandgap of the alloy approaches the energy of the laser, in good agreement with previously published results.[20,26,35–37,45]

The cross section for different resonant mechanisms can be approximated as[177]

$$\frac{d\sigma}{d\Omega}(x) \sim \frac{1}{[E_{exc} - E_g(x)]^2 + \Gamma_g^2}\,, \qquad [5.23]$$

which simply takes into account the fact that the resonant condition takes place when $E_{exc} \approx E_g(x)$. It has to be noted that Eq. [5.23] is a mere approximation to describe the broad resonant profile of InGaN. Using a broadening parameter of Γ_g = 0.1 eV, the bandgap dependency of InGaN described in Eq. [5.1] (bowing parameter b = 1.5 eV) and using an excitation energy E_{exc} = 2.41 eV, the experimental results shown in Fig. 5.12 are satisfactorily reproduced. Note that this simple approach does not take into account many contributions to the cross section scattering such as the scattering volume. For this reason the model fails to fit the intensity of the phonon mode well away from the resonant profile (around x = 0.7 in Fig. 5.12.).

A model for the selective resonance excitation

In order to explain the excitation-energy dependency of the frequency of the A_1(LO) mode, namely ω_{A1}, the selective resonance excitation mechanism has been proposed in several previous works.[30,35,37,45] This is, for a given excitation energy, the compositional regions satisfying the resonant condition contribute more significantly to the A_1(LO) peak intensity.

The line shape of the A_1(LO) peak in inhomogeneous InGaN layers for a given excitation energy can be calculated by integrating the intensities arising from regions with different indium content, weighted by the resonant profile. Assuming

for simplicity that the composition inhomogeneity follows a Gaussian distribution, the line shape of the A_1(LO) Raman peaks can be calculated as

$$\mathrm{I}(\omega, x) \sim \int e^{-\frac{(x'-x)^2}{2\sigma^2}} \frac{1}{[\omega-\omega(x')]^2+\left(\frac{\Gamma_p}{2}\right)^2} \frac{1}{\left(E_{exc}-E_g(x')\right)^2+\Gamma_g^2} dx' \,, \qquad [5.24]$$

where x is the mean indium composition of the sample, and σ is the standard deviation which takes into account the degree of composition inhomogeneity (a typical value of σ is between 5% and 10%). The line shape of the phonon for a given composition x' is expressed as a Lorentzian function with a typical phononic damping value of Γ_p = 5 cm^{-1}. For the calculations, the frequency of the A_1(LO) mode at composition x' is linearly interpolated using the values of InN and GaN. With regard to the resonant term, the parameters used to calculate the curve of Fig. 5.12 have been used.

Then, from the maximum of the line shape calculated by using Eq. [5.24] it is possible to plot ω_{A1} as a function of composition for a given excitation energy. This is shown in Fig. 5.13 for four excitation energies (laser lines in the resonant 633-nm, 514.5-nm and 488.0-nm and away from resonance 325-nm regimes). It can be seen that the dependency of ω_{A1} on the excitation energy is complex due to the effect of the compositional inhomogeneity, and strongly depends on the composition of the sample. It is interesting to note that, for a given excitation energy, ω_{A1} is almost composition independent near the corresponding resonant composition. For instance, for the 514.5-nm line this is [x] = 26 % and for the 633.0-nm line [x] = 40 %. This flat dependence of ω_{A1} with composition partly agrees with previous works that assumed that, under excitation conditions, the intensity of the A_1(LO) mode corresponds to InGaN regions with indium concentration strictly satisfying the resonant condition.[30,37,40,45] This is equivalent to substitute the resonant term in Eq. [5.24] by a delta function, $\delta(E_{exc}-E_g(x'))$. Nevertheless, such assumption overestimates the shift of the ω_{A1} between two excitation energies.

The here measured ω_{A1} for the samples of Table 5.1 (MBE-grown) and Table 5.2 (MOCVD-grown) under different excitation energies are plotted in Fig. 5.13. Despite the simplicity of the model here described, it qualitatively describes the

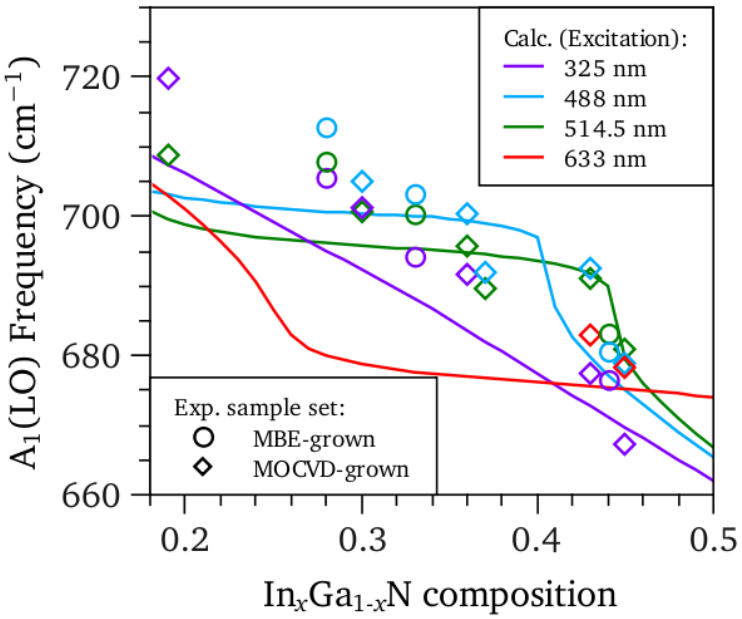

Fig. 5.13. The frequencies of the A_1(LO) mode measured under different excitation laser lines for two set of samples are plot versus the sample composition (open symbols). Theoretical calculations are shown as solid lines. The theoretical model qualitatively describes the ordering of the A_1(LO) frequency with excitation energy.

ordering of the A_1(LO) frequencies with excitation energy. For instance, as it can be seen in Fig. 5.13, the ω_{A1} value measured with the 514.5-nm line is larger than that measured with the 488.0-nm line for samples with less than ~40%. This trend is inverted for samples with indium composition higher than ~40%. Similarly, ω_{A1} exhibits larger values when measured under the 514.5-nm excitation energy with respect the 325-nm line for indium content higher than 28 %, but displays similar values for samples with indium content around 28% (this is a composition close to the resonant condition of the 514.5-nm line, around 26%) and even lower values when the composition is <28%. The calculations based on Eq. [5.24] are in agreement with these trends.

The above model does not aim to account precisely for the dependence of the A_1(LO) frequency with excitation energy. Despite all the simplifications, the calculations plotted in Fig. 5.13 qualitatively agree with the Raman results published in the literature for this mode as a function of excitation energy. To give some examples, the frequency of the A_1(LO) mode measured with blue (λ ~ 488 nm) light is higher than that measured with green laser light (λ ~ 514.5 nm) for indium composition around 18% − 40%.[20,30,35,40,45,174] Also, the frequency of the A_1(LO) mode is

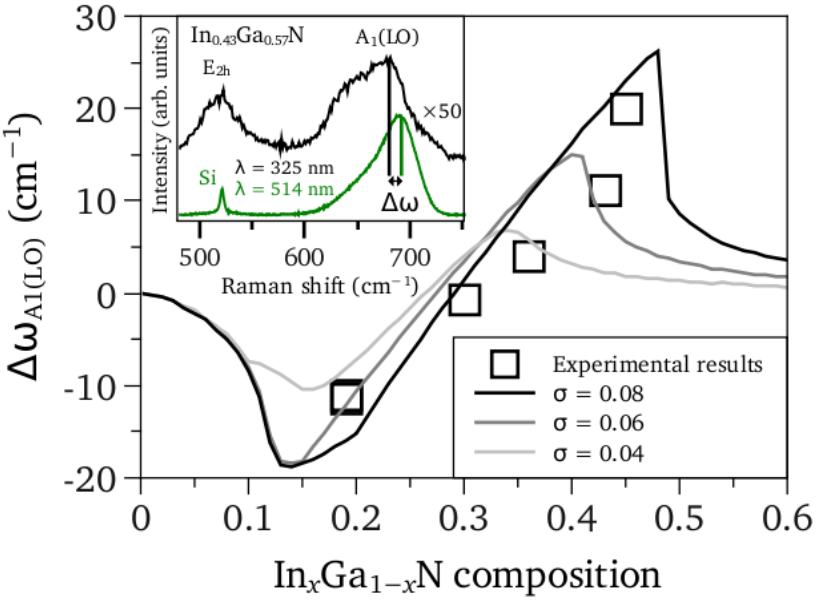

Fig. 5.14. The difference of the A_1(LO) frequency between the 514.5-nm and 325-nm laser lines is shown as a function of composition. The experimental results for the samples of Table 5.2 are shown in open squares. The theoretical dependence as calculated from the model here proposed is shown in solid lines for different degrees of compositional inhomogeneity. Inset: Two spectra measured with the 514.5-nm and 325-nm laser lines for the sample MD7195.

substantially lower when measured with red excitation light (λ ~ 633 nm) in comparison to blue or green light (λ ~ 488 nm to 514.5 nm) in the composition range 24% − 48%.[20,35] Finally, the A_1(LO) phonon mode exhibits larger frequency when the green excitation light is used in comparison to the UV for alloy compositions larger than 26%,[32] and lower frequencies when the composition is lower than 26%.[45]

In order to verify the ability of Eq. [5.24] to reproduce the behavior of the A_1(LO) mode with excitation wavelength due to compositional inhomogeneities, we have performed additional measurements under resonant (514.5-nm laser line) and away from resonance (325-nm laser line) conditions for the InGaN/Si(111) samples grown by MOCVD (Table 5.2). These samples are expected to be more inhomogeneous than the MBE-grown samples (Table 5.1), and therefore we expect to observe larger shits in these samples. Two Raman spectra are shown in the inset of Fig. 5.14 for the sample MD7195 with x = 0.43. It can be seen that for this sample the A_1(LO) frequency as measured under resonant conditions is much larger than that measured with ultraviolet excitation light. The difference between both peaks, $\Delta\omega_{A1}$, has been plotted in Fig. 5.14 for all the MOCVD-grown samples. Also, the

figure shows $\Delta\omega_{A1}$ values calculated from Eq. [5.24] for the same excitation wavelengths, considering different degrees of inhomogeneity. It can be seen that the model reproduces fairly well the trends shown by the Raman measurements. Note that the frequency of the A_1(LO) mode measured with the green excitation line is larger than that measured with ultraviolet light for the out-going resonant regime (compositions higher than 26%) and the trend reverses for compositions in the incoming resonance regime (compositions lower than 26%).

Vibrational properties under high pressure

Optical modes of wurtzite InGaN under high pressure

As already discussed above, the pressure coefficients of the optical modes (and the mode Grüneisen parameter, see Eq. [4.23]) are related to the phonon deformation potentials (PDPs). Owing to the fact that the $a_i(x)$ and $b_i(x)$ PDPs of InGaN (defined in Eq. [5.16]) have not been measured so far, some works linearly interpolate a_i and b_i from the compositional end members or use those of the closest end member in terms of indium composition.[32,35]

Strain in the InGaN epilayers arising from the substrate might affect the experimental pressure coefficients due to the different bulk modulus between the substrate and the epilayer. In order to illustrate this, Eq. [5.16] can be derived with respect the pressure so that the pressure coefficient for the optical modes in strained samples is

$$\omega'_{LO} = \frac{d\omega_{LO}}{dP} = 2a_i \frac{d\epsilon_{xx}}{dP} + b_i \frac{d\epsilon_{zz}}{dP} \,. \qquad [5.25]$$

The variation of the in-plane lattice parameter of the substrate with pressure is related to the bulk modulus by

$$\frac{da}{dP} \approx -\frac{a_0}{3B} \,, \qquad [5.26]$$

which has been derived under the assumption that the ratio of the lattice parameters, c/a, does not vary with pressure. Hence, owing to the fact that the bulk modu-

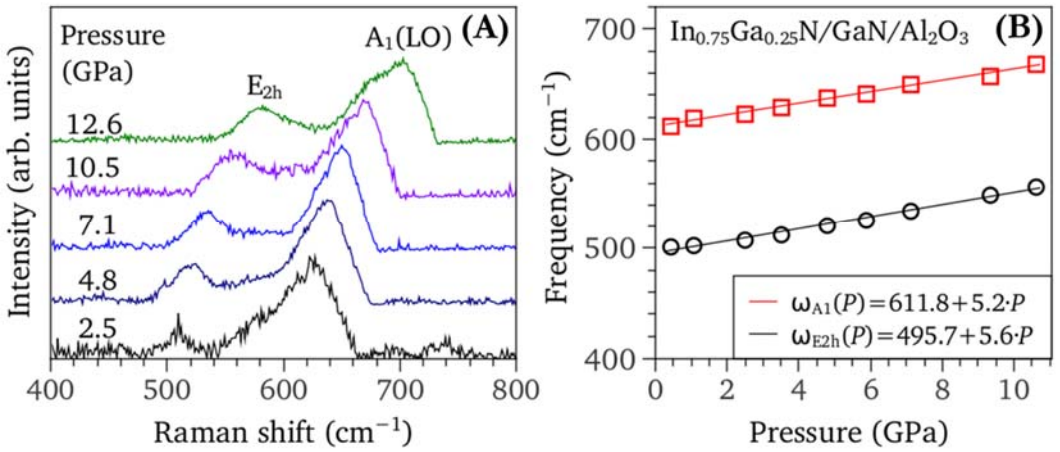

Fig. 5.15. Panel A, Raman spectra of the sample A1182 at different pressures, the E_{2h} and A_1(LO) features can be seen. **Panel B**, pressure-dependence of the frequency of the E_{2h} and A_1(LO) modes and linear fit. These measurements have been performed using a HR460 spectrometer with a single grating and a thermoelectrically cooled CCD. For the excitation source the 514.5-nm line of an Ar^+ laser have been used. The sample has been loaded in a DAC using Neon acting as a pressure-transmitting medium.

lus of Si(111) (GaN) is lower (larger) than that of InGaN, the epilayers studied in this thesis (Tables 5.1 and 5.2) may be expected to exhibit experimental pressure coefficients that are sizably different to those of unstrained material.

The pressure coefficients of the A_1(LO) mode for samples grown on Si(111) and GaN substrates with indium compositions $0.19 < x < 0.45$ are determined in the results section of this chapter (see Article 5.3). For completeness, an indium-rich InGaN/GaN/sapphire sample (A1182, $x = 0.75$, see Table 5.1 for more details) has been additionally measured by high-pressure Raman scattering. The Raman spectra acquired at different pressures for this sample is shown in the panel A of Fig. 5.15. It can be seen that the A_1(LO) mode is not resonant, as expected for an indium rich-sample measured with the 514.5-nm laser line. This allowed measuring simultaneously the A_1(LO) and E_{2h} phonon modes. The pressure coefficients have been obtained from a linear fitting (see Fig. 5.15-B), these are $\omega'_{LO} = 5.2$ cm^{-1}GPa^{-1} and $\omega'_{E2h} = 5.6$ cm^{-1}GPa^{-1}. The here obtained pressure coefficient of the A_1(LO) mode is somewhat lower than the $\omega'_{LO} = 4.9$ cm^{-1}GPa^{-1} expected from the linear interpolation between the values of InN and GaN. As discussed, the reduced pressure coefficient of this sample can be attributed to the effect of the low-compressibility GaN/Al_2O_3 substrate.

Acoustic phonon modes

Brillouin scattering in solids

Light can scatter inelastically with acoustic waves by two distinct mechanisms. The ripple mechanism takes place for surface acoustic waves, and is important for opaque materials. The wave vector is only conserved in the direction parallel to the surface; the wave vector component perpendicular to the surface is complex as a consequence of the complex permittivity in an opaque solid. On the other hand, the elasto-optic mechanism takes place in the bulk and is dominant for transparent materials. For the study of InGaN it is important to consider both mechanisms because InGaN is transparent (opaque) to visible light for low (large) indium concentrations. So far, the elastic constants of InGaN have been evaluated under transparent[178] and opaque Brillouin-scattering conditions (Article 5.3.).

From a classical description of the ripple mechanism, the incident light is reflected from the dynamically corrugated surface as a consequence of the presence of surface-acoustic waves. This effect can be regarded as the diffraction of incoming light by a moving grating, where the Doppler effect accounts for the redshift of the scattered light.[179] In general, a surface or interface acting as a mechanical boundary results in different acoustic excitations (Rayleigh, Lamb, Sezawa, Love modes), typically localized within a wavelength from the surface.[177] It can be shown[180] that the scattering cross section is proportional to

$$\frac{d^2\sigma}{d\Omega_s d\omega} \sim \frac{D}{\omega} \mathrm{Im}\ \tilde{\mathrm{G}}_{33}\left(\boldsymbol{k}_{\parallel}, \omega + i0\right) , \qquad [5.27]$$

where $\tilde{\mathrm{G}}_{33}(\boldsymbol{k}_{\parallel}, \omega + i0)$ is the component of the Fourier domain surface elastodynamic Green's function tensor pertaining to force and response normal to the surface, and D is a factor that depends on the scattering geometry, incident photon frequency, temperature, density and the optical properties of the medium.[181]

On the other hand, the light scattered by the elasto-optical mechanism can be described as the diffraction of the incident light by local fluctuations of the dielectric constant caused by the dynamic fluctuations of the strain field (thermal acoustic waves). All the components of the wave vectors are real and conserved. In

this case, the Brillouin shift can be easily described similarly to the Bragg law. Assuming that the incident and scattered light form an angle; θ, the wavelength of the acoustic wave, γ, must satisfy,

$$2n\gamma \sin\frac{\theta}{2} = \lambda \ , \qquad [5.28]$$

where λ is the wavelength of the light and n the refractive index of the medium. The frequency undergoes a Doppler shift, $\Delta\omega = \upsilon q$, where the scattering wave vector is $q = \frac{2\pi}{\gamma}$ and υ is the phase velocity of the wave. Taking the photon wave vector, $k = \frac{2\pi}{\lambda}$, it follows that

$$\upsilon = \frac{\Delta\omega}{2nk\sin\frac{\theta}{2}} \ . \qquad [5.29]$$

This equation can be likewise derived from a quantum mechanical approach considering the creation/anhihilation of an acoustic phonon imposing the conservation of energy and wave vector.

Solving the elastodynamic wave equation for a transparentent solid

The dynamics of acoustic waves travelling in a solid in a general direction (defined by the Cartesian components, x_i) can be analyzed by defining the displacement field, $u_i(x_j, t)$, that satisfy the elastodynamic wave equation

$$\rho\frac{\partial^2 u_i}{\partial t^2} = C_{ijkl}\frac{\partial^2 u_l}{\partial x_j \partial x_k} \ , \qquad [5.30]$$

where C_{ijkl} is the stiffness tensor for a general solid and ρ is the density. Taking a plane wave

$$u_i(x_j, t) = U_i exp[iq(l_j x_j - \upsilon t)] \ , \qquad [5.31]$$

where U_i is the amplitude of motion along the x_i direction (i.e. the direction of displacement). The propagation direction of the wave is defined by the l_j cosines, with a phase velocity, υ. Solving Eq. [5.30] yields

$$(C_{ijkl}l_j l_l - \rho v^2 \delta_{ik})U_k = 0 \ , \qquad [5.32]$$

which is known as the *Christoffel equation* and is an eigenvalue problem with the polarization U_k as eigenvector of the $C_{ijkl}l_j l_l$ tensor and the eigenvalue ρv^2. Introducing the second rang tensor

$$\Gamma_{ik} = C_{ijkl}l_j l_l \ , \qquad [5.33]$$

Eq. [5.32] has non-trivial solutions when

$$|\Gamma_{ik} - \rho v^2 \delta_{ik}| = 0 \ . \qquad [5.34]$$

For a given propagation direction the roots of Eq. [5.34] are a cubic solution in v^2, this is, two quasi-transversal and two quasi longitudinal bulk waves. These solutions are purely transversal or longitudinal for pure high-symmetry directions, where the polarization vector is respectively perpendicular or parallel to the propagation direction.

For the case of the wurtzite structure, the velocities of the different longitudinal and transversal modes can be obtained by solving Eq. [5.34] (the tensor Γ_{ik} is obtained from the stiffness tensor of the wurtzite structure, Eq. [5.19] and the Voight notation, Table 5.4.). Considering a propagation direction forming an angle θ with the c-axis of the crystal, $l_j = (\sin\theta\,, 0, \cos\theta)$, the sound velocities of the quasi-longitudinal and quasi-transversal mode (positive and negative sign, respectively) are

$$2\rho v^2 = (C_{11}\sin^2\theta + C_{33}\cos^2\theta + C_{44}) \pm \sqrt{[(C_{11} - C_{44})\sin^2\theta - (C_{33} - C_{44})\cos^2\theta]^2 + (C_{13} + C_{44})^2 \sin^2\theta\cos^2\theta} \ , \qquad [5.35]$$

and the transversal mode,

$$\rho v^2 = C_{66}\sin^2\theta + C_{44}\cos^2\theta \ . \qquad [5.36]$$

Note that for θ equal to 0 and $\pi/2$, the modes of Eq. [5.35] are strictly longitudinal and transversal.

Calculating the velocity of SAW for opaque InGaN/GaN thin films

In order to calculate the scattering cross section of the surface acoustic waves (SAW) of InGaN/GaN (see Eq. [5.27]), a fast guide to calculate $\tilde{G}_{33}$ for an opaque thin film on a fast substrate is presented. The method here used follows closely the approaches published elsewhere.[179,182]

Similarly to the transparent case in the previous section, the velocity of a SAW for an opaque layer must satisfy the Christoffel equation. In this case, the in-plane wave vector components are real and are given by the cosines of the scattering geometry. However, the perpendicular component, k_3, is complex and must be determined solving Eq. [5.34] for a given velocity. There are six solutions of k_3 for the bulk and the thin film which are either outgoing waves (real solutions) or evanescent waves ($Im\{k_3^{(n)}\} > 0$). Hence, only three solutions have physical meaning for the bulk, n = 7, 8, 9. The solutions of the elastodynamic wave equation that satisfy the boundary conditions (these are the continuity of the in-plane stress field and displacement field at the interface) take the form

$$u_i^{\pm}(d,\omega) = \sum_{n=1}^{9} A_3^{(n)} U_i^{(n)} \exp\{ik_3^{(n)} d\} \ , \qquad [5.37]$$

where the negative subscript of $u_i^{\pm}$ is referred to the thin film (solutions n = 1, …, 6) and the positive subscript to the bulk (solutions, n = 7, 8, 9). The thickness of the thin film is expressed as d.

The displacement Green function for the free surface of the layer is

$$\tilde{G}_{33}(\boldsymbol{k}_{\parallel},\omega) = \sum_{n=1}^{6} \frac{i}{\omega} (B^{-1})_3^{(n)} U_3^{(n)} \exp\{-ik_3^{(n)} d\} \ , \qquad [5.38]$$

where the polarization eigenvectors, $U_3^{(n)}$, are obtained by solving the Christoffel equation, and the matrix $B_l^{(n)}$ is, for the case n = 1, … , 6 and l = 1, 2, 3

$$B_l^{(n)} = \sum_{pq} C_{3lpq}^{-} U_p^{(n)} k_q^{(n)} \exp\{-ik_3^{(n)} d\} / \omega \ . \qquad [5.39]$$

For n = 7, 8, 9 and l = 4, 5, 6

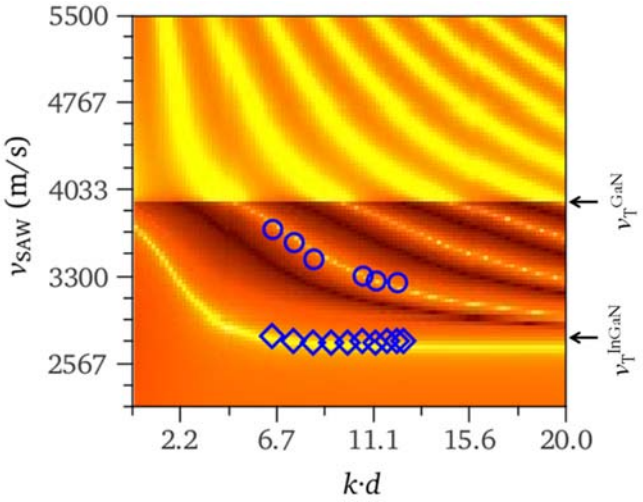

Fig. 5.16.

The wave velocities of the Rayleigh (blue rhombus) and Sezawa (blue circles) modes for the sample A1182 measured under different sagittal angles is compared with the velocity dispersion modes calculated within the Green's function method. The transversal velocities of the substrate, v_T^{GaN} = 3923 m/s, and thin film, v_T^{InGaN} = 2821 m/s are indicated with arrows.

$$B_l^{(n)} = \sum_{pq} C^{+}_{3(l-3)pq} U_p^{(n)} k_q^{(n)} / \omega \ . \qquad [5.40]$$

For n = 1, …, 6 and l = 4, 5, 6

$$B_l^{(n)} = -\sum_{pq} C^{-}_{3(l-3)pq} U_p^{(n)} k_q^{(n)} / \omega \ . \qquad [5.41]$$

Finally, for n = 1, …, 9 and l = 7, 8, 9

$$B_l^{(n)} = \pm U_{l-6}^{(n)} \ , \qquad [5.42]$$

with positive sign for n = 7, 8, 9, and negative sign for n = 1, …, 6.

This model has been used to calculate the cross section of the SAW modes for different InGaN epilayers grown on GaN (see Article 5.3.), which allows to find a good set of elastic constants for InGaN. Illustratively, the velocity dispersion of the different modes is shown in Fig. 5.16 for an $In_{0.75}Ga_{0.25}N$ thin film on a GaN substrate. For the calculations, the density of the alloy has been calculated assuming the Vegard law of the lattice parameters and a bowing-like dependence for the elastic constants (the elastic constants have been taken from Table 5.5).[24,183–185] In Fig. 5.16, the experimental velocities of the Rayleigh and Sezawa modes for sample A1182 (75% indium composition) are also shown, and are in good agreement with the calculations. These have been calculated from the Brillouin shift, $v = 2\pi\Delta\omega/k$.

	C_{11}	C_{12}	C_{13}	C_{33}	C_{34}
GaN	376.4	137.2	114.0	406.8	94.6
InN	222.7	112.1	107.5	258.0	48.5
b	100	43	−4.5	−1	35

Table 5.5. Elastic constants (in GPa) of GaN[183,184] and InN,[185] and bowing parameter[24] for InGaN. Note that for the wurtzite structure $C_{66} = (C_{11} - C_{12})/2$.

The measurements have been performed at different sagittal angles, from 30º to 75º, which relates to the wave vector by $k = 4\pi \sin\alpha / \lambda$.

Raman scattering by acoustic modes in InGaN/GaN superlattices

There is a large interest in the study of semiconductor superlattices (SLs) because of the potential applications for novel devices. These include accommodation layers, high-frequency oscillators, quantum-cascade lasers, or thermoelectric devices.[10] For the case of optoelectronic devices with active material consisting of InGaN/GaN SLs, solar cells have been demonstrated[186] and improved of InGaN/GaN-based LEDs are being developed.[187]

Raman scattering is widely employed to gain information on the elastic properties, crystal quality or periodicity of SLs. Still, in the particular case of InGaN/GaN SLs, the large lattice mismatch between InN and GaN results in important in-plane strains that affect their optical, elastic and vibrational properties. For the case of the InGaN/GaN superlattices studied in this work (see Table 4.3), we have found that the phonon frequency as measured by Raman scattering is mostly determined by the periodicity of the SL rather than the strain state of the samples. In this section, the theoretical background for the analysis of the acoustic modes of InGaN/GaN SL's as measured by Raman scattering is presented.

The presence of a superlattice periodicity strongly influences the structure of the BZ. For the case of SLs with a periodicity, l, and a lattice parameter, a, the edge of the BZ zone is reduced from the one corresponding to the bulk, π/a, to that corresponding to the SL, π/l. The reduced BZ is known as mini-Brillouin zone (mini-

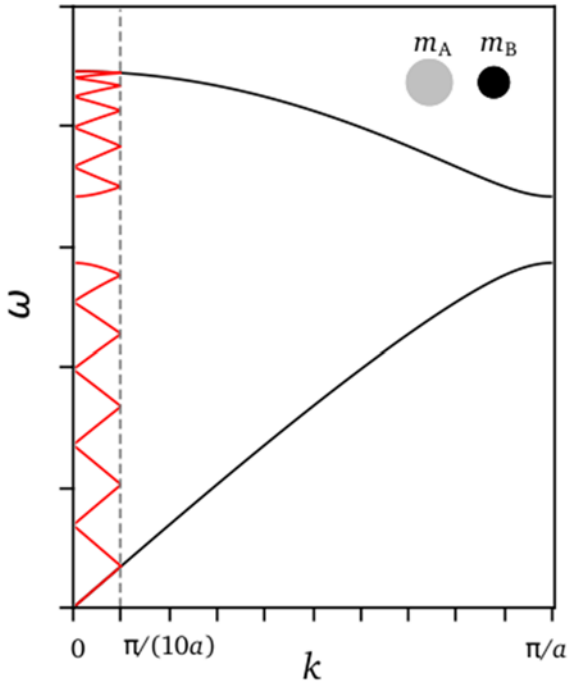

Fig. 5.17.

A linear-chain model calculation of the phonon dispersion curves for the longitudinal acoustic and optical modes. The folding effect can be seen inside the mini-BZ. For the calculation, a 1.5 ratio has been taken between m_A and m_B. The periodicity of the superlattice, *d*, has been taken as 10 times the lattice parameter.

BZ). Contrary to the optical modes, which might be confined within particular layers of the SL, the acoustic modes propagate through the SL with an average velocity given by[188]

$$v = d\left[\frac{d_A^2}{v_A^2} + \frac{d_B^2}{v_B^2} + \frac{d_A d_B}{v_A v_B}\left(Z + \frac{1}{Z}\right)\right]^{-1/2}, \qquad [5.43]$$

where the parameter Z is defined as

$$Z = \frac{\rho_A v_A}{\rho_B v_B}, \qquad [5.44]$$

where ρ is the density of each material and $d = d_A + d_B$.

The phonon dispersion of the acoustic modes exhibits a *folding* inside the mini-BZ. This is shown in Fig. 5.17 for a linear chain model consisting of two atoms with $m_A = 1.5 \cdot m_B$.

The dispersion relation of the folded acoustic modes can be easily calculated within the elastic limit (i.e. at frequencies where the dispersion relation is linear for both constituents),[189] as derived from an elastic continuum model,[190]

$$\cos(kd) = cos\left[\omega\left(\frac{d_A}{v_A} + \frac{d_B}{v_B}\right)\right] - \frac{\varepsilon^2}{2} sin\left(\frac{\omega d_A}{v_A}\right) sin\left(\frac{\omega d_B}{v_B}\right), \qquad [5.45]$$

where

$$\varepsilon = \frac{\rho_B v_B - \rho_A v_A}{\sqrt{\rho_A v_A \rho_B v_B}} \,. \qquad [5.46]$$

The Eq. [5.45] takes into account the splitting of the acoustic branches near Γ and the BZ zone edge, which is a consequence of the different masses of the ions of each constituent.[91] Far from this region, the dispersion relation is simply given by

$$\omega_m(q) = \frac{mv}{d} \pm \frac{qv}{2\pi} \,, \qquad [5.47]$$

in SI units (the frequency is expressed in Hz), where v is the mean sound velocity defined in Eq. [5.43] and m is a natural number including the zero. For a given wave vector, Eq. [5.45] has two solutions, known as *doublets*. The scattering efficiency of these modes decreases with increasing the order of the folding, m. Still, it is possible to estimate v from the splitting of a single doublet from

$$\Delta\omega(q) = \frac{qv}{\pi} \,, \qquad [5.48]$$

while the bandgap opening near the zone center or zone edge can be derived from Eq. [5.45] and is[189]

$$\Delta\omega(q) \cong \pm\varepsilon \frac{v}{d} sin\left[\frac{m\pi}{2}\frac{(1-\alpha)v_B - \alpha v_A}{(1-\alpha)v_B + \alpha v_A}\right] \,, \qquad [5.49]$$

where

$$\alpha = \frac{v_B}{v_A + v_B} \,. \qquad [5.50]$$

The study of the doublets in InGaN/GaN SL's performed in this thesis (see Article 5.2.) allowed us to estimate the sound speed of $In_xGa_{1-x}N$ within the range of experimental error. The values of v_{InGaN} for $0.15 < x < 0.30$ (see Table 5.3 for more details) here obtained are qualitatively in agreement with a linear interpolation of the composition end members (using $8.0 \cdot 10^5$ cm/s and $5.2 \cdot 10^5$ cm/s for GaN and InN, respectively[191]).

5.3. Results and list of published works

The work performed in this thesis dealing with the room-pressure and high-pressure optical and vibrational properties of InGaN has given rise to four publications, Articles 5.1 to 5.4, which have been attached in the following pages:

- **Article 5.1**: *Raman scattering by E_{2h} and A_1(LO) phonons of InxGa1-xN epilayers (0.25<x<0.75) grown by molecular beam epitaxy*, by R. Oliva, J. Ibáñez, R. Cuscó, R. Kudrawiec, J. Serafinczuk, O. Martínez, J. Jiménez, M. Henini, C. Boney, A. Bensaoula and L. Artús.
Published in Journal of Applied Physics (2012), vol. 111, p. 063502.

In this work, we have used Raman spectroscopy to investigate the lattice dynamics, and in particular the composition behavior of the E_{2h} and A_1(LO) phonons of the $In_xGa_{1-x}N$ ternary alloy. One of the main objectives of this work is to understand the room-pressure behavior of the optical phonons in InGaN, prior to the high-pressure Raman studies. For this purpose, we evaluate the role of lateral compositional fluctuations and in-depth strain/composition gradients on the frequency of the A_1(LO) bands. To this end, we have performed visible and ultraviolet Raman measurements on a set of high-quality InGaN epilayers grown by MBE with In contents over a wide composition range ($0.25 < x < 0.75$, see the description of the samples in Table 5.1). In this work we find that the as-measured A_1(LO) frequency values strongly deviate from the linear dispersion predicted by the modified random-element isodisplacement (MREI) model. However, we show that the strain-corrected A_1(LO) frequencies are qualitatively in good agreement with the expected linear dependence. In contrast, we find that the strain-corrected E_{2h} frequencies exhibit a bowing in relation to the linear behavior predicted by the MREI model. Such bowing should be taken into account to evaluate the composition or the strain state of InGaN material from the E_{2h} peak frequencies. We show that in-depth strain/composition gradients and selective resonance excitation effects have a strong impact on the frequency of the A_1(LO) mode, making very difficult the use of this mode to evaluate the strain state or the composition of InGaN material.

- Article 5.2: *Raman scattering by folded acoustic phonons in InGaN/GaN superlattices*, by J. Ibáñez, A. Rapaport, C. Boney, R. Oliva, R. Cuscó, A. Bensaoula, and L. Artús. Published in Journal of Raman Spectroscopy (2012), vol. 43, p. 237.

In this article, Raman scattering is used to investigate the folded longitudinal acoustic (LA) phonons in a series of $In_xGa_{1-x}N$/GaN superlattices (SLs) grown by MBE with different compositions (15% < x < 38%) and SL periods (from 8 to 20 nm). Details of the samples studied in this work can be found in Table 5.3. One particularity of this study is that a novel, ultralow wavenumber filtering module, which provides access to ultralow wavenumber Raman modes on single-grating spectrometers, is used to perform the Raman measurements. The aim of this work is to experimentally detect the acoustic phonons of InGaN by means of Raman spectroscopy. The measurements on the SLs allow us to observe zone-folding effects. The wavenumber behavior of the folded LA modes is well reproduced with a linear dispersion for the folded LA modes as predicted by elastic continuum theory. Finally, we employ the wavenumber of the doublets to evaluate the period of the SLs.

- Article 5.3: *Brillouin scattering determination of the surface acoustic wave velocity in InGaN: A probe into the elastic constants,* by R. J. Jiménez-Riobóo, R. Cuscó, R. Oliva, N. Domènech-Amador, C. Prieto, J. Ibáñez, C. Boney, A. Bensaoula, and L. Artús. Published in Applied Physics Letters (2012), vol. 101, p. 062103.

The aim of this work is to determine the surface acoustic wave velocity in the high-quality $In_xGa_{1-x}N$ layers used in Article 5.1 ($0.34 < x < 0.75$) by means of high resolution Brillouin spectroscopy, with the aim of obtaining information about the compositional behavior of the elastic constants of the InGaN alloy. The sagittal dependence of the surface acoustic velocity has been analyzed by comparing the experimental results with theoretical simulations based on the Green's function formalism. We find the best agreement with our data when the bowing parameters for

the elastic constants as obtained from DFT calculations published in the literature are taken into account. The dependence of the surface acoustic wave velocity on alloy composition is given.

- **Article 5.4:** *High-pressure Raman scattering in InGaN heteroepitaxial layers: Effect of the substrate on the phonon pressure coefficients,* by R. Oliva, J. Ibáñez, R. Cuscó, A. Dadgar, A. Krost, J. Gandhi, A. Bensaoula, and L. Artús.
Published in Applied Physics Letters (2014), vol. 104, p. 142101.

In this article, we present high-pressure Raman-scattering measurements on different $In_xGa_{1-x}N$/Si(111) epilayers ($0.19 < x < 0.45$, see details in Table 5.2). The aim of this work is to determine the mode Grüneisen parameters of InGaN as a function of composition. To our knowledge, this is the first experimental determination of these parameters in the InGaN alloy. We find that the experimental pressure coefficient of the A_1(LO) mode measured in these samples is larger than that expected from the linear interpolation between the corresponding values of GaN and InN. Similar measurements in the InGaN epilayers grown on GaN/sapphire templates used in Articles 5.1 and 5.3 yield much lower values, below the linearly interpolated pressure coefficients. The different results in both types of samples allow us to conclude that the phonon pressure coefficients measured in InGaN are mainly determined by the different compressibility of the substrate and epilayer material. Thus, it is concluded that neglecting substrate effects may yield highly inaccurate phonon pressure coefficients and mode Grüneisen parameters.

JOURNAL OF APPLIED PHYSICS **111**, 063502 (2012)

Raman scattering by the E_{2h} and A_1(LO) phonons of $In_xGa_{1-x}N$ epilayers ($0.25 < x < 0.75$) grown by molecular beam epitaxy

R. Oliva,[1] J. Ibáñez,[1] R. Cuscó,[1] R. Kudrawiec,[2] J. Serafinczuk,[3] O. Martínez,[4] J. Jiménez,[4] M. Henini,[5] C. Boney,[6] A. Bensaoula,[6] and L. Artús[1]
[1]*Institut Jaume Almera, Consell Superior d'Investigacions Científiques (CSIC), Lluís Solé i Sabarís s.n, 08028 Barcelona, Catalonia, Spain*
[2]*Institute of Physics, Wrocław University of Technology, Wybrzeże Wyspiańskiego 27, 50-370 Wrocław, Poland*
[3]*Faculty of Microsystem Electronics and Photonics, Wrocław University of Technology, Janiszewskiego 11/17, 50-372 Wrocław, Poland*
[4]*Departamento de Física de la Materia Condensada, Cristalografía, y Mineralogía, Universidad de Valladolid, 47011 Valladolid, Spain*
[5]*Nottingham Nanotechnology and Nanoscience Centre, University of Nottingham, Nottingham NG7 2RD, United Kingdom*
[6]*Department of Physics, University of Houston, 4800 Calhoun, Houston, Texas 77004, USA*

(Received 16 November 2011; accepted 14 February 2012; published online 16 March 2012)

We use Raman scattering to investigate the composition behavior of the E_{2h} and A_1(LO) phonons of $In_xGa_{1-x}N$ and to evaluate the role of lateral compositional fluctuations and in-depth strain/composition gradients on the frequency of the A_1(LO) bands. For this purpose, we have performed visible and ultraviolet Raman measurements on a set of high-quality epilayers grown by molecular beam epitaxy with In contents over a wide composition range ($0.25 < x < 0.75$). While the as-measured A_1(LO) frequency values strongly deviate from the linear dispersion predicted by the modified random-element isodisplacement (MREI) model, we show that the strain-corrected A_1(LO) frequencies are qualitatively in good agreement with the expected linear dependence. In contrast, we find that the strain-corrected E_{2h} frequencies exhibit a bowing in relation to the linear behavior predicted by the MREI model. Such bowing should be taken into account to evaluate the composition or the strain state of InGaN material from the E_{2h} peak frequencies. We show that in-depth strain/composition gradients and selective resonance excitation effects have a strong impact on the frequency of the A_1(LO) mode, making very difficult the use of this mode to evaluate the strain state or the composition of InGaN material. © *2012 American Institute of Physics*.
[http://dx.doi.org/10.1063/1.3693579]

I. INTRODUCTION

Group-III nitride semiconductors (AlN, GaN, InN, and related alloys) are already employed in a variety of commercial device applications, including InGaN/GaN light emitting diodes and lasers operating in the green-to-blue spectral range, and AlGaN/GaN high-power microwave transistors. The discovery of the low energy bandgap value of InN (0.67 eV) gave rise to renewed research interest in the InGaN ternary alloy, the bandgap of which can be tuned to cover the entire visible spectral range, from the ultraviolet (UV) down to near-infrared wavelengths. This unique property could be exploited for the fabrication of high-efficiency multijunction solar cells, infrared detectors or white-light emitting devices. However, the performance of the applications based on In-rich InGaN alloys is still limited by the poor crystalline quality of the as-grown material. A great deal of research work is currently being devoted to produce InGaN samples with improved crystal quality.[1,2]

Raman scattering is a highly valuable tool to investigate and characterize semiconductor materials and structures. In the case of ternary and quaternary alloys, Raman scattering provides a powerful, non-destructive means to evaluate the composition of the samples (see Ref. 3 for a review on III-V alloys). Numerous studies have been devoted to study the vibrational properties of hexagonal InGaN thin films[4–21] and InGaN/GaN quantum wells.[22–24] Although it is well accepted that both the A_1(LO) and the E_{2h} phonon modes of InGaN display a one-mode behavior,[15,16] there are still open questions regarding the behavior of the optical phonons in the InGaN alloy. While the modified random-element isodisplacement (MREI) model[25] predicts that the frequency of both modes varies linearly from those of the two binary end-members (GaN and InN), some authors have measured E_{2h} frequencies that seem to exhibit a significant bowing in relation to the linear frequency dependence.[9,10,13,21] On the other hand, strong deviations from the linear behavior have also been observed for the A_1(LO) polar mode of bulk InGaN (see for instance the data over the whole composition range reported in Ref. 16. Such deviations are usually attributed to the strain of the samples.[12,20] However, many authors have shown that the A_1(LO) frequency strongly depends on the excitation wavelength and/or on temperature, and different effects have been invoked to explain the observations: i) strain and/or compositional gradients over depth;[13,19] ii) compositional inhomogeneities giving rise to selective

resonant excitation of domains with a particular In content;[5,7,15,17] iii) relaxation of the wave-vector selection rule.[18] Thus, it remains necessary to identify which mechanisms are actually playing a key role in the behavior of the A_1(LO) mode of InGaN.

In the present work we use resonant and non-resonant Raman scattering to investigate the behavior of the A_1(LO) and E_{2h} modes in $In_xGa_{1-x}N$ epilayers grown by molecular beam epitaxy (MBE) ($0.25 < x < 0.75$). Given that the frequency of the optical phonons is highly sensitive to the strain state and composition of the samples, we first present a structural and optical characterization of the InGaN epilayers. High-resolution x-ray diffraction (HRXRD) is used to determine the In composition and the strain state of the InGaN epilayers. The In content of the epilayers is further confirmed by photoluminescence (PL) and cathodoluminescence (CL) measurements. The degree of (lateral) compositional homogeneity of the samples is also studied by CL. Both the resonant and non-resonant spectra reveal that the frequency of the A_1(LO) mode strongly deviates from the expected linear dependence in the samples with $0.25 < x < 0.44$. We show that such strong deviations can be mainly attributed to strain effects. In contrast, we find that the strain-corrected E_{2h} frequencies are redshifted over the whole composition range in relation to the linear behavior, in agreement with previous observations on Ga-rich samples.[9,10] The possible role of lateral compositional fluctuations and in-depth strain/composition gradients on the frequency behavior of the A_1(LO) mode of InGaN is analyzed and discussed.

II. EXPERIMENT

The InGaN epilayers used in this work, with nominal thicknesses in the 0.2–0.96 μm range, were grown by plasma-assisted MBE on (0001)-sapphire substrates with a 4-μm thick GaN buffer layer. Details of the growth procedure can be found elsewhere.[26] HRXRD measurements were performed with a Philips X-Pert PRO diffractometer. Reciprocal space maps (RSMs) around the symmetrical (00.2) and the asymmetrical (11.4) and (01.5) reflections were obtained. From the analysis of the RSMs, the composition and strain state of the InGaN epilayers were evaluated. For details of the procedure, see Ref. 27. Table I shows the In molar fraction and the degree of plastic relaxation of these samples as obtained from the RSMs.

TABLE I. Indium molar fraction (x), degree of plastic relaxation (R), and thickness (d) of the MBE-grown $In_xGa_{1-x}N$ epilayers studied in this work. For samples A969, A1004, A1035, and A1177, x and R were obtained from HRXRD measurements. For samples A1018 and A1182, x and R were estimated by using the HRXRD data from similar InGaN epilayers.

Sample	In content (x)	Plastic relaxation (R) (%)	Thickness (d) (nm)
A969	0.25	68%	200
A1004	0.33	40%	960
A1010	0.34	57%	710
A1018	0.42	~50%	710
A1035	0.44	50%	560
A1177	0.68	100%	500
A1182	0.75	~100%	500

PL spectra were acquired with a FHR1000 Jobin-Yvon spectrometer equipped with a Peltier-cooled CCD camera (514.5-nm excitation). Sample A1182 ($x = 0.75$) was not included in the PL study because the optical emission of this sample is below the detection limit of the experimental set-up. CL measurements were performed in order to study the lateral homogeneity of the InGaN layers at the sub-micron scale. The CL measurements were carried out at low temperature (80 K) on four of the samples (A969, A1004, A1010, and A1018). A XiCLOne (Gatan UK) CL system equipped with a Peltier-cooled charge-coupled device (CCD) camera was employed.

Raman scattering measurements were performed at room temperature in backscattering configuration using a Jobin-Yvon T64000 spectrometer equipped with a liquid N_2-cooled CCD. The experiments were carried out with the 514.5-nm line of an Ar^+ laser for resonant or near-resonant excitation conditions (samples with $0.25 \lesssim x \lesssim 0.44$), and with the 325.0-nm line of an He-Cd laser for non-resonant conditions.

III. RESULTS AND DISCUSSION

A. Structural and optical-emission characterization

Given that the frequency of the optical phonons of InGaN is strongly affected by the In content and strain state of the samples, we first carried out a structural and optical characterization of the InGaN epilayers studied in this work. HRXRD measurements were performed to evaluate the composition and the degree of lattice-constant relaxation in six of the samples (A969, A1004, A1010, A1035, and A1177). Figure 1 shows selected x-ray rocking curves [(00.2) reflection] for samples A1004 ($x = 0.33$), A1035 ($x = 0.44$), and A1177 ($x = 0.68$). Importantly, no phase segregation is observed in any of the rocking curves. The broadening of the x-ray reflections suggests that strain and/or composition gradients may exist along the growth direction. Lateral composition/strain fluctuations may also contribute to the observed broadening.

The nominal thickness of all the InGaN epilayers studied here, in the 0.2–0.96 μm range, is above the expected critical layer thickness.[28] Thus, a partial strain relaxation can be anticipated in all the epilayers. RSMs around the symmetrical (00.2) and the asymmetrical (11.4) or (01.5) reflections

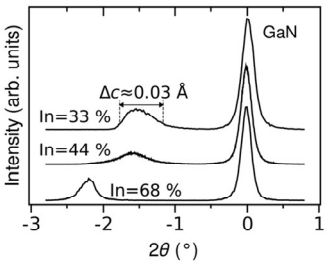

FIG. 1. HRXRD rocking curve corresponding to the (00.2) reflection of three $In_xGa_{1-x}N$ epilayers with $x = 0.33$ (sample A1004), $x = 0.44$ (sample A1035), and $x = 0.68$ (sample A1177).

were obtained for samples A969, A1004, A1010, A1035, and A1177 (not shown). From both the symmetrical and asymmetrical RSMs, information about the in-plane and out-of-plane lattice spacings can be simultaneously obtained, and thus the average In content and the strain state of the InGaN epilayers can be evaluated.[27] In the case of samples A1018 and A1182, the In composition and the degree of lattice relaxation have been evaluated by using the HRXRD data of InGaN epilayers grown under similar conditions. On the other hand, sample A969 exhibited a fairly nonuniform color across the whole wafer. Most probably, the results obtained for this particular sample have larger errors than those obtained for the rest of epilayers. Table I shows the In molar fraction and the degree of plastic relaxation, R, thus obtained. $R(\%)$ is defined as a function of the in-plane component of the strain tensor for the epilayer, $\epsilon_{\parallel} = [(a - a_0)/a_0]$ (a is obtained from the HRXRD measurements), so that $\epsilon_{\parallel} = -[(a_{GaN} - a_0)/a_0](R(\%) - 100)/100$, where a_{GaN} is the in-plane lattice parameter of the GaN substrate and $a_0 = xa_{InN} + (1 - x)a_{GaN}$ corresponds to the relaxed lattice parameter of $In_xGa_{1-x}N$. As can be seen in Table I, the resulting R values show that only the In-rich samples ($x \gtrsim 0.68$) are fully relaxed, while the rest of samples are partially relaxed, with R values ranging from 40% to 70%.

As in the case of the HRXRD curves of Fig. 1, none of the RSMs obtained from our samples (not shown) displayed any signal of phase segregation. The RSMs confirmed that strain and/or composition gradients exist in these epilayers. However, the RSMs did not allow us to discern between composition and strain gradients, as performed for instance in Ref. 29. Nevertheless, the broadening of the x-ray peaks in Fig. 1 can still be used to obtain a rough estimation of the maximum variation of the lattice parameter along the growth direction, Δc, that may arise from in-depth strain and/or composition gradients. For this purpose, we use Bragg's law and assume that all the observed broadening in the (00.2) reflections is originated by in-depth changes in the lattice parameter c. Note that for the present discussion we are deliberately neglecting the contribution of other sources of peak broadening (i.e., the finite coherence length of the microcrystalline domains, microstrain effects, lateral compositional fluctuations, etc.) because our goal is to find an upper limit for the impact of in-depth compositional/strain gradients on the observed broadening. Thus, from the width of the (00.2) reflections we estimate that $\Delta c \lesssim 0.03$ Å in all our samples. In the following sections this value will be used to delimit the impact of strain and composition gradients on the frequency of the A_1(LO) phonon mode of InGaN.

To confirm the In-content values obtained by HRXRD and obtain additional information about the lateral homogeneity of the InGaN layers, PL and CL measurements were carried out on several of the samples studied in this work. The PL peak emission energy obtained for all the samples investigated (not shown) was found to be in good agreement with that measured on InGaN samples of similar compositions.[30] All samples displayed a single, well-defined PL emission band, thus confirming that no measurable phase segregation is present in our samples. This was further corroborated with CL measurements, which allow one to probe the compositional homogeneity of InGaN epilayers and heterostructures at the submicron scale.[14] Fig. 2 shows a typical low-temperature (80 K) CL spectrum of these epilayers, corresponding to a sample with $x = 0.42$ (sample A1018). As in the case of the PL measurements, the CL spectra are dominated by a single peak. The inset of the figure shows a mapping of the CL peak wavelength corresponding to a sample area of 2 μm $\times$ 6 μm. As can be seen in the figure, the CL signal is highly homogeneous, with peak-wavelength variations that are lower than 3 nm over the whole area investigated. Similar results were obtained in the rest of samples investigated with the exception of sample A1004 ($x = 0.33$), where small submicron domains weakly emitting 0.2-0.3 eV below the average emission energy were found to appear in the CL mappings. Such CL signal, arising from regions with slightly larger In contents, is fully compatible with the broadening of the HRXRD reflections and may be attributed to dot-like In-rich regions near the surface of the InGaN epilayers.[31,32] In the rest of epilayers the CL signal was highly homogeneous, with no evidence of InN-rich segregated phases.

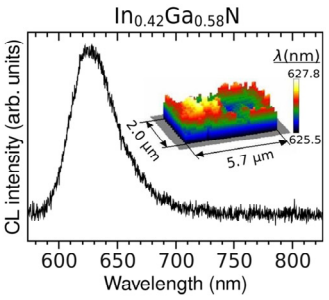

FIG. 2. (Color online) CL spectrum at 80 K of an $In_xGa_{1-x}N$ epilayer with $x = 0.42$ (sample A1018). The inset shows a mapping of the CL peak wavelength over a sample region of 2 μm $\times$ 6 μm.

B. Raman scattering by A_1(LO) and E_{2h} phonons

Figure 3 shows Raman spectra of four representative $In_xGa_{1-x}N$ epilayers. The measurements of Fig. 3 were excited at room temperature with 325.0-nm radiation. Although this excitation wavelength (3.81 eV) is far away from the fundamental band-gap of the $In_xGa_{1-x}N$ samples investigated in this work (~2.4 eV for $x \sim 0.3$), a significant intensity enhancement of the A_1(LO) mode in relation to the E_{2h} peaks is observed with increasing Ga content. This indicates that the Fröhlich interaction mechanisms contribute strongly to the A_1(LO) signal observed in the Ga-rich samples. Taking into account the large energy difference between the excitation radiation and the fundamental band-gap of the samples, the enhancement of the A_1(LO) bands with increasing Ga content can be attributed to a disorder-induced broadening of the resonance profile. Similar results have been reported in disordered III-nitride samples such as ion-beam implanted GaN.[33]

The spectra of Fig. 3 exhibit the expected one-mode behavior for both the E_{2h} and A_1(LO) modes, as predicted by the MREI model[25] and reported in previous studies over

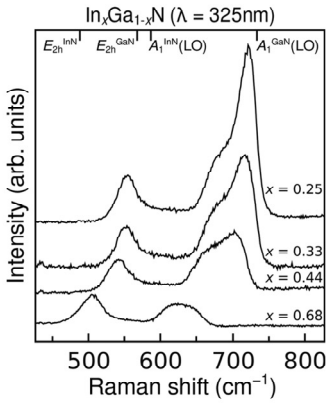

FIG. 3. Selected room-temperature Raman spectra of the $In_xGa_{1-x}N$ epilayers studied in this work, excited with 325.0-nm radiation. The marks on the top axis show the frequency position of the E_{2h} and A_1(LO) modes of the pure binary end memebers of the alloy. For scaling reasons, the spectra have been normalized to the E_{2h} intensity and vertically shifted.

the entire composition range of the alloy.[15,16] A broad feature is also visible in all the spectra below the A_1(LO) band.[12,13,15,17,19] The intensity of this band, which is usually labeled as "S band" in the literature,[12,17] is maximum in relation to the E_{2h} mode for intermediate In compositions, i.e., in the samples with the highest degree of alloy disorder. Thus, most authors attribute this feature to Raman scattering by disorder-activated optical modes arising from alloy disorder. As discussed in Ref. 17, it cannot be ruled out that this band has an important contribution from the B_1 silent mode.

When the laser excitation approaches the direct bandgap of $In_xGa_{1-x}N$, the A_1(LO) band displays a dramatic intensity increase because the A_1(LO) phonon is resonantly excited via the Fröhlich interaction mechanisms. This is illustrated in Fig. 4, which shows selected room-temperature Raman spectra of the InGaN epilayers studied in this work, excited with the 514.5-nm line of an Ar^+ laser. This excitation wavelength yields resonant or near resonant conditions for the Ga-rich samples. In this case, strong multiphonon bands are also observed (not shown, see for instance Refs. 15 and 16). In the particular case of the sample with

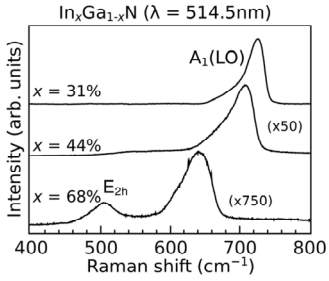

FIG. 4. Selected room-temperature Raman spectra of the $In_xGa_{1-x}N$ epilayers studied in this work, excited with 514.5-nm light. The spectra have been normalized and vertically shifted for scaling reasons. In the spectra of the Ga-rich epilayers, a strong luminescence background has also been subtracted.

$x = 0.68$, the bandgap of which is lower than 1.3 eV, the 514.5-nm spectrum (Fig. 4) shows an increased $A_1(LO)/E_{2h}$ intensity ratio in relation to the 325.0-nm spectrum (Fig. 3). Thus, in the 514.5-nm spectra of the In-rich samples the Fröhlich mechanisms still contribute to the A_1(LO) signal, which again is a consequence of disorder-induced broadening of the resonance profile.

Figure 5 shows the composition dependence of the A_1(LO) peak frequency for all the samples studied in this work as obtained from the 325.0- and 514.5-nm Raman spectra. In the case of the two In-rich samples it was not possible to determine the A_1(LO) peak frequency from the UV measurements because, as can be seen in Fig. 3, the A_1(LO) mode is weaker and superimposed to the S band. In Fig. 5 the solid line represents the frequency behavior predicted by the MREI model,[25] i.e., the linear interpolation between the GaN and InN frequency values. Even considering the relatively large errors associated with the In content determination by HRXRD, it is clear that the Ga-rich samples ($x < 0.5$) do not follow the frequency dependence predicted by the MREI model, while only the In-rich samples seem to exhibit the linear behavior. Similar observations were reported by Hernández *et al.* [15] and by Ager *et al.*, [16] who found that in the $0.2 < x < 0.5$ range the frequency of the A_1(LO) mode tends to be significantly upshifted in relation to the predictions of the MREI model. On the other hand, the figure also shows that the peak frequencies extracted from the visible spectra are consistently higher, around 7–10 cm^{-1}, than those obtained with the UV measurements. The possible origin of these shifts will be discussed later.

C. Strain-corrected A_1(LO) and E_{2h} frequencies

As observed by HRXRD, our Ga-rich samples exhibit significant degrees of lattice strain. On the other hand, the fact that only the In-rich (i.e., fully-relaxed) samples seem to follow the frequency behavior predicted by the MREI model suggests that the A_1(LO) frequency of the Ga-rich epilayers must be strongly affected by strain. To further evaluate this point, we have calculated the A_1(LO) frequency in strain-free $In_xGa_{1-x}N$, $\omega_0(x)$, as a function of the In molar fraction (x) by using the A_1(LO) frequencies measured in our samples, $\omega_{exp.}$, and correcting them for strain according to the plastic

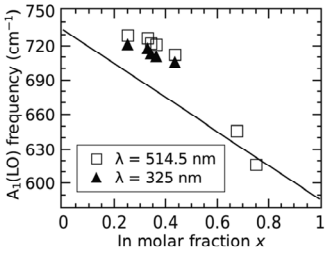

FIG. 5. Experimental frequency values for the A_1(LO) mode of InGaN as a function of In composition. Squares correspond to visible measurements (514.5-nm excitation) whereas triangles correspond to UV experiments (325 nm). The solid line displays the composition dependence of the A_1(LO) frequency predicted by the modified random-element isodisplacement model (Ref. 25).

relaxation values obtained by HRXRD (see Table I). Note that in the case of the two In-rich epilayers, the strain-corrected frequency values just correspond to the experimental frequencies, since these two samples are fully relaxed as indicated by the HRXRD measurements. For the calculations, we have assumed biaxial strain conditions and we have used the standard expression for the strain-induced phonon frequency shift in wurtzite compounds together with the appropriate phonon deformation potentials, $a_\lambda(x)$ and $b_\lambda(x)$, as a function of In content,

$$\omega_0(x) = \omega_{\text{exp.}} - \left(b_\lambda(x) - \frac{a_\lambda(x)C_{33}(x)}{C_{13}(x)}\right)\epsilon_\perp, \qquad (1)$$

where $C_{13}(x)$ and $C_{33}(x)$ are elastic constants for the wurtzite crystal and $\epsilon_\perp = [(c - c_0)/c_0]$ is the out-of-plane component of the biaxial strain, with $c_0 = xc_{\text{InN}} + (1 - x)c_{\text{GaN}}$. The phonon deformation potentials for the pure GaN and InN compounds have been taken from Refs. 34 and 35, and we have used the A_1(LO) frequency values obtained with the non-resonance measurements (325.0 nm in the case of the Ga-rich samples) to minimize possible frequency shifts arising from selective resonant-excitation effects (see discussion below). We show in Fig. 6 the resulting frequency values for the A_1(LO) mode in strain-free $In_xGa_{1-x}N$ as a function of x. As can be seen in the figure, the strain-corrected A_1(LO) frequencies are much closer to those predicted by the MREI model, which confirms that strain strongly affects the frequency behavior of the A_1(LO) mode of the InGaN alloy. Similar conclusions were reached by Correia *et al.* [12] on pseudomorphic $In_xGa_{1-x}N$ epilayers in the low-In composition range ($x < 0.11$). In that work, the A_1(LO) mode was found to be almost composition independent owing to the opposite contribution of biaxial strain and In content. In the case of the present work, the observed deviations between calculated and experimental A_1(LO) frequencies (Fig. 6) can be most probably attributed to the relatively large errors in the evaluation of the strain and composition of the samples by HRXRD, and also to errors in the phonon deformation potential values used in the calculations. However, as can be seen in Fig. 6, the strain-corrected A_1(LO) frequency values are still higher than the predictions of the MREI model. With regard to this, one should also recall that the probe depth of the UV Raman measurements (a few nanometers) is much smaller than that of the HRXRD measurements. Thus, the effective R values corresponding to the shallowest regions of the epilayers probed by the UV light (i.e., the more relaxed regions) may be expected to be larger than the R values given in Table I. This implies that the A_1(LO) frequency values of Fig. 6 have been overcorrected (i.e., the strain-corrected A_1(LO) frequency values of the figure should actually lie more separated from the MREI predictions). More work should be carried out in order to ascertain if the results of Fig. 6 can be solely attributed to experimental errors or to an additional effect. For instance, the observed deviations could be originated by a contribution of the forbidden E_1(LO) mode due to disorder or to sample mosaicity, as occurs in disordered III-nitrides[36,37] or in nanostructured material.[38,39]

A similar analysis using the appropriate phonon deformation potentials can be applied to obtain the compositional dependence of the frequency of the E_{2h} mode in strain-free $In_xGa_{1-x}N$. Figure 7 shows the calculated frequency values for the E_{2h} mode of strain-free $In_xGa_{1-x}N$ for the samples studied in this work. a_λ and b_λ values for the E_{2h} mode of GaN and InN have been taken from Refs. 34 and 35. For the In-rich samples the E_{2h} data points just correspond to the experimental values since, as observed by HRXRD, these samples are fully relaxed. In the figure, we have included data points from Refs. 10 and 21 and also from the In-rich samples of Ref. 16. Clearly, the strain-corrected E_{2h} frequencies do not follow the expected linear dependence predicted by the MREI model[25] but exhibit a marked bowing effect. A fit to the data of Fig. 7 with an expression of the type $\omega(x) = x\omega_{\text{InN}} + (1 - x)\omega_{\text{GaN}} - bx(1 - x)$, where $\omega(x)$ is the frequency of the E_{2h} mode for a given composition x, yields a value of $b = 46$ cm^{-1}. In Ref. 10, a similar observation in $In_xGa_{1-x}N$ films with $x < 0.5$ led the authors to conclude that the E_{2h} mode exhibits a two-mode behavior, as occurs in $Al_xGa_{1-x}N$.[40] In the present work, using data over the whole composition range, we conclude that the E_{2h} mode of $In_xGa_{1-x}N$ exhibits a one-mode behavior and suffers a strong bowing effect. Very recent work by Kim *et al.* [21] seems to point in the same direction. The observed frequency bowing might be related to a disorder-induced mixing between the E_{2h} and E_1(TO) phonons, since the atomic vibrations of these

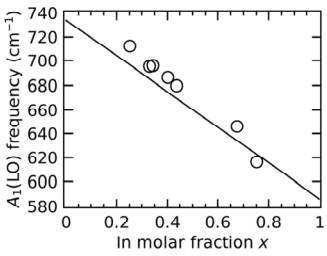

FIG. 6. Strain-corrected frequency of the A_1(LO) mode of the $In_xGa_{1-x}N$ epilayers studied in this work as a function of x. The solid line represents the linear composition dependence predicted by the modified random-element isodisplacement model (Ref. 25).

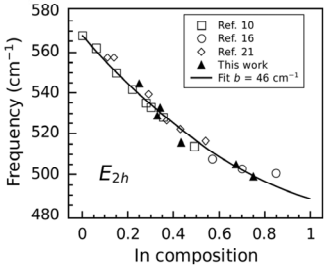

FIG. 7. Strain-corrected E_{2h} frequency values vs In molar fraction for the InGaN epilayers studied in this work (triangles). Additional data reported in the literature from strain-free samples have been included in the plot (squares and circles). The solid line shows the result of a parabolic fit for all the experimental points. From the fit, a bowing parameter equal to 46 cm^{-1} was obtained.

two modes are both perpendicular to the c axis of wurtzite. In the case of $Al_xGa_{1-x}N$, it has been reported that the E_{2h} and E_1(TO) peaks from different scattering configurations have identical shapes and frequencies, which has been attributed to mixing of these two modes.[40] More work is necessary in order to fully understand the origin of these observations.

D. Dependence on the excitation wavelength of the A_1(LO) frequency

As observed in Fig. 5, the A_1(LO) peak frequencies obtained from the UV Raman spectra of our $In_xGa_{1-x}N$ samples ($0.25 < x < 0.45$) are consistently lower than those obtained with the visible measurements. Note that the present measurements did not allow us to study the wavelength dependence of the E_{2h} peaks, since this mode was only visible under non-resonant excitation conditions.

Significant frequency variations of the A_1(LO) mode of InGaN as a function of the excitation wavelength have been reported in the literature.[13,15,17–19] Different effects such as strain/compositional gradients,[13,19] selective resonant excitation,[5,7,15,17] or disorder-induced breakdown of wave-vector conservation[18] have been invoked to explain the observed shifts.

With regard to the latter effect, it should be noted that the participation of phonons with increased wave-vectors for excitation wavelengths approaching the band-gap of the material would be expected to yield lower A_1(LO) frequencies.[18] In the case the present study we observe the opposite effect, i.e., close to resonance (514.5 nm) the frequency of the A_1(LO) mode in the Ga-rich samples is significantly higher than in the case of the UV spectra. Hence, wave-vector non-conservation can be ruled out as the underlying mechanism giving rise to the results of Fig. 5.

On the other hand, strain and/or compositional gradients are good candidates to explain the observed frequency variations of the A_1(LO) mode.[13,19] The presence of in-depth strain and composition gradients in the InGaN alloy seems to depend on the particular growth method and growth conditions. For instance, Pereira *et al.*[29] showed that the relaxation of strain in InGaN epilayers grown by metal organic chemical vapor deposition (MOCVD) is accompanied by increased In contents. Similarly, Wang *et al.*[41] reported increased In contents along the growth direction in Ga-rich InGaN layers grown by MOCVD. Quantum-dot-like emission from In-rich regions arising from the upper part of MOCVD-grown InGaN epilayers has been reported.[32] On the other hand, the laterally averaged In content was found to be constant, and even to slightly decrease along the growth direction, in InGaN epilayers grown by MBE.[42]

Bearing in mind the strong impact of strain on the frequency of the A_1(LO) and E_{2h} phonons of InGaN (see Fig. 6 and related discussion), one should recall that the 325.0-nm excitation radiation only probes the shallowest regions of the epilayers (~35 nm in the case of GaN). Thus, the lower A_1(LO) peak frequency obtained with the UV Raman measurements in the Ga-rich samples might be partly accounted for by a higher degree of strain relaxation and/or a higher In content of the shallowest regions in comparison to the deeper regions probed by the 514.5-nm light. As discussed in Sec. III A, the x-ray reflections observed with HRXRD are fairly broad, indicating that strain and/or composition gradients may exist in the epilayers along the growth direction. Unfortunately, given that the enhancement of In content along the growth direction is in general linked to the strain relaxation of the InGaN films,[41] it is very difficult to discriminate between in-depth strain gradients and composition gradients from the Raman spectra alone.

To understand the results of Fig. 5 and also to shed additional light on the origin of the large dispersion of results in the literature regarding the behavior of the A_1(LO) mode of $In_xGa_{1-x}N$, we have performed a series of simple calculations to evaluate the impact of lateral compositional fluctuations and of strain/composition gradients on the frequency of this mode. The aim of such calculations is not to find out the exact mechanism underlying our experimental results and those reported in the literature, but to provide additional clues about the impact of each effect on the Raman spectra of InGaN alloys.

1. In-depth composition and strain gradients under non-resonant conditions

First, we concentrate on in-depth composition gradients for non-resonance Raman scattering by the A_1(LO) mode of InGaN. We make use of the Δc value extracted from the HRXRD spectra and assume, for simplicity, that all the broadening of the (00.2) x-ray reflections (see Fig. 1) solely arises from in-depth compositional gradients, with no contribution of strain gradients. As discussed in Sec. III A, we estimate that the observed peak broadening roughly corresponds to lattice-parameter variations lower than 0.03 Å. Using Vegard's law for the composition dependence of the relaxed lattice parameter of $In_xGa_{1-x}N$, we infer that the maximum in-depth composition gradients that may be present in our samples are of the order of $\Delta x = 0.05$–0.08. Taking into account the linear composition dependence of the A_1(LO) mode of InGaN predicted by the MREI model, we estimate that such x variations should yield frequency shifts of about $7-12\ cm^{-1}$, consistent with the frequency shift of the A_1(LO) mode that we observe between the visible and UV Raman measurements ($7-10\ cm^{-1}$).

Conversely, if we assume that all the broadening observed by HRXRD in the (00.2) reflections is solely originated by in-depth strain gradients, the corresponding A_1(LO) frequency variation can be estimated through error propagation arguments from the derivative of Eq. (1) and employing the definition of $\epsilon_\perp$,

$$\Delta\omega_{exp} = \left(b_i(x) - \frac{a_i(x)C_{33}(x)}{C_{13}(x)}\right)\frac{\Delta c}{c_0(x)}. \qquad (2)$$

By using this expression together with the value $\Delta c \lesssim 0.03$ Å extracted from the x-ray reflections, we estimate that the A_1(LO) mode of $In_xGa_{1-x}N$ should exhibit frequency shifts of ~10–12 cm^{-1} in our samples. These values are also compatible with the observed frequency shift exhibited by the A_1(LO) mode observed in our samples as a function of the

excitation wavelength. Following these analyses, it can be concluded that a combination of in-depth strain relaxation and compositional gradients may be very well responsible for the consistently higher A_1(LO) frequency values measured in our samples with 514.5-nm radiation relative to the 325.0-nm spectra.

2. Selective resonance excitation

The previous discussion has been restricted to non-resonant conditions. Lateral compositional fluctuations have not been considered since they are expected to yield broadening of the Raman peaks, with no effect on the A_1(LO) frequency. With regard to resonant excitation, several authors have reported frequency shifts of the A_1(LO) mode of InGaN as a function of the excitation wavelength that are most likely related to selective resonant excitation of regions with different In contents.[5,7,15,17] In general, however, it is not easy to discriminate in a particular sample between strain effects and the selective excitation of the A_1(LO) band, since both types of effects may yield frequency shifts of equal or opposite direction depending on the excitation wavelength used to perform the Raman experiments. Note also that the magnitude of the selective excitation on the frequency behavior of the A_1(LO) mode is expected to depend upon the particular degree of compositional inhomogeneity of the sample under study.

To qualitatively illustrate the effect of selective excitation on the frequency of the A_1(LO) frequency of $In_xGa_{1-x}N$, we have performed a simple calculation of the A_1(LO) phonon frequency under resonant excitation for a sample in which the compositional inhomogeneity is assumed to follow a Gaussian distribution. For simplicity, we consider only lateral compositional fluctuations and neglect the effect of in-depth fluctuations, since these should yield modified A_1(LO) line shapes due to the depth dependence of the absorption coefficient related to different In contents. Within this crude approach, theoretical Raman line shapes may be obtained with the following expression:

$$I(\omega) = \int \exp\left(-\frac{(x'-x)^2}{2\sigma^2}\right) \mathcal{L}[\omega(x')] \frac{1}{[E_{exc} - E_g(x')]^2 + \Gamma_g^2} dx', \tag{3}$$

where the first term in the integral corresponds to a Gaussian distribution centered at a composition x and standard deviation equal to σ. In the previous expression, $\mathcal{L}(\omega)$ represents a Lorentzian function for the A_1(LO) bands arising from domains with an In content equal to x' (i.e., a Lorentzian function centered at a frequency $\omega(x') = x'\omega_{InN} + (1 - x')\omega_{GaN}$ as given by the MREI model). For simplicity, we have taken a constant full-width at half maximum for the Lorentzian function $\mathcal{L}[\omega(x')]$ equal to $\Gamma = 5$ cm^{-1}. The last term of Eq. (3) represents the profile of the resonant enhancement for the Fröhlich interaction mechanisms which, following Ref. 43, we have taken as a Lorentzian function. In the last term of the equation, E_{exc} stands for the energy of the excitation radiation, $E_g(x')$ is the fundamental bandgap of the alloy for domains with a composition x', and Γ_g is the broadening parameter of the resonance profile. For simplicity, we have assumed that Γ_g does not depend on In content, and we have taken a value $\Gamma_g = 0.1$ eV to model the broad resonance profile of the InGaN alloy.[16]

Figure 8 shows A_1(LO) peak frequencies obtained with Eq. (3) as a function of the energy of E_{exc}, for $In_xGa_{1-x}N$ material with an average In content of $x = 0.3$ and different σ values. As can be seen in the figure, for resonant excitation below the bandgap energy (2.32 eV for $x = 0.3$) Eq. (3) predicts a downward frequency shift of the A_1(LO) mode due to the compositional fluctuations, with a minimum A_1(LO) peak frequency value that depends on σ. As expected, the effect of the compositional inhomogeneity on the frequency shifts becomes larger when σ is increased. For lower E_{exc} values, far away from resonance, the theoretical A_1(LO) peak frequency tends to the A_1(LO) frequency corresponding to the average composition of the sample (x in Eq. (3)). Conversely, the lateral composition fluctuations give rise to an upward frequency shift of the A_1(LO) mode for above-bandgap excitation, reaching a maximum that again depends on σ. As can be seen in the figure, Eq. (3) predicts strong shifts of the A_1(LO) peak frequency, relative to the average A_1(LO) frequency, for excitation wavelengths just around the average bandgap value of the material. In particular, the model predicts frequency shifts as large as 10 cm^{-1} for $\sigma = 6\%$. Note that similar compositional fluctuations, and comparable upward frequency shifts for near-resonant above-bandgap excitation, have been reported in the literature and attributed to compositional fluctuations.[7] Thus, leaving aside the simplicity of this model, the results of Fig. 8 show that selective resonance effects also play an important role in the behavior of the A_1(LO) mode in InGaN material with significant degrees of compositional inhomogeneity. This is clearly the case of many of the samples studied in the literature.[5,7,15,17]

With regard to the samples studied in this work, the higher A_1(LO) frequencies measured in the Ga-rich epilayers ($0.25 < x < 0.45$) under near-resonant excitation (514.5 nm) in relation to the UV spectra (see Fig. 5) might be partly explained by selective resonant-excitation effects. However,

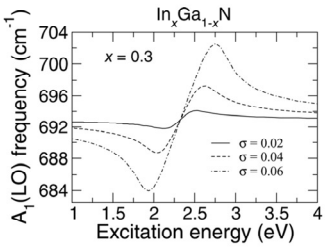

FIG. 8. Calculated A_1(LO) frequency of $In_xGa_{1-x}N$ for resonant Raman-scattering measurements as a function of the excitation energy. The theoretical curves are obtained within a simple approach in which the effect of selective resonant excitation due to lateral compositional fluctuations is evaluated by assuming that the compositional inhomogeneities follow a Gaussian distribution centered at a composition x. σ is the standard deviation of the Gaussian distribution. The curves in the figure were obtained for $x = 0.3$ and different values of σ.

as can be seen in Fig. 5, all the A_1(LO) frequency values extracted from the 514.5-nm spectra exhibit comparable frequency shifts relative to the UV data, ranging from 7 up to ~10 cm^{-1}. In contrast, the corresponding bandgap values of these samples is drastically reduced from ~2.3 eV for $x = 0.25$ down to ~1.6 eV for $x = 0.43$. Thus, different frequency shifts arising from selective resonance effects should be expected for these samples. The almost constant frequency shift observed between the UV and visible spectra, together with the high lateral homogeneity of the epilayers as observed by CL (see Sec. III A), suggests that in-depth strain/composition gradients are probably the main factors responsible for the wavelength dependence of the A_1(LO) frequency in the samples studied in this work.

IV. CONCLUSION

We have performed Raman-scattering measurements on a series of $In_xGa_{1-x}N$ epilayers grown by MBE with In contents in the 0.25-0.75 range. The Raman spectra of Ga-rich samples ($0.25 < x < 0.44$) reveal that the frequency of the A_1(LO) mode is significantly higher than that calculated within the framework of the MREI model,[25] which predicts a linear composition dependence between the GaN and InN A_1(LO) frequencies. In the case of In-rich samples, which are fully relaxed, the experimental A_1(LO) frequencies are in much better agreement with the predictions of the MREI model. The deviations observed for $0.25 < x < 0.44$ can be accounted for if the strain state of the layers is taken into account. We have performed HRXRD measurements to evaluate the In content and strain relaxation of the samples, and we have shown that the strain-corrected A_1(LO) frequency values are in agreement with the MREI model. We have analyzed the effect of in-depth strain gradients, in-depth composition gradients and selective resonant excitation on the frequency of the A_1(LO) mode of $In_xGa_{1-x}N$. These effects have a strong impact on the frequency of this mode, making very difficult to evaluate the strain state and/or the composition of the InGaN material from the A_1(LO) peak frequency alone. In the case of the E_{2h} mode, we have shown that the strain-corrected frequencies exhibit a clear bowing effect over the whole composition range in relation to the linearly interpolated values predicted by the MREI model. This bowing effect has to be taken into account to evaluate from the E_{2h} frequency the composition and/or the strain state of InGaN material.

ACKNOWLEDGMENTS

Work supported by the Spanish Ministry of Science and Innovation (MICINN) through Project MAT2010-16116.

[1]W. Walukiewicz, J. W. Ager III, K. M. Yu, Z. Liliental-Weber, J. Wu, S. X. Li, R. E. Jones, and J. D. Denlinger, J. Phys. D: Appl. Phys. **39**, R83 (2006).
[2]J. Wu, J. Appl. Phys. **106**, 011101 (2009).
[3]J. Menéndez, *Raman Scattering in Materials Science*, Springer Series in Materials Science, edited by W. H. Weber and R. Merlin (Springer-Verlag, Berlin Heidelberg, 2000), Chap. 3, Vol. 42.
[4]H. Harima, J. Phys.: Condens. Matter **14**, R967 (2002).
[5]D. Behr, J. Wagner, A. Ramakrishnan, H. Obloh, and K. H. Bachem, Appl. Phys. Lett. **73**, 241 (1998).
[6]H. Harima, E. Kurimoto, Y. Sone, S. Nakashima, S. Chu, A. Ishida, and H. Fujiyasu, Phys. Stat. Sol. (b) **216**, 785 (1999).
[7]N. Wieser, O. Ambacher, H. P. Felsl, L. Görgens, and M. Stutzmann, Appl. Phys. Lett. **74**, 3981 (1999).
[8]A. Kaschner, A. Hoffmann, C. Thomsen, T. Böttcher, S. Einfeldt, and D. Hommel, Phys. Stat. Sol. (a) **179**, R4 (2000).
[9]T. Sugiura, Y. Kawaguchi, T. Tsukamoto, H. Andoh, M. Yamaguchi, K. Hiramatsu, and N. Sawaki, Jpn. J. Appl. Phys. **40**, 5955 (2001).
[10]D. Alexson, L. Bergman, R. J. Nemanich, M. Dutta, M. A. Stroscio, C. A. Parker, S. M. Bedair, N.A. El-Masry, and F. Adar, J. Appl. Phys. **89**, 798 (2001).
[11]V. Yu. Davydov, A. A. Klochikhin, V. V. Emtsev, A. N. Smirnov, I. N. Goncharuk, A. V. Sakharov, D. A. Kurdyukov, M. V. Baidakova, V. A. Vekshin, S. V. Ivanov, J. Aderhold, J. Graul, A. Hashimoto, and A. Yamamoto, Phys. Stat. Sol. (b) **240**, 425 (2003).
[12]M. R. Correia, S. Pereira, E. Pereira, J. Frandon, and E. Alves, Appl. Phys. Lett. **83**, 4761 (2003).
[13]M. R. Correia, S. Pereira, E. Pereira, J. Frandon, I. M. Watson, C. Liu, E. Alves, A. D. Sequeira, and N. Franco, Appl. Phys. Lett. **85**, 2235 (2004).
[14]M. Bosi, R. Fornari, S. Scardova, M. Avella, O. Martinez, and J. Jiménez, Semicond. Sci. Technol. **19**, 147 (2004).
[15]S. Hernández, R. Cuscó, D. Pastor, L. Artús, K. P. O'Donnell, R. W. Martin, I. M. Watson, Y. Nanishi, and E. Calleja, J. Appl. Phys. **98**, 013511 (2005).
[16]J. W. Ager III, W. Walukiewicz, W. Shan, K. M. Yu, S. X. Li, E. E. Haller, H. Lu, and W. J. Schaff, Phys. Rev. B. **72**, 155204 (2005).
[17]A. G. Kontos, Y. S. Raptis, N. T. Pelekanos, A. Georgakilas,E. Bellet-Amalric, and D. Jalabert, Phys. Rev. B. **72**, 155336 (2005).
[18]V. Y. Davydov, A. A. Klochikhin, I. N. Goncharuk, A. N. Smirnov, A. V. Sakharov, A. P. Skvortsov, M. A. Yagovkina, V. M. Lebedev, H. Lu, and W. J. Schaff, Phys. Stat. Sol. (b) **243**, 1494 (2006).
[19]A. Kar, D. Alexson, M. Dutta, and M. Stroscio, J. Appl. Phys. **104**, 073502 (2008).
[20]E. Tiras, M. Gunes, N. Balkan, and W. J. Schaff, Phys. Status Solidi B **247**, 189 (2010).
[21]J. G. Kim, Y. Kamei, A. Kimura, N. Hasuike, H. Harima, K. Kisoda, T. Hotta, K. Sasamoto, and A. Yamamoto, Phys. Status Solidi C, "Observation of A_1(LO), E_2(high) and B_1(high) phonon modes in $In_xGa_{1-x}N$ alloys with $x = 0.11$–0.54," (in press). DOI 10.1002/pssc.201100401.
[22]J. Wagner, A. Ramakrishnan, H. Obloh, and M. Maier, Appl. Phys. Lett. **74**, 3863 (1999).
[23]S. Lazić, M. Moreno, J. M. Calleja, A. Trampert, K. H. Ploog, F. B. Naranjo, S. Fernandez, and E. Calleja, Appl. Phys. Lett. **86**, 061905 (2005).
[24]H. C. Yang, P. F. Kuo, T. Y. Lin, Y. F. Chen, K. H. Chen, L. C. Chen, J. I. Chyi, Appl. Phys. Lett. **76**, 3712 (2000).
[25]H. Grille, C. Schnittler, and F. Bechstedt, Phys. Rev. B **61**, 6091 (2000).
[26]P. Misra, C. Boney, N. Medelci, D. Starikov, A. Freundlich, and A. Bensaoula, 33rd IEEE Photovoltaic Specialists Conference **1–4**, 1380 (2008).
[27]R. Kudrawiec, M. Siekacz, M. Kryśko, G. Cywiński, J. Misiewicz, and C. Skierbiszewski, J. Appl. Phys. **106**, 113517 (2009).
[28]D. Holec, P. Costa, M. J. Kappers, and C. J. Humphreys, J. Cryst. Growth **303**, 314 (2007).
[29]S. Pereira, M. R. Correia, E. Pereira, K. P. O'Donnell, E. Alves, A. D. Sequeira, N. Franco, I. M. Watson, and C. J. Deatcher, Appl. Phys. Lett. **80**, 3913 (2002).
[30]G. Franssen, I. Gorczyca, T. Suski,A. Kamińska, J. Pereiro, E. Muñoz, E. Iliopoulos, A. Georgakilas, S. B. Che, Y. Ishitani, A. Yoshikawa, N. E. Christensen, and A. Svane, J. Appl. Phys. **103**, 033514 (2008).
[31]S. Srinivasan, F. Bertram, A. Bell, F. A. Ponce, S. Tanaka, H. Omiya, and Y. Nakagawa, Appl. Phys. Lett. **80**, 550 (2002).
[32]Y. T. Moon, D. J. Kim, J. S. Park, J. T. Oh, J. M. Lee, Y. W. Ok, H. Kim, and S. J. Park, Appl. Phys. Lett. **79**, 599 (2001).
[33]D. Pastor, J. Ibáñez, R. Cuscó, L. Artús, G. González-Díaz, and E. Calleja, Semicond. Sci. Technol. **22**, 70 (2007).
[34]J. M. Wagner and F. Bechstedt, Appl. Phys. Lett. **77**, 346 (2000).
[35]X. Q. Wang, S. B. Che, Y. Ishitani, and A. Yoshikawa, Appl. Phys. Lett. **89**, 171907 (2006).
[36]R. Cuscó, J. Ibáñez, E. Alarcón-Lladó, L. Artús, T. Yamaguchi, and Y. Nanishi, Phys. Rev. B **79**, 155210 (2009).
[37]J. Ibáñez, F. J. Manjón, A. Segura, R. Oliva, R. Cuscó, R. Vilaplana, T. Yamaguchi, Y. Nanishi, and L. Artús, Appl. Phys. Lett. **99**, 011908 (2011).

[38]E. Alarcón-Lladó, J. Ibáñez, R. Cuscó, L. Artús, J. D. Prades, S. Estradé, and J. R. Morante, J. Raman Spectr. **42**, 153 (2011).
[39]R. Cuscó, N. Domènech-Amador, L. Artús, T. Gotschke, K. Jeganathan, T. Stoica, and R. Calarco, Appl. Phys. Lett. **97**, 221906 (2010).
[40]V. Y. Davydov, I. N. Goncharuk, A. N. Smirnov, A. E. Nikolaev, W. V. Lundin, A. S. Usikov, A. A. Klochikhin, J. Aderhold, J. Graul, O. Semchinova, and H. Harima, Phys. Rev. B **65**, 125203 (2002).
[41]H. Wang, D. S. Jiang, U. Jahn, J. J. Zhu, D. G. Zhao, Z. S. Liu, S. M. Zhang, and H. Yang, Thin Solid Films **518**, 5028 (2010).
[42]H. Selke, M. Amirsawadkouhi, P. L. Ryder, T. Böttcher, S. Einfeldt, D. Hommel, F. Bertram, and J. Christen, Mat. Sci. Eng. B **59**, 279 (1999).
[43]M. Cardona, in *Light Scattering in Solids II*, edited by M. Cardona and G. Güntherodt, Topics in Applied Physics Vol. 50 (Springer-Verlag, Berlin, 1982).

Research Article

Journal of RAMAN SPECTROSCOPY

Received: 12 April 2011 Revised: 7 June 2011 Accepted: 7 June 2011 Published online in Wiley Online Library: 14 July 2011

(wileyonlinelibrary.com) DOI 10.1002/jrs.3028

Raman scattering by folded acoustic phonons in InGaN/GaN superlattices

J. Ibáñez,[a] A. Rapaport,[b] C. Boney,[c] R. Oliva,[a] R. Cuscó,[a] A. Bensaoula,[c] and L. Artús[a]*

We use Raman scattering to investigate the folded longitudinal acoustic (LA) phonons in a series of $In_xGa_{1-x}N$/GaN superlattices (SLs) grown by molecular beam epitaxy with different compositions (15% < x < 38%) and SL periods (from 8 to 20 nm). A novel, ultralow wavenumber filtering module, which provides access to ultralow wavenumber Raman modes on single-grating spectrometers, has been used to perform the Raman measurements. Zone-folding effects are observed, and the wavenumber behavior of the folded LA modes is well reproduced with a linear dispersion for the folded LA modes as predicted by elastic continuum theory. We employ the wavenumber of the doublets to evaluate the period of the SLs.

Keywords: Raman scattering; superlattices; folded acoustic phonons

Introduction

$In_xGa_{1-x}N$ alloys are currently attracting much research attention as their bandgap can be tuned to cover the emission and detection spectral range from the ultraviolet to the near-infrared. Whereas GaN-based light-emitting diodes (LEDs) and laser diodes are already commercially available, In-rich InGaN alloys are promising candidates for the fabrication of high-efficiency solar cells and infrared detectors.

Although the production of high-quality InGaN layers is still an open issue, the improved crystal quality of Ga-rich alloys permits one to explore the growth of multilayer structures such as superlattices (SLs). Semiconductor SLs are of great interest not only for their unique physical properties arising from the superperiodicity of the structure but also for their great potential to fabricate novel devices such as high-frequency oscillators, quantum-cascade lasers, or thermoelectric devices. In the case of group-III nitrides, generation of terahertz coherent longitudinal acoustic (LA) phonons has been demonstrated in a GaN/AlN SL by femtosecond laser excitation.[1] GaN-based SLs are also expected to play a key role in optical emitters based on interband and intersubband electron transitions.[2]

Raman scattering is a powerful nondestructive technique that is routinely employed for the characterization of semiconductor layers and heterostructures. The study of folded acoustic modes by means of Raman scattering allows one to gain information about the crystal quality and the period of the SLs.[3–6] The wavenumber, as well as splitting of the folded modes, is linked to the dispersion of the acoustic phonon modes and to the sound velocities of the layers. In the case of III-nitrides, Raman scattering by folded acoustic modes has been used to characterize the period of GaN/$Al_{0.28}Ga_{0.72}N$ SLs.[7,8] In spite of the large interest of InGaN-based SLs both from fundamental and applications points of view, very little data on the vibrational properties of InGaN/GaN SLs has been published so far. Kisoda *et al.*[9] studied the A_1(LO) mode in $In_{0.2}Ga_{0.8}N$/GaN SLs, and, recently, confocal Raman scattering by optical modes has been employed to obtain information about the crystal quality and spatial distribution of strains in InGaN/GaN layers within an LED structure.[10]

In the present work, we use Raman scattering to investigate the folded acoustic modes in a series of $In_xGa_{1-x}N$/GaN SLs grown by molecular beam epitaxy (MBE) with different SL periods (8 nm < D < 20 nm) and compositions (15% < x < 38%). The Raman experiments were performed with a novel ultralow wavenumber filter based on narrow-bandwidth volume Bragg gratings (VBGs), providing access to ultralow wavenumber modes by using a single-grating Raman spectrometer. The results are discussed in terms of the theory of acoustic vibrations in multilayered structures, and the Raman spectra are used to characterize the period of the SLs.

Experiment

$In_xGa_{1-x}N$/GaN SLs with 15% < x < 38% and periods ranging from D = 8 to 20 nm were grown by plasma-assisted MBE. The growth was performed in a custom-made MBE chamber equipped with standard effusion cells and a Veeco Uni-Bulb radio frequency plasma source. The InGaN–GaN layers were deposited on 5–7-μm thick GaN/sapphire templates from commercial vendors. Two gallium sources were used, each with the appropriate flux for the growth of InGaN and GaN. All layers in the SLs were deposited at the same growth temperature, which ranged from 530 to 630 °C. The growth temperature was chosen to be low enough

* *Correspondence to: L. Artús, Institut Jaume Almera, Consell Superior d'Investigacions Científiques, 08028 Barcelona, Catalonia, Spain. E-mail: lartus@ija.csic.es*

a *Institut Jaume Almera, Consell Superior d'Investigacions Científiques, 08028 Barcelona, Catalonia, Spain*

b *HORIBA Jobin Yvon S.A.S., 59650 Villeneuve d'Ascq, France*

c *Department of Physics, University of Houston, Houston, TX 77004, USA*

Journal of RAMAN SPECTROSCOPY

to avoid substantial InGaN decomposition, resulting in the InGaN composition being mainly controlled by the Ga/N flux ratio. Both GaN and InGaN were grown under slightly metal-rich conditions (In-rich in the case of InGaN). A brief pause under the nitrogen plasma was used at the end of each layer deposition to eliminate any excess metal from the growth surface. No metal droplets were observed on the samples at the end of the growth runs. Details about the growth of the SL samples can be found in Ref. [11].

X-ray diffraction (XRD) measurements consisting of $\omega/2\theta$ scans and reciprocal space maps (RSMs) were carried out in order to evaluate the SL periodicity, composition, and layer thicknesses. Details of the X-ray analysis of some of the samples have been published elsewhere.[11] RSMs around the asymmetric (10–15) reflection were used to determine the degree of relaxation and the average In content of the SLs, while the period of each SL was evaluated from the spacing of the fringes in a symmetric (0002) $\omega/2\theta$ scan. The In fraction and thickness of the InGaN layers were then evaluated by comparing the (0002) scans with theoretical curves calculated with the average In concentration of the SLs and the degree of relaxation estimated from the RSMs.[11] In the case of samples without available RSM data, the In fraction of the InGaN layers was evaluated by taking the InGaN growth conditions from samples with a known composition as reference points. In Table 1, we summarize the structural properties of the SL samples studied in this work as obtained from the analysis of the XRD data.

Raman spectra were acquired with a single-stage LabRAM HR spectrometer from HORIBA Jobin Yvon, which is composed of a confocal microscope coupled to a 800-mm focal length Czerny–Turner achromatic spectrograph and a two-dimensional multichannel charge-coupled device (CCD). A grating with 1800 grooves/mm was used for dispersing the Raman signal over the CCD detector. The Raman spectra were excited with 532 and 632.8 nm radiation. All measurements were performed in a backscattering configuration on a *c* face, with no polarization analysis. Low-temperature measurements were carried out using a Linkam heating and freezing stage (THMS600) with liquid nitrogen cooling. To enable measurements down to ~6 cm^{-1} on a single-grating spectrometer, an ultralow wavenumber (ULF™) filtering accessory for 532 and 632.8 nm wavelengths was used. The ULF™ accessory, developed by HORIBA Jobin Yvon, is based on VBGs. This accessory enables measurements of Raman features that are located very close to the Rayleigh line with a signal throughput that is considerably higher than can be achieved on triple-stage spectrometers traditionally used for such low wavenumber measurements. Access to both the Stokes and anti-Stokes components is thereby available down to wavenumbers of about 6 cm^{-1} with better than 50% transmission compared to current top-of-the-line edge technology. The ULF™ accessory consists of a spectral filtering module for the laser, coupled with a Raman signal filtering module. Both modules include VBGs recorded in photo-thermo-refractive (PTR) glass.[12] The spectral filtering of the laser beam was performed with a BragGrate bandpass filter with a full-width at half maximum (FWHM) of about 4 cm^{-1}. It consists of a reflecting VBG with a diffraction efficiency of ~95%, which can be easily angle-tuned to the resonant wavelength of the laser. The Raman signal filtering module, which enables one to perform Raman measurements below 10 cm^{-1} with a single monochromator system, consists of a BragGrate™ notch filter. This is a reflecting VBG formed by holographic techniques in bulk PTR glass. The specific technology of high-efficiency VBGs allows fabrication of a single 3-mm thick notch filter with optical density 3–4 and a line width of 5–10 cm^{-1} at FWHM. At 632.8 nm, the throughput of the complete module is better than 70%. At 532 nm, scattering causes a slight decrease in throughput, but it remains better than 50%.

Table 1. Details of the $In_xGa_{1-x}N$/GaN SLs studied in this work

Sample	Thickness (nm)	Thickness InGaN (nm)	Thickness GaN (nm)	*x* (%)	*D* (nm)	D_{Raman} (nm)
A	500	3.5	4.5	30	8	8.2
B	800	4.6	4.2	18	8.8	9.1
C	400	4.5	4.5	23	9	9.2
D	500	4.4	8.1	15	12.5	12.5
E	500	7.7	7.7	33	15.4	16.5
F	450	7.5	9.8	38	17.3	17.1
G	620	4.5	13.3	19	17.8	17.8

The sixth and seventh columns show the periodicity of the SL samples as obtained from the analysis of XRD scans (*D*) and Raman spectra (D_{Raman}).

Results and Discussion

The ULF™ filtering accessory allows one to detect Raman features with wavenumbers below 10 cm^{-1} in a single monochromator system, with access to both the Stokes and anti-Stokes components of the inelastically scattered radiation. This is illustrated in Fig. 1, which shows a room-temperature Raman spectrum excited with 532-nm radiation of a InGaN/GaN SL sample with $D = 8.8$ nm and $x = 18\%$ (sample B). Besides the Rayleigh line, two doublets of narrow peaks are observed both in the Stokes and the anti-Sokes spectrum. These features can be assigned to folded LA modes from the SLs. On account of the low wavenumbers of these phonon modes, measurements performed at liquid-nitrogen temperature, which showed negligible wavenumber shifts in relation to the room-temperature values.

Figure 2 shows selected room-temperature Raman spectra (Stokes component), excited with 532-nm radiation, of the InGaN/GaN SLs studied in this work (samples A, C, D, and F). Doublets of narrow peaks are clearly observed in all the spectra. While the samples with higher In content display only a single doublet (upper and lower curves), a couple of doublets is observed in the two intermediate curves. Two doublets are also detected in samples B (Fig. 1) and G (not shown). As can be seen in Fig. 2, the

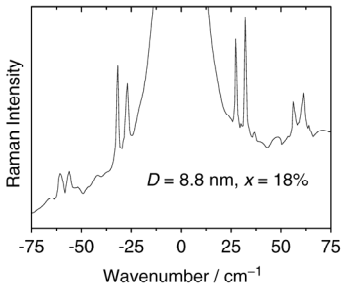

Figure 1. Raman spectrum of a $In_xGa_{1-x}N$/GaN SL with $x = 18\%$ and SL period (*D*) equal to 8.8 nm.

Journal of RAMAN SPECTROSCOPY

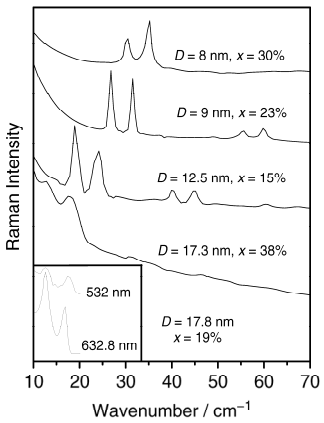

Figure 2. Raman spectra of $In_xGa_{1-x}N$/GaN SLs with different periods (D) and compositions (x), excited with 532-nm radiation. Inset: Raman spectra of a $In_xGa_{1-x}N$/GaN SL with $x = 19\%$ and $D = 17.8$ nm, excited with 532 nm (upper curve) and 632.8 nm (lower curve).

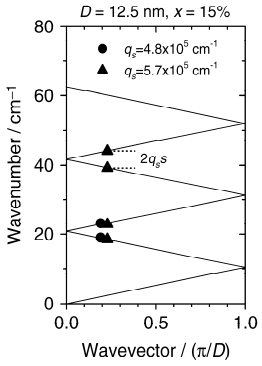

Figure 3. Dispersion of the folded LA phonon modes in a $In_xGa_{1-x}N$/GaN SL with $x = 15\%$ and SL period (D) equal to 12.5 nm. Experimental wavenumbers measured with 532.0 nm ($q_s = 5.7 \times 10^5$ cm^{-1}, plotted with triangles) and 632.8 nm ($q_s = 4.8 \times 10^5$ cm^{-1}, plotted with dots) are also shown.

doublets shift to higher wavenumbers with decreasing SL period. Thus, the observed features can be unambiguously attributed to folded LA modes in the SLs. The observation of two doublets in the samples with lower In content, up to $x = 23\%$, is a consequence of the high crystal and interface quality of these SLs. Note that, in previous Raman studies on GaN/$Al_{0.28}Ga_{0.72}N$ SLs, only the first folded doublet was detected.[7,8]

Raman measurements of all samples were also carried out with the 632.8-nm radiation. The inset of Fig. 2 shows the first doublet of sample G ($D = 17.8$ nm and $x = 19\%$). These spectra were obtained with excitations at 532 (upper curve) and 632.8 nm (lower curve). As expected, given that the attained phonon wave vector is larger in the case of the experiments excited with 532-nm radiation, the doublet splitting was found to be lower, around $\sim$0.6 cm^{-1}, in the 632.8-nm spectra.

For the present samples and excitation conditions, $\pi/D > q_s$ where q_s is the phonon wave vector as defined by the excitation wavelength and the scattering geometry (q_s is parallel to the c-axis of wurtzite in these experiments). Under these conditions, the elastic continuum theory predicts that the dispersion of the folded LA modes can be approximated with a linear dependence[3,5]:

$$\tilde{\upsilon}_m^{\pm}(q_s) = \tilde{\upsilon}_{m0} + q_s s/(2\pi c) \qquad (1)$$

where $\tilde{\upsilon}_m^{\pm}(q_s)$ is the wavenumber of the LA modes ($m = 0, 1, \ldots$), $\tilde{\upsilon}_{m0} = ms/(cD)$ is the $q_s = 0$ wavenumber of the m-th branch, s is the average sound velocity in the SL, and c is the speed of light. Within this linear approximation, the doublet splitting $\Delta(q_s)$ is equal to $2q_s s/(2\pi c)$.

Figure 3 shows the dispersion of the folded LA modes for the case of sample D ($D = 12.5$ nm, $x = 15\%$), calculated with Eqn (1). For the calculations, we obtained the average sound velocity in the SLs as described in Ref. [4] by using the sound velocity values of InGaN that result from the linear interpolation between the GaN value (8.0×10^5 cm/s) and the InN value (5.2×10^5 cm/s). These values have been obtained from the elastic constants of Ref. [13]. Figure 3 also shows the experimental wavenumbers (dots) of the two doublets that appear in the Raman spectra of sample D for the 532.0-nm excitation ($q_s = 5.7 \times 10^5$ cm^{-1}) and the 632.8-nm excitation ($q_s = 4.8 \times 10^5$ cm^{-1}). As can be seen in the figure, very good agreement is obtained between the experimental and calculated wavenumbers for all the doublets, which confirms the validity of the linear phonon dispersion in these samples. Similar results are obtained for the rest of the SLs. It should be emphasized that a full calculation within the elastic continuum limit[4,14] (not shown) confirms that the dispersion of the folded LA modes in these SLs suffers only minor deviations from linearity around the zone edges. For the InGaN/GaN SLs studied in this work, we find that the zone-center gap between the folded LA branches is lower than 0.4 cm^{-1}, which is below the instrumental resolution of the present measurements.

As discussed in detail in Ref. [6] for the case of Si/SiGe SLs, the sound velocity s of the samples can be directly evaluated from the experimental doublet splittings $\Delta(q_s)$. For the case of the samples studied in this work, we find that, regardless of the SL period, $\Delta(q_s)$ is nearly constant, around 4.6 ± 0.3 cm^{-1} for $\lambda_{exc} = 532$ nm. This value is approximately 0.6 cm^{-1} lower in the case of 632.8-nm excitation. From these values and the expression for the doublet splitting, neglecting any variations in $\Delta(q_s)$ (the observed variations are in any case below the instrumental resolution), we find that a value of $s \sim 7.6 \times 10^5$ cm/s provides a good approximation for all the samples. To extract this value, for simplicity we have used a constant value of $q_s = 5.7 \times 10^5$ cm^{-1} ($\lambda_{exc} = 532$ nm), i.e. we have taken the same refractive index for all the samples. Although one may expect a slight increase of the refractive index of $In_xGa_{1-x}N$ with increasing x, it can be shown that such an increase does not affect significantly the resulting q_s values, leading to a very small decrease in the average sound velocities extracted from the doublet splittings. From the value of s in the InGaN/GaN SLs, the sound velocity of the $In_xGa_{1-x}N$ layers can be directly estimated.[4,6] As expected from the excellent agreement between theoretical phonon dispersions and experimental wavenumbers, the values thus obtained are in good agreement with the values that result from the linear interpolation between the GaN and InN sound velocities (Fig. 3 and discussion above). The fact that the average sound velocity turns out to be very similar in these SLs (i.e. it is not strongly affected by the In content of the InGaN layers) implies that the behavior of the folded acoustic modes is mainly determined by the SL period.

Journal of RAMAN SPECTROSCOPY

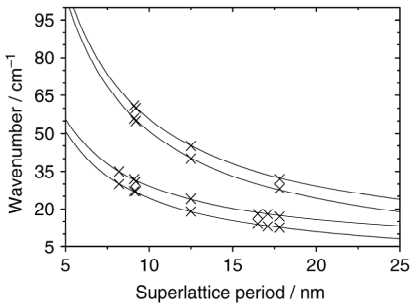

Figure 4. Calculated wavenumbers for the two first doublets as a function of the SL period. The plot of the experimental wavenumbers allows one to obtain the SL period for the samples studied in this work.

The wavenumber position of the folded LA peaks can be used to determine the period of the SLs. We show in Fig. 4 the calculated wavenumbers of the first two doublets as a function of the SL period. The curves, obtained with Eqn (1) ($m = 1,2$) for $\lambda_{exc} = 532$ nm, display the expected wavenumber reduction of the folded acoustic modes with increasing D. From the experimental wavenumbers of the folded LA phonons measured at $\lambda_{exc} = 532$ nm, we evaluate the SL period of the samples studied in this work by using the calculated wavenumber dependence plotted in Fig. 4. The values of the SL period thus obtained are plotted in this figure and displayed in the last column of Table 1. Note the good agreement between the experimental and calculated wavenumbers for the samples, which exhibit two doublets of folded acoustic modes. It can be seen that the values thus obtained exhibit small variations in relation to the values obtained from the XRD scans (sixth column of Table 1), which confirms that Raman scattering is a powerful tool for the determination of the period of InGaN/GaN SLs over a broad range of SL periods and compositions.

Conclusions

We have used Raman scattering to investigate the zone-folding effects on the acoustic phonons of a series of $In_xGa_{1-x}N$/GaN SLs grown by MBE ($15\% < x < 38\%$ and SL period ranging from 8 to 20 nm). The Raman measurements have been performed with 532- and 632.8-nm excitations by using a single grating spectrometer in combination with a novel ultralow wavenumber filtering module, which provides access to ultralow wavenumber Raman modes. These experiments have allowed us to detect doublets arising from folded LA modes in the SLs. The wavenumber behavior of the observed doublets is well reproduced with a linear dispersion for the folded LA modes as predicted by elastic continuum theory. We have used the wavenumber of the doublets to evaluate the SL period. The results thus obtained are in very good agreement with the SL period values obtained from XRD.

Acknowledgements

Financial support from the Spanish Ministry and Innovation (Project MAT2010-16116) and from CSIC (PIE 2009) is acknowledged. At the University of Houston (UH), the work was supported by grants from the Institute of Space Systems on Operations (ISSO, UH).

References

[1] C. E. Martinez, N. M. Stanton, P. M. Walker, A. J. Kent, S. V. Novikov, C. T. Foxon, *Appl. Phys. Lett.* **2005**, *86*, 221915.
[2] H. Machhadani, P. Kandaswamy, S. Sakr, A. Vardi, A. Wirtmüller, L. Nevou, F. Guillot, G. Pozzovivo, M. Tchernycheva, A. Lupu, L. Vivien, P. Crozat, E. Warde, C. Bougerol, S. Schacham, G. Strasser, G. Bahir, E. Monroy, F. H. Julien, *New J. Physics* **2010**, *11*, 125023.
[3] B. Jusserand, M. Cardona, in *Light Scattering in Solids V*, (Eds: M. Cardona, G. Güntherodt), Springer-Verlag: Berlin, **1988**.
[4] J. Sapriel, J. C. Michel, J. C. Toledano, R. Vacher, J. Kervarec, A. Regreny, *Phys. Rev. B* **1983**, *28*, 2007.
[5] C. Colvard, T. A. Gant, M. V. Klein, R. Merlin, R. Fischer, H. Morkoc, A. C. Gossard, *Phys. Rev. B* **1985**, *31*, 2080.
[6] H. Brugger, G. Abstreiter, H. Jorke, H. J. Herzog, E. Kasper, *Phys. Rev. B* **1986**, *33*, 5928.
[7] V. Y. Davydov, A. A. Klochikhin, I. E. Kozin, V. V. Emtsev, I. N. Goncharuk, A. N. Smirnov, R. N. Kyutt, M. P. Scheglov, A. V. Sakharov, W. V. Lundin, E. E. Zavarin, A. S. Usikov, *Phys. Stat. Sol. (a)* **2001**, *188*, 863.
[8] V. Y. Davydov, A. N. Smirnov, I. N. Goncharuk, R. N. Kyutt, M. P. Scheglov, M. V. Baidakova, W. V. Lundin, E. E. Zavarin, M. B. Smirnov, S. V. Karpov, H. Harima, *Phys. Stat. Sol. (b)* **2002**, *234*, 975.
[9] K. Kisoda, K. Hirakura, H. Harima, *Phys. Stat. Sol. (c)* **2006**, *3*, 1997.
[10] V. V. Strelchuk, V. P. Kladko, E. A. Avramenko, O. F. Kolomys, N. V. Safryuk, R. V. Konakova, B. S. Yavich, M. Y. Valakh, V. F. Machulin, A. E. Belyaev, *Semiconductors* **2010**, *44*, 1199.
[11] C. Boney, D. Starikov, I. Hernandez, R. Pillai, A. Bensaoula, *J. Vac. Sci. Technol. B* **2011**, *29*, 03C106.
[12] L. B. Glebov, in *Encyclopedia of Smart Materials 2*, (Ed.: M. Schwartz), John Willey & Sons: **2002**, pp. 770.
[13] A. F. Wright, *J. Appl. Phys.* **1997**, *82*, 2833.
[14] S. M. Rytov, *Sov. Phys. Acoust.* **1956**, *2*, 68.

APPLIED PHYSICS LETTERS **101**, 062103 (2012)

Brillouin scattering determination of the surface acoustic wave velocity in $In_xGa_{1-x}N$: A probe into the elastic constants

R. J. Jiménez-Riobóo,[1] R. Cuscó,[2] R. Oliva,[2] N. Domènech-Amador,[2] C. Prieto,[1] J. Ibáñez,[2] C. Boney,[3] A. Bensaoula,[3] and L. Artús[2]
[1]*Instituto de Ciencia de Materiales de Madrid, CSIC, Cantoblanco, Madrid 28049, Spain*
[2]*Institut Jaume Almera, Consell Superior d'Investigacions Científiques (CSIC), Lluís Solé i Sabarís s.n., 08028 Barcelona, Catalonia, Spain*
[3]*Department of Physics, University of Houston, 4800 Calhoun, Houston, Texas 77004, USA*

(Received 15 June 2012; accepted 26 July 2012; published online 8 August 2012)

We have determined the surface acoustic wave velocity in $In_xGa_{1-x}N$ layers for $0.34 < x < 0.75$ by means of high resolution Brillouin spectroscopy. The sagittal dependence of the surface acoustic velocity has been analyzed by comparing the experimental results with theoretical simulations based on the Green's function formalism. We find the best agreement with our data when the bowing parameters for the elastic constants recently reported from density functional theory calculations are taken into account. The dependence of the surface acoustic wave velocity on alloy composition is given. © *2012 American Institute of Physics*. [http://dx.doi.org/10.1063/1.4744961]

Group III nitride-based materials have important applications in optoelectronics and high-power/high-temperature electronics. Alloying in this material system offers a great flexibility for tailoring the physical properties of the active layers of electronic devices. GaN-based heterostructure field effect transistors (HFET) with InN-containing barrier/channel layers are the subject of intense current research.[1] The piezoelectric properties of group III nitrides also make these materials very attractive for surface acoustic wave (SAW) device applications. AlN is one of the most suitable materials for high-frequency filters, duplexers, and resonators because of its high SAW velocity and its insulating nature.[2,3] On the other hand, GaN-based SAW delay-line oscillators have shown their potential as visible-blind remote UV sensors.[4] Given that the bandgap of $In_xGa_{1-x}N$ can be tuned from 0.64 eV ($x = 1$) to 3.4 eV ($x = 0$)[5] and that the alloy exhibits a higher electromechanical coupling than GaN, InGaN-based SAW devices are good candidates for sensitive visible light sensors.

Despite the enormous technological interest of group III-nitride alloys for piezoelectric applications, there is relatively little information about the elastic properties of these materials. The knowledge of the elastic constants of $In_xGa_{1-x}N$ is necessary to model and optimize the design of InGaN-based piezoelectric and strained layer devices. Brillouin scattering is a powerful technique for an accurate determination of the elastic constants.[6,7] Whereas Brillouin scattering studies have been reported for GaN (Refs. 8–10) and InN (Ref. 11), no experimental determinations of the elastic constants of wurtzite $In_xGa_{1-x}N$ are available so far. Thus, a Vegard-like linear interpolation between the values of the binary compounds is usually assumed when strain analysis is required for the InGaN alloy.[12,13]

It is well known that In has a tendency to segregation and clustering in nitride alloys, and this may have a strong impact on their optical emission[14,15] and piezoelectric[16] properties. Recently, *ab initio* calculations of the dependence of the elastic constants on composition have been reported for $In_xGa_{1-x}N$ and $In_xAl_{1-x}N$ wurtzite alloys.[17] These calculations reveal significant sublinear deviations for some of the elastic constants of $In_xGa_{1-x}N$, and considerable differences are found if In clustering is taken into account in the supercell model. A comparison of these theoretical predictions with experimental data has not been reported so far.

In this letter, we present a high resolution Brillouin scattering (HRBS) study of the SAW velocity in $In_xGa_{1-x}N$ alloys with In compositions ranging from $x = 0.34$ to $x = 0.75$. The sagittal dependence of the observed Rayleigh and Sezawa modes is analyzed by comparing with simulations based on the Green's function formalism for SAW propagation.[18]

The InGaN epilayers used in this work (see Table I) were grown by plasma-assisted molecular beam epitaxy on a 4-μm thick GaN template on (0001)-sapphire substrates. Growth details and characterization of these samples have been published elsewhere.[19] HRBS experiments were performed in backscattering geometry for different sagittal angles using the $\lambda_0 = 514.5$ nm excitation wavelength. A description of the experimental set-up can be found in Ref. 20. The studied samples have In compositions above $x = 0.34$. For these compositions, the strong optical absorption prevents the signal of the bulk acoustic phonons to be detected and therefore the scattering signal from the SAW can be measured. It was not possible to study samples with

TABLE I. Characteristics of the $In_xGa_{1-x}N$ samples and their respective SAW velocity determined from the Brillouin measurements. The SAW velocity values were determined by averaging the measurements with $kh > 10$, for which the influence of the substrate is negligible. Here, h is the thickness of the $In_xGa_{1-x}N$ layer and k is the acoustic scattering wave vector (see text).

Sample	In content	h (nm)	v_{SAW} (ms^{-1})
A1010	0.34	710	3161
A1018	0.42	710	3114
A1035	0.44	560	3057
A1177	0.68	500	2880
A1182	0.75	500	2754

less In content because in the transparency regime the strong luminescence background and the dominance of the substrate modes precluded the observation of the SAW peaks.

Figure 1 shows representative Brillouin spectra obtained from sample A1182 for different values of the sagittal angle α, which is defined by the incident laser beam and the normal to the film surface. Since we are measuring opaque samples, contribution to inelastic light scattering is due to surface corrugation produced by the propagation of SAW (ripple effect). This ripple mechanism accounts for most of the scattered light giving rise to surface Rayleigh phonons and makes it possible the presence of guided waves in addition to the Rayleigh wave when the transverse velocity of phonons in the film is smaller than that of the substrate.[6,7] This guided waves, which have a higher energy than the Rayleigh modes, are known as Sezawa modes. Thus, the most intense peak is assigned to the Rayleigh mode and the weaker peaks at higher energies are assigned to the Sezawa modes. Both peaks shift to higher frequencies for increasing α, which reflects the increase in the component along the surface of the acoustic scattering wave vector $k = 4\pi\sin\alpha/\lambda_0$. The SAW velocity can be directly obtained from the Rayleigh peak frequency ν_R as $v_{SAW} = 2\pi\nu_R/k$. Lorentzian line shape fits were carried out to extract the ν_R values from the spectra. Brillouin spectra taken at different sagittal angles α (from $\alpha = 30°$ to $\alpha = 75°$ at 5° steps) have allowed us to obtain v_{SAW} values for a range of kh values $6 < kh < 13$.

In thin films, the substrate can affect the v_{SAW} of the layer depending on the kh value. This is illustrated by the calculated curves shown in Fig. 2, where it can be seen that to measure the intrinsic v_{SAW} of the thin-film material kh values in the flat, asymptotic region of the curves must be reached. Given the layer thickness of the samples used in this study (see Table I), the sagittal angles used in the experiments yield kh values that are high enough to render the Rayleigh SAW velocity nearly independent of the substrate. By contrast, in this range of kh values the Sezawa SAW velocity still shows a marked dependence on the sagittal angle α.

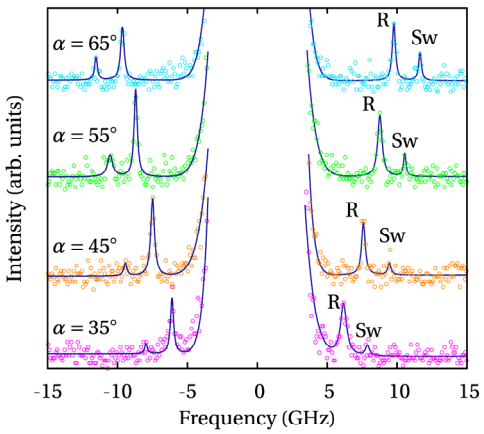

FIG. 1. Brillouin spectra of sample A1182 ($x = 0.75$) obtained at different sagittal angles. Solid lines are Lorentzian line shape fits to the spectra. The Rayleigh and Sezawa peaks are labeled as R and Sw, respectively.

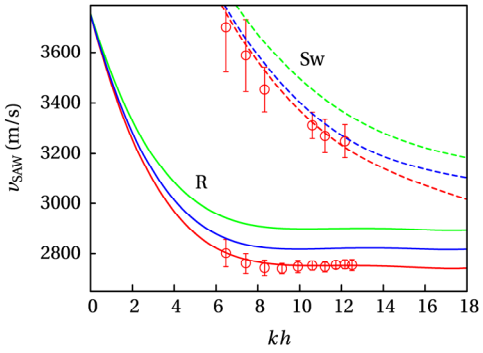

FIG. 2. Surface acoustic wave velocities as a function of kh for an $In_xGa_{1-x}N$ layer with $x = 0.75$, as obtained from the Green's function simulations using different interpolation schemes for the elastic constants: Vegard-like linear interpolation (green lines), *ab initio* results for a uniform alloy (blue lines), *idem* for a clustered alloy (red lines). The circles represent the experimental Brillouin data. R and Sw stand for Rayleigh and Sezawa modes, respectively.

The sagittal dependence of the scattered light intensity for $In_xGa_{1-x}N$ thin films on GaN/sapphire was simulated using the Green's function formalism developed by Zhang *et al.*[18] The density used for $In_xGa_{1-x}N$ was interpolated from those of InN (6.81 g cm^{-3}) and GaN (6.15 g cm^{-3}),[5] assuming a linear dependence of the lattice parameters with composition (Vegard's law). Three different sets of elastic constants were considered in the simulations: (*i*) Vegard-like linear interpolation between the elastic constants of GaN and InN, (*ii*) quadratic parametrization of the elastic constants calculated using *ab initio* methods[17] with the bowing parameter corresponding to a uniform distribution of In atoms, and (*iii*) *idem* with the bowing parameter corresponding to a clustered distribution of In atoms. In the last two cases, the values of the elastic constants are obtained as a function of the In concentration using

$$c_{ij}^{InGaN}(x) = (1-x)c_{ij}^{GaN} + xc_{ij}^{InN} - b_{ij}x(1-x) \qquad (1)$$

with the bowing parameters b_{ij} reported in Ref. 17 (see Table II). In all cases, the elastic constants for the end member compounds were taken from previous Brillouin studies.[9–11] As can be seen in Table II, substantial values of the bowing parameters for the c_{11} and c_{33} elastic constants are obtained

TABLE II. Elastic constants for the end-member compounds (in GPa) and bowing parameters used in the $In_xGa_{1-x}N$ SAW simulations. Note that in hexagonal symmetry crystals $c_{66} = (c_{11} - c_{12})/2$.

	c_{11}	c_{12}	c_{13}	c_{33}	c_{44}
GaN[a]	376.4	137.2	114.0	406.8	94.6
InN[b]	222.7	112.1	107.5	258	48.5
b (uniform)[c]	60	14	−4	71	16
b (clustered)[c]	100	43	−4.5	−1	35

[a]Reference 10. The c_{13} value, which was not determined in Ref. 10, has been taken from Ref. 9.
[b]Reference 11.
[c]Reference 17.

from the *ab initio* calculations when a uniform In distribution is assumed, which imply a significant sublinear dependence on composition of these elastic constants. On the other hand, if In clustering is taken into account, the greatest bowing is exhibited by the c_{11}, c_{12}, and c_{44} elastic constants. The different composition dependence of the elastic constants in each case results in different values of the v_{SAW}.

The Rayleigh (solid lines) and Sezawa (dashed lines) acoustic wave velocities simulated using the three different sets of alloy elastic constants mentioned above are plotted in Fig. 2 for an In concentration of $x = 0.75$. In the same figure, we have plotted the Rayleigh and Sezawa acoustic wave velocities measured at different *kh* values in sample A1182, which as shown in Ref. 19 corresponds to a fully relaxed $In_{0.75}Ga_{0.25}N$ epilayer. As can be seen in Fig. 2, the simulation with the linearly interpolated elastic constants (case *i*) overestimates the SAW velocity by about 10% (green lines). If the set of constants obtained for the homogeneous alloy from *ab-initio* calculations (case *ii*) is considered in the simulations, the resulting SAW velocities (blue lines) are in better agreement with the experimental points, although they still overestimate the measured velocity. Finally, if we consider the elastic constants calculated for clustered alloys (case *iii*), an excellent agreement with the experimental velocities of both Rayleigh and Sezawa modes is obtained (red line). Although the full determination of the elastic constants from the v_{SAW} measurements is not possible, this result suggests that a significant degree of bowing in the composition dependence of the elastic constants, which may be related with an inhomogeneous In distribution,[17] has to be considered. Similar quality fits are obtained for all the alloy compositions studied.

As can be seen in Fig. 2, for the *kh* values used in this study the Rayleigh acoustic wave velocity is nearly independent of the substrate. By performing HRBS experiments at high *kh* values on different alloy composition samples, the composition dependence of the intrinsic SAW velocity was obtained and it is plotted in Fig. 3. In contrast with the linear dependence on composition of the sound velocity found in $Al_xGa_{1-x}N$ (Ref. 10), the SAW velocity in $In_xGa_{1-x}N$ exhibits a noticeable bowing. A good agreement is found between the measured v_{SAW} values and the composition dependence obtained from the simulations using the set of elastic constants of case *iii* (solid line in Fig. 3). Although, as reported in Ref. 19, a residual strain is present in the samples with In concentration between 0.34 and 0.44, the results shown in Fig. 3 indicate that this has not a significant influence on the measured SAW velocities, which are well described by the simulations using the elastic constants given by Eq. (1) throughout all the composition range. Whereas the compressive strain in the $In_xGa_{1-x}N$ layer induces an increase in the elastic constants via nonlinear elasticity effects[21] and tends to increase the sound velocity, the concomitant reduction of the unit cell volume results in an increase of the density and hence lowers the sound velocity. These compensating effects, together with a possible strain relaxation towards the surface, may explain the observation that the v_{SAW} values measured in the layers with residual strain are in good agreement with the composition dependence of v_{SAW} calculated for relaxed samples.

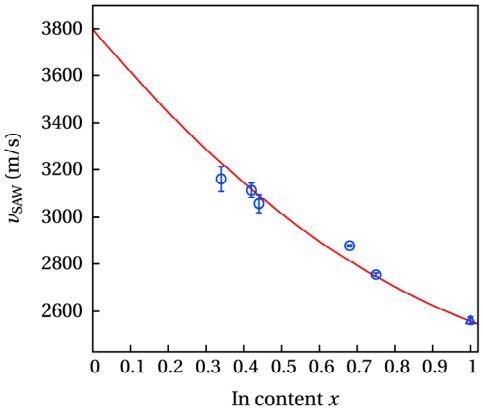

FIG. 3. Composition dependence of the surface acoustic velocity of $In_xGa_{1-x}N$. Circles are the experimental values measured in this work. The triangle represents the measured v_{SAW} value for InN reported in Ref. 11. The solid line is the simulated v_{SAW} considering the set of elastic constants of case *iii* (see text), which take into account the effect of In clustering in the alloy.

In summary, we have performed an experimental determination of the SAW velocity of the $In_xGa_{1-x}N$ alloy by means of HRBS measurements. The sagittal dependence of the SAW velocities we find for both Rayleigh and Sezawa modes is well described by a Green's function simulation of the scattered intensity only when a significant bowing is included in the composition dependence of the elastic constants, as given by *ab initio* calculations on clustered supercells. The bowing values of the elastic constants required to explain the v_{SAW} values for the different InGaN alloys suggest that some degree of inhomogeneity in In distribution may exist in these alloys. Because of the relatively large layer thicknesses of the studied samples, the Rayleigh SAW velocity was found to be independent of the sagittal angles used in the experiments, and the intrinsic SAW velocity of $In_xGa_{1-x}N$ alloys could be determined from the HRBS measurements. The good agreement of the Green's function simulations with both the composition and the sagittal-angle dependence of v_{SAW} obtained from Brillouin measurements reinforces the knowledge gained from these measurements on the elastic properties of the $In_xGa_{1-x}N$ alloys.

This work has been partially supported by the Spanish Ministry under Grants MAT2010-16116 and MAT2009-08786.

[1]J. Liberis, I. Matulionienė, A. Matulionis, E. Šermukšnis, J. Xie, J. H. Leach, and H. Morkoç, Phys. Status Solidi A **206**, 1385 (2009).
[2]O. Ambacher, J. Phys. D **31**, 2653 (1998).
[3]Y. Takagaki, P. Santos, E. Wiebicke, O. Brandt, H. Schonherr, and K. Ploog, Appl. Phys. Lett. **81**, 2538 (2002).
[4]D. Ciplys, R. Rimeika, M. S. Shur, S. Rumyantsev, R. Gaska, A. Sereika, J. Yang, and M. A. Khan, Appl. Phys. Lett. **80**, 2020 (2002).
[5]J. Wu, J. Appl. Phys. **106**, 011101 (2009).
[6]J. R. Sandercock, *Light Scattering in Solids III, Topics in Applied Physics Vol. 51*, edited by M. Cardona and G. Güntherodt (Springer-Verlag, Berlin, 1982).
[7]P. Mutti, C. E. Bottani, G. Ghislotti, M. Beghi, G. A. D. Briggs, and J. R. Sandercock, *Advanced in Acoustic Microscopy*, edited by A. Briggs (Plenum, New York, 1995), Vol. 1.
[8]A. Polian, M. Grimsditch, and I. Grzegory, J. Appl. Phys. **79**, 3343 (1996).

[9]M. Yamaguchi, T. Yagi, T. Sota, T. Deguchi, K. Shimada, and S. Nakamura, J. Appl. Phys. **85**, 8502 (1999).
[10]R. J. Jiménez Rioboo, E. Rodríguez-Cañas, M. Vila, C. Prieto, F. Calle, T. Palacios, M. A. Sánchez, F. Omnès, O. Ambacher, B. Assouar, and O. Elmazria, J. Appl. Phys. **92**, 6868 (2002).
[11]R. J. Jiménez-Rioboó, R. Cuscó, N. Domènech-Amador, C. Prieto, T. Yamaguchi, Y. Nanishi, and L. Artús, Phys. Status Solidi (RRL) **6**, 256 (2012).
[12]S. Pereira, M. R. Correia, T. Monteiro, E. Pereira, E. Alves, A. D. Sequeira, and N. Franco, Appl. Phys. Lett. **78**, 2137 (2001).
[13]M. Winkelnkemper, A. Schliwa, and D. Bimberg, Phys. Rev. B **74**, 155322 (2006).
[14]S. Chichibu, T. Azuhata, T. Sota, and S. Nakamura, Appl. Phys. Lett. **70**, 2822 (1997).
[15]K. O'Donnell, R. Martin, and P. Middleton, Phys. Rev. Lett. **82**, 237 (1999).
[16]A. Al-Yacoub, L. Bellaiche, and S. Wei, Phys. Rev. Lett. **89**, 057601 (2002).
[17]S. P. Łepkowski and I. Gorczyca, Phys. Rev. B **83**, 203201 (2011).
[18]X. Zhang, J. D. Comins, A. G. Every, P. R. Stoddart, W. Pang, and T. E. Derry, Phys. Rev. B **58**, 13677 (1998).
[19]R. Oliva, J. Ibáñez, R. Cuscó, R. Kudrawiec, J. Serafinczuk, O. Martínez, J. Jiménez, M. Henini, C. Boney, A. Bensaoula, and L. Artús, J. Appl. Phys. **111**, 063502 (2012).
[20]R. J. Jiménez Rioboo, M. García-Hernández, C. Prieto, J. J. Fuentes-Gallego, E. Blanco, and M. Ramírez del Solar, J. Appl. Phys. **81**, 7739 (1997).
[21]S. P. Łepkowski, Phys. Rev. B **75**, 195303 (2007).

APPLIED PHYSICS LETTERS **104**, 142101 (2014)

High-pressure Raman scattering in InGaN heteroepitaxial layers: Effect of the substrate on the phonon pressure coefficients

R. Oliva,[1] J. Ibáñez,[1,a)] R. Cuscó,[1] A. Dadgar,[2] A. Krost,[2] J. Gandhi,[3] A. Bensaoula,[3] and L. Artús[1]
[1]*Institut Jaume Almera, Consell Superior d'Investigacions Científiques (CSIC), Lluís Solé I Sabarís s.n. 08028 Barcelona, Catalonia, Spain*
[2]*Institut für Experimentelle Physik, Otto-von-Guericke-Universität Magdeburg, Universitätsplatz 2, 39016 Magdeburg, Germany*
[3]*Department of Physics, University of Houston, 4800 Calhoun, Houston, Texas 77004, USA*

(Received 7 March 2014; accepted 25 March 2014; published online 7 April 2014)

We perform high-pressure Raman-scattering measurements on different $In_xGa_{1-x}N$/Si(111) epilayers ($0.19 < x < 0.45$). We find that the experimental pressure coefficient of the A_1(LO) mode measured in these samples is larger than that expected from the linear interpolation between the corresponding values of GaN and InN. Similar measurements in InGaN epilayers grown on GaN/sapphire templates yield much lower values, below the linearly interpolated pressure coefficients. We conclude that the phonon pressure coefficients measured in InGaN are mainly determined by the different compressibility of the substrate and epilayer material. Neglecting substrate effects may yield highly inaccurate phonon pressure coefficients and mode Grüneisen parameters. © *2014 AIP Publishing LLC*. [http://dx.doi.org/10.1063/1.4870529]

Group-III nitrides and their alloys are already being used as the active material of a variety of commercial electronic and optoelectronic devices. The bandgap energy of InGaN can be tuned to cover the entire visible spectral range, from the ultraviolet (UV) down to the near-infrared, and this could be exploited to design and fabricate high-efficiency multijunction solar cells, infrared detectors, or white-light emitting devices.[1] InGaN alloys are also being studied as a promising candidate to fabricate photoelectrochemical cells for hydrogen generation by solar water splitting.[2] Thus, a great deal of research work is currently being devoted to improve the crystal quality of InGaN layers, which are most usually grown on sapphire substrates. The growth of InGaN on Si offers a potential alternative for low-cost production of device applications based on this alloy system. In the particular case of multijunction solar cells, the bandgap of Si at 1.1 eV makes it ideally suited for the bottom junction of the stucture.[3]

Raman spectroscopy is widely employed to characterize the strain, composition, and crystal quality of semiconductor materials and structures. Raman-scattering experiments performed under high hydrostatic pressures also allow one to determine important thermodynamic properties of crystalline compounds such as the mode Grüneisen parameters. In addition, the high-pressure Raman measurements provide a highly useful benchmark to test existing models for the calculation of the lattice-dynamical properties of semiconductors. The measurement of phonon pressure coefficients from heterostructured material, however, may be strongly affected by the particular substrate employed for the growth. This might be particularly relevant for the case of III-nitrides, which are grown on a variety of different substrates.

Several works have been devoted to carry out high-pressure Raman-scattering measurements on GaN[4–6] and InN.[7–11] Pressure coefficients and mode Grüneisen parameters for the non-polar E_2 modes and the polar A_1 and E_1 modes of these two compounds have been measured. Also, the softening of the E_{2l} mode in both GaN and InN has been observed and the pressure dependence of the TO-LO splitting has been investigated and analyzed. The wurtzite-to-rocksalt transition has been found to occur at 42–49 GPa in GaN[5] and at 12–14 GPa in InN,[8,11] and the pressure behavior of the Raman modes of the rocksalt phases has been monitored. The rocksalt-to-wurtzite backtransition has also been observed in InN in the downstroke cycle at pressure values as low as 3.6 GPa.[11] No substrate effects on the experimental phonon pressure coefficients of these two compounds have been observed so far.[11]

The compositional dependence of several structural and vibrational properties of the InGaN alloy has been found to display important deviations from the linear behavior. For instance, the ambient-pressure E_{2h} frequencies seem to exhibit a sizable bowing in relation to the linear dependence predicted by the modified random-element isodisplacement (MREI) model.[12] Similarly, the surface acoustic wave velocity of InGaN has been recently found to exhibit a sublinear dependence on alloy composition.[13] This observation supports the predictions of *ab initio* calculations of the elastic constants of wurtzite InGaN.[14] According to these calculations, the elastic constants of InGaN may significantly deviate from the linearly interpolated values between GaN and InN. The bulk modulus of InGaN, however, seems to follow an almost compositional linear behavior between the pure binary compounds.[14] With regard to the compositional behavior of the phonon pressure coefficients and mode Grüneisen parameters of InGaN, no data are available so far.

In the present work, we report high-pressure Raman-scattering measurements on $In_xGa_{1-x}N$/Si(111) epilayers with $0.19 < x < 0.45$. The aim of this work is to experimentally determine the pressure coefficient and mode Grüneisen parameters of the A_1(LO) phonons of InGaN as a function of

a)jibanez@ictja.csic.es

composition. We find that the experimental pressure coefficient of this mode measured in InGaN/Si(111) is larger than the values obtained by linear interpolation between GaN and InN. Additional experiments with different excitation wavelengths and on InGaN epilayers grown on GaN/sapphire suggest that the experimental phonon pressure coefficients are mainly determined by the differential compressibility between InGaN and the substrate material.

$In_xGa_{1-x}N$ layers were grown by metal-organic chemical vapor deposition on 10-nm-thick $In_yAl_{1-y}N$ buffer layers deposited on Si(111) substrates. The indium content (thickness) of the different $In_xGa_{1-x}N$/Si(111) epilayers was $x = 19\%$ (300 nm), 30% (360 nm), 37% (463 nm), 43% (541 nm), and 45% (446 nm). Two of these samples ($x = 43\%$ and 45%) were chemically etched with nitric acid to remove metallic In clusters from the surface. As-grown and etched samples were both included in this study. Three additional $In_xGa_{1-x}N$ layers ($x = 33\%$, 34%, and 42%) grown by molecular beam epitaxy on GaN/sapphire templates were also used in this work. Details about these samples can be found elsewhere.[12]

Small flakes ($\approx 30\,\mu$m thick) of the samples were loaded in a gasketed membrane-type diamond anvil cell (DAC). A mixture of methanol-ethanol-water (16:3:1) was used as pressure transmission medium, and the applied pressure was determined by the ruby fluorescence method. Confocal micro-Raman measurements were performed at room temperature with a Jobin-Yvon T-64000 spectrometer equipped with a LN_2-cooled CCD detector. The 514.5-nm line of an Ar^+ laser was used as excitation source. To investigate the role of excitation wavelength on the measured pressure coefficients, additional experiments were performed with 457.9-nm radiation. A 50× objective was used to focus the laser beam and to collect the backscattered radiation. The applied pressure was kept below the diamond-to-metallic β-Sn phase transition of Si at ~12 GPa.

Figure 1 shows selected room-temperature Raman spectra excited with 514.5-nm radiation at different hydrostatic pressures (upstroke cycle) for the case of the $In_{0.45}Ga_{0.55}N$/Si(111) epilayer. Similar results are found for the rest of InGaN/Si(111) samples investigated in this work. In Fig. 1, the intensity of the different curves has been normalized for scaling reasons, and a strong photoluminescence background signal has been removed from the spectra. As can be seen in the figure, the spectra are dominated by a broad band arising from the A_1(LO) mode of InGaN, which displays the expected blueshift with increasing pressure. In the spectra excited with 514.5-nm radiation, and given the In content of the samples studied in this work ($0.19 < x < 0.45$), the A_1(LO) phonons in all the samples are resonantly or near-resonantly excited via the Fröhlich interaction mechanisms. Below the A_1(LO) band, a broad shoulder related to alloy disorder is also observed. Besides, a weak feature corresponding to the first-order optical phonon of Si shows up in the spectra. The pressure coefficient that we obtain for this mode is $4.6 \pm 0.3\,cm^{-1}\,GPa^{-1}$ in all the InGaN/Si(111) samples, in agreement with the $\sim 4.5\,cm^{-1}\,GPa^{-1}$ value reported in the literature for bulk Si.[15]

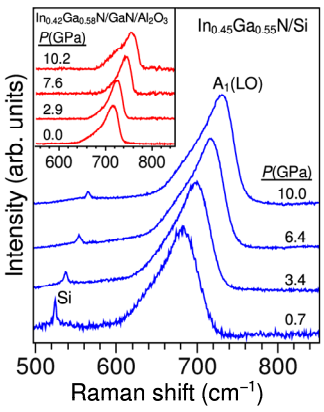

FIG. 1. Raman spectra acquired at different hydrostatic pressures up to 10 GPa from an $In_xGa_{1-x}N$ epilayer ($x = 0.45$) grown on Si(111). Inset: High-pressure Raman spectra of $In_xGa_{1-x}N$ /GaN/sapphire ($x = 0.42$).

Figure 2 shows the frequency of the A_1(LO) mode (ω_{LO}) as a function of applied pressure for three of the as-grown InGaN/Si(111) samples. In all cases, the A_1(LO) frequency is found to display a linear pressure dependence. From a linear fit to the experimental data, linear pressure coefficients $(d\omega_{LO}/dp)_{p=0}$ in the 4.2–5.3 $cm^{-1}\,GPa^{-1}$ range are obtained. The figure clearly shows the expected reduction of the zero-pressure A_1(LO) frequency with increasing In content.

We have plotted in Fig. 3 the linear pressure coefficient of the A_1(LO) mode obtained for all the as-grown (triangle symbols) and the etched (crosses) InGaN/Si(111) epilayers studied in this work. This figure shows that, within the experimental error associated to DAC experiments, the measured pressure coefficients tend to be larger in the samples with higher In contents. In contrast, no significant differences are found between as-grown and etched samples, which suggests that the presence of In clusters at the surface does not affect the pressure behavior of the InGaN/Si(111) epilayers. The dashed line in Fig. 3 corresponds to linearly interpolated pressure coefficients obtained from the values measured in InN and GaN. Note that there is a relatively large dispersion of reported pressure-coefficient values in the literature for these two compounds. For instance, in the case of the A_1(LO) mode of w-InN, pressure coefficients ranging from $4.73\,cm^{-1}\,GPa^{-1}$ (Ref. 9) up to $5.96\,cm^{-1}\,GPa^{-1}$ (Ref. 8) have been reported. The pressure coefficient values used to plot the linear composition dependence in Fig. 3 (3.8 and

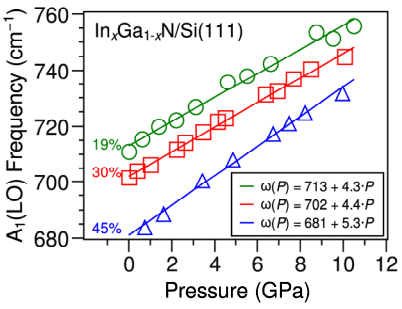

FIG. 2. Pressure dependence of the A_1(LO) phonon frequency of InGaN as measured in three different $In_xGa_{1-x}N$/Si(111) epilayers with $x = 0.19$, 0.3, and 0.45. The solid lines are linear fits to the experimental data.

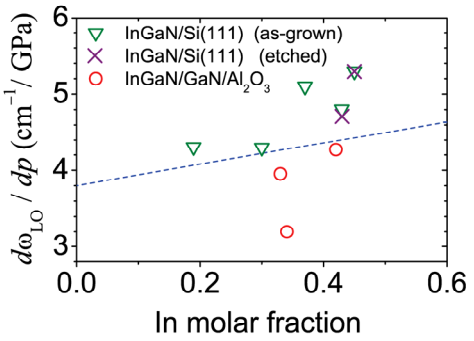

FIG. 3. Pressure coefficient of the A_1(LO) phonon mode as a function of In content as obtained by high-pressure Raman-scattering measurements on all the InGaN/Si(111) and InGaN/GaN/sapphire epilayers studied in this work. The dashed line shows the pressure coefficient values expected from a linear interpolation between the GaN and InN end members.

$5.2\,cm^{-1}\,GPa^{-1}$ for GaN and InN, respectively) were taken by averaging the data available in the literature (Refs. 4–6 for GaN and Refs. 8, 9, and 11 for InN). In the particular case of InN, recent measurements on several high-quality InN/Al_2O_3 epilayers of different thicknesses[11] suggest that the A_1(LO) pressure coefficient for InN is not larger than $5.2\,cm^{-1}\,GPa^{-1}$, not far from the value measured in strain-free InN nanowires ($4.73\,cm^{-1}\,GPa^{-1}$).[9]

As can be seen in Fig. 3, for intermediate In compositions, the experimental pressure coefficients measured on InGaN/Si(111) tend to be larger, up to $0.8\,cm^{-1}\,GPa^{-1}$, than those expected from the linear interpolation between the corresponding values of GaN and InN. Although the observed deviation is relatively low, it is consistently observed in the etched and non-etched samples with intermediate compositions ($x \sim 0.4$). This result could be attributed to a compositional bowing of the pressure coefficients that would also affect to the resulting mode Grüneisen parameters. However, two additional effects may be invoked to explain the present results: (i) variations of the measured pressure coefficients induced by compositional fluctuation in the InGaN layers; (ii) a strain-related substrate effect.

It is well-known that, in resonant or near-resonant Raman-scattering by the A_1(LO) phonons in InGaN, lateral and in-depth compositional fluctuations give rise to the selective excitation of sample regions with a particular In content.[16,17] Due to this effect, sizable frequency shifts of the A_1(LO) bands are reported in the literature as a function of the excitation wavelength used to perform the Raman measurements.[12,17] Given that hydrostatic pressure modifies the band-gap energy of the material, the A_1(LO) pressure coefficient ($d\omega_{LO}/dp$) in inhomogeneous samples may be affected by the selective excitation process. For instance, in InGaN layers with a band-gap energy slightly below the exciting photon energy (2.41 eV for 514.5-nm wavelength), the Raman-scattering cross section of sample domains with high In contents should become larger with increasing pressure, since the band-gap energy of such domains progressively approaches the excitation energy. Given that the A_1(LO) frequency of InGaN decreases with increasing In content, this effect could yield reduced pressure coefficients. In contrast, given that the A_1(LO) pressure coefficient is larger in InN than in GaN, large compositional fluctuations in In-rich samples could yield increased $d\omega_{LO}/dp$ values relative to the homogeneous alloy (i.e., relative to the linear behavior plotted in Fig. 3). These two competing effects could counteract each other or, depending on their relative magnitudes, give rise to sizable variations of the measured pressure coefficients.

To evaluate the role of compositional fluctuations on the measured pressure coefficients in InGaN/Si(111), we have performed additional high-pressure Raman experiments on the sample with the largest In content ($x = 0.45$) using a much shorter wavelength (457.9-nm), i.e., with excitation photon energies far from the bandgap energy corresponding to the In concentration of this sample. The pressure coefficient thus obtained turns out to be virtually identical to that obtained with 514.5-nm radiation ($5.3 \pm 0.2\,cm^{-1}\,GPa^{-1}$). This result suggests that selective resonant excitation does not have any significant bearing on the measured pressure coefficients of this InGaN epilayer.

On the other hand, the large experimental $d\omega_{LO}/dp$ values of Fig. 3 could be attributed to the different compressibility of the epilayer and the substrate. Since the bulk modulus of InGaN (175 GPa for $x \sim 40\%$)[14] is sizably larger than that of Si (98 GPa),[18] the effective pressure that is applied to the epilayer may be significantly larger, as it tries to accommodate to the more compressed substrate. The pressure amplification effect arising from the larger substrate compressibility may be expected to occur in material that is totally or partially lattice-matched to the substrate, regardless of the sign of the strain built-in in the epilayer.

To assess the influence of the particular substrate on the $d\omega_{LO}/dp$ values measured in InGaN epilayers, we have carried out additional high-pressure Raman experiments on InGaN material grown on GaN/sapphire. Given that the GaN/sapphire templates are much less compressible than InGaN (the bulk modulus of sapphire is around 250 GPa),[19] an opposite effect would be expected in this case, i.e., lowered $d\omega_{LO}/dp$ values. We plot in the inset of Fig. 1 selected Raman spectra as a function of applied pressure for one of the $In_xGa_{1-x}N$/GaN/sapphire heterostructures studied in this work ($x = 0.42$). As can be seen in Fig. 3 (circles), our measurements yield sizably lower A_1(LO) pressure coefficients on the three InGaN/GaN/sapphire samples. The measured pressure coefficients lie below the linear interpolation between the GaN and InN values. This result confirms that in the InGaN/Si(111) samples, increased $d\omega_{LO}/dp$ values are measured as a consequence of the high compressibility of the Si substrate. In the case of the InGaN/GaN/sapphire epilayers, the opposite effect is observed because the compressibility of the GaN/sapphire template is significantly lower than that of InGaN.[18] It is thus concluded that the actual A_1(LO) pressure coefficients of InGaN are not far from the linearly interpolated values between the pure binary compounds, GaN and InN.

In conclusion, neglecting substrate effects for the measurement of the phonon pressure coefficients in InGaN epilayers may yield highly inaccurate results. We have performed high-pressure Raman measurements on InGaN epilayers grown on two different substrates (silicon and

sapphire) and found that the experimental phonon pressure coefficients exhibit an important substrate effect. In InGaN layers grown on Si(111), the measured A_1(LO) pressure coefficients turn out to be above the linear compositional dependence between GaN and InN, while the opposite effect is observed in InGaN grown on GaN/sapphire templates. This observation may be attributed to the lower (larger) compressibility of InGaN relative to silicon (GaN/sapphire), giving rise to increased (decreased) effective applied pressures on the epilayer. Thus, we conclude that the A_1(LO) pressure coefficients and the corresponding mode Grüneisen parameters in the InGaN alloy are not far from the linear composition dependence. While further studies on free-standing material would be required to measure the actual phonon pressure coefficients of InGaN, our work also suggests that it might be necessary to reevaluate the pressure coefficient of the fundamental bandgap of InGaN, since the experimental values so far obtained[20,21] might also exhibit important substrate effects. These conclusions can be extrapolated to other heterostructures in which the bulk modulus of the substrate and the epilayer are markedly different. In such cases, free-standing material should be employed in order to obtain accurate pressure dependencies of the fundamental properties of the epilayer material.

The work was supported by the Spanish Ministry of Economy and Competitiveness (MINECO) under project MAT2010-16116.

[1]J. Wu, J. Appl. Phys. **106**, 011101 (2009).
[2]K. Aryal, B. N. Pantha, J. Li, J. Y. Lin, and H. X. Jiang, Appl. Phys. Lett. **96**, 052110 (2010).
[3]L. Hsu and W. Walukiewicz, J. Appl. Phys. **104**, 024507 (2008).
[4]P. Perlin, T. Suski, J. W. Ager, G. Conti, A. Polian, N. E. Christensen, I. Gorczyca, I. Grzegory, E. R. Weber, and E. E. Haller, Phys. Rev. B **60**, 1480 (1999).
[5]M. P. Halsall, P. Harmer, P. J. Parbrook, and S. J. Henley, Phys. Rev. B **69**, 235207 (2004).
[6]A. R. Goñi, H. Siegle, K. Syassen, C. Thomsen, and J.-M. Wagner, Phys. Rev. B **64**, 035205 (2001).
[7]C. Pinquier, F. Demangeot, J. Frandon, J. W. Pomeroy, M. Kuball, H. Hubel, N. W. A. van Uden, D. J. Dunstan, O. Briot, B. Maleyre, S. Ruffenach, and B. Gil, Phys. Rev. B **70**, 113202 (2004).
[8]C. Pinquier, F. Demangeot, J. Frandon, J.-C. Chervin, A. Polian, B. Couzinet, P. Munsch, O. Briot, S. Ruffenach, B. Gil, and B. Maleyre, Phys. Rev. B **73**, 115211 (2006).
[9]L. D. Yao, S. D. Luo, X. Shen, S. J. You, L. X. Yang, S. J. Zhang, S. Jiang, Y. C. Li, J. Liu, K. Zhu, Y. L. Liu, W. Y. Zhou, L. C. Chen, C. Q. Jin, R. C. Yu, and S. S. Xie, J. Mater. Res. **25**, 2330 (2010).
[10]J. Ibáñez, F. J. Manjón, A. Segura, R. Oliva, R. Cuscó, R. Vilaplana, T. Yamaguchi, Y. Nanishi, and L. Artús, Appl. Phys. Lett. **99**, 011908 (2011).
[11]J. Ibáñez, R. Oliva, F. J. Manjón, A. Segura, T. Yamaguchi, Y. Nanishi, R. Cuscó, and L. Artús, Phys. Rev. B **88**, 115202 (2013).
[12]R. Oliva, J. Ibáñez, R. Cuscó, R. Kudrawiec, J. Serafinczuk, O. Martínez, J. Jiménez, M. Henini, C. Boney, A. Bensaoula, and L. Artús, J. Appl. Phys. **111**, 063502 (2012).
[13]R. J. Jiménez-Riobóo, R. Cuscó, R. Oliva, N. Domènech-Amador, C. Prieto, J. Ibáñez, C. Boney, A. Bensaoula, and L. Artús, Appl. Phys. Lett. **101**, 062103 (2012).
[14]S. P. Łepkowski and I. Gorczyca, Phys. Rev. B **83**, 203201 (2011).
[15]B. A. Weinstein and G. J. Piermarini, Phys. Rev. B **12**, 1172 (1975).
[16]D. Behr, J. Wagner, A. Ramakrishnan, H. Obloh, and K.-H. Bachem, Appl. Phys. Lett. **73**, 241 (1998).
[17]S. Hernández, R. Cuscó, D. Pastor, L. Artús, K. P. O'Donnell, R. W. Martin, I. M. Watson, Y. Nanishi, and E. Calleja, J. Appl. Phys. **98**, 013511 (2005).
[18]S. Adachi, *Properties of Group-IV, III-V and II-VI Semiconductors* (John Wiley & Sons, Ltd., 2005), pp. 41–72.
[19]G. H. Watson, Jr., W. B. Daniels, and C. S. Wang, J. Appl. Phys. **52**, 956 (1981).
[20]G. Franssen, I. Gorczyca, T. Suski, A. Kamińska, J. Pereiro, E. Muñoz, E. Iliopoulos, A. Georgakilas, S. B. Che, Y. Ishitani, A. Yoshikawa, N. E. Christensen, and A. Svane, J. Appl. Phys. **103**, 033514 (2008).
[21]M. Millot, Z. M. Geballe, K. M. Yu, W. Walukiewicz, and R. Jeanloz, Appl. Phys. Lett. **100**, 162103 (2012).

5.4. References

[1] K. Osamura, S. Naka, and Y. Murakami, J. Appl. Phys. **46**, 3432 (1975).
[2] K. Osamura, K. Nakajima, Y. Murakami, P.H. Shingu, and A. Ohtsuki, Solid State Commun. **11**, 617 (1972).
[3] N. Yoshimoto, T. Matsuoka, T. Sasaki, and A. Katsui, Appl. Phys. Lett. **59**, 2251 (1991).
[4] T. Nagatomo, T. Kuboyama, H. Minamino, and O. Omoto, Jpn. J. Appl. Phys. **28**, L1334 (1989).
[5] S. Nakamura and T. Mukai, Jpn. J. Appl. Phys. **31**, L1457 (1992).
[6] S. Nakamura, J. Vac. Sci. Technol. A **13**, 705 (1995).
[7] S. Nakamura, Science **281**, 956 (1998).
[8] S. Nakamura, M. Senoh, N. Iwasa, S. Nagahama, T. Yamada, and T. Mukai, Jpn. J. Appl. Phys. **34**, L1332 (1995).
[9] T. Matsuoka, H. Okamoto, M. Nakao, H. Harima, and E. Kurimoto, Appl. Phys. Lett. **81**, 1246 (2002).
[10] J. Wu, J. Appl. Phys. **106**, 011101 (2009).
[11] D. Doppalapudi, S.N. Basu, K.F.L. Jr, and T.D. Moustakas, J. Appl. Phys. **84**, 1389 (1998).
[12] Y.-T. Moon, D.-J. Kim, J.-S. Park, J.-T. Oh, J.-M. Lee, Y.-W. Ok, H. Kim, and S.-J. Park, Appl. Phys. Lett. **79**, 599 (2001).
[13] S. Srinivasan, F. Bertram, A. Bell, F.A. Ponce, S. Tanaka, H. Omiya, and Y. Nakagawa, Appl. Phys. Lett. **80**, 550 (2002).
[14] D. Dobrovolskas, A. Vaitkevičius, J. Mickevičius, Ö. Tuna, C. Giesen, M. Heuken, and G. Tamulaitis, J. Appl. Phys. **114**, 163516 (2013).
[15] R. Oliva Vidal, Optical Emission and Raman Scattering in InGaN Thin Films Grown by Molecular Beam Epitaxy, Master Thesis. University of Barcelona. http://diposit.ub.edu/dspace/handle/2445/14763, 2010.
[16] M.E. Aumer, S.F. LeBoeuf, S.M. Bedair, M. Smith, J.Y. Lin, and H.X. Jiang, Appl. Phys. Lett. **77**, 821 (2000).
[17] O. Donmez, M. Gunes, A. Erol, M.C. Arikan, and N. Balkan, J. Appl. Phys. **110**, 103506 (2011).
[18] M. Hori, K. Kano, T. Yamaguchi, Y. Saito, T. Araki, Y. Nanishi, N. Teraguchi, and A. Suzuki, Phys. Status Solidi B **234**, 750 (2002).
[19] V.Y. Davydov, A. a. Klochikhin, V. v. Emtsev, D. a. Kurdyukov, S. v. Ivanov, V. a. Vekshin, F. Bechstedt, J. Furthmüller, J. Aderhold, J. Graul, A. v. Mudryi, H. Harima, A. Hashimoto, A. Yamamoto, and E. e. Haller, Phys. Status Solidi B **234**, 787 (2002).
[20] V.Y. Davydov, A.A. Klochikhin, I.N. Goncharuk, A.N. Smirnov, A.V. Sakharov, A.P. Skvortsov, M.A. Yagovkina, V.M. Lebedev, H. Lu, and W.J. Schaff, Phys. Status Solidi B **243**, 1494 (2006).
[21] J. Wu, W. Walukiewicz, K.M. Yu, J.W.A. Iii, E.E. Haller, H. Lu, and W.J. Schaff, Appl. Phys. Lett. **80**, 4741 (2002).
[22] R.W. Martin, P.G. Middleton, K.P. O'Donnell, and W.V. der Stricht, Appl. Phys. Lett. **74**, 263 (1999).

[23] M.J.W. P. Scharoch, Comput. Mater. Sci. **81**, (2014).
[24] S.P. Łepkowski and I. Gorczyca, Phys. Rev. B **83**, 203201 (2011).
[25] C. Li, F. Wu, S.-S. Li, J.-B. Xia, and J. Li, Appl. Phys. Lett. **101**, 062102 (2012).
[26] J.W. Ager, W. Walukiewicz, W. Shan, K.M. Yu, S.X. Li, E.E. Haller, H. Lu, and W.J. Schaff, Phys. Rev. B **72**, 155204 (2005).
[27] H. Harima, E. Kurimoto, Y. Sone, S. Nakashima, S. Chu, A. Ishida, and H. Fujiyasu, Phys. Status Solidi B **216**, 785 (1999).
[28] D. Alexson, L. Bergman, R.J. Nemanich, M. Dutta, M.A. Stroscio, C.A. Parker, S.M. Bedair, N.A. El-Masry, and F. Adar, J. Appl. Phys. **89**, 798 (2001).
[29] V.Y. Davydov, A.A. Klochikhin, V.V. Emtsev, A.N. Smirnov, I.N. Goncharuk, A.V. Sakharov, D.A. Kurdyukov, M.V. Baidakova, V.A. Vekshin, S.V. Ivanov, J. Aderhold, J. Graul, A. Hashimoto, and A. Yamamoto, Phys. Status Solidi B **240**, 425 (2003).
[30] S. Hernández, R. Cuscó, D. Pastor, L. Artús, K.P. O'Donnell, R.W. Martin, I.M. Watson, Y. Nanishi, and E. Calleja, J. Appl. Phys. **98**, 013511 (2005).
[31] E. Tiras, M. Gunes, N. Balkan, and W.J. Schaff, Phys. Status Solidi B **247**, 189 (2010).
[32] R. Oliva, J. Ibáñez, R. Cuscó, R. Kudrawiec, J. Serafinczuk, O. Martínez, J. Jiménez, M. Henini, C. Boney, A. Bensaoula, and L. Artús, J. Appl. Phys. **111**, 063502 (2012).
[33] T. Sugiura, Y. Kawaguchi, T. Tsukamoto, H. Andoh, M. Yamaguchi, K. Hiramatsu, and N. Sawaki, Jpn. J. Appl. Phys. **40**, 5955 (2001).
[34] M. Bosi, R. Fornari, S. Scardova, M. Avella, O. Mart?nez, and J. Jimenez, Semicond. Sci. Technol. **19**, 147 (2004).
[35] A.G. Kontos, Y.S. Raptis, N.T. Pelekanos, A. Georgakilas, E. Bellet-Amalric, and D. Jalabert, Phys. Rev. B **72**, 155336 (2005).
[36] D. Behr, J. Wagner, A. Ramakrishnan, H. Obloh, and K.-H. Bachem, Appl. Phys. Lett. **73**, 241 (1998).
[37] N. Wieser, O. Ambacher, H.-P. Felsl, L. Görgens, and M. Stutzmann, Appl. Phys. Lett. **74**, 3981 (1999).
[38] A. Kaschner, A. Hoffmann, C. Thomsen, T. Böttcher, S. Einfeldt, and D. Hommel, Phys. Status Solidi A **179**, R4 (2000).
[39] M.R. Correia, S. Pereira, E. Pereira, J. Frandon, I.M. Watson, C. Liu, E. Alves, A.D. Sequeira, and N. Franco, Appl. Phys. Lett. **85**, 2235 (2004).
[40] A. Kar, D. Alexson, M. Dutta, and M.A. Stroscio, J. Appl. Phys. **104**, 073502 (2008).
[41] H.C. Yang, P.F. Kuo, T.Y. Lin, Y.F. Chen, K.H. Chen, L.C. Chen, and J.-I. Chyi, Appl. Phys. Lett. **76**, 3712 (2000).
[42] H. Harima, J. Phys. Condens. Matter **14**, R967 (2002).
[43] M.R. Correia, S. Pereira, E. Pereira, J. Frandon, and E. Alves, Appl. Phys. Lett. **83**, 4761 (2003).
[44] J. Wagner, A. Ramakrishnan, H. Obloh, and M. Maier, Appl. Phys. Lett. **74**, 3863 (1999).
[45] S. Lazić, M. Moreno, J.M. Calleja, A. Trampert, K.H. Ploog, F.B. Naranjo, S. Fernandez, and E. Calleja, Appl. Phys. Lett. **86**, 061905 (2005).
[46] H. Grille, C. Schnittler, and F. Bechstedt, Phys. Rev. B **61**, 6091 (2000).
[47] M.S. Liu, L.A. Bursill, and S. Prawer, J. Appl. Phys. **90**, 1761 (2001).

[48] R. Zheng, T. Taguchi, and M. Matsuura, Phys. Rev. B **66**, 075327 (2002).
[49] C. Boney, I. Hernandez, R. Pillai, D. Starikov, A. Bensaoula, M. Henini, M. Syperek, J. Misiewicz, and R. Kudrawiec, 35th Ieee Photovolt. Spec. Conf. 3316 (2010).
[50] L.R. Bailey, T.D. Veal, P.D.C. King, C.F. McConville, J. Pereiro, J. Grandal, M.A. Sánchez-García, E. Muñoz, and E. Calleja, J. Appl. Phys. **104**, 113716 (2008).
[51] C. Boney, D. Starikov, I. Hernandez, R. Pillai, and A. Bensaoula, J. Vac. Sci. Technol. B **29**, 03C106 (2011).
[52] J.A. Van Vechten and T.K. Bergstresser, Phys. Rev. B **1**, 3351 (1970).
[53] A. Ben Fredj, M. Debbichi, and M. Said, Microelectron. J. **38**, 860 (2007).
[54] F. Sökeland, M. Rohlfing, P. Krüger, and J. Pollmann, Phys. Rev. B **68**, 075203 (2003).
[55] J. Wu, W. Walukiewicz, K.. Yu, J.. Ager, S.. Li, E.. Haller, H. Lu, and W.J. Schaff, Solid State Commun. **127**, 411 (2003).
[56] T.Y. Wu, C.C. Chang, K.K. Tiong, Y.C. Lee, S.Y. Hu, L.Y. Lin, T.Y. Lin, and Z.C. Feng, Opt. Mater. **35**, 1829 (2013).
[57] M.D. McCluskey, C.G.V. de Walle, C.P. Master, L.T. Romano, and N.M. Johnson, Appl. Phys. Lett. **72**, 2725 (1998).
[58] S. Pereira, M.R. Correia, T. Monteiro, E. Pereira, E. Alves, A.D. Sequeira, and N. Franco, Appl. Phys. Lett. **78**, 2137 (2001).
[59] P.G. Moses and C.G.V. de Walle, Appl. Phys. Lett. **96**, 021908 (2010).
[60] C.G. Van de Walle, M.D. McCluskey, C.P. Master, L.T. Romano, and N.M. Johnson, Mater. Sci. Eng. B **59**, 274 (1999).
[61] M. Kurouchi, T. Araki, H. Naoi, T. Yamaguchi, A. Suzuki, and Y. Nanishi, Phys. Status Solidi B **241**, 2843 (2004).
[62] R.R. Pelá, C. Caetano, M. Marques, L.G. Ferreira, J. Furthmüller, and L.K. Teles, Appl. Phys. Lett. **98**, 151907 (2011).
[63] C. Caetano, L.K. Teles, M. Marques, A. Dal Pino, and L.G. Ferreira, Phys. Rev. B **74**, 045215 (2006).
[64] B. Lee and L.W. Wang, J. Appl. Phys. **100**, 093717 (2006).
[65] I. Vurgaftman and J.R. Meyer, J. Appl. Phys. **94**, 3675 (2003).
[66] M. Ferhat, Phys. Status Solidi B **241**, R38 (2004).
[67] J.A. Chan, J.Z. Liu, and A. Zunger, Phys. Rev. B **82**, 045112 (2010).
[68] S. Zhang, J. Shi, S. Zhu, F. Wang, M. Yang, and Z. Bao, Phys. Lett. A **374**, 4767 (2010).
[69] I. Gorczyca, T. Suski, N.E. Christensen, and A. Svane, Appl. Phys. Lett. **98**, 241905 (2011).
[70] A. Laref, A. Altujar, and S.J. Luo, Eur. Phys. J. B **86**, 1 (2013).
[71] W. Walukiewicz, J.W.A. Iii, K.M. Yu, Z. Liliental-Weber, J. Wu, S.X. Li, R.E. Jones, and J.D. Denlinger, J. Phys. Appl. Phys. **39**, R83 (2006).
[72] P.G. Moses, M. Miao, Q. Yan, and C.G.V. de Walle, J. Chem. Phys. **134**, 084703 (2011).
[73] X. Wu, E.J. Walter, A.M. Rappe, R. Car, and A. Selloni, Phys. Rev. B **80**, 115201 (2009).
[74] Y.H. Huang, C.L. Cheng, T.T. Chen, Y.F. Chen, and K.T. Tsen, J. Appl. Phys. **101**, 103521 (2007).
[75] K. Kazlauskas, G. Tamulaitis, P. Pobedinskas, A. Žukauskas, M. Springis, C.-F. Huang, Y.-C. Cheng, and C.C. Yang, Phys. Rev. B **71**, 085306 (2005).

[76] G. Franssen, I. Gorczyca, T. Suski, A. Kamińska, J. Pereiro, E. Muñoz, E. Iliopoulos, A. Georgakilas, S.B. Che, Y. Ishitani, A. Yoshikawa, N.E. Christensen, and A. Svane, J. Appl. Phys. **103**, 033514 (2008).
[77] K.P. O'Donnell, R.W. Martin, and P.G. Middleton, Phys. Rev. Lett. **82**, 237 (1999).
[78] J.-L. Reverchon, F. Huet, M.-A. Poisson, J.-Y. Duboz, B. Damilano, N. Grandjean, and J. Massies, Mater. Sci. Eng. B **82**, 197 (2001).
[79] W. Shan, W. Walukiewicz, E.E. Haller, B.D. Little, J.J. Song, M.D. McCluskey, N.M. Johnson, Z.C. Feng, M. Schurman, and R.A. Stall, J. Appl. Phys. **84**, 4452 (1998).
[80] J. Misiewicz, P. Sitarek, G. Sęk, and R. Kudrawiec, Mater. Sci. 263 (2003).
[81] Y.L. Li, X.J. Wang, S.M. He, B. Zhang, L.X. Sun, Y.D. Li, Q. Guo, C.Q. Chen, Z.H. Chen, and W. Lu, J. Appl. Phys. **112**, 123515 (2012).
[82] H.J. Chang, C.H. Chen, Y.F. Chen, T.Y. Lin, L.C. Chen, K.H. Chen, and Z.H. Lan, Appl. Phys. Lett. **86**, 021911 (2005).
[83] H. Wang, D.S. Jiang, U. Jahn, J.J. Zhu, D.G. Zhao, Z.S. Liu, S.M. Zhang, and H. Yang, Thin Solid Films **518**, 5028 (2010).
[84] F. Urbach, Phys. Rev. **92**, 1324 (1953).
[85] K. Boubaker, Eur. Phys. J. Plus **126**, 1 (2011).
[86] C.H. Qiu, C. Hoggatt, W. Melton, M.W. Leksono, and J.I. Pankove, Appl. Phys. Lett. **66**, 2712 (1995).
[87] Gordon and Breach, Comments Cond Mat Phys **13**, 35 (1987).
[88] P. Schley, R. Goldhahn, A.T. Winzer, G. Gobsch, V. Cimalla, O. Ambacher, M. Rakel, C. Cobet, N. Esser, H. Lu, and W.J. Schaff, Phys. Status Solidi B **243**, 1572 (2006).
[89] M. Feneberg, S. Osterburg, K. Lange, C. Lidig, B. Garke, R. Goldhahn, E. Richter, C. Netzel, M.D. Neumann, N. Esser, S. Fritze, H. Witte, J. Bläsing, A. Dadgar, and A. Krost, Phys. Rev. B **90**, 075203 (2014).
[90] M. Millot, N. Ubrig, J.-M. Poumirol, I. Gherasoiu, W. Walukiewicz, S. George, O. Portugall, J. Léotin, M. Goiran, and J.-M. Broto, Phys. Rev. B **83**, 125204 (2011).
[91] P.Y. Yu and M. Cardona, *Fundamentals of Semiconductors* (Springer Berlin Heidelberg, Berlin, Heidelberg, 2010).
[92] D.A. Broido and L.J. Sham, Phys. Rev. B **31**, 888 (1985).
[93] C.J. Sun, M.Z. Anwar, Q. Chen, J.W. Yang, M.A. Khan, M.S. Shur, A.D. Bykhovski, Z. Liliental-Weber, C. Kisielowski, M. Smith, J.Y. Lin, and H.X. Jiang, Appl. Phys. Lett. **70**, 2978 (1997).
[94] J. Piprek and S. Nakamura, Optoelectron. IEE Proc. **149**, 145 (2002).
[95] J.-Y. Chang and Y.-K. Kuo, J. Appl. Phys. **93**, 4992 (2003).
[96] M.M.Y. Leung, A.B. Djurišić, and E.H. Li, J. Appl. Phys. **84**, 6312 (1998).
[97] M.D. McCluskey, C.G.V. de Walle, L.T. Romano, B.S. Krusor, and N.M. Johnson, J. Appl. Phys. **93**, 4340 (2003).
[98] G. Orsal, Y. El Gmili, N. Fressengeas, J. Streque, R. Djerboub, T. Moudakir, S. Sundaram, A. Ougazzaden, and J.P. Salvestrini, Opt. Mater. Express **4**, 1030 (2014).
[99] Q. Yan, P. Rinke, A. Janotti, M. Scheffler, and C.G. Van de Walle, Phys. Rev. B **90**, 125118 (2014).
[100] H. Lu, W.J. Schaff, J. Hwang, H. Wu, G. Koley, and L.F. Eastman, Appl. Phys. Lett. **79**, 1489 (2001).

[101] C.A. Parker, J.C. Roberts, S.M. Bedair, M.J. Reed, S.X. Liu, and N.A. El-Masry, Appl. Phys. Lett. **75**, 2776 (1999).
[102] E. Sakalauskas, ö. Tuna, A. Kraus, H. Bremers, U. Rossow, C. Giesen, M. Heuken, A. Hangleiter, G. Gobsch, and R. Goldhahn, Phys. Status Solidi B **249**, 485 (2012).
[103] G.L. Bir and G.E. Pikus, *Symmetry and Strain-Induced Effects in Semiconductors* (Wiley, 1974).
[104] S.L. Chuang and C.S. Chang, Phys. Rev. B **54**, 2491 (1996).
[105] S.K. Jana, S. Ghosh, S.M. Dinara, T.D. Das, and D. Biswas, IOP Conf. Ser. Mater. Sci. Eng. **73**, 012151 (2015).
[106] T. Hanada, in *Oxide Nitride Semicond.*, edited by P.T. Yao and P.D.S.-K. Hong (Springer Berlin Heidelberg, 2009), pp. 1–19.
[107] I. Gorczyca, S.P. Łepkowski, T. Suski, N.E. Christensen, and A. Svane, Phys. Rev. B **80**, 075202 (2009).
[108] R.J. Jiménez-Riobóo, R. Cuscó, R. Oliva, N. Domènech-Amador, C. Prieto, J. Ibáñez, C. Boney, A. Bensaoula, and L. Artús, Appl. Phys. Lett. **101**, 062103 (2012).
[109] F.B. Naranjo, M.A. Sánchez-Garcı□ a, F. Calle, E. Calleja, B. Jenichen, and K.H. Ploog, Appl. Phys. Lett. **80**, 231 (2002).
[110] E. Sakalauskas, B. Reuters, L.R. Khoshroo, H. Kalisch, M. Heuken, A. Vescan, M. Röppischer, C. Cobet, G. Gobsch, and R. Goldhahn, J. Appl. Phys. **110**, 013102 (2011).
[111] Q. Yan, P. Rinke, M. Scheffler, and C.G.V. de Walle, Appl. Phys. Lett. **95**, 121111 (2009).
[112] L.C. de Carvalho, A. Schleife, J. Furthmüller, and F. Bechstedt, Phys. Rev. B **87**, (2013).
[113] I. Gorczyca, T. Suski, N.E. Christensen, and A. Svane, Phys. Rev. B **83**, 153301 (2011).
[114] J. Ibáñez, A. Segura, B. García-Domene, R. Oliva, F.J. Manjón, T. Yamaguchi, Y. Nanishi, and L. Artús, Phys. Rev. B **86**, 035210 (2012).
[115] P. Rinke, M. Winkelnkemper, A. Qteish, D. Bimberg, J. Neugebauer, and M. Scheffler, Phys. Rev. B **77**, 075202 (2008).
[116] S. Adachi, J. Appl. Phys. **58**, R1 (1985).
[117] A.R. Goñi and K. Syassen, in *Semicond. Semimet.*, edited by T.S. and W. Paul (Elsevier, 1998), pp. 247–425.
[118] I. Gorczyca, A. Kamińska, G. Staszczak, R. Czernecki, S.P. Łepkowski, T. Suski, H.P.D. Schenk, M. Glauser, R. Butté, J.-F. Carlin, E. Feltin, N. Grandjean, N.E. Christensen, and A. Svane, Phys. Rev. B **81**, 235206 (2010).
[119] I. Gorczyca, T. Suski, N.E. Christensen, and A. Svane, Phys. Status Solidi C **6**, S368 (2009).
[120] T. Suski, H. Teisseyre, S.P. Łepkowski, P. Perlin, H. Mariette, T. Kitamura, Y. Ishida, H. Okumura, and S.F. Chichibu, Phys. Status Solidi B **235**, 225 (2003).
[121] S.X. Li, J. Wu, E.E. Haller, W. Walukiewicz, W. Shan, H. Lu, and W.J. Schaff, Appl. Phys. Lett. **83**, 4963 (2003).
[122] A. Kamińska, G. Franssen, T. Suski, I. Gorczyca, N.E. Christensen, A. Svane, A. Suchocki, H. Lu, W.J. Schaff, E. Dimakis, and A. Georgakilas, Phys. Rev. B **76**, 075203 (2007).

[123] P. Perlin, I. Gorczyca, S. Porowski, T. Suski, N.E. Christensen, and A. Polian, Jpn. J. Appl. Phys. **32**, 334 (1993).
[124] G. Franssen, T. Suski, P. Perlin, H. Teisseyre, A. Khachapuridze, L.H. Dmowski, J.A. Plesiewicz, A. Kamińska, M. Kurouchi, Y. Nanishi, H. Lu, and W. Schaff, Appl. Phys. Lett. **89**, 121915 (2006).
[125] M. Millot, Z.M. Geballe, K.M. Yu, W. Walukiewicz, and R. Jeanloz, Appl. Phys. Lett. **100**, 162103 (2012).
[126] Z. Dridi, B. Bouhafs, and P. Ruterana, New J. Phys. **4**, 94 (2002).
[127] S.P. Łepkowski, J.A. Majewski, and G. Jurczak, Phys. Rev. B **72**, 245201 (2005).
[128] J. Groenen, R. Carles, G. Landa, C. Guerret-Piécourt, C. Fontaine, and M. Gendry, Phys. Rev. B **58**, 10452 (1998).
[129] T.-T. Kang, A. Hashimoto, and A. Yamamoto, Phys. Rev. B **79**, 033301 (2009).
[130] O.K. Kim and W.G. Spitzer, J. Appl. Phys. **50**, 4362 (1979).
[131] A. Milekhin, A. Kalagin, A. Vasilenko, A. Toropov, N. Surovtsev, and D.R.T. Zahn, in *AIP Conf. Proc.* (AIP Publishing, 2010), pp. 43–44.
[132] G. Armelles, J.M. Calleja, and E. Muñoz, Solid State Commun. **65**, 779 (1988).
[133] H. Asahi, S. Emura, S. Gonda, Y. Kawamura, and H. Tanaka, J. Appl. Phys. **65**, 5007 (1989).
[134] B. Jusserand and S. Slempkes, Solid State Commun. **49**, 95 (1984).
[135] O. Pagès, J. Souhabi, A.V. Postnikov, and A. Chafi, Phys. Rev. B **80**, 035204 (2009).
[136] Y.B. Li, S.S. Dosanjh, I.T. Ferguson, A.G. Norman, A.G. de Oliveira, R.A. Stradling, and R. Zallen, Semicond. Sci. Technol. **7**, 567 (1992).
[137] T.C. McGlinn, T.N. Krabach, M.V. Klein, G. Bajor, J.E. Greene, B. Kramer, S.A. Barnett, A. Lastras, and S. Gorbatkin, Phys. Rev. B **33**, 8396 (1986).
[138] J.G. Kim, Y. Kamei, A. Kimura, N. Hasuike, H. Harima, K. Kisoda, T. Hotta, K. Sasamoto, and A. Yamamoto, Phys. Status Solidi C **9**, 730 (2012).
[139] T.D. Veal, C.F. McConville, and W.J. Schaff, *Indium Nitride and Related Alloys* (CRC Press, 2011).
[140] G.P.S. H. M. Tütüncü, Phys. B-Condens. Matter - Phys. B **316**, 190 (2002).
[141] T. Inushima, T. Shiraishi, and V.Y. Davydov, Solid State Commun. **110**, 491 (1999).
[142] F. Demangeot, J. Groenen, J. Frandon, M.A. Renucci, O. Briot, S. Clur, and R.L. Aulombard, Appl. Phys. Lett. **72**, 2674 (1998).
[143] J.H.V.D. Merwe, J. Appl. Phys. **34**, 123 (1963).
[144] W. Zhao, L. Wang, J. Wang, Z. Hao, and Y. Luo, J. Cryst. Growth **327**, 202 (2011).
[145] D. Holec, Y. Zhang, D.V.S. Rao, M.J. Kappers, C. McAleese, and C.J. Humphreys, J. Appl. Phys. **104**, 123514 (2008).
[146] S.J. Rosner, E.C. Carr, M.J. Ludowise, G. Girolami, and H.I. Erikson, Appl. Phys. Lett. **70**, 420 (1997).
[147] R. People and J.C. Bean, Appl. Phys. Lett. **47**, 322 (1985).
[148] S. Pereira, Thin Solid Films **515**, 164 (2006).
[149] C.H. Belgacem and M. Fnaiech, J. Electron. Mater. **39**, 2248 (2010).
[150] D. Holec, P.M.F.J. Costa, M.J. Kappers, and C.J. Humphreys, J. Cryst. Growth **303**, 314 (2007).

[151] S. Ploch, T. Wernicke, M. Frentrup, M. Pristovsek, M. Weyers, and M. Kneissl, Appl. Phys. Lett. **101**, 202102 (2012).
[152] M.E. Levinshtein, S.L. Rumyantsev, and M.S. Shur, editors , *Properties of Advanced Semiconductor Materials: GaN, A1N, InN, BN, SiC, SiGe*, 1st edition (Wiley-Interscience, New York, 2001).
[153] M.J. Reed, N.A. El-Masry, C.A. Parker, J.C. Roberts, and S.M. Bedair, Appl. Phys. Lett. **77**, 4121 (2000).
[154] J.-P. Reithmaier, H. Cerva, and R. Lösch, Appl. Phys. Lett. **54**, 48 (1989).
[155] P.J. Orders and B.F. Usher, Appl. Phys. Lett. **50**, 980 (1987).
[156] S. Pereira, M.R. Correia, E. Pereira, C. Trager-Cowan, F. Sweeney, K.P. O'Donnell, E. Alves, N. Franco, and A.D. Sequeira, Appl. Phys. Lett. **81**, 1207 (2002).
[157] V.Y. Davydov, N.S. Averkiev, I.N. Goncharuk, D.K. Nelson, I.P. Nikitina, A.S. Polkovnikov, A.N. Smirnov, M.A. Jacobson, and O.K. Semchinova, J. Appl. Phys. **82**, 5097 (1997).
[158] R.J. Briggs and A.K. Ramdas, Phys. Rev. B **13**, 5518 (1976).
[159] G. Callsen, J.S. Reparaz, M.R. Wagner, R. Kirste, C. Nenstiel, A. Hoffmann, and M.R. Phillips, Appl. Phys. Lett. **98**, 061906 (2011).
[160] W.J. Meng and T.A. Perry, J. Appl. Phys. **76**, 7824 (1994).
[161] F. Agulló-Rueda, E.E. Mendez, B. Bojarczuk, and S. Guha, Solid State Commun. **115**, 19 (2000).
[162] W. Rieger, T. Metzger, H. Angerer, R. Dimitrov, O. Ambacher, and M. Stutzmann, Appl. Phys. Lett. **68**, 970 (1996).
[163] C. Kisielowski, J. Krüger, S. Ruvimov, T. Suski, J.W. Ager, E. Jones, Z. Liliental-Weber, M. Rubin, E.R. Weber, M.D. Bremser, and R.F. Davis, Phys. Rev. B **54**, 17745 (1996).
[164] B.H. Bairamov, O. Gürdal, A. Botchkarev, H. Morkoç, G. Irmer, and J. Monecke, Phys. Rev. B **60**, 16741 (1999).
[165] D.G. Zhao, S.J. Xu, M.H. Xie, S.Y. Tong, and H. Yang, Appl. Phys. Lett. **83**, 677 (2003).
[166] F. Demangeot, J. Frandon, P. Baules, F. Natali, F. Semond, and J. Massies, Phys. Rev. B **69**, 155215 (2004).
[167] V. Darakchieva, P.P. Paskov, E. Valcheva, T. Paskova, B. Monemar, M. Schubert, H. Lu, and W.J. Schaff, Appl. Phys. Lett. **84**, 3636 (2004).
[168] X. Wang, S.-B. Che, Y. Ishitani, and A. Yoshikawa, Appl. Phys. Lett. **89**, 171907 (2006).
[169] J.-Y. Lu, Z.-J. Wang, D.-M. Deng, Y. Wang, K.J. Chen, K.-M. Lau, and T.-Y. Zhang, J. Appl. Phys. **108**, 123520 (2010).
[170] J.-Y. Lu, D.-M. Deng, Y. Wang, K.J. Chen, K.-M. Lau, and T.-Y. Zhang, AIP Adv. **1**, 032132 (2011).
[171] J.-M. Wagner and F. Bechstedt, Appl. Phys. Lett. **77**, 346 (2000).
[172] J.-M. Wagner and F. Bechstedt, Phys. Rev. B **66**, 115202 (2002).
[173] X. Wang, S.-B. Che, Y. Ishitani, and A. Yoshikawa, J. Appl. Phys. **99**, 073512 (2006).
[174] M. r. Correia, S. Pereira, J. Frandon, M. a. Renucci, E. Alves, A. d. Sequeira, and N. Franco, Phys. Status Solidi C **0**, 563 (2003).

[175] E. Silveira, A. Tabata, J.R. Leite, R. Trentin, V. Lemos, T. Frey, D.J. As, D. Schikora, and K. Lischka, Appl. Phys. Lett. **75**, 3602 (1999).
[176] N. Domènech-Amador, R. Cuscó, R. García-Hernansanz, G. González-Díaz, J. Gandhi, A. Bensaoula, and L. Artús, Semicond. Sci. Technol. **29**, 045013 (2014).
[177] Cardona, M and Güntherodt, G, *Light Scattering in Solids II: Basic Concepts and Instrumentation* (Springer, New York, 1982).
[178] T.H. Wu, Z.C. Feng, F. Li, C.C. Lin, I. Ferguson, R.H. Horng, and W. Lu, in (2010), pp. 1141–1142.
[179] C. Sumanya, J.D. Comins, and A.G. Every, J. Phys. Conf. Ser. **92**, 012103 (2007).
[180] R. Loudon and J.R. Sandercock, J. Phys. C Solid State Phys. **13**, 2609 (1980).
[181] K.R. Subbaswamy and A.A. Maradudin, Phys. Rev. B **18**, 4181 (1978).
[182] X. Zhang, J.D. Comins, A.G. Every, P.R. Stoddart, W. Pang, and T.E. Derry, Phys. Rev. B **58**, 13677 (1998).
[183] M. Yamaguchi, T. Yagi, T. Sota, T. Deguchi, K. Shimada, and S. Nakamura, J. Appl. Phys. **85**, 8502 (1999).
[184] R.J.J. Riobóo, E. Rodrı guez-Cañas, M. Vila, C. Prieto, F. Calle, T. Palacios, M.A. Sánchez, F. Omnès, O. Ambacher, B. Assouar, and O. Elmazria, J. Appl. Phys. **92**, 6868 (2002).
[185] R.J. Jiménez-Riobóo, R. Cuscó, N. Domènech-Amador, C. Prieto, T. Yamaguchi, Y. Nanishi, and L. Artús, Phys. Status Solidi RRL – Rapid Res. Lett. **6**, 256 (2012).
[186] J.-K. Sheu, C.-C. Yang, S.-J. Tu, K.-H. Chang, M.-L. Lee, W.-C. Lai, and L.-C. Peng, Ieee Electron Device Lett. **30**, 225 (2009).
[187] G. Verzellesi, D. Saguatti, M. Meneghini, F. Bertazzi, M. Goano, G. Meneghesso, and E. Zanoni, J. Appl. Phys. **114**, 071101 (2013).
[188] J. Sapriel, J.C. Michel, J.C. Tolédano, R. Vacher, J. Kervarec, and A. Regreny, Phys. Rev. B **28**, 2007 (1983).
[189] B. Jusserand and M. Cardona, in *Light Scatt. Solids V*, edited by P.D. Dres h c Manuel Cardona and P.D.G. Güntherodt (Springer Berlin Heidelberg, 1989), pp. 49–152.
[190] C. Colvard, T.A. Gant, M.V. Klein, R. Merlin, R. Fischer, H. Morkoc, and A.C. Gossard, Phys. Rev. B **31**, 2080 (1985).
[191] J. Ibáñez, A. Rapaport, C. Boney, R. Oliva, R. Cuscó, A. Bensaoula, and L. Artús, J. Raman Spectrosc. **43**, 237 (2012).

CHAPTER 6

Summary and conclusions

This work has been aimed at providing a deeper insight into the optical and vibrational properties of InN and $In_xGa_{1-x}N$ at room and high pressure. For this purpose, a large set of InN and InGaN epilayers and heterostructures have been studied with different spectroscopic techniques. Next, we present the main conclusions obtained in the previous chapters and attached articles.

6.1. Optical properties of InN

- A pressure coefficient of 32 meV/GPa has been obtained for the fundamental band gap of InN by means of high-pressure optical absorption measurements.

- It has been observed that the pressure coefficient of the optical band gap of InN decreases with increasing electron concentration. This observation can be explained with a model that takes into account the band gap filling effect.

- The wurtzite to rocksalt phase transition has been observed around 15 GPa in high-pressure optical absorption measurements. Around the phase transition, the indirect band gap of rocksalt InN was measured as 0.7 eV, and its pressure coefficient as ~23 meV/GPa.

- The refractive index of wurtzite and rocksalt InN has been measured by optical reflectivity under high-pressure in the 1000-7000 cm^{-1} infrared spectral range. A model for the dielectric function of InN including high-electronic transitions, lattice vibrations, free carriers and the fundamental band gap of InN has been used to determine the high-frequency dielectric constant. The relative pressure coefficient, $(1/\varepsilon_\infty)d\varepsilon_\infty/dP$, thus obtained for

wurtzite and rocksalt InN is $-8.8{\cdot}10^{-3}$ GPa^{-1} and $-14.8{\cdot}10^{-3}$ GPa^{-1}, respectively.

6.2. Vibrational properties of InN

- The pressure coefficient of the E_{2l}, E_{2h}, $A_1(TO)$, $E_1(TO)$ and LO optical phonon modes of wurtzite InN have been measured by high-pressure Raman scattering on InN thin films grown on GaN/sapphire templates. From these results the corresponding mode Grüneisen parameters have been obtained. The experimental data have been compared with *ab initio* lattice-dynamical calculations. Good agreement has been found between experimental and calculated values.

- The pressure dependence of the L^- longitudinal optical plasmon coupled mode has been measured by Raman scattering under high pressure for a sample with high free electron concentration. From the pressure coefficient of this mode, the pressure dependency of the effective mass of InN has been evaluated: $(1/m^*)dm^*/dP = 0.031$ GPa^{-1}, which is in good agreement with $\boldsymbol{k}\cdot\boldsymbol{p}$ theory.

- The effect of Martin's double resonance mechanism on the pressure coefficient of the LO modes of InN has been evaluated considering a two-band $\boldsymbol{k}\cdot\boldsymbol{p}$ Kane model. It has been found that the pressure coefficient could be somewhat larger, up to 1-2 cm^{-1}/GPa, if an excitation energy close to the band gap of the semiconductor was employed.

- The wurtzite to rocksalt phase transition has been observed by high-pressure Raman scattering at ~13 GPa. The pressure coefficients and mode Grüneisen parameters of the different Raman features have been obtained. Also, the rocksalt to wurtzite back transition has been found at ~2 GPa. It has been found that, after the transitions, the Raman spectra are dominated by disorder-activated first order modes. The Raman features have been

compared to the phonon density of states obtained from *ab initio* lattice dynamical calculations.

6.3. Optical and vibrational properties of InGaN

- The optical band gap of InGaN epilayers grown on GaN/sapphire substrates has been determined by optical absorption, photoluminescence and cathodoluminescence for the whole composition range. Composition inhomogeneity, residual electron concentration and strain modify the optical band gap measured with absorption or luminescence techniques. We have obtained corrected bandgap values for the InGaN samples studied in this thesis. From these values we infer a bowing parameter of $b = 1.5$ eV.

- The frequency of the $A_1(LO)$ and E_{2h} phonon modes of $In_xGa_{1-x}N$ epilayers grown on GaN buffer layers and sapphire substrates have been reported for different indium compositions in the range $0.25 < x < 0.75$. After correcting strain effects it has been found that the dependency of the frequency with composition is linear for the $A_1(LO)$ mode and parabolic for the E_{2h} mode. The fitted bowing parameter for the dependency of the E_{2h} mode is $b = 46$ cm^{-1}.

- It has been shown that selective resonant excitation arising from composition fluctuations importantly affect the frequency of the $A_1(LO)$ mode as measured by Raman scattering under resonant excitation conditions. The dependence of the frequency of the $A_1(LO)$ Raman peak with excitation energy has been qualitatively described by a model that assumes a non-homogeneous composition distribution.

- High-pressure Raman measurements have been performed on InGaN epilayers grown on GaN/sapphire and Si(111) substrates. It has been found that the phonon pressure coefficient of the $A_1(LO)$ phonon mode is higher for the samples grown on silicon and lower for the samples grown on GaN.

This result has been attributed to the difference in compressibility of the substrates.

- Taking into account the substrate effect on the pressure coefficient of InGaN epilayers it has been found that the dependency of the pressure coefficient of the A_1(LO) for InGaN is well described by a linear interpolation of the pressure coefficient of the compositional end members, using 3.8 cm^{-1}/GPa for GaN and 5.2 cm^{-1}/GPa for InN.

- The zone-folding effect on the acoustic modes of InGaN/GaN superlattices has been investigated by means of Raman scattering. For the Raman measurements, a novel ultralow wavenumber filtering module has been used to gain access to low wavenumber Raman modes. It has been found that the wavenumber of the LA doublets is well described by the elastic continuum theory. From the Raman measurements, the period of the superlattices has been calculated and found to be in good agreement with XRD measurements.

- The surface acoustic wave velocities of InGaN epilayers grown on GaN/Al_2O_3 substrates have been measured by means of high-resolution Brillouin spectroscopy. These results have been evaluated with simulations based on the calculation of Green's function for the determination of surface acoustic waves in epilayers. We conclude that the elastic constants of InGaN can be described with a parabolic dependence, in agreement with previous *ab initio* calculations on clustered supercells.

APPENDIXES

A. Attributions

I hereby declare that, to the best of my knowledge, all the publications presented in this thesis contain original results, and that any of these articles has been previously used for the dissertation of any doctorate degree. Also, this thesis accomplishes the University of Barcelona regulations for thesis presented as a compendium of articles. With regard to this, I would like to note that the present thesis contains 4 or more articles published in research journals of the first quartile in the thematic classification of the "Science Citation Index" ranking (Articles 3.1, 3.2, 4.1, 4.3, 5.2, 5.3 and 5.4). In addition, more than half of these articles are not in a "letter" format (Articles 3.1, 4.2, 4.3, 5.1 and 5.2).

The articles presented in this thesis are the result of the collaborative work between the members of the Optical Properties Group at the Institute of Earth Sciences Jaume Almera (CSIC) as well as of scientific collaborations with other research groups such as the Applied Physics Departments at University of Valencia and Polytechnic University of Valencia, and ICMM-CSIC in Madrid. The samples studied in this thesis were provided by laboratories at Ritsumeikan University, Japan, the Otto-von-Guericke University, Germany, and the University of Houston, USA.

My personal contribution to each of the presented articles is summarized in Table A.1.

Article	3.1	3.2	4.1	4.2	4.3	5.1	5.2	5.3	5.4
Design of the experiment		✓		✓	✓	✓			✓
Experimental measurements	✓	✓	✓	✓	✓	✓			✓
Analysis of the experimental data	✓	✓	✓	✓	✓	✓	✓	✓	✓
Preparation of figures and tables	✓	✓	✓	✓	✓	✓	✓		✓
Discussion of the results	✓	✓	✓	✓	✓	✓	✓	✓	✓
Writing up of the manuscript		✓		✓		✓			✓
Review and correction of the article	✓	✓	✓	✓	✓	✓	✓	✓	✓
First author		✓		✓		✓			✓

Table A.1. Personal attributions to the articles included in the results section of this thesis.

B. List of published works

The format of the present thesis is a compendium of nine published articles. The full reference to each of these articles is listed below.

I. J. Ibáñez, A. Segura, B. García-Domene, R. Oliva, F. J. Manjón, T. Yamaguchi, Y. Nanishi and L. Artús. *High-pressure optical absorption in InN: Electron density dependence in the wurtzite phase and reevaluation of the indirect band gap of rocksalt InN*. Phys. Rev. B **86**, 035210 (2012).

II. R. Oliva, A. Segura, J. Ibáñez, T. Yamaguchi, Y. Nanishi and L. Artús. *Pressure dependence of the refractive index in wurtzite and rocksalt indium nitride*. Appl. Phys. Lett. **105**, 232111 (2014).

III. J. Ibáñez, F. J. Manjón, A. Segura, R. Oliva, R. Cuscó, R. Vilaplana, T. Yamaguchi, Y. Nanishi and L. Artús. *High-pressure Raman scattering in wurtzite indium nitride*. Appl. Phys. Lett. **99**, 011908 (2011).

IV. R. Oliva, J. Ibáñez, L. Artús, R. Cuscó, J. Zúñiga-Pérez, and V. Muñoz-Sanjosé. *High-pressure Raman scattering of CdO thin films grown by metal-organic vapor phase epitaxy*. J. Appl. Phys. **113**, 053514 (2013).

V. J. Ibáñez, R. Oliva, F. J. Manjón, A. Segura, T. Yamaguchi, Y. Nanishi, R. Cuscó, and L. Artús. *High-pressure lattice dynamics in wurtzite and rocksalt indium nitride investigated by means of Raman spectroscopy*. Phys. Rev. B **88**, 115202 (2013).

VI. R. Oliva, J. Ibáñez, R. Cuscó, R. Kudrawiec, J. Serafinczuk, O. Martínez, J. Jiménez, M. Henini, C. Boney, A. Bensaoula and L. Artús. *Raman scattering by E_{2h} and A_1(LO) phonons of $In_xGa_{1-x}N$ epilayers ($0.25 < x < 0.75$) grown by molecular beam epitaxy*. J. Appl. Phys. **111**, 063502 (2012).

VII. J. Ibáñez, A. Rapaport, C. Boney, R. Oliva, R. Cuscó, A. Bensaoula, and L. Artús. *Raman scattering by folded acoustic phonons in InGaN/GaN superlattices*. J. Raman Spectrosc. **43**, 237 (2012).

VIII. R. J. Jiménez-Riobóo, R. Cuscó, R. Oliva, N. Domènech-Amador, C. Prieto, J. Ibáñez, C. Boney, A. Bensaoula, and L. Artús. *Brillouin scattering determination of the surface acoustic wave velocity in $In_xGa_{1-x}N$: A probe into the elastic constants*. Appl. Phys. Lett. **101**, 062103 (2012).

IX. R. Oliva, J. Ibáñez, R. Cuscó, A. Dadgar, A. Krost, J. Gandhi, A. Bensaoula, and L. Artús. *High-pressure Raman scattering in InGaN heteroepitaxial layers: Effect of the substrate on the phonon pressure coefficients*. Appl. Phys. Lett. **104**, 142101 (2014).

C. Resum en català

Introducció

En la darrera dècada l'estudi dels materials semiconductors ha augmentat significativament per les potencials aplicacions que aquests ofereixen en el creixent mercat de la optoelectrònica. Un dels semiconductors més prometedors és el nitrur de gal·li indi ($In_xGa_{1-x}N$). L'interès per aquest aliatge va créixer arran del descobriment l'any 2002 del gap del nitrur d'indi (InN), establert als 0.7 eV. Aquesta troballa mostrava que l'InGaN és un semiconductor de gap directe que cobreix tot l'espectre visible, des dels 0.7 eV per al InN fins als 3.4 eV per al GaN. A més, tenint en compte que tant el InN com el GaN posseeixen propietats electròniques i òptiques excepcionals (tals com l'alta conductivitat del InN o l'alta tensió de ruptura del GaN), les perspectives per al InGaN actuant com a material actiu en una gran varietat de dispositius optoelectrònics són excel·lents. Cal destacar que la obtenció de díodes emissors de llum altament eficients basats en nitrur de gal·li (GaN) i nitrur de gal·li indi ($In_xGa_{1-x}N$) va merèixer el premi Nobel de física per a I. Akasaki, H. Amano i S. Nakamura l'any 2014.

Malgrat l'alt interès tecnològic del InGaN i els seus compostos binaris, avui en dia les seves propietats optoelectròniques no estan totalment caracteritzades. Per tant, és necessari continuar investigant amb la finalitat de desvetllar les propietats fonamentals rellevants d'aquest compost, millorar el creixement cristal·lí i conseqüentment optimitzar el disseny de dispositius optoelectrònics.

L'absorció òptica o l'espectroscòpia de transformada de Fourier en infraroig (FTIR) són tècniques espectroscòpies molt útils per a l'estudi de propietats optoelectròniques dels semiconductors, tals com la banda prohibida electrònica (en anglès *bandgap*) o l'índex de refracció. Des d'un punt de vista de caracterització, també resulten molt informatives les tècniques vibracionals com les espectroscòpies de Raman o Brillouin. Aquestes aporten informació com les fases cristal·lines, tensió a la xarxa cristal·lina o la presència de defectes així com també ens permeten mesurar propietats vibracionals, per exemple les energies fonòniques o la velocitat del so. La

combinació d'aquestes tècniques amb l'alta pressió permet mesurar l'efecte de les distàncies interatòmiques en les propietats fonamentals dels semiconductors. L'ús de l'alta pressió també ens permet contrastar models computacionals (com la teoria del funcional densitat, DFT) utilitzats per a calcular les propietats optoelectròniques i estructurals dels cristalls. En aquesta tesi les tècniques prèviament esmentades s'han implementant a una cel·la d'enclusa de diamant (DAC) per a l'estudi de les propietats fonamentals del InGaN i del InN en condicions d'alta pressió. Cal notar que la DAC resulta especialment adient per a la realització d'experiments òptics ja que les encluses són transparents en un ampli rang espectral i permeten fer mesures *in situ*. Els experiments presentats en aquesta tesi s'han realitzat fins a una pressió de 20 GPa.

Propietats òptiques del InN

Una de les principals dificultats per a la caracterització de les propietats òptiques del InN ha estat la dificultat de créixer InN lliure de defectes i amb baixa densitat de càrrega. En aquesta tesi, hem estudiat mostres d'alta qualitat cristal·lina amb diferents densitat de càrrega per tal d'esbrinar-ne l'efecte en el coeficient de pressió de la banda prohibida mesurat per absorció òptica. Aquest estudi ens ha permès establir el coeficient de pressió de la banda prohibida fonamental del InN a 32 meV/GPa. A més, també hem mesurat la transició de wurtzita-a-halita del InN. Això ens ha permès establir la banda prohibida fonamental de la fase halita del nitrur d'indi a 0.7 eV per a la pressió de transició (~15 GPa) i el seu coeficient de pressió ~23 meV/GPa.

En un segon treball, hem mesurat la dependència amb pressió de l'índex de refracció de les fases wurtzita i halita del InN mitjançant FTIR en condicions d'alta pressió. A partir de l'anàlisi de l'espectre FTIR del InN mitjançant un model de la funció dielèctrica que inclou les contribucions fonòniques, plasmòniques, de gap directe i gaps d'alta energia, n'hem obtingut el coeficient de pressió de la constant dielèctrica d'alta freqüència: $-8.8\cdot10^{-3}$ GPa^{-1} i $-14.8\cdot10^{-3}$ GPa^{-1} per les fases wurtzita i halita, respectivament.

Propietats vibracionals del InN

El nitrur d'indi en fase wurtzita (grup espacial C_{6v}^4) té sis modes fonònics amb activitat Raman (*Raman active modes*). Utilitzant capes primes de InN crescudes en diferents direccions (cares *c* i *a*), hem mesurat les freqüències fonòniques de tots els modes i les seves dependències amb pressió. Aquests resultats ens han permès calcular els modes de Grüneisen associats a cada mode fonònic. Aquests valors han estat comparats amb càlculs de dinàmica de xarxa a primers principis. Els càlculs i els experiments mostren bon acord. Hem observat que les freqüències de tots els modes fonònics augmenten amb la pressió excepte per al mode E_{2l}, que presenta un caràcter *soft mode*, indicatiu d'una inestabilitat estructural que resulta en la transició de fase wurtzita a halita.

Per a l'estructura halita no s'espera observar modes Raman actius de primer ordre. Per al cas del CdO hem mostrat com els experiments de Raman sota pressió juntament amb càlculs *ab initio* ens permeten identificar l'origen de les bandes fonòniques de segon ordre. Tanmateix, en el cas del InN, l'estructura cristal·lina es desordena després de la transició de fase i presenta defectes estructurals que relaxen les regles de selecció Raman. Això permet que els modes de primer ordre participin en el procés Raman. L'espectre Raman resultant es correspon la densitat d'estats fonónics. Mitjançant càlculs de corbes de dispersió fonòniques per a les estructures wurtzita i halita a diferents pressions, hem pogut identificar totes les característiques de l'espectre Raman per a ambdues fases.

D'altra banda, analitzant una mostra amb alta densitat de càrrega (N_e = $1.6 \cdot 10^{19}$ cm^{-3}) hem obtingut la dependència amb pressió d'un mode longitudinal òptic acoblat amb el plasma (LOPCM). A partir d'aquesta dependència hem estimat el coeficient de pressió de la massa efectiva del nitrur d'indi, $3.1 \cdot 10^{-2}$ GPa^{-1}, que correspon bé amb el obtingut a partir de la teoria **k·p**.

Per a validar els coeficients de pressió dels modes fonònics mesurats experimentalment, hem avaluat l'efecte de dues possibles fonts d'error. En primer lloc, el possible efecte de substrat o de densitat de càrrega residual. Estudiant mostres crescudes en diferents condicions hem conclòs que aquests efectes no són rellevants. En segon lloc, hem considerat l'impacte del mecanisme de Martin de doble

ressonància en els coeficients de pressió dels modes longitudinals òptics (en el que fonons de llarg vector d'ona participen en el procés Raman). Hem conclòs que aquest efecte és inferior a l'error experimental.

Propietats òptiques i vibracionals del InGaN

Actualment se sap que la dependència composicional de la banda prohibida del InGaN és sublineal i pot ser ajustada amb una funció parabòlica que depèn de les bandes prohibides dels extrems composicionals i d'un coeficient anomenat paràmetre de parabolicitat (en anglès *bowing parameter*), *b*. La dependència composicional de la banda prohibida del InGaN és difícil de determinar degut a diferents defectes presents en les mostres, els més rellevants són; 1- l'alta densitat de càrrega electrònica residual, 2- tensió elàstica a la xarxa cristal·lina i 3- inhomogeneïtats composicionals. En aquesta tesi hem estimat el paràmetre de parabolicitat tenint en compte aquests tres efectes a partir de mesures de fotoluminescència i absorció òptica en mostres de InGaN d'alta qualitat cristal·lina. El nostre resultat, b = 1.45 eV, és compatible amb els valors de la literatura. A més, hem realitzat un experiment de fotoluminescència sota condicions d'alta pressió hidrostàtica a fi de mesurar el coeficient de pressió de la banda prohibida d'una mostra de $In_{11}Ga_{89}N$.

Pel que fa a les propietats vibracionals, la dependència composicional de les energies fonòniques del InGaN no està totalment ben establerta. Actualment se sap que els modes fonònics A_1(LO) i E_{2h} del InGaN són de comportament a un mode (*one-mode behaviour*), és a dir, les seves freqüències varien contínuament amb la composició, des d'un extrem (InN) fins a l'altre (GaN). Tanmateix, la freqüència del mode A_1(LO) mesurat en aquesta tesi presenta fortes desviacions d'aquesta tendència. Això és degut a que les capes primes aquí utilitzades estan acomodades a un substrat de GaN de paràmetre de xarxa diferent. Aquest acoblament epitaxial resulta en una tensió a la xarxa cristal·lina de la capa prima que incrementa significativament les freqüències fonòniques. Gràcies a mesures de difracció de rajos X d'alta resolució (HRXRD) en les nostres mostres hem pogut quantificar aquesta tensió i corregir-la per a obtenir la dependència composicional de les freqüències dels modes A_1(LO) i E_{2h}. Hem conclòs que el mode A_1(LO) segueix una dependència lineal amb la composició, mentre que el mode E_{2h} segueix una dependència sublineal que es pot

descriure per una funció parabòlica amb un paràmetre de parabolicitat de $b = 46$ cm^{-1}. D'altra banda, els nostres experiments constaten que les freqüències mesurades del mode A_1(LO) són fortament dependents de la longitud d'excitació utilitzada en l'experiment Raman. Hem atribuït aquest fenomen a un efecte de ressonància selectiva, fruit de la naturalesa ressonant del mode A_1(LO) i de la inhomogeneïtat composicional. Hem proposat un model quantitatiu que explica satisfactòriament l'efecte de ressonància selectiva mesurat a la literatura i en aquest treball.

Hem realitzat mesures d'alta pressió hidrostàtica per a obtenir el coeficient de pressió del mode A_1(LO) i el seu mode de Grüneisen. A fi d'avaluar l'efecte de substrat en el coeficient de pressió, hem realitzat experiments amb capes primes crescudes sobre dos tipus de substrats. Els substrats són més o menys (Si i GaN, respectivament) compressius que la capa prima de InGaN. Hem observat que les mostres crescudes sobre un substrat més (menys) compressiu presenten un coeficient de pressió major (menor). Aquestes observacions ens han permès concloure que la dependència composicional del coeficient de pressió i mode de Grüneisen del InGaN són lineals.

Per a l'estudi dels modes fonònics acústics, hem mesurat els modes LA plegats (LA *folded modes*) de superxarxes de InGaN/GaN crescudes sobre safir mitjançant un espectròmetre Raman acoblat a un mòdul de filtrat de baixa freqüència. Hem reproduït el comportament de dispersió lineal dels modes LA d'acord amb la teoria elàstica de medis continus (*elàstic continuum theory*). A partir de les freqüències dels modes plegats LA, hem calculat la periodicitat de la superxarxa i hem obtingut un bon acord amb els valors obtinguts per mesures de difracció de rajos X. Per tal d'obtenir informació sobre la dependència composicional de les constants elàstiques, hem mesurat els modes superficials acústics (SAW) de capes primes de InGaN amb espectroscòpia de Brillouin d'alta resolució. Ajustant simulacions basades en el formulisme de Green, hem conclòs que els resultats experimentals queden ben descrits si s'assumeix una dependència composicional de tipus parabòlica de les constants elàstiques.